The University Of Sheffield.

Department of Materials Science and Engineering

The University of Sheffield

Synthesis and Electrical Characterization of Calcia-stabilised Zirconia and Mg-doped Alumina

---

Submitted for the Degree of Doctor of Philosophy

Julia Ramírez González

Supervisor: Prof. Anthony R. West

September 2020

Declaration

This thesis is submitted in consideration for the award of Doctor of Philosophy. It is believed to be completely original, except where references have been made.

I, the author, confirm that the Thesis is my own work. I am aware of the University's Guidance on the Use of Unfair Means (www.sheffield.ac.uk/ssid/unfair-means). This work has not been previously been presented for an award at this, or any other, university.

Part of this work resulted in the following manuscripts which have been published or submitted to publication and have been added as result chapters in this thesis.

- J. Ramírez-González and A. R. West, "Flash phenomena in lime-stabilised zirconia oxide ion conductor," *Energy Reports*, vol. 6, pp. 142–147, 2020. DOI: 10.1016/j.egyr.2020.03.008
- J. Ramírez-González and A. R. West, "Electrical properties of calcia-stabilised zirconia ceramics," *J. Eur. Ceram. Soc.*, vol. 40, pp. 5602–5611, 2020. DOI: 10.1016/j.jeurceramsoc.2020.06.023
- J. Ramírez-González and A. R. West, "Electrical properties of Mg-doped and Mg, Si co-doped alumina," *J. Eur. Ceram. Soc.*, (in press), 2020. DOI: 10.1016/j.jeurceramsoc.2020.12.040
- J. Ramírez-González and A. R. West, "Electrical properties of calcia-stabilised zirconia ceramics: *dc* bias effect. In preparation

Julia Ramírez González

September 2020

A mis padres, Verónica y Francisco,
los pilares que me sustentan todos los días.

A Daniel,
mi compañero en la cotidianidad de la vida científica.

Acknowledgements

I would like to express my sincere gratitude to my patient and supportive supervisor Prof Anthony R West, who has guided me and kept me motivated throughout this process. I am extremely grateful for all the shared knowledge during our multitude of meetings.

From the Functional Materials and Devices Group, I would the to thank:

- All the Post-docs, Dr Linhao Li (Leo), Dr Ge Wang, Dr Fan Yang, Dr Dawei Wang, Dr Zhilun Lu (Jack), Dr Whitney Schmidt, Dr Ali Mostaed for having the patience and taking the time to solve all of my questions regarding equipment or techniques. Specials thanks to Dr Xavier Vendrell who I bother the most as we worked on similar projects.
- My labmates Jessica Andrews, George Kerridge, Daniel Martin, Daniel Button, Ed Rackley, Ana Casas, Xiaoliang Fang, Xuan Xi (Joanna) Meshari Alotaibi, Fawaz Almutairi, Laurie Middlemiss, Wadir Kargar, Xiaoyuan Zhu (Amos), and the ones that have finished their degree Dr Wan Fareen Shazli, Dr Yun Dang, Dr Bo Dong, Dr Emilio Pradal, Dr Shunsuke Murakami and Dr Sinan El-Faouri for making my days in the lab and the office enjoyable.
- The lab technicians Kerry MacLaughlin and Andrew Mould for always helping me to find my way around the lab.

From the XRD Research Facility and the Sorby Centre I would like to thank Nik Reeves-McLaren and Le Ma for guiding me around the XRD and SEM equipment.

I am also very grateful to my internal examiners from my first- and second-year viva, Prof Derek Sinclair and Dr Colin Freeman for pointing out the opportunity areas and weakness of the work, in order to improve it.

For the assistance on the setting up of the flash sintering equipment, I would like to thank Frank Fletcher, Mark McIntosh and Zarah Hill from the technical support for electronic and electrical services, Adrian Lumby, Andy Patrick and Charles V Walsh at the workshop and Health and Safety department. Without their input this project would have not been possible.

I thank the PGR Tutors Dr Rebecca Boston and Dr Tom Hayward for giving a space and time to talk with them. Also, I want to thank Andy Keating and Ann Newbold, for their help in all of the admin work I needed to do along these years.

To the Centre of Doctoral Training I am grateful for giving me the opportunity to be part of cohort 3, meet incredible people from different backgrounds, and make aware of the big picture of the energy system/market. I want to give a special thanks to Sharon Brown, who always supported me since the day of my application.

For keeping me mentally sane during my writing period along the lockdown, I want to thank Dr Sarah Price, my writing mentor.

Special thanks to CONACYT for funding my postgraduate studies under the scholarship: "*Becas CONACYT al extranjero" registro 578893*.

Abstract

In order to gain further understanding about the onset mechanisms of flash sintering, the electrical properties of cubic calcia-stabilised zirconia, CSZ ($Ca_xZr_{1-x}O_{2-x}$: $0.12 \leq x \leq 0.18$) and Mg-doped alumina (0.05wt%MgO-Al_2O_3 and 0.5wt%(MgO/SiO_2)-Al_2O_3) ceramics were investigated using impedance spectroscopy as a function of temperature, oxygen partial pressure and applied *dc* bias. Equivalent circuit analysis was carried out to identify the electrical microstructure of the materials. As part of this process, the relative importance of individual elements to the overall impedance response was highlighted by a new approach by the deconvolution of the impedance spectra.

The bulk, grain boundary and electrode contact impedances of CSZ ceramics were characterised over the temperature range 200-930°C. The most appropriate equivalent circuit to characterise the bulk response required inclusion of a dielectric component, represented by a series RC element, in parallel with the oxide ion conductivity represented by a parallel combination of a resistance, capacitance and constant phase element. The dielectric component may be attributed to defect complexes involving Ca_{Zr}''–$V_O^{\bullet\bullet}$ pairs whereas long range conduction involves single oxygen vacancies. The activation energy for the dielectric component increased with increasing *x*. This was attributed to an increase in the number of pairs or to their coalescence into larger aggregates, causing greater difficulty in reorientation of the dipoles. The sample-electrode interface response was deconvoluted into two components, the charge transfer (R_{ct}) and diffusion resistance (R_{diff}), where $R_{ct} << R_{diff}$.

Impedance analysis of CSZ ceramics under different atmospheres showed that the limits of the electrolytic domain vary with temperature and composition. Around 400°C, the bulk conductivity of all compositions remained independent of pO_2 and the samples were pure oxide ion conductors, but near 930°C, x=0.12 showed introduction of n-type conduction and x=0.18 showed p-type whereas the intermediate composition x=0.15 did not show any pO_2 dependence.

The total resistance of CSZ ceramics decreased with application of a *dc* bias. This was attributed to the introduction of p-type conductivity. Electron holes might be located on under-bonded oxygen ions, associated either with the Ca dopant ions, or those near the ceramic surface, resulting in a mixed ionic-electronic conduction pathway.

A flash sintering set-up was built. Flash sintering experiments on CSZ x=0.15 showed increased conductivity and emission of light, but no sample densification. It was concluded that the sintering process can be separated from the emission of light and increase in conductivity and therefore, that the origin of these phenomena, ie flash and sintering, might be different.

Impedance measurements on two Mg-doped alumina ceramics, over the temperature range 400-910°C, showed a combination of low-level oxide ion conductivity and p-type electronic conductivity, depending on temperature, oxygen partial pressure and dopant content. The oxide ion conductivity was attributed to oxygen vacancies, introduced as charge compensation for the Mg dopant. The p-type conductivity was attributed to hole location on under-bonded oxide ions and was identified as the dominant conduction pathway for measurements in air at high temperatures. The sample resistance increased on application of a *dc* bias. This was attributed to electron-hole recombination and the loss of p-type conductivity associated with oxygen loss.

Content

Chapter 1
Introduction and aims

1.1 Ceramic industry

The global ceramic market its growing and expected to reach a value of approximately $407 billion dollars by 2025, according to the 2019 Grand View Research, Inc forecast [1]. The development of technical ceramic sector, will contribute to this growth as it is foreseen to have a compound annual growth rate (CAGR) of 9.1% from 2019 to 2025 [2].

The demand of this type of ceramics relies on their magnetic, optical, thermal and electrical properties, that can be tailored to specific applications [3], Figure 1.1. Therefore, they can be used in a wide range of applications, as battery electrodes, spark plug insulators in the automotive industry, cutting tools, material for implants as hip joints or, in the purification of natural gas, among others.

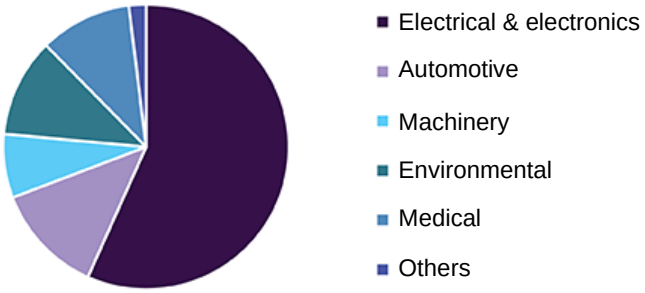

Figure 1.1. *End use of advance ceramics, 2015* [3]

Out of the different sectors in the ceramic industry, the advance or technical ceramics is the one with the highest energy consumption [4], Table 1.1.

Table 1.1. *Specific energy consumption in the ceramic industry in Europe, 2003* [4].

Sector	**Specific energy consumption (*GJ/t*)**
Brick and roof tiles	2.31
Wall and floor tiles	5.60
Refractory products	5.57
Sanitaryware	21.87
Vitrified clay pipes	5.23
Table-and ornamentalware	45.18
Technical ceramics	50.39

One of the main reasons for the high energy consumption, is the firing temperature required during the manufacture of these type of ceramic, ranging from 450 to 2500°C, reaching higher temperatures compared to the rest of the ceramic sectors, Figure 1.2.

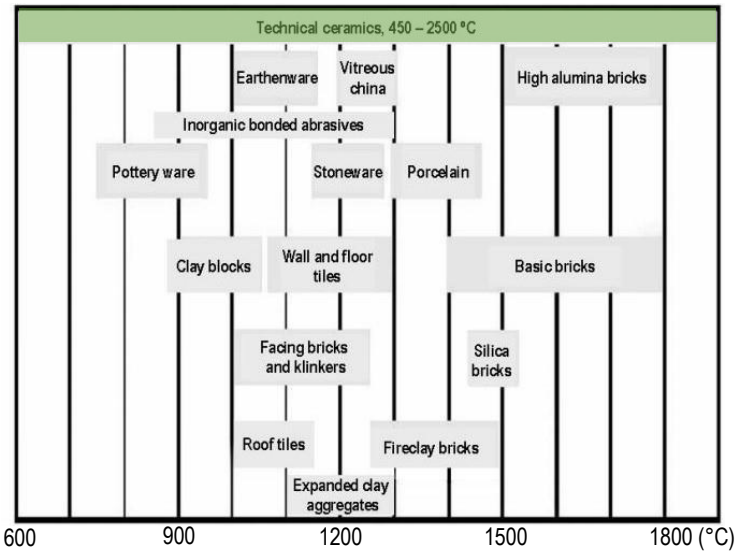

Figure 1.2. *Firing temperature range for different ceramic products* [4].

The type of fuel used in the production of ceramics in mainly natural gas and liquified petroleum gas (LPG), therefore the carbon footprint of these materials is high, Figure 1.3(a). The industry sector is aware of the issue and wants to take action, according to the Industrial Decarbonisation & Energy Efficiency Roadmaps for the Ceramic sector to 2050, published in March 2015, prepared for the Department of Energy and Climate Change and the Department for Business, Innovation and Skills [5]. The target relies on the electrification of kilns, Figure 1.3(b).

(a) (b)

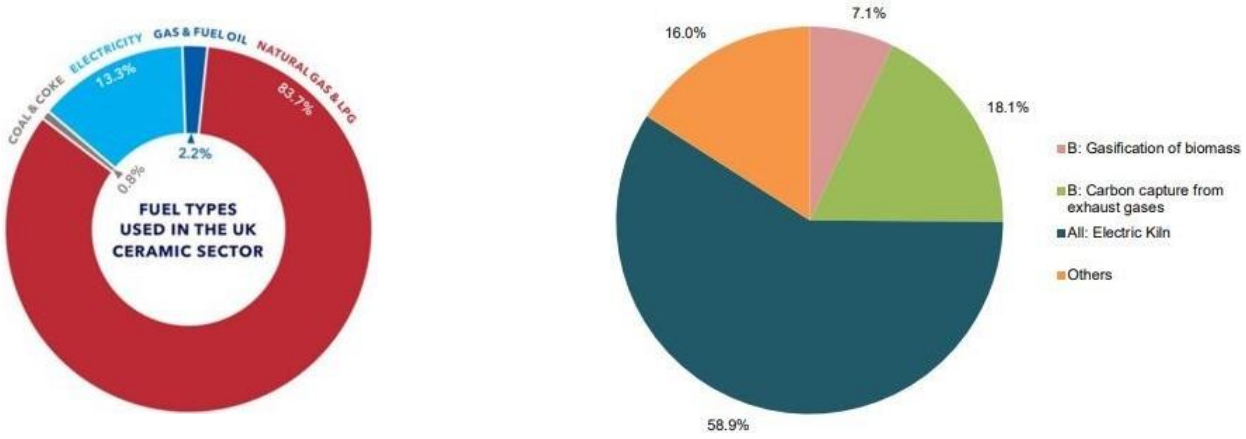

Figure 1.3. *(a) Types of fuels in the ceramic sector, (b) Trend in order to reduce the CO_2 emissions by 2050, according to the Maximum Technical Pathway* [5].

1.2 Flash sintering and project aims

Having an idea of the future direction of the ceramic industry, electric field assisted sintering techniques have become attractive. *Flash sintering*, is able to reduce the sintering time from hours to ≤ 1 minute [6]. The potential of this technique has been already put into practice by Lucideon [7], the first company to incorporate flash sintering in their production line. Nevertheless, this technique is quite new, as it was discovered in 2010, and there are still fundamental questions about chemical and physical processes occurring during the sintering process [8].

For this reason, *the main aim of this project is to try to understand more about the onset mechanisms of flash sintering*, by choosing materials that already have been successfully flash sintered; such as cubic-stabilised zirconia and Mg-doped alumina [8],[9]. These two materials are ionic

conductors[10][11] with a conductivity typically in the order of 10^{-3} Scm^{-1} [12] and 10^{-8} Scm^{-1} [13] at 500°C, respectively. However, the introduction of electronic conduction in yttria-stabilised zirconia (YSZ) [14][15] and the dielectric breakdown of alumina [16] under certain conditions may be related to the onset of the flash sintering. Calcia-stabilised zirconia (CSZ) was chosen over YSZ as in the former the number of cations needed to obtain the same number of defects in the crystal structure is halved [10].

Therefore, calcia-stabilised zirconia and Mg-doped alumina were chosen to investigate the pre-monitoring region of flash sintering, which can be regarded as lower temperatures and lower electric field than the ones required for the *flash event.* In doing so, this study gives an insight to the conductivity dependence of oxygen partial pressure (pO_2) and *dc* bias, along with a detailed equivalent circuit analysis which explores new ways to deconvolute the impedance spectra. In addition, a flash sintering machine was set up and CSZ samples were tested.

1.3 References

[1] Grand View Research, "Ceramics Market Size Worth $407.72 Billion By 2025," 2019. [Online]. Available: https://www.grandviewresearch.com/press-release/global-ceramics-market.

[2] Grand View Research, "Ceramics Market Size, Share & Trends Analysis Report By Product (Traditional, Advanced), By Application (Sanitary Ware, Abrasives, Tiles), By End-Use; By Region, And Segment Forecasts, 2019 - 2025," 2019. [Online]. Available: https://www.grandviewresearch.com/industry-analysis/ceramics-market.

[3] Grand View Research, "Global Advanced Ceramics Market Size | Industry Report, 2018-2024," 2018. [Online]. Available: https://www.grandviewresearch.com/industry-analysis/advanced-ceramics-market. [Accessed: 26-May-2018].

[4] European Comission, "Reference Document on Best Available Techniques in the Ceramic Manufacturing Industry," *Ceram. Manuf. Ind.*, no. August, pp. 210–211, 2007.

[5] WSP, Parsons Brinkerhoff, and DNV-GL, "Industrial Decarbonisation and Energy Efficiency Roadmaps to 2050, Ceramic Sector," 2015.

[6] M. Biesuz and V. M. Sglavo, "Flash sintering of ceramics," *J. Eur. Ceram. Soc.*, vol. 39, no. May 2018, pp. 115–143, 2018.

[7] "Flash Sintering of Ceramics | Lucideon." [Online]. Available: https://www.lucideon.com/healthcare/technologies/flash-sintering. [Accessed: 26-May-2018].

[8] M. Cologna, B. Rashkova, and R. Raj, "Flash sintering of nanograin zirconia in < 5s at 850°C," *J. Am. Ceram. Soc.*, vol. 93, no. 11, pp. 3556–3559, 2010.

[9] M. Cologna, J. S. C. Francis, and R. Raj, "Field assisted and flash sintering of alumina and its relationship to conductivity and MgO-doping," *J. Eur. Ceram. Soc.*, vol. 31, no. 15, pp. 2827–2837, 2011.

[10] T. H. Etsell and S. N. Flengas, "The electrical properties of solid oxide electrolytes," *Chem. Rev.*, vol. 70, no. 3, pp. 339–376, 1970.

[11] A. H. Heuer and K. P. D. Lagerlof, "Oxygen self-diffusion in corundum (α-Al_2O_3): A conundrum," *Philos. Mag. Lett.*, vol. 79, no. 8, pp. 619–627, 1999.

[12] J. Zhang, C. Lenser, N. H. Menzler, and O. Guillon, "Comparison of solid oxide fuel cell (SOFC) electrolyte materials for operation at 500 °C," *Solid State Ionics*, vol. 344, no. November 2019, p. 115138, 2020.

[13] J. Öijerholm, J. Pan, and B. Jönsson, "Influence of Grain Size on Ionic Conductivity of Pure and Dense alpha-Al_2O_3 in the Temperature Range 400-1000 degrees°C," in *6th International Symposium on High Temperature Corrosion and Protection of Materials Les Embiez, FRANCE*, 2004, pp. 865–872.

[14] J.-H. Park and R. N. Blumenthal, "Electronic Transport in 8 Mole Percent Y_2O_3-ZrO_2," *J. Electrochem. Soc.*, vol. 136, no. 10, p. 2867, 1989.

[15] X. Vendrell and A. R. West, "Induced p-type semiconductivity in yttria-stabilized zirconia," *J. Am. Ceram. Soc.*, vol. 102, no. 10, pp. 6100–6106, 2019.

[16] C. Neusel, H. Jelitto, D. Schmidt, R. Janssen, F. Felten, and G. A. Schneider, “Dielectric breakdown of alumina single crystals,” *J. Eur. Ceram. Soc.*, vol. 32, no. 5, pp. 1053–1057, 2012.

Chapter 2
Literature Review

2.1 Zirconia

Zirconium dioxide (ZrO_2) commonly known as "zirconia" is a pale crystalline oxide, between ivory and white [1]. This compound can be found in three different crystal structures: monoclinic ($P2_1/c$) below 1,170°C, tetragonal ($P4_2/nmc$) from 1,170°C to 2,370°C and, cubic (Fm3m) above 2,370°C until its melting point around 2,680°C [2], Figure 2.1.

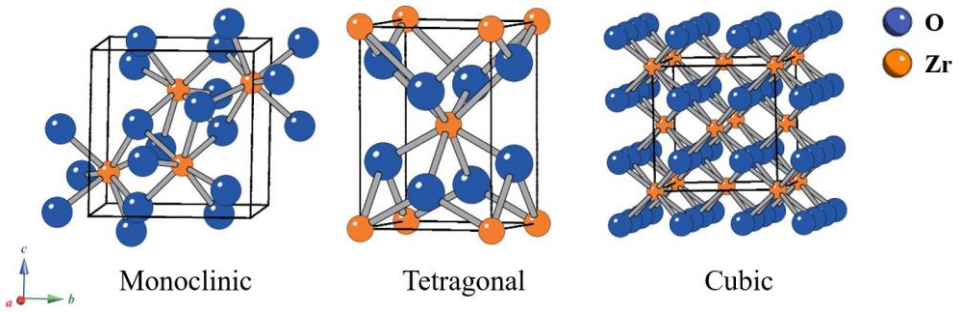

Figure 2.1. *Crystal structures of the zirconia polymorphs* [3].

Volume changes are present in the transition from one crystal structure to another, which induces mechanical stresses that deteriorates the material. In order to avoid these volume changes, the tetragonal and cubic phases can be stabilised at room temperature by adding small percentages of other oxides (typically alkaline earth or rare earth oxides) as: magnesium oxide (MgO), yttrium oxide (Y_2O_3), cerium oxide (CeO_2), calcium oxide (CaO) or, scandium oxide (Sc_2O_3) [4]. Stabilised zirconias can be classified in two types: "partially stabilised", which have a tetragonal crystal structure or a combination of cubic and tetragonal and, "fully stabilised", which are single-phase cubic [4].

The first attempt to make zirconia stable at room temperature was by the Norton Co., in the 1950s. Their main purpose was to create a thermally insulating material for induction furnace applications and as refractory bricks [5]. Nowadays, stabilised zirconias have a wide range of applications; they are still used as heating elements, but also as part of medical devices, cutting tools, and materials for implants, due to their wear and chemical resistance and biocompatibility [6]. A further set of applications are related to the high oxide ion conduction of this material and its stability in reducing atmospheres; these characteristics make it suitable to be part of oxygen sensors [7] and, be used as an electrolyte in solid oxide fuel cells [8]. More recently, the possibility to take this material to Mars has been discussed and use it as an electrolyser for carbon monoxide and oxygen, storing chemical energy, which will help to explore the surface of the planet [9].

2.1.1 Yttria-stabilised zirconia

As mentioned above, oxygen ion conduction is one of the main and important characteristics of this material. In the case of yttria-stabilised zirconia (YSZ), ionic conduction is possible due to the presence of oxygen vacancies, which are mobile species. Oxygen vacancies are the product of the compensation mechanism due to the incorporation of dopant, Equation (2.1)

$$Y_2O_3 \xrightarrow{ZrO_2} 2Y'_{Zr} + 3O_O^x + V_O^{\bullet\bullet} \tag{2.1}$$

Nevertheless, mixed conduction (ionic-electronic) behaviour has been found under certain conditions: under different oxygen partial pressures (pO_2) and in the presence of an applied electric field.
There are two equilibrium reactions to consider [10]. The first one at low pO_2, Equation (2.2)

$$O_O^x \rightarrow V_O^{\bullet\bullet} + \tfrac{1}{2}O_{2(g)} + 2e' \tag{2.2}$$

and the second one at high pO_2, Equation (2.3)

$$V_O^{\bullet\bullet} + \tfrac{1}{2}O_{2(g)} \rightarrow O_O^x + 2h^{\bullet} \tag{2.3}$$

To distinguish between p-type and n-type conduction, measurements of conductivity as a function of oxygen partial pressure can be performed. If the slope turns out to be positive, the material would be a p-type conductor, and if is negative the material would be n-type. Usually the slope is of the magnitude between $1/4$ to $1/6$. This can be deducted by writing the point defect reaction for the compensation mechanism on the Kröger-Vink notation, followed by applying the law of mass action and solving for the equilibrium constant to obtain the relation between the charge carrier concentration and the oxygen partial pressure [11], as shown in the supplemtary section. The conductivity of an oxide ion conductor would be independent of oxygen partial pressure. Therefore, a diagram with the conductivity domains of an n-type, p-type and an oxide ion conductor as function of oxygen partial pressure, can be built up, as shown in Figure 2.2.

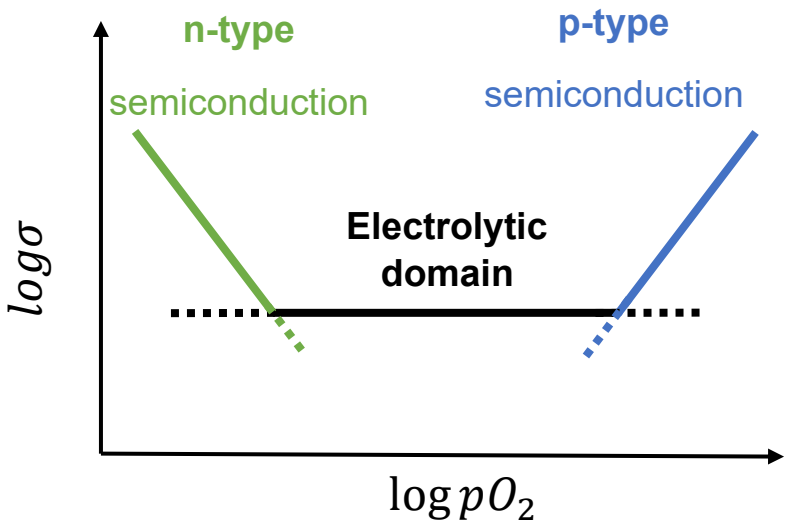

Figure 2.2. *Conductivity as a function of oxygen partial pressure.*

The ionic and electronic conductivity in 8 mole % Y_2O_3-ZrO_2, as function of temperature (800˚-1050°C) and pO_2 (0.21-10^{17}atm), was studied by Park and Blumenthal [12]. They performed oxygen permeation measurements in a gas-tight electrochemical cell and, to obtain the ionic, hole and electron conductivities, the four-probe method was employed. Also, non-steady state permeation measurements, using the gas-switch method, was used to calculate the mobility and diffusion of holes and electrons. They found out that, as temperature increases the p-n transition shifts to higher pO_2, and that holes and electrons are thermally activated moving by a hopping mechanism, Figure 2.3. They assume possible trapping sites for the electronic charge carriers: Y_{Zr}' for the holes and, Zr_{Zr}^{x} for the electrons.

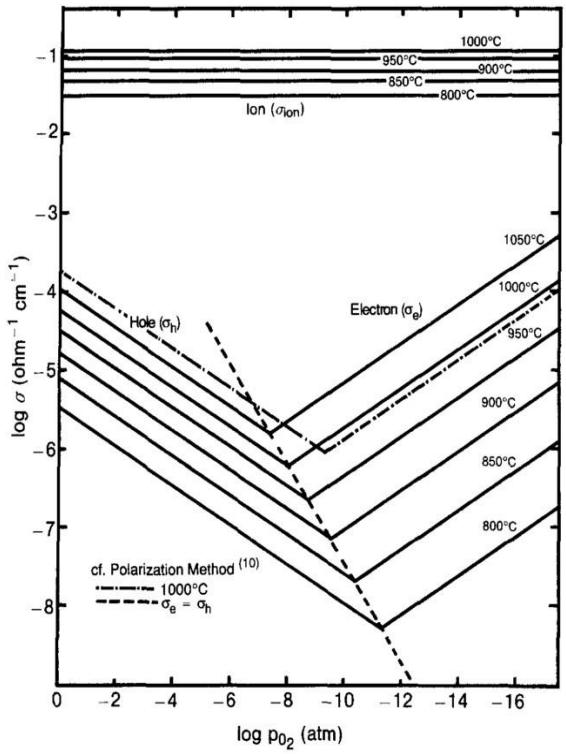

Figure 2.3. *Conductivity of 8 %mole YSZ as function of pO_2, showing electrolytic domain (ionic conduction) at high conductivity values and, transition from hole conductivity (p-type) to electron conduction (n-type) at lower conductivities* [12].

Introduction of p-type conduction in YSZ has been studied by Masó and West [13] and Jovani *et al.* [14]. Samples with composition 8 mole % and 40-70 mole % of yttria were used respectively. Impedance measurements were performed under different pO_2 concentrations (using N_2, air and, O_2 gas). It was found that the bulk and grain boundary resistance decreased with increasing pO_2, which is evidence of p-type conduction. The same effect was found when applying a small *dc* bias. It was proposed that the location of the holes is on oxide ions, situated in the vicinity of acceptor dopants. As these oxide ions are underbonded, they are prone to redox activity: Equation (2.4)

$$O_O^x \rightarrow O_O^{\bullet} + e' \tag{2.4}$$

The resulting electrons participate in surface reactions to maintain the equilibrium for the absorption of the molecular oxygen (left hand side of Equation (2.3)).

Recently, Kirchheim proposed two types of reaction that account for the increment in electronic conductivity in YSZ [15]. He mentions that by applying an electric field, the chemical potential of oxygen vacancies will change. In order to counteract these changes, after an incubation time, the following reactions might occur, driven by Le Chatelier's Principle.

1. *External reaction at the electrolyte-gas interface, controlling the creation of defects*. For samples with large surface areas exposed to oxygen gas, reaction Equations (2.2) and (2.3) might occur. As a consequence, charged regions may be created: n-type and p-type, separated by a mainly ionic region. Molecular oxygen generated at the n-region, is consumed at the p-region, Figure 2.4.

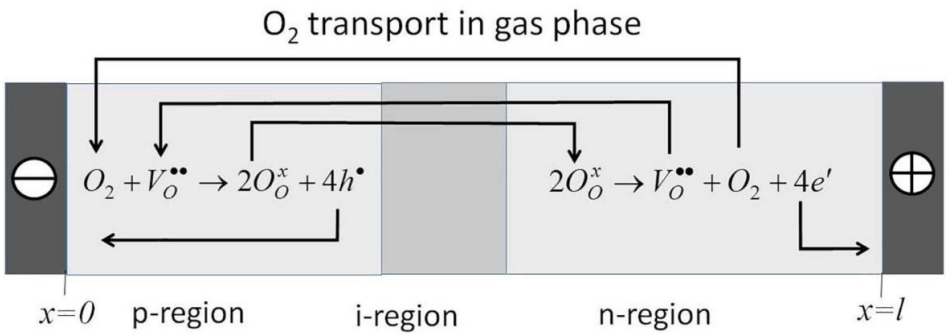

Figure 2.4. *Sample with large surface area exposed to oxygen gas in presence of an electric field. Oxygen vacancies will be attracted to the negative electrode, the high concentration of these species will create a p- region, and depletion of this species near the positive electrode a n-region. In order, to neutralise this flux, lattice oxygen will travel to the n-region. Electrons and holes will be trapped at the corresponding electrodes* [15].

2. *Internal defect reactions*. For samples in the absence of oxygen gas, the creation of internal defects, that compensate the effect of the applied field was proposed. In this case, the generation of single-charged vacancies in the p-region (Equation (2.5)), when present in sufficient in concentration, travel to the n-type region (following Le Chatelier's Principle), and then react according to Equation (2.6), Figure 2.5. Holes and electrons are neutralized at the corresponding electrodes.

$V_O^{\bullet\bullet} \rightarrow V_O^{\bullet} + h^{\bullet}$ (2.5)

$V_O^{\bullet} \rightarrow V_O^{\bullet\bullet} + e'$ (2.6)

The steady state is reached after electromigration occurs and the chemical and electrical potential are in equilibrium, taking into account the polarization of the cell.

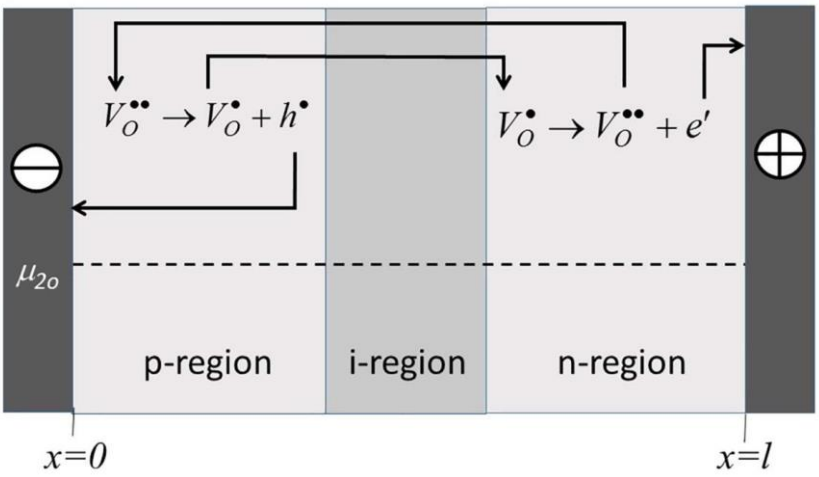

Figure 2.5. *Sample in the absence of oxygen gas in presence of an electric field. Oxygen vacancies will be attracted to the negative electrode, creating a p-region and an n-region on the opposite side. Single charge oxygen vacancies will be created the p-region, and to keep a stationary electric current these will travel to the n-region. If the chemical potential of the concentration $V_O^{\bullet}$ is larger than the electric potential, the latter is possible* [15].

These studies highlight that these conduction mechanisms need further study.

2.1.2 Calcia-stabilised zirconia

Calcia stabilised zirconia (CSZ) has a fluorite structure. This structure consists of a face centred cubic array of cations, with tetahedral sites filled with anions and, empty octahedral sites [12], Figure 2.6. As

a compensation mechanism for the replacement of Zr^{4+} with Ca^{2+}, oxygen vacancies are generated, Equation (2.7)

$$CaO \xrightarrow{ZrO_2} Ca''_{Zr} + O_O^x + V_O^{\bullet\bullet} \tag{2.7}$$

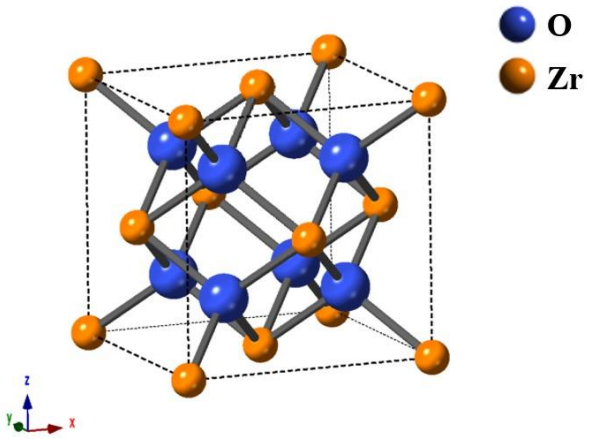

Figure 2.6. *Fluorite crystal structure* [12].

The cubic solid solution in the system $ZrO_2 - CaO$ can be achieved by adding between 13 to 20 mole % of CaO and heating above 1500°C [16]. This phase has an eutectoid temperature around 1140°C ±40°C, at a composition of ~ 17 mol % CaO, [17], [18]. However, this phase has no obvious decomposition, as it can decompose into several phases with increasing Ca content: cubic + tetragonal, pure cubic, cubic + $CaZr_4O_9$ (φ_1), cubic + $Ca_6Zr_{29}O_{44}$ (φ_2), $CaZr_4O_9$ (φ_1) + $Ca_6Zr_{29}O_{44}$ (φ_2) and $Ca_6Zr_{29}O_{44}$ (φ_2) + $CaZrO_3$, Figure 2.7.

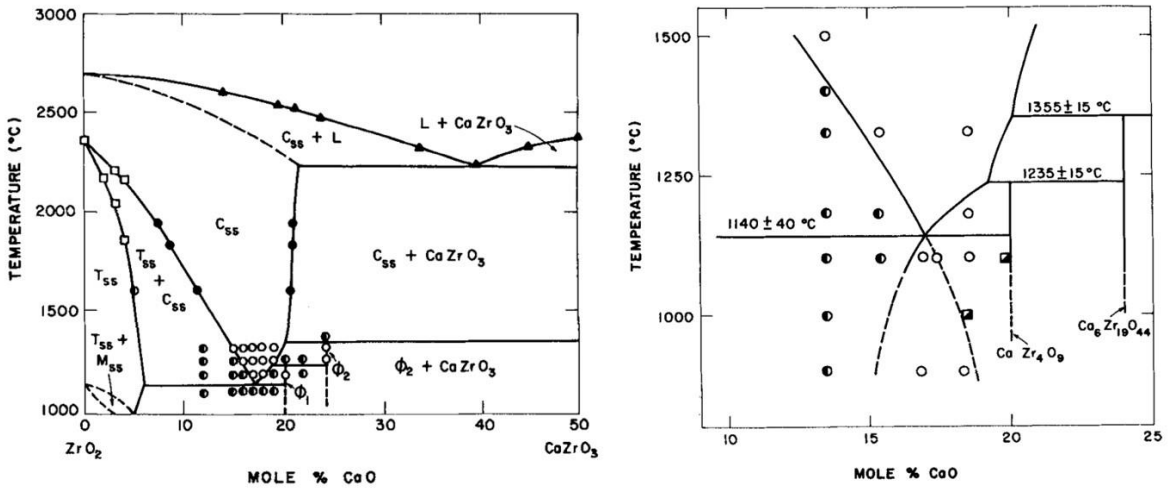

Figure 2.7. *Phase diagram of the $ZrO_2 - CaO$ system. Css: cubic solid solution, Tss: tetragonal solid solution, Mss: monoclinic solid solution, L: liquid, φ_1 :$CaZr_4O_9$, φ_2 : $Ca_6Zr_{19}O_{44}$, empty circles: cubic solid solution , half-filled circles: cubic + tetragonal solid solutions, half-filled squares: cubic solid solution + φ_1* [17].

2.1.2.1 Early characterisation of CSZ

A few years after the discovery of stabilised zirconias, several studies on CSZ were performed. Tian and Subbaro performed a phase and electrical analysis of the $ZrO_2 - CaO$ system in 1963 [19], in which, they found that below 11 mol % CaO, monoclinic ZrO_2 was present, and above 24 mol % of CaO, $CaZrO_3$ was detected.

Two compensation mechanism models were discussed at that time, (1) cation interstitials located at the position $[\frac{1}{2}, \frac{1}{2}, \frac{1}{2}]$ with full anion site occupancy and, (2) oxygen vacancies with cation sites filled randomly. Samples were heated at 2000°C for 2 hours, annealed at 1400°C for one week, and finally air-quenched from 1400°C. The structures factor was calculated for both models as part of x-ray diffraction intensity studies. When comparing the calculated values with the experimental ones, it was concluded that the second model was more appropriate.

They also observed that conductivity decreases, and activation energy increases with *CaO* content. This behaviour was attributed to (1) lattice constriction due to the dopant size, as the ionic radius of Ca^{2+} (0.99 Å) is larger than Zr^{4+} (0.78 Å) or, (2) constriction due to increment in the number of Ca^{2+} surrounding oxygen ions, as *CaO* content increases.

Moreover, superstructure lines in x-ray diffraction patterns were found when the samples were annealed at 1000°C, but the evidence of these disappeared after re-heating the samples at 1400°C. This temperature dependence phenomenon was attributed to an order-disorder transition, associated to a Coulombic interaction between oxygen vacancies and the acceptor dopants (Ca_{Zr}''- V_O¨).

Three years later, Kröger explored the idea of free charged species in CSZ, in contrast to a neutral association of defects. His analysis, based in the law of mass action, offers an explanation for the introduction of electronic conduction as function of pO_2 [16].

In 1980, Schoenlein *et al.* analysed the extra 'order-disorder transition' in calcia- and yttria-stabilised zirconia [20]. Their samples were single crystals with composition: 15 mole% *CaO* and 9 mole% of Y_2O_3, which were analysed by electron diffraction and dark-field transmission electron microscopy. They found that the extra reflections also called fluorite-forbidden reflections, that in previous papers were attributed to 'ordered' CSZ, were actually precipitations of tetragonal ZrO_2 and that the 'disordered' CSZ lacking those extra peaks, was due to the re-solution of the precipitates, into the solid solution. Another feature they observed, independent of the presence of the precipitates, was a diffuse intensity from discrete region in the cubic matrix. They interpreted these results, as an indication of domains or imperfect long-range order, which are formed below a critical temperature.

2.1.2.2 Defect structure and conductivity

The electrical properties of solid oxide electrolytes have been studied for over half a century, including the cubic $CaO{-}ZrO_2$ system [3]. Nevertheless, the broadening of our understanding of these systems has not stopped.

Further research on the relation between conductivity and dopant concentration was carried out [21], [22]. It was found that the ionic conductivity increases with dopant concentration until a maximum conductivity value is reached, between 12-13 mole % of *CaO*, then the conductivity decreases with increasing dopant. In order to understand this behaviour, the defect structure was studied, and theoretical models proposed. Nakamura *et al*, used a general formula in terms of oxygen vacancies, instead of dopant concentration, in order to obtain the variation of conductivity in terms of oxygen vacancies. By knowing the concentration of oxygen vacancies, the diffusion coefficients and mobilities of these defects were calculated, in addition to the equilibrium constant of the oxide ions and the oxygen vacancies. They concluded, by presenting a theoretical model that predicts the maximum conductivity value as a function of oxygen vacancy concentration and temperature. The justification they propose for this behaviour is the formation of Ca_{Zr}''- V_O¨ complexes that cover the entire anion sub-lattice.

2.1.2.3 Presence of dipoles

The effects of composition have been extensively studied. Etsell and Flengas [23] mentioned that the decrease in oxygen ion mobility with increasing Ca content might be the result of lattice distortion due to the difference in radii between cations, the presence of Ca^{2+} ion-anion vacancy complexes or vacancy interaction.

The idea of Ca_{Zr}''- $V_O^{\bullet\bullet}$ pairs gained some interest and therefore, in order to find experimental evidence of them, mechanical loss measurements were performed by Weller [24]. This experiment subjected single crystals of cubic zirconias with composition 10mol% yttria and 16mol% calcia and orientations [100], [110] and [111] to torsional and flexural oscillations (at approximately 1 Hz for the former and, 1 kHz for the latter). To obtain the maximum losses, relaxation amplitudes and dipole concentrations several calculations were performed. The presence of elastic dipoles such as $(Y_{Zr}'$ -$V_O^{\bullet\bullet})^{\bullet}$ and $(Ca_{Zr}''$-$V_O^{\bullet\bullet})^{x}$ with a trigonal orientation [111] was confirmed by a related extra loss maxima at higher temperatures, associated with the relaxation of oxygen vacancies located inside dopant clusters. Accordingly, it was concluded that the oxygen vacancies are surrounded by eight acceptor dopants. In addition, the broadness of the loss maxima, was related to a possible interaction between dipoles or the presence of partly ordered domains.

Perry et al. [25] identified two plateaus as part of the bulk response in the capacitance spectroscopy plot at low temperatures in a 7 mol % YSZ single crystal. The intermediate plateau was attributed to the combination of more than one kind of point defects to form a dipole, or to the presence of larger defects, such as twin boundaries. In addition, an increase in the effective dielectric constant with temperature was observed between 350-500 K, which was associated with the thermal activation of a dipole polarization mechanism, where oxygen vacancies hop locally around the related acceptor dopants.

A new type of associated defect points has been identified in doped zirconias other than the dipolar attraction between acceptor dopants and oxygen vacancies. Norberg et al. [26] by molecular dynamic simulations of neutron powder diffraction results assessed the local ordering of anion vacancies and their preference to be close to a specific cation, in the systems $Zr_{0.8}Y_{0.2}O_{1.9}$ and $Zr_{0.8}Sc_{0.2}O_{1.9}$. $Zr_{0.8}Y_{0.2}O_{1.9}$ showed that the number of oxygen vacancies near the host cation Zr^{4+} was higher than near the acceptor dopant Y^{3+}; and for the case of $Zr_{0.8}Sc_{0.2}O_{1.9}$ there was no preference. Marrocchelli et al. [27] in the second part of the paper previously mentioned, identified the vacancy-vacancy interaction as an intrinsic characteristic of the fluorite structure and the main factor responsible for the change of conductivity with dopant concentration. As vacancies are charged and distort the lattice, the rise in number of these species will increase the defect-lattice interactions. The doped structure may try to compensate for these interactions by ordering the species within the lattice, which could restrict their mobility.

2.1.2.4 Voltage-dependence experiments

With the objective of understanding the conductivity in CSZ, direct voltage and current experiments were conducted. Yanagida *et. al*, performed voltage and pO_2 dependence experiments on CSZ (composition: $Ca_{0.15}Zr_{0.85}O_{1.85}$) symmetrical cells [28]. The samples were pellets of 10mm in diameter and 1mm thick, with Pt paste electrodes, oxygen pressures ranging from 1 to 10^{-20} atm, applied voltages from 0-6V and all the measurements were taken at 560°C. They observed two behaviours, figure 2.8, which were attributed to specific rate-limiting steps. At low voltages ($< 2V$) the dynamic resistance varied with pO_2; rate limiting step: *diffusion of oxygen through the Pt electrode*, Equation (2.8).

$$O(Pt/g) \rightarrow O(Pt/CSZ) \qquad (2.8)$$

Whereas at higher voltages (> 2*V*) almost null dependence on pO_2 was observed; rate limiting step: *adsorption of neutral oxygen at the surface of CSZ/gas interface* that interact with neutral oxygen vacancies(V_O^x; oxygen vacancy with 2 trapped electrons, F-center [28]), created due to polarization effects, to form O_O^x Equation (2.9)

$$O(CSZ/g) + V_O^x \rightarrow O_O^x \tag{2.9}$$

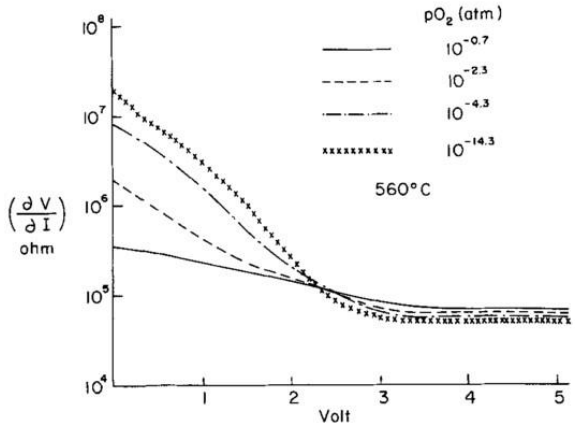

Figure 2.8. *Dynamic resistance of CSZ (15 mol % CaO) as function of an applied voltage and* pO_2 [28].

Electrode effects Brook *et. al*, studied the electrode processes in CSZ with different types of platinum electrodes by performing polarization measurements, [29]. Experimental procedures and mathematical models were similar to the ones previously published [16] and [28]. Here are the types of electrodes used and their corresponding behaviours:

• ***Non-porous Pt foil electrode***: Analogous to porous Pt paste described above. At low voltages (< 2*V*), oxygen diffusion through platinum, rate limiting process. The limiting value is approached when $V \rightarrow$ inf, and it can be identified as a saturation plateau of the current, Equation (2.10)

$$I = pO_2^{1/2} B \tag{2.10}$$

where *B* describes the electrode characteristics, Equation (2.11)

$$B = 2FS\frac{D}{\delta}K_1 \tag{2.11}$$

where *F* is the Faraday constant, *S* the surface area of the electrode, *D* the diffusion coefficient of oxygen through Pt, δ the electrode thickness and K_1 the equilibrium constant of the reaction of Equation (2.12)

$$1/2O_2 \rightarrow O(Pt) \tag{2.12}$$

Therefore, it is important to consider the thickness of the electrode, as the thickness increases the saturation current will decrease.
At high voltages (> 2*V*) polarization occurs, surface of CSZ in contact with the electrode becomes electronically conductive, and oxygen can be directly introduced into the materials, Equation (2.9).

• ***Non-porous Pt sputtered electrodes:*** Electrode thickness, < 1μm. Ohmic behaviour was found, Equation (2.13), where R_b is the bulk resistance of the electrolyte.

$$R = R_b = I \cdot V \tag{2.13}$$

• ***Porous paste Pt electrodes:*** Two behaviours were observed according to the firing temperature of the paste. At 850°C, the samples showed an ohmic behaviour as the sputter samples, as the grain size of the Pt in the suspension was < 1μ. When the electrodes were fired at 1350°C, grain growth of the Pt particles occurred, and non-ohmic behaviour was observed, as described above [28].

• ***Non-porous Pt paste electrode with borosilicate as fluxing agent:*** Electronic behaviour at high voltages (> 2*V*), as glass prevents contact with the gas phase, and no free surface is available.

They conclude by making three suggestions. The first one is to use thin sputtered electrodes for the study of bulk effects. The second one, is to use electrodes that cover the surface area of the sample faces, to study polarization effects. Finally, the third one is to keep the applied voltage below the decomposition voltage of the solid electrolyte, in order to avoid electrolysis.

2.1.3 Modelling of sample-electrode contact

Equivalent circuits have been used to model the kinetics of sample-electrode reactions since the 1940's when J.E.B. Randles proposed the Randles circuit, Figure 2.9(a). Since then, a wide variety of systems [30]–[46], have used equivalent circuits based on the Randles cell to analyse and interpret their results. These equivalent circuits include a double layer capacitance, modelled with a capacitor $C_{dl,}$ or a constant phase element CPE_{dl}, a charge transfer resistance R_{ct}, and a diffusion process, modelled with a Warburg impedance Z_W or a constant phase element CPE_{diff}.

The difference among the proposed circuits, is the placement of these parameters, which is usually found in two formats. The first one, is a series R_{ct}-Z_W element in parallel with C_{dl}, Figure 2.9(a) [40]. The second one, is a parallel R_{ct}-C_{dl} element in series with Z_W, Figure 2.9(b) [37]. Usually, the Warburg impedance is modelled using a CPE (CPE_{diff})with a fixed n value of 0.5 [32], other studies set the n parameter free[37], and some other studies do not specify how Z_W was modelled [46]. When the Warburg impedance appears to be a semicircle rather than a spike in the Z* plane, it is usually referred to as a finite-Warburg impedance. The resistance it added to Z_W is usually added in two ways. Either R_{diff} is included in the Z_W equation ($Z_{w\text{-finite or diff}} = R_{diff} \tanh(jT\omega)^n/(jT\omega)^n$; where in the diffusion interpretation $T = L_2/D$, where L is the effective diffusion thickness, and D the effective diffusion coefficient), meaning that when using a software, such as Zview[47], to fit the measured impedance data, it will ask for the resistance parameter, figure 2.11(a) and (b). The other approach is to add R_{diff} in parallel with CPE_{diff}[48], Figure 2.11 Lit-C.

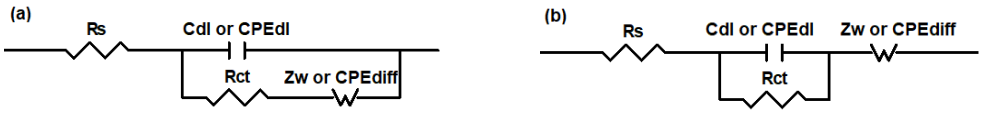

Figure 2.9. *Randles circuit.*

For our interest the oxide ion solid electrolyte-electrode interface between stabilised zirconias and noble metals have been studied [1][2][11]–[13].

Schwandt and Weppner [1][2], studied the electrode reactions of stabilised zirconias using Pt and Au as electrodes, in the temperature range between 500 to 900°C and pO_2 from 10^0-10^5 Pa. Three main step reactions were considered:

1. Dissociation and absorption of molecular oxygen at the electrode surface, which may be fast and reversible

$O_{2(g)}+2V_{ad(Pt)} = 2O_{ad(Pt)}$

2. Surface diffusion of adsorbed oxygen towards electrochemical reaction sites (ers)
   $O_{ad(Pt)}+V_{ad(ers)}=O_{ad(ers)}+V_{ad(Pt)}$
3. Charge transfer reaction of adsorbed oxygen
   $O_{ad(ers)}+V_O^{\bullet\bullet}+2e'=O_O^x$

In the case of the Pt electrode, the conductivity was found to be dependent on pO_2, with a maxima that shifts to low oxygen pressures as temperature decreases, with slopes around -0.45 and +0.55 at low and high pO_2, respectively Figure 2.10(a). For Au, the conductivity increased with pO_2, showing two slopes and therefore two competing limiting-rate reactions; at high pO_2 slope of +0.50, related to the diffusion of adsorbed oxygen and at low pO_2 slope of +0.25, related to the charge transfer reaction of adsorbed oxygen in the vicinity of a three-phase boundary, Figure 2.10(b). When comparing the total conductivity of Pt and Au electrodes, Au resistance was larger than Pt, attributed to higher catalytic activity of Pt.

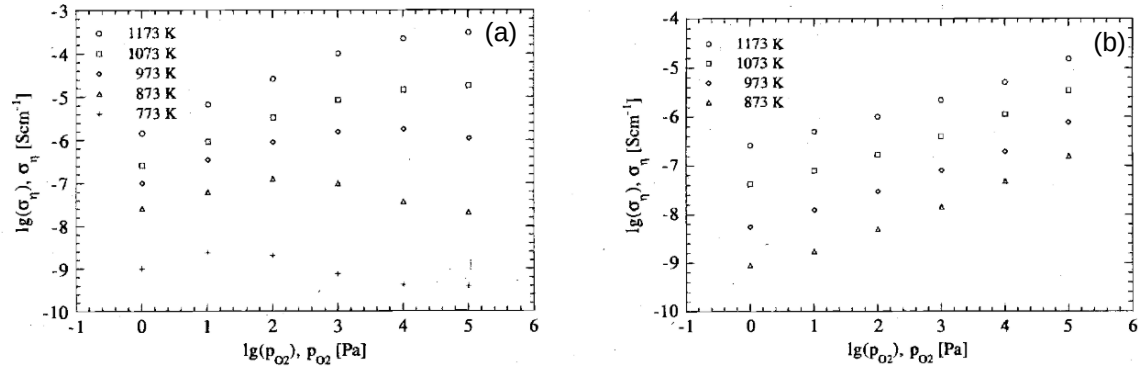

Figure 2.10. *Pt (a) and Au (b) electrode conductivity as function of pO_2, under different temperatures. Extracted from [1][2].*

Various equivalent circuits were used to fit the electrode response of Pt and Au, Figure 2.11. The Pt response was fitted to circuits Lit A-C. Circuit Lit-A gave a good fit at high temperatures and Lit-C at low, in all the pO_2 range. Au electrode was fitted to circuits Lit B-F. At high pO_2 (10^3-10^5Pa) 3 parallel R-CPE elements were needed to fit the response with the best fit given by circuit Lit-F, and at low pO_2 (10^0-10^2 Pa) by Lit-C. For the case of Pt electrode, it was mentioned that the bigger resistance will account for 85% of the total electrode resistance; nevertheless, no further interpretation of the fitted parameters was given. For the analysis of the kinetic reactions the total resistance of the electrode was used.

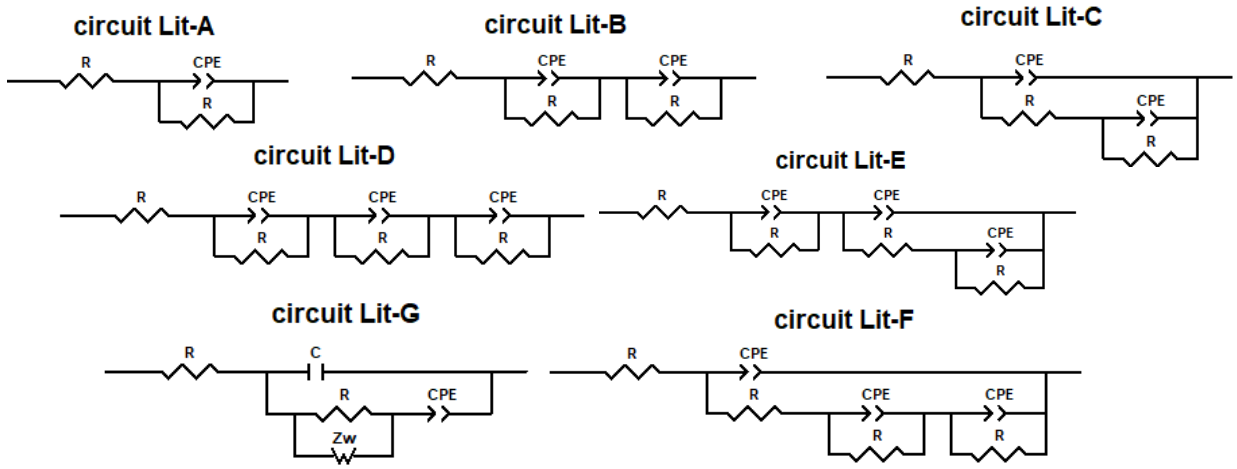

Figure 2.11. *Various equivalent circuits used in the literature to fit the electrode response of stabilised zirconias. Adapted from* [31], [40]–[42].

Sakurai *et al.* [40] studied the interfacial impedance of Pt and 8mol%YSZ. Two types of electrodes were employed paste and evaporated (or sputtered) Pt. Impedance measurements were taken in the temperature range from 650-850°C and pO_2 from 10^1-10^5 Pa, frequencies from 10^{-3}-10^5Hz. The two consecutive step reactions were considered, which are the same as step reaction 1 and 3 considered by Schwandt[31]. A good fit using the equivalent circuit Figure 2.9 (a) was found, the equations they used to describe Z_W, R_{diff}, R_{ct} and the relationship between the effective length diffusion and the diffusion constant can be found in equations [12-15] in ref[40]. It was concluded that the magnitude of R_{diff} and R_{ct} will be affected by electrolyte and the morphology of the electrode. Nevertheless, this latter will not affect the mechanism of the electrode process.

The relationship between the fitted parameters and the morphological characteristics of the sample-electrode interface was studied by Nakagawa *et al.* [41] Using circuit Lit-G, it was found that a paste electrode gave a larger charge transfer resistance and smaller double layer capacitance than the sputtered electrode, which was attributed to a reduced three-phase boundary and sample-electrode contact area.

B.A. Boukamp *et al.* [42] performed *dc* polarization, impedance spectroscopy and isotope exchange experiments on YSZ and erbia stabilised delta-bismuth oxide (BE25) to investigate the oxygen transfer process at the sample-electrode contact. Au and Pt were used as electrodes. Au/ YSZ samples were fitted to equivalent circuit Lit-F, in agreement with Schwandt[31], with the difference that the outer parallel CPE was changed for a capacitor. The two parallel R-CPE elements in series are attributed to electrode reactions, without giving any further explanations. For the case of Au/BE25, circuit Lit-B gave a good fit.

2.2 Alumina

Alumina (Al_2O_3) is a dielectric [49], its electrical insulating nature makes it suitable for applications such as electronic substrate, thermocouple and laser tubes, vacuum interrupters, among others [50], [51]. For this reason, it is of great interest to know the conditions of the failure transitioning from an insulator to a conductor. Several experiments in different fields of study have applied a large electric field and observed an increase in conductivity.

2.2.1 Electrical characterisation

The most common test is dielectric breakdown [52]–[54], which is usually carried out at room temperature and the sample is immersed in a dielectric liquid to avoid current along the surface or so called *flashover*. The electrical breakdown strength (E_s) of sapphire and polycrystalline alumina has been measured as function of temperature, up to 1400°C [55]. Two methods were used: i) increased the voltage in steps with a fixed temperature and ii) increased the temperature with a fixed voltage. The electric field was in the order of $10^5 Vcm^{-1}$. It was also found that the E_s decreases with temperature and with sample thickness (t) following equation 2.14,

$$E_s \approx 1/t^n ; \; n=0.1\text{-}0.5 \qquad (2.14)$$

When using method ii) a small current peak at the beginning of each voltage step was observed and described as current absorption or leakage current; which caused localized Joule heating, increasing the current. It was pointed out that the sample heating will be balanced by heat loss through conduction and radiation, until the critical value was overcome leading to thermal runaway and dielectric breakdown [55].

In addition the role of Si, MgO and CaO in the dielectric strength of alumina has been studied [56]. As a general observation it was found that the dielectric strength was higher in alumina ceramics than in

single crystals. Regarding the impurities the dielectric strength increased when Si was the major impurity and decreases with the addition of MgO and CaO. This was attributed to enhanced solubility of Si in the presence of MgO and CaO. Si segregation at the grain boundaries was proposed, causing enhanced dielectric strength, by electron trapping in shallow traps as $(3Si^{\bullet}_{Al}:V'''_{Al})^{x}$ clusters.

As previously mentioned, the *flashover* phenomenon, which is the electric breakdown along the surface of an insulator has been studied in a wide range of materials including alumina [57]–[61]. These types of experiments are usually carried out under vacuum with applied electric fields on the order of $10^{5}Vcm^{-1}$. Different models have been proposed where the process starts either at the cathode or anode. Nevertheless, there is still controversy and it has been stated that no single model can explain all the cases of surface flashover, and that the dominated mechanism will change according to the experimental conditions [57]. For our interest it is important to note the relationship between the flashover voltages and the waveform (dc, ac or pulse), as the highest are given by short pulses, intermediate by μs and dc, and lowest by ac voltages, and that there is an inverse relationship between relative permittivity and its flashover voltage [59], [61]. Moreover, the *flashover* event will have a life span in the order of ns [59].

The reversibility of the surface charge accumulation was observed after applying nanosecond pulse voltage under vacuum at samples with different sintering conditions (temperature and dwell time). Dissipation of the charge after 1h of the cut off the voltage showing less than 7% of the maximum charge density [60].

Flash sintering is a process in which a green body is subjected to an electric field and high temperature. After reaching an onset temperature and an incubation time, the samples conductivity increases abruptly, along with emission and light and densification, this stage is known as the *flash-event* [62]. Further explanation about the flash sintering process will be given in the following section. Flash sintering of pure and 0.25wt% MgO-doped alumina using an electric field from 250 to $1000Vcm^{-1}$, was one of the first experiments of this kind [63]. It showed that pure alumina did not flash, whereas MgO-alumina flashed between 1260-1400°C. Nevertheless, conductivity Arrhenius plot under the application of 25 to 1000 Vcm^{-1}, showed similar activation energies for pure and MgO-alumina, between ~1.5-2.3eV.

Similarity between flash sintering experiments and electrical breakdown strength in dielectrics, has been pointed out [64] [65], as these two processes present a transition from insulator to conductor, need an incubation time which decreases with the applied field and is sensitive to the sample geometry. Samples of α-alumina pre-sintered at different temperatures were used for a flash sintering experiment, by applying $500\text{-}1500Vcm^{-1}$ [65]. It was found that the Poole-Frenkel model* [66], used to describe the *pre-breakdown* behaviour of the dielectric breakdown process can also described the increase in electrical conductivity.

The combination of radiation and electric field has also been studied [68]. Alumina single crystal at ~500°C in air, under an electron dose of 1.8MeV and $2.12kVcm^{-1}$, showed an increase in conductivity by 3 orders of magnitude. The conclusion was that the increase in conductivity could not be only attributed to the presence of anion vacancies.

* Describes how the potential energy barrier of a trapped electronic charge carrier (e^{-} or h^{+}) is reduced in the presence of an electric field, increasing the corresponding densities of free charged carriers [66], [67].

Current density measurements during the application of a lower range of electric fields were performed on alumina and sapphire, between 1000 to 1650°C [69]. In the case of alumina from 0 to 40Vcm^{-1}, and for sapphire between 0 to ~560Vcm^{-1}, with a dwell time of 2 minutes. Measurements were between the outside and inside surface of a thin-walled hollow tube to eliminated effects of gas or surface conduction. Ohmic voltage dependence up to 10-20Vcm^{-1}, from where departure from linearity was observed, Figure 2.12. Behaviour of electrodes was established as non-blocking, allowing oxygen diffusion through the porous Pt-film. It was concluded that purely electronic or ionic conduction could not account for the magnitude of the observed conductivity.

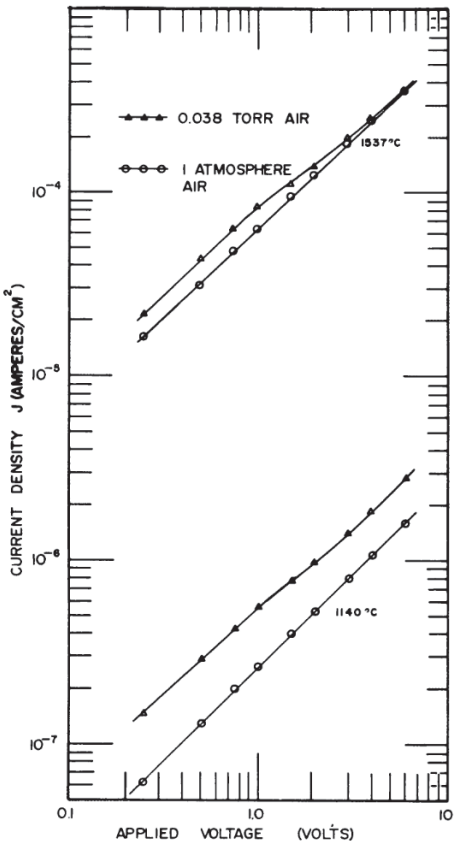

Figure 2.12. *Current density as a function of applied voltage for a ceramic alumina tube in vacuum and in air at different temperatures* [69].

It is known that the electrical conductivity of alumina varies with oxygen partial pressure at high temperatures [70]–[72]. Dielectric relaxation experiments between 700 and 1200°C identified a capacitance dispersion which varied its conductivity and thickness from 5 to 50 μm as a function of pO_2 [73]. These results were attributed to a surface layer or an internal interface, as they were interpreted by the interfacial polarization model. The formation of this layer was suggested to be a consequence of the time required to attain equilibrium by the moving species. Also, the possibility of second phase distributed as spheres or spheroids throughout the crystal could not be ruled out. In addition, the surface layer had a higher resistance than the bulk.

2.3 Flash sintering

2.3.1 Introduction to flash sintering

Reduction of sintering temperatures and enhancement in densification are a few of the driving forces in the search for alternative sintering techniques. Electric current activated/assisted sintering (ECAS) incorporates, as its name states, the application of electric current during the sintering process. This can

be classified according to the discharge time; if it is less than 0.1*s* it is known as "ultrafast ECAS", but if it is higher than 0.1*s*, it is called "fast ECAS", Figure 2.13. The first one is related to capacitive discharge, and the second one can be further divided into "resistance sintering", which applies a constant direct current and "pulsed electric current" [74].

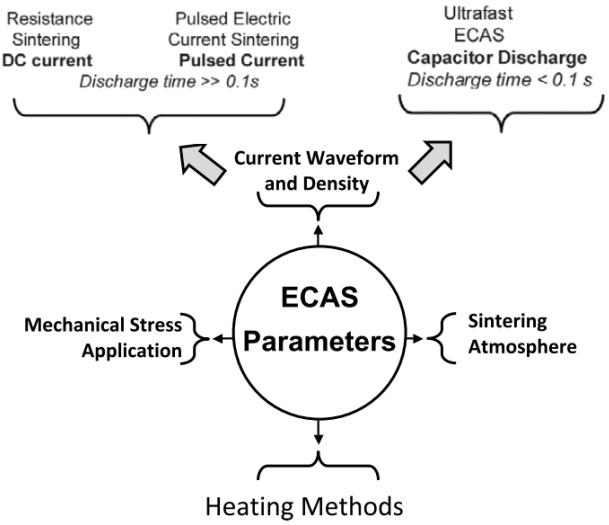

Figure 2.13. *Main electric current activated/assisted sintering (ECAS) parameters* [74].

Research in ECAS techniques started over a 100 years ago, with the first patent by Bloxam in 1906. In the patent, the fabrication of tungsten or molybdenum filaments for incandescent lamps is described, with the help of current in a reducing atmosphere or vacuum [75]. Since then, this field has been developing to the point of reaching commercial deployment, one example is the 3,000 Spark Plasma Sintering (SPS) furnaces installed around the world by 2016 [62]. In 2010, a peculiar behaviour was identified by Cologna *et al*. [76] at Colorado University, which was referred to as the *flash event*. Therefore, the technique was called "Flash Sintering" (FS). This process consists in sintering a material within less than one minute, with the presence of power dissipation (between 10-1000$mWmm^{-3}$) and, a non-linear increment in conductivity, when heat and an electric field (between 7.5-1000$V\ cm^{-1}$) are applied [62].

Since then, this technique has been intensely studied and slightly modified according to the availability of equipment of the different research groups. Therefore, there are different configurations that are described in the following section.

2.3.2 Flash sintering methods

Before trying to perform a flash sintering experiment there are several points to consider as: the machine configuration, sample geometry and inputs and outputs for the equipment. These points are described in this section, in addition to the possible sintering mechanisms.

2.3.2.1 Apparatus configuration There are two main groups of machine configuration, the ones that are pressure-assisted and the pressure-less.

Pressure-less. Three set-ups without the use of pressure have been identified, wire suspended sample, contactless and sliding. The first configuration consists of a vertical tube furnace, or a muffle furnace with a window, the sample is suspended at the hot zone with platinum wires, which work as electrodes. To increase the contact between the sample and the electrodes, the platinum ink or paste is deposited

where the wire is going to be attached. Silver, carbon and stainless-steel electrodes, have also been used. A CCD (charge couple device) camera is placed at the bottom of the tube furnace or, in front of the window of the muffle furnace, with its specific filters to record the shrinkage and luminescence events [63], [77]. The second approach is to make use of plasma as electrodes [78], the rectangular sample is loaded into a ceramic holder, and placed between two plasma arcs, which are powered by transformer welders. In order to measure the current, Hall effect sensors are used. Finally, the third one makes use of sliding electrodes, but limited data has been publish using this set up [62].

Pressure assisted. The pressure-assisted set-ups are modifications of commercial dilatometers, mechanical loading frames or spark plasma sintering (SPS) machines [77]. The first two make use of a heating chamber, in which the pellet-shaped sample is placed between platinum electrodes and mounted between alumina push rods that provide the uniaxial pressure. The electrodes are connected to the power supply by platinum wires [77][79]. When an SPS machine is used for FS, the process is referred "flash spark plasma sintering" (FSPS), the difference between these two is that in FSPS the current goes through the sample, instead of going through a graphite die, which heats the sample. Therefore, in FSPS the graphite die is separated from the sample by an insulating material, to avoid the current passing through the sample and heat losses. Another option is not to use the graphite die and put the sample directly between the electrodes [80][81][82]. Graphite punches are used as electrodes when the sample is not susceptible to carbon contamination, otherwise refractory metal foils such as Ta, Mo or W are placed between the sample and the graphite punch [62]. In some cases, graphite felt is placed around the sample to reduce heat losses [80]. Some configurations, as FSPS, allow the use of different atmospheres, from reducing to oxidizing.

2.3.2.2 Geometry of the sample

As one can see from the different set-ups, there are a variety of sample geometries, Figure 2.14. Dog-shaped bones and bars are usually used in pressure-less configurations, while pellets of different ratios and heights are used in pressure-assisted.

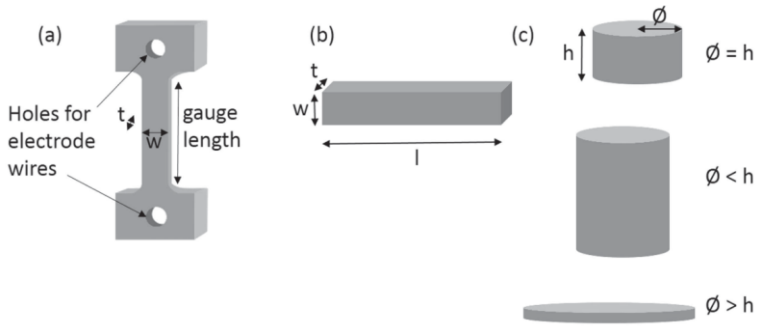

Figure 2.14. *Sample geometries. a)dog-bone shape, b)rectangular bar, c)different types of pellets* [77].

The green sample has to be able to maintain its shape while handling and placing in the FS machine. For this reason, additives, such as binders, dispersants and sintering aids, are added to the powder mixture. In addition, the green body can be cold-pressed or pre-sintered.

2.3.2.3 Inputs

The two main aspects to consider before a FS experiments are the type of experiment in terms of heating profile and application of current and voltage and, the kind of power supply that is going to be used.

Experimental designs. There are two main experimental designs, dynamic and isothermal, Figure 2.15 [83]. The dynamic applies constant voltage, while the sample is heating at a constant rate (usually $10^{\circ}C min^{-1}$). The experiment changes from voltage control to current control, after the *flash event* occurs or when the current has reac e power supply (normally $60 mA mm^{-2}$) [63]. In an isotherm lesired temperature, then an electric potential is applied unti nts change from voltage to current control [84].

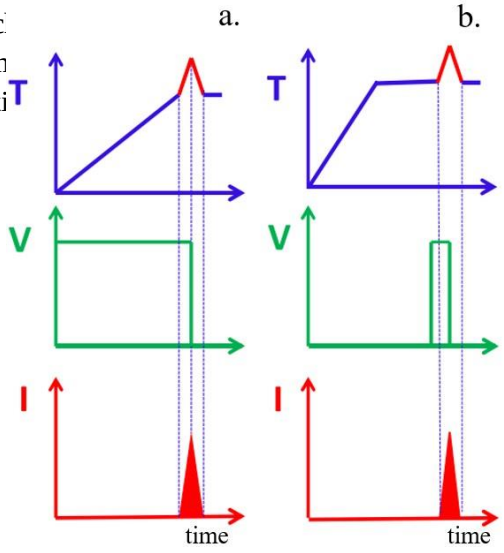

Figure 2.15. *Flash sintering experimental profiles. Dynamic (a) and isothermal (b)* [83].

•***Power supply.*** According to a recent review [62], the majority of FS experiments use DC power supplies instead of AC. When using a DC power supply the voltage and current are around 10-5000V and 0.515A, respectively. In this case, the samples show a resistive load behaviour. In the case of an AC power supply, the voltage and current are in the range 10-62V and 0.1-2A, and can operate in a low-mid frequency range (50-1kHz) or, a high frequency range (up to 1 MHz). In this mode, the samples can present capacitive or inductive behaviour. Prior to performing an FS experiment, it is important to calculate the maximum initial electric field, Equation (2.15)

$$E = V/l \tag{2.15}$$

where V is the applied voltage and l is the length between the electrodes; the current density, Equation (2.16) for a pellet and, Equation (2.17) for a dog-bone or a bar is

$$J = I/\pi r^2 \tag{2.16}$$

where I is the current and r is the radius of the pellet

$$J = I/a \tag{2.17}$$

and a is the cross-section area of the bar [77]. This means that these two parameters can be tuned according to the dimensions of the sample.

2.3.2.4 Outputs

Here are some of the most common parameters and effects that can be measured during and after a FS experiment.

Shrinkage. The densification or shrinkage of the sample can be measured by optical methods, with CCD camera or lasers, or using a dilatometer. Therefore, the true linear shrinkage strain can be then calculated, Equation (2.18)

$$\varepsilon = ln(l/l_0) \tag{2.18}$$

where l is the time-dependent gauge length and l_0 is the initial gauge length [62].

Electrical behaviour. After the shrinkage, the most common parameters to measure are the voltage and current, in order to calculate the power and conductivity of the sample. The power dissipation during current control is given by Equation (2.19)

$$P=I^2R \quad (2.19)$$

where I is the current and R the resistance. The peak power density, that separates the switch from voltage to current control is defined by Equation (2.20)

$$P_w = EJ \quad (2.20)$$

where E is the electric field and J the current density. Therefore, under voltage control the conductivity is given by Equation (2.21) and, under current control by Equation (2.22) [85].

$$\sigma = P_w/E^2 \quad (2.21)$$

$$\sigma = J^2/P_w \quad (2.22)$$

Temperature. To determine the temperature of the sample during the *flash event* is a challenge, due to the high heating rates (10^3-10^5°Cmin^{-1}). Many approaches have been tried using thermocouples, fitting black body radiation from pyrometer data and using the relationship between the thermal expansion coefficient and lattice parameters of the material. This last technique is an indirect way of measuring the average temperature; the sample is heated in a modified furnace while XRD measurements are taken [62]. It is important to take into consideration that a temperature gradient, in different scales, might be present in the sample. The causes could be higher electron scattering in disordered or different chemical composition regions; differences in electrical conductivity between phases and the heat losses at the surface due to radiation.

Phase analysis. As mentioned before, by modifying a furnace, in situ XRD measurements can be taken while the *flash event* occurs. This technique allows direct study of any reversible phase transformations, which may not be possible to identify at room temperature after sintering [62].

Electroluminescence. This term refers to the generation of light, when an electric field is applied or is passing through a material [86]. Different materials have the ability to absorb and/or emit light of a particular wavelength. Therefore, during FS experiments any emitted light can be deconvoluted. Then, an analysis could determine whether that emitted light corresponds to electroluminescence. Nevertheless, it has been commented that incandescence might be stronger than the electroluminescence effect [62].

A brief summary of the inputs and outputs of a flash sintering experiment is given in Table 2.1.

Table 2.1. *Parameters that can be modified and obtained from a flash sintering experiment. Adapted from* [62].

Input	**Output**
Experimental designs	Shrinkage
Power supply	Electric behaviour
Material (crystallite size, sample preparation, etc.)	Temperature
Sample geometry	Phase analysis
	Electroluminescence

2.3.3 Possible sintering mechanisms

There are several proposals that, in their own way, give an explanation for the increase in conductivity and/or rapid densification, during the *flash event*.

Joule heating. Todd *et al*, suggested that the thermal and electrical behaviours observed during flash sintering are a consequence of thermal runaway initiated by Joule heating. In their model, the resistivity is independent of time, and has an inverse Arrhenius relationship with temperature. It is also assumed that the material behaves with a negative temperature coefficient (NTC), meaning that its resistance decreases with temperature [87]. Therefore, current constriction at the contact points of particles, produces localised heat, promoting atomic diffusion and, finally densification [62].

Frenkel pairs. Creation of defects has been suggested as a mechanism for flash sintering [63]. Cologna *et al*, mentioned that the applied field can induce the nucleation of Frenkel pairs, by removing an electron from a vacancy and a hole from an interstitial. Therefore, densification can occur as vacancies are drawn to the grain boundaries, and interstitials to the pores. Finally, the electron-hole pairs will contribute to the rise in conductivity.

Electrochemical reduction effects. The effects of polarization, due to an applied field, have also been taken into consideration [15], [62]. When an ionic conductor is subjected to a voltage higher than its decomposition potential, electrolysis can occur [29]. This means that, electronic carriers become present and dominant over the mobile ions, which degrade, resulting in an increase of electronic conduction and decrease of ionic conduction.

2.4 References

[1] Royal Society of Chemistry, "Zirconium dioxide," *ChemSpider*, 2018. [Online]. Available: http://www.chemspider.com/Chemical-Structure.56183.html?rid=b8336612-89dd-4f7e-84c1-c4ac0ab5791b.

[2] P. Platt, P. Frankel, M. Gass, R. Howells, and M. Preuss, "Finite element analysis of the tetragonal to monoclinic phase transformation during oxidation of zirconium alloys," *J. Nucl. Mater.*, vol. 454, no. 1–3, pp. 290–297, 2014.

[3] H. Ikeno *et al.*, "Variation of Zr-$L_{2,3}$ XANES in tetravalent zirconium oxides," *J. Phys. Condens. Matter*, vol. 25, no. 16, 2013.

[4] C. J. Howard, R. J. Hill, and B. E. Reichert, "Structures of ZrO_2 polymorphs at room temperature by high-resolution neutron powder diffraction," *Acta Crystallogr. Sect. B*, vol. 44, no. 2, pp. 116–120, 1988.

[5] A. H. Ballard and D. W. Marshall, "Stabilized zirconia and method for producing same," US2535526, 1950.

[6] Kyocera Global, "Zirconia Products | Fine Ceramics (Advanced Ceramics) | Kyocera." [Online]. Available: https://global.kyocera.com/prdct/fc/list/material/zirconia/index.html. [Accessed: 16-Apr-2018].

[7] J. W. Fergus, "Doping and defect association in oxides for use in oxygen sensors," *J. Mater. Sci.*, vol. 38, no. 21, pp. 4259–4270, 2003.

[8] A. J. Feighery and J. T. S. Irvine, "Effect of alumina additions upon electrical properties of 8 mol.% yttria-stabilized zirconia," *Solid State Ionics*, vol. 121, no. 1, pp. 209–216, 1999.

[9] A. J. Boiron and B. J. Cantwell, "Hybrid Rocket Propulsion and In - Situ Propellant Production for Future Mars Missions," in *49th AIAA/ASME/SAE/ASEE Joint Propulsion Conference and Exhibit*, 2013, pp. 1–21.

[10] A. Brune, M. Lajavardi, D. Fisler, and J. . Wagner Jr., "The electrical conductivity of yttria-stabilized zirconia prepared by precipitation from inorganic aqueous solutions," *Solid State Ionics*, vol. 106, no. 1–2, pp. 89–101, 1998.

[11] D. Sinclair, "'Functional and Structural Ceramics, Topic II: Thermodynamic treatment of defects and conduction models.'" Sheffield, 2016.

[12] J.-H. Park and R. N. Blumenthal, "Electronic Transport in 8 Mole Percent Y_2O_3-ZrO_2," *J. Electrochem. Soc.*, vol. 136, no. 10, p. 2867, 1989.

[13] N. Masó and A. R. West, "Electronic conductivity in Yttria-stabilized zirconia under a small dc bias," *Chem. Mater.*, vol. 27, no. 5, pp. 1552–1558, 2015.

[14] M. Jovaní, H. Beltrán-Mir, E. Cordoncillo, and A. R. West, "Atmosphere- and voltage-dependent electronic conductivity of oxide-ion-conducting $Zr_{1-x}Y_xO_{2-x/2}$ ceramics," *Inorg.*

Chem., vol. 56, no. 12, pp. 7081–7088, 2017.
[15] R. Kirchheim, "On the mixed ionic and electronic conductivity in polarized yttria stabilized zirconia," *Solid State Ionics*, vol. 320, pp. 239–258, Jul. 2018.
[16] F. A. Kröger, "Electronic conductivity of calcia-stabilized zirconia," *J. Am. Ceram. Soc.*, vol. 49, no. 4, pp. 215–218, 1966.
[17] J. R. Hellmann and V. S. Stubican, "Stable and Metastable Phase Relations in the System ZrO_2-CaO," *J. Am. Ceram. Soc.*, vol. 66, no. 4, pp. 260–264, 1983.
[18] R. M. Dickerson and A. H. Heuer, "The calcia-zirconia phase diagram revivited: stability of the ordered phases φ1 and φ2," *J. Am. Ceram. Soc.*, vol. 74, no. 1, pp. 234–237, 1991.
[19] T. Y. Tien and E. C. Subbarao, "X-ray and electrical conductivity study of the fluorite phase in the system ZrO_2-CaO," *J. Chem. Phys.*, vol. 39, no. 4, pp. 1041–1047, 1963.
[20] L. H. Schoenlein, L. W. Hobbs, and a. H. Heuer, "Precipitation and ordering in calcia- and yttria-stabilized zirconia," *J. Appl. Crystallogr.*, vol. 13, no. 4, pp. 375–379, 1980.
[21] A. Nakamura and J. B. Wagner, "Defect structure, ionic conductivity, and diffusion in calcia-stabilized zirconia," *J. Electrochem. Soc.*, vol. 127, no. 11, pp. 2325–2333, 1980.
[22] A. Nakamura and J. B. Wagner, "Defect structure, ionic conductivity, and diffusion in yttria stabilized zirconia and related oxide electrolytes with fluorite structure," *J. Electrochem. Soc.*, vol. 133, no. 8, p. 1542, 1986.
[23] T. H. Etsell and S. N. Flengas, "The electrical properties of solid oxide electrolytes," *Chem. Rev.*, vol. 70, no. 3, pp. 339–376, 1970.
[24] M. Weller, "Mechanical loss measurements on yttria- and calcia-stabilized zirconia," *J. Alloys Compd.*, vol. 211–212, no. C, pp. 66–70, 1994.
[25] N. H. Perry, T. C. Yeh, and T. O. Mason, "Temperature dependence of effective grain core/single crystal dielectric constants for acceptor-doped oxygen ion conductors," *J. Am. Ceram. Soc.*, vol. 94, no. 2, pp. 508–515, 2011.
[26] S. T. Norberg *et al.*, "Structural disorder in doped zirconias, part I: the $Zr_{0.8}Sc_{0.2-x}Y_xO_{1.9}$ ($0.0 \leq x \leq 0.2$) System," *Chem. Mater.*, vol. 23, no. 6, pp. 1356–1364, 2011.
[27] D. Marrocchelli, P. A. Madden, S. T. Norberg, and S. Hull, "Structural disorder in doped zirconias, part II: vacancy ordering effects and the conductivity maximum.," *Chem. Mater.*, vol. 23, no. 6, pp. 1365–1373, 2011.
[28] H. Yanagida, R. J. Brook, and F. a. Kröger, "Direct Current-Voltage Characteristics of Calcia Stabilized Zirconia with Porous Platinum Electrodes," *J. Electrochem. Soc.*, vol. 117, no. 5, p. 593, 1970.
[29] R. . Brook, W. L. Pelzmann, and F. A. Kröger, "Platinum electrodes and Calcia-Stabilized Zirconia," *J. Electrochem. Soc.*, pp. 185–192, 1971.
[30] C. Schwandt and W. Weppner, "Electrode reactions at oxygen, noble metal / stabilized zirconia interfaces," *Ionics (Kiel).*, vol. 2, no. 2, pp. 113–122, 1996.
[31] C. Schwandt and W. Weppner, "Kinetics of oxygen, platinum/stabilized zirconia and oxygen, gold/stabilized zirconia electrodes under equilibrium conditions," *J. Electrochem. Soc.*, vol. 144, no. 11, pp. 3728–3738, 1997.
[32] P. Tomczyk and M. Mosialek, "Investigation of the oxygen electrode reaction in basic molten carbonates using electrochemical impedance spectroscopy," *Electrochim. Acta*, vol. 46, no. 19, pp. 3023–3032, 2001.
[33] A. Sacco, "Electrochemical impedance spectroscopy as a tool to investigate the electroreduction of carbon dioxide: A short review," *J. CO_2 Util.*, vol. 27, pp. 22–31, Oct. 2018.
[34] A. A. Moya, "Identification of characteristic time constants in the initial dynamic response of electric double layer capacitors from high-frequency electrochemical impedance," *J. Power Sources*, vol. 397, pp. 124–133, Sep. 2018.
[35] A. Lasia, "Impedance of porous electrodes," *J. Electroanal. Chem.*, vol. 397, no. 1–2, pp. 27–33, 1995.
[36] P. Kurzweil and H. J. Fischle, "A new monitoring method for electrochemical aggregates by impedance spectroscopy," *J. Power Sources*, vol. 127, no. 1–2, pp. 331–340, 2004.
[37] A. Nasser-Eddine, B. Huard, J. D. Gabano, and T. Poinot, "A two steps method for electrochemical impedance modeling using fractional order system in time and frequency domains," *Control Eng. Pract.*, vol. 86, pp. 96–104, May 2019.

[38] T. Q. Nguyen and C. Breitkopf, "Determination of Diffusion Coefficients Using Impedance Spectroscopy Data," *J. Electrochem. Soc.*, vol. 165, no. 14, pp. E826–E831, 2018.
[39] C. Schwandt and W. Weppner, "Variation of the oxygen exchange rate of zirconia-based electrodes by electrochemical pretreatment," *Solid State Ionics*, vol. 112, no. 3–4, pp. 229–236, 1998.
[40] K. Sakurai, H. Nagamoto, and H. Inoue, "Microstructure of Pt electrodes over solid-electrolyte and its effects on interfacial impedance," *Solid State Ionics*, vol. 35, no. 3–4, pp. 405–410, 1989.
[41] N. Nakagawa, C. Kuroda, and M. Ishida, "A new equivalent circuit for Pt/YSZ of a solid oxide electrolyte fuel cell: Relation between the model parameters and the interface characteristics," *Solid State Ionics*, vol. 40–41, no. PART 1, pp. 411–414, 1990.
[42] B. A. Boukamp, B. A. van Hassel, I. C. Vinke, K. J. De Vries, and A. J. Burggraaf, "The oxygen transfer process on solid oxide/noble metal electrodes, studied with impedance spectroscopy, dc polarization and isotope exchange," *Electrochim. Acta*, vol. 38, no. 14, pp. 1817–1825, 1993.
[43] R. De Levie, "On impedance measurements: The determination of the double layer capacitance in the presence of an electrode reaction," *Electrochim. Acta*, vol. 10, no. 4, pp. 395–402, 1965.
[44] R. de Levie, "On the impedance of electrodes with rough interfaces," *J. Electroanal. Chem.*, vol. 261, no. 1, pp. 1–9, 1989.
[45] H. Moreira and R. De Levie, "On the coupling of interfacial and diffusional impedances.II," *J. Electroanalitical Chem*, vol. 29, no. 1, pp. 353–374, 1971.
[46] H. Manjunatha, K. C. Mahesh, G. S. Suresh, and T. V Venkatesha, "The study of lithium ion de-insertion/insertion in $LiMn_2O_4$ and determination of kinetic parameters in aqueous Li_2SO_4 solution using electrochemical impedance spectroscopy," *Electrochim. Acta*, vol. 56, no. 3, pp. 1439–1446, 2011.
[47] Scribner Associates Inc., "ZView Operating Manual (version 3.5)." 2016.
[48] J. H. Chang, J. Park, Y. K. Pak, and J. J. Pak, "Fitting improvement using a new electrical circuit model for the electrode-electrolyte interface," *Proc. 3rd Int. IEEE EMBS Conf. Neural Eng.*, no. c, pp. 572–574, 2007.
[49] K. Z. Rajab *et al.*, "Broadband dielectric characterization of aluminum oxide (Al_2O_3)," *J. Microelectron. Electron. Packag.*, vol. 5, no. 1, pp. 2–7, 2008.
[50] Materials Morgan Advanced, "Alumina Ceramics (Al_2O_3)." [Online]. Available: http://www.morgantechnicalceramics.com/en-gb/materials/alumina/. [Accessed: 28-Apr-2020].
[51] Kyocera Global, "Alumina." [Online]. Available: https://global.kyocera.com/prdct/fc/list/material/alumina/index.html#.m1.p9. [Accessed: 28-Apr-2020].
[52] F. Talbi, F. Lalam, and D. Malec, "Dielectric breakdown characteristics of alumina," *Proc. 2010 IEEE Int. Conf. Solid Dielectr. ICSD 2010*, pp. 4–7, 2010.
[53] C. Neusel, H. Jelitto, D. Schmidt, R. Janssen, F. Felten, and G. A. Schneider, "Dielectric breakdown of alumina single crystals," *J. Eur. Ceram. Soc.*, vol. 32, no. 5, pp. 1053–1057, 2012.
[54] B. Block, Y. Kim, and D. K. Shetty, "Dielectric breakdown of polycrystalline alumina: A weakest-link failure analysis," *J. Am. Ceram. Soc.*, vol. 96, no. 11, pp. 3430–3439, 2013.
[55] M. Yoshimura and H. K. Bowen, "Electrical Breakdown Strength of Alumina at High Temperatures," *J. Am. Ceram. Soc.*, vol. 64, no. 7, pp. 404–410, Jul. 1981.
[56] K. Zarbout *et al.*, "Consequences of Silicon Segregation on the Dielectric Properties of Sintered Alumina," *Defect Diffus. Forum*, vol. 249, pp. 281–285, 2006.
[57] J. R. Harris, "A Tutorial on Vacuum Surface Flashover," *IEEE Trans. Plasma Sci.*, vol. 46, no. 6, pp. 1872–1880, 2018.
[58] Y. Cheng, A. Xu, W. Xiang, Y. Lei, L. Chen, and B. Tang, "Surface Flashover o f Alumina Ceramic Insulators i n Vacuum," in *28th International Symposium on Discharges and Electrical Insulation in Vaccum (ISDEIV)*, 2018, pp. 111–114.
[59] H. C. Miller, "Surface Flashover of Insulators," *IEEE Trans. Electr. Insul.*, vol. 24, no. 5, pp. 765–786, 1989.
[60] C. Gao, B. Qi, C. Li, M. Huang, and Y. Lv, "The surface charge of Al_2O_3 ceramic insulator under nanosecond pulse voltage in high vacuum: Characteristics and its impact on surface electric field," *J. Phys. D. Appl. Phys.*, vol. 53, no. 5, 2020.
[61] H. C. Miller, "Flashover of insulators in vacuum: The last twenty years," *IEEE Trans. Dielectr.*

Electr. Insul., vol. 22, no. 6, pp. 3641–3657, 2015.
[62] M. Yu, S. Grasso, R. Mckinnon, T. Saunders, and M. J. Reece, "Review of flash sintering: materials, mechanisms and modelling," *Adv. Appl. Ceram.*, vol. 116, no. 1, pp. 24–60, 2017.
[63] M. Cologna, J. S. C. Francis, and R. Raj, "Field assisted and flash sintering of alumina and its relationship to conductivity and MgO-doping," *J. Eur. Ceram. Soc.*, vol. 31, no. 15, pp. 2827–2837, 2011.
[64] M. Biesuz, "Flash Sintering of Alumina-based Ceramics," University of Trento, 2017.
[65] M. Biesuz, P. Luchi, A. Quaranta, and V. M. Sglavo, "Theoretical and phenomenological analogies between flash sintering and dielectric breakdown in α-alumina," *J. Appl. Phys.*, vol. 120, no. 14, 2016.
[66] J. Frenkel, "On Pre-Breakdown Phenomena in Insulators and Electronic Semi-Conductors," *Phys. Rev.*, vol. 54, no. 8, pp. 647–648, 1938.
[67] H. Schroeder, "Poole-Frenkel-effect as dominating current mechanism in thin oxide films - An illusion?!," *J. Appl. Phys.*, vol. 117, no. 21, 2015.
[68] X. F. Zong *et al.*, "Radiation-induced electrical degradation in crystalline Al_2O_3," *Phys. Rev. B*, vol. 49, no. 22, pp. 15514–15524, 1994.
[69] H. P. R. Frederikse and W. R. Holser, *High Temperature Electrical Conductivity of Aluminum Oxide*, vol. 9. Boston, 1975.
[70] R. J. Brook, J. Yee, and F. A. Kröger, "Electrochemical Cells and Electrical Conduction of Pure and Doped Al_2O_3," *J. Am. Ceram. Soc.*, vol. 54, no. 9, pp. 444–451, 1971.
[71] K. Kitazawa and R. L. Coble, "Electrical Conduction in Single-Crystal and Polycrystalline Al_2O_3 at High Temperatures," *J. Am. Ceram. Soc.*, vol. 57, no. 6, pp. 245–250, 1974.
[72] J. Pappis and W. D. Kingery, "Electrical Properties of Single-Crystal and Polycrystalline Alumina at High Temperatures," *J. Am. Ceram. Soc.*, vol. 44, no. 9, pp. 459–464, Sep. 1961.
[73] N. M. Tallan and H. C. Graham, "Interfacial Polarization and Electrical Conductivity in Sapphire," *J. Am. Ceram. Soc.*, vol. 48, no. 10, pp. 512–516, 1965.
[74] S. Grasso, Y. Sakka, and G. Maizza, "Electric current activated/assisted sintering (ECAS): A review of patents 1906-2008," *Sci. Technol. Adv. Mater.*, vol. 10, no. 5, pp. 53001–24, 2009.
[75] A. G. Bloxam, "Improved manufacture of electric incandescence lamp laments from tungsten or molybdenum or an alloy thereof," GBD190609020 19060414, 1906.
[76] M. Cologna, B. Rashkova, and R. Raj, "Flash sintering of nanograin zirconia in < 5s at 850°C," *J. Am. Ceram. Soc.*, vol. 93, no. 11, pp. 3556–3559, 2010.
[77] C. E. J. Dancer, "Flash sintering of ceramic materials," *Mater. Res. Express*, vol. 3, no. 10, 2016.
[78] T. Saunders, S. Grasso, and M. J. Reece, "Ultrafast-Contactless Flash Sintering using Plasma Electrodes," *Sci. Rep.*, vol. 6, 2016.
[79] L. B. Caliman, E. Bichaud, P. Soudant, D. Gouvea, and M. C. Steil, "A simple flash sintering setup under applied mechanical stress and controlled atmosphere," *MethodsX*, vol. 2, pp. 392–398, 2015.
[80] S. Grasso *et al.*, "Flash spark plasma sintering (FSPS) of pure ZrB_2," *J. Am. Ceram. Soc.*, vol. 97, no. 8, pp. 2405–2408, 2014.
[81] C. Manière, G. Lee, and E. A. Olevsky, "All-Materials-Inclusive Flash Spark Plasma Sintering," *Sci. Rep.*, vol. 7, no. 1, 2017.
[82] E. Zapata-Solvas, D. Gómez-García, A. Domínguez-Rodríguez, and R. I. Todd, "Ultra-fast and energy-efficient sintering of ceramics by electric current concentration," *Sci. Rep.*, vol. 5, 2015.
[83] R. Muccillo and E. N. S. Muccillo, "Electric field assisted sintering of electroceramics and in situ analysis by impedance spectroscopy," *J. Electroceramics*, vol. 38, no. 1, pp. 24–42, 2017.
[84] J. S. C. Francis and R. Raj, "Influence of the field and the current limit on flash sintering at isothermal furnace temperatures," *J. Am. Ceram. Soc.*, vol. 96, no. 9, pp. 2754–2758, 2013.
[85] K. Naik, S. K. Jha, and R. Raj, "Correlations between conductivity, electroluminescence and flash sintering," *Scr. Mater.*, vol. 118, pp. 1–4, 2016.
[86] "Electroluminescence - an overview | ScienceDirect Topics." [Online]. Available: https://www.sciencedirect.com/topics/agricultural-and-biological-sciences/electroluminescence. [Accessed: 26-Jan-2018].
[87] R. I. Todd, E. Zapata-Solvas, R. S. Bonilla, T. Sneddon, and P. R. Wilshaw, "Electrical characteristics of flash sintering: Thermal runaway of Joule heating," *J. Eur. Ceram. Soc.*, vol.

35, no. 6, pp. 1865–1877, 2015.

2.5 Supplementary

2.5.1 p-type semi conductivity, $MO \rightarrow M_{1-x}O$

Case (a):

$$1/2\, O_{2(g)} \underset{K_a}{\overset{T_a}{\leftrightarrow}} O_O^x + V''_M + 2h^\bullet \quad \text{(S2.1)}$$

Therefore, $[V''_M] = [h^\bullet]/2$ (S2.2)

K_a=equilibrium constant for a fixed temperature, T_a

$$K_a = \frac{[O_O^x][V''_M][h^\bullet]^2}{pO_2^{1/2}} \quad \text{(S2.3)}$$

Replacing S2.2 in S2.3

$$K_a = \frac{[O_O^x][h^\bullet]^3}{2pO_2^{1/2}} \quad \text{(S2.4)}$$

Rearranging S2.4 to get relationship between $[h^\bullet]$ and pO_2

$$[h^\bullet] = \sqrt[3]{\frac{2K_a}{[O_O^x]}} \cdot pO_2^{1/6} \quad \text{(S2.5)}$$

Case (b):

$$1/2\, O_{2(g)} \underset{K_b}{\overset{T_b}{\leftrightarrow}} O_O^x + V'_M + h^\bullet \quad \text{(S2.6)}$$

Therefore, $[V'_M] = [h^\bullet]$ (S2.7)

K_b=equilibrium constant for a fixed temperature, T_b

$$K_b = \frac{[O_O^x][V'_M][h^\bullet]}{pO_2^{1/2}} \quad \text{(S2.8)}$$

Replacing S2.7 in S2.8

$$K_b = \frac{[O_O^x][h^\bullet]^2}{pO_2^{1/2}} \quad \text{(S2.9)}$$

Rearranging S2.9 to get relationship between $[h^\bullet]$ and pO_2

$$[h^\bullet] = \sqrt{\frac{K_b}{[O_O^x]}} \cdot pO_2^{1/4} \quad \text{(S2.10)}$$

2.5.2 n-type semi conductivity, $MO_2 \rightarrow MO_{2-x}$

Case (c):

$$O_O^x \underset{K_c}{\overset{T_c}{\leftrightarrow}} 1/2\, O_{2(g)} + V_O^{\bullet\bullet} + 2e' \quad \text{(S2.11)}$$

Therefore, $[V_O^{\bullet\bullet}] = [e']/2$ (S2.12)

K_c=equilibrium constant for a fixed temperature, T_c

$$K_c = \frac{pO_2^{1/2}[V_O^{\bullet\bullet}][e']^2}{[O_O^x]} \quad \text{(S2.13)}$$

Replacing S2.12 in S2.13

$$K_c = \frac{pO_2^{1/2}[e']^3}{2[O_O^x]} \quad \text{(S2.14)}$$

Rearranging S2.4 to get relationship between $[e']$ and pO_2

$$[e'] = \sqrt[3]{2K_c[O_O^x]} \cdot pO_2^{-1/6} \quad \text{(S2.15)}$$

Case (d):

$$O_O^x \overset{T_d}{\underset{K_d}{\leftrightarrow}} {}^1/_2\, O_{2(g)} + V_O^{\bullet} + e' \quad \text{(S2.16)}$$

Therefore, $[V_O^{\bullet}] = [e']$ (S2.17)

K_d=equilibrium constant for a fixed temperature, T_d

$$K_d = \frac{pO_2^{1/2}[V_O^{\bullet}][e']}{[O_O^x]} \quad \text{(S2.18)}$$

Replacing S2.6 in S2.7

$$K_d = \frac{pO_2^{1/2}[e']^2}{[O_O^x]} \quad \text{(S2.19)}$$

Rearranging S2.19 to get relationship between $[e']$ and pO_2

$$[e'] = \sqrt{K_d[O_O^x]} \cdot pO_2^{-1/4} \quad \text{(S2.20)}$$

CHAPTER 3
Experimental Procedures

3.1 Solid state synthesis

Samples* were prepared by solid-state reaction, using reagents on Table 3.1, which were dried overnight. Stoichiometric amounts of reagents were weighted on a Sartorius Entris balance with a tolerance of ± 0.0003 grams. Then, the mixtures were manually ground with acetone using a pestle and mortar, and heated in alumina crucibles at 1150°C to decarbonate $CaCO_3$ and start the reaction. Next, the powders were reground and uniaxially pressed into pellets of 10mm in diameter at around 98MPa and heated to sintering temperature for 10 h, with a heating and cooling rate of 5°C/min.

Table 3.1. *Drying temperature, purity and source of reagents*

Reagent	Drying Temperature (°C)	Purity	Company
$CaCO_3$	180°C	99%	Fisher
ZrO_2	1000°C	99%	Aldrich

3.2 Flash sintering

Synthesised powders with 5wt% of PVA were uniaxially pressed into dog bone-shaped samples by applying ~ 1ton. To burn out the binder, the samples were taken up to 550°C for 2 h with a heating rate of 2 °C/min, and then heated to the pre-sintered temperature for 2h. Pt paste electrodes were painted inside the holes of the dog-bones and dried at 900 °C for 2 h. The samples were suspended inside a tube furnace using Pt wires and heated from room temperature with a heating rate of 10 °C/min; a constant electric field was applied, 100 V/cm, with a limit current density set at 100 mA/mm^2.

3.3 Density determination

Theoretical and experimental densities were calculated. The theoretical density (ρ_{th}) was obtained from equation 3.1

$$\rho_{th} = \frac{mZ}{VN_A} \tag{3.1}$$

where ρ_{th} is the density (g/cm^3), m is the molecular weight of the composition (g/mol), Z is the number of formula units per unit cell, V is the volume of the unit cell (cm^3) and N_A is Avogadro's number. For the calcia-stabilised zirconia, the crystal structure is face centred cubic, therefore $Z = 4$. To obtain the volume of the unit cell, first the lattice parameter of the samples was calculated by taking one reflection plane of the diffraction pattern, and then applying Bragg's Law, equation (3.2)

$$2d\sin\theta = n\lambda \tag{3.2}$$

Then, taking the relationship between the d-spacing of that plane and the lattice parameter of a cubic arrangement, equation (3)

$$d = \frac{a}{\sqrt{h^2+k^2+l^2}} \tag{3.3}$$

where d is the d-spacing, θ the Bragg angle, 2θ the peak position, λ is the wavelength of the incident radiation, n is the order of reflection (integer number), a is the lattice parameter and hkl represent the Miller Indices. Finally, the volume of the unit cell was obtained by equation (3.4)

$$V = a^3 \tag{3.4}$$

*Alumina samples with compositions 0.05wt%MgO-Al_2O_3 (Mg0.05) and 0.5wt%(MgO/SiO_2)-Al_2O_3 were provided by an industrial contact. These are typically prepared from reagent grade (> 99%) Al_2O_3, $Mg(NO_3)_2{\cdot}4H_2O$ and $Si(OC_2H_5)_4$, and sintered at 1550°C for 8 h in air [1]–[3].

For the experimental density (ρ_{exp}), the mass of the pellet was divided by the volume of the pellet, which was obtained by measuring its thickness and diameter. In order to find out relative density of the sample, ρ_{exp} was divided by ρ_{th} and multiplied by 100.

3.4 X-ray diffraction (XRD)

Sintered powders were analysed using the diffractometers on Table 3.2. Data were collected from 2θ = 20-80° and compared to various diffraction patterns, Table 3.3, using the JCPDS database. The cubic lattice parameter was determined by least-squares refinement using STOE WinXPOW version 2.25, with Si powder as internal standard.

***Table 3.2**. Diffractometers*

Diffractometer	Radiation	Purpose
Bruker D2	Cu Kα	Phase analysis
STOE STADI P	Cu $K\alpha_1$	Lattice parameter calibration

***Table 3.3**. Diffractions patterns from JCPDS database*

Diffraction pattern	PDF card
$CaCO_3$	00-041-1475
CaO	00-037-1484
$CaZrO_3$	00-035-0790
$CaZr_4O_9$	00-031-0323
ZrO_2 monoclinic	00-037-1484
ZrO_2 tetragonal	01-078-5752
ZrO_2 cubic	01-070-7361
Al_2O_3	04-005-4213
$MgAl_2O_4$	04-008-8339

3.5 Electron microscopy

Samples were grinded and polished metallographically using an AutoMet™ grinder-polisher following the conditions on Table 3.4, based on Struers Inc. recommendations [4]. For thermal etching, samples were heated up to 80% of its sintering temperature for 30 minutes, following the procedure mentioned by Täffner et al. [5]. Next, samples were mounted in aluminium stubs with Ag paste and sputter with 10nm of carbon. Scanning electron microscopy (SEM) images were taken on a field-emission scanning electron microscope (FEI Inspect F50) using an acceleration voltage of 15 kV and energy- dispersion analysis of X-rays (EDX) from Oxford Instruments using 20 kV.

***Table 3.4**. Metallographic grinding and polishing conditions*

Step	Grind paper or paste	Time (minutes)	Force (N)	Rotational speed (rpm)
1	800P	1	20	300
2	2500P	1	20	300
3	6 μm	10	20	150
4	3μm	10	20	150
5	1μm	10	20	150
6	¼ μm	10	10	150
7	0.04μm colloidal SiO_2	20	10	150

3.6 Impedance Spectroscopy

For impedance measurements, Pt paste electrodes were applied to both faces of the pellets and dried at 900 °C for 2 h. Three impedance analysers were used throughout this study, with the accuracy measurements, frequency ranges and nominal ac voltages listed in Table 3.5.

***Table 3.5**. Impedance analysers*

Impedance analyser	Frequency range (Hz)	Nominal ac voltage (mV)	Measurement accuracy (± %)
Agilent 4294A	0.04k-1M	100	0.08
Solartron SI 1260	10m-1M	100	0.1
Modulab XM MTS	10m-1M	100	0.1

Electroded pellets were attached to the Pt leads of an in-house conductivity jig with the facility to vary the atmosphere flowing over the pellet. Prior to pO_2 measurements gases were dried by directing the flow through a desiccator to avoid protonic conduction. Two sets of corrections were made to the collected data: (i) a geometric factor concerning pellet thickness and sample-electrode contact area and (ii) jig characteristics consisting of the blank, open circuit capacitance, typically 6 pF and the closed circuit resistance of, primarily, the leads, 1–2 Ω. Data analysis and equivalent circuit fitting was performed using ZVIEW software (ZVIEW-Impedance Software version 2.4 Scribner Associates).

The Brickwork model [6] was employed for the identification of the electrical microstructure of the samples, which uses the magnitude of the capacitance as the determination parameter, based on the parallel plate capacitor relationship, equation 3.5

$$C = \varepsilon' \varepsilon_0 \frac{A}{l} \qquad (3.5)$$

Where ε' is the relative permittivity of the material, ε_0 the permittivity of the free space, A the sample's surface area and l the sample's thickness. Assuming a constant unit A/l =1 and a typical ε' of ~10, results in a capacitance of ~ 1pFcm^{-1}, which is a typical bulk response. If the grains are represented by cubes of dimension l_b, separated by grain boundary of thickness l_{gb}, with a sample-electrode interface of thickness l_e, Figure 3.1, these regions can be identified making use of Table 3.6, taking into account the inverse relationship between the thickness and capacitance.

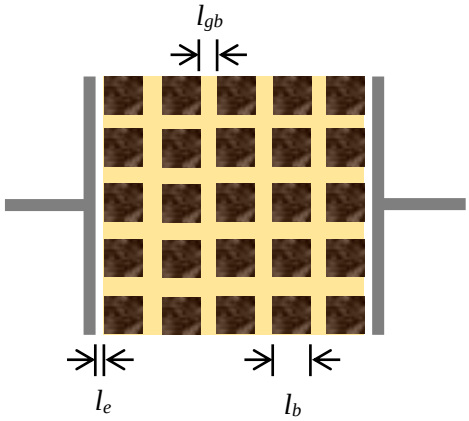

***Figure 3.1**. Representation of the Brickwork layer model, showing the thickness of the grains, grain boundaries and sample-electrode interface.*

***Table 3.6**. Capacitance values and their possible interpretation* [6].

Phenomenon or region responsible	Capacitance (Fcm^{-1})
Bulk/grain	10^{-12}
Minor, second phase; constriction resistance	10^{-11}
Grain boundary	10^{-11} to 10^{-8}
Bulk ferroelectric	10^{-10} to 10^{-9}
Surface layer; depletion layer	10^{-9} to 10^{-7}
Sample-electrode interface	10^{-7} to 10^{-5}
Electrochemical reactions	10^{-4} or higher

Each of these regions has a time constant τ, which is independent from geometry and it is related to the conductivity (σ) and permittivity, and consequently to its resistance and capacitance, equation 3.6

$$\tau = \varepsilon' \varepsilon_0 / \sigma = RC \tag{3.6}$$

These regions will relax-out at their corresponding ω_{max} (ω=2πf). Therefore, they can be identified by their time constant, following equation 3.7, and separated from each other.

$$\omega_{max}\tau = \omega_{max}RC = 1 \tag{3.7}$$

To have a broader data analysis perspective, impedance data was also plotted in the different complex formalisms listed on Table 3.7. Each of these formalisms will highlight different features of the same data set. Spectroscopic plots of log Y' will show the total dc conductivity as a plateau at low frequencies, M'' the element with the smallest capacitance in the spectra and log C' the plateaus of the different elements, with the one at the high frequencies related to the bulk capacitance and therefore the permittivity of the material.

Typically, at a fixed temperature the frequency window does not show all the regions or elements of the impedance spectra. Therefore, there is the need to perform measurements at different temperatures to have access to the whole spectra and observe all elements.

To have a broader data analysis perspective, impedance data was also plotted in the different complex formalisms listed on Table 3.7.

***Table 3.7**. Interrelation of complex formalisms* [7].

Formalism	Symbol	Relation to Z*
Admittance	Y*	$[Z^*]^{-1}$
Electric modulus	M*	$j\omega Z^*$
Complex capacitance	E*	$[j\omega Z^*]^{-1}$

Absolute values multiply by C_0 to get relative values, where $C_0 = \varepsilon_0 A/l$; capacitance of empty cell.

3.7 Simulation of equivalent circuits and their impedance response

The aim of this section is to have a visual representation of the change in the impedance response when the values of specific parameters are modified. The effect of a constant phase element (CPE), a dielectric response (series RC element), and an inductor is explored. Relevant equivalent circuits equations were derived. In addition, a new approach to show the relative importance of individual elements to the

overall impedance response is presented. The values used for the simulations are approximations of a sample that has been corrected for its overall geometry.

Data simulation was performed using ZVIEW software (ZVIEW-Impedance Software version 2.4 Scribner Associates) and plotted using Origin Pro 2019 software. For data fitted to an equivalent circuit, residuals were calculated using equations 3.8 and 3.9.

$$Z'_{residual} = \frac{Z'_{measured} - Z'_{calculated}}{|Z'_{measured}|} \quad (3.8)$$

$$Z''_{residual} = \frac{Z''_{measured} - Z''_{calculated}}{|Z''_{measured}|} \quad (3.9)$$

The type of data weighting was 'Calc-Proportional' which normalizes each real and imaginary value separately. To compare different equivalent circuits using the same data, the goodness of fit was determined by the sum of squares (chi-squares) which is proportional to the average error between the original data and the calculated values [8].

3.7.1 Derivation of impedance equations

The following points were considered:

- Admittances add in parallel and impedances in series
- $j = \sqrt{-1} \therefore\ j^2 = -1$
- To remove j from denominator:
    - Multiply by j/j $\quad \frac{1}{jb} \times \frac{j}{j} = \frac{j}{j^2 b} = -\frac{j}{b}$
    - Use complex conjugate $\quad \frac{1}{a-jb} \times \frac{a+jb}{a+jb} = \frac{a+jb}{a^2 - j^2 b^2} = \frac{a+jb}{a^2+b^2}$

3.7.2 Effect of constant phase element (CPE)

To illustrate the change in the impedance response of a parallel R-CPE-C equivalent circuit by varying each parameter, a set of simulations was performed. While one parameter was set as a variable, the rest were kept fixed. No material was used as reference, and the data range for each variable was chosen to show a general trend.

The effect of varying R is shown in Figure 3.2. The Z* plane (a) shows that the arc scales to the value of R. The log C' plot (b), appears to be independent of R, as it does not change. The log Y' plot (c), shows that the low frequency intercept with the y axis increases with decreasing R, and the shift from a constant Y' value to the high frequency dispersion moves to lower frequencies with increasing R. The Z'' peak (d) decreases significantly and moves to higher frequencies with decreasing R. And the M'' peak (e), increases slightly and moves to higher frequencies with decreasing R.

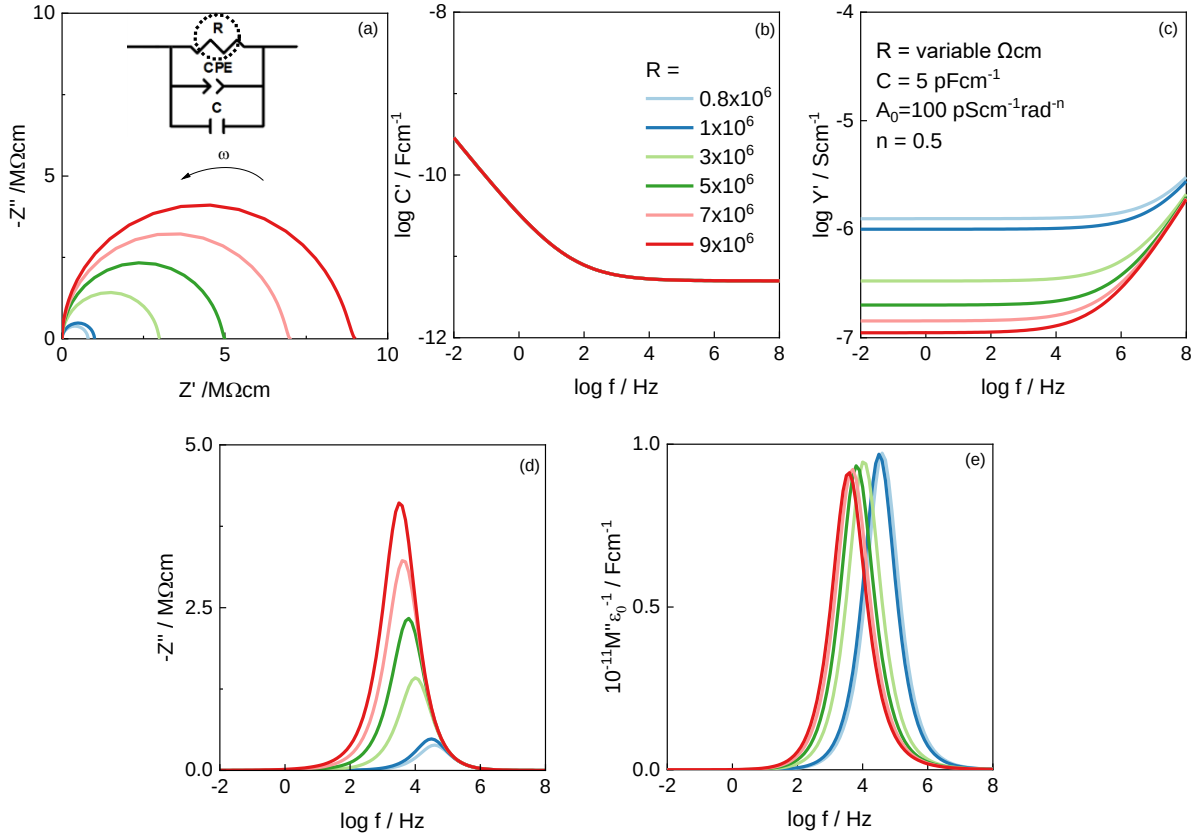

Figure 3.2 *Simulation of the change in R of the impedance response of a parallel R-CPE-C element represented with an (a) impedance complex plane and spectroscopic plots of (b) capacitance, (c) admittance, (d) Z'' and (e) M''.*

The effect of varying C is shown in Figure 3.3. The Z* plane (a) shows that the arc intercepts remain the same, but its height decreases with decreasing C. The log C' plot (b), shows that the high frequency limiting plateau decreases with decreasing C, but the low frequency dispersion remains the same. The log Y' plot (c), appears to be independent of C, as it did not change. The Z'' peak (d) increases slightly and moves to higher frequencies with decreasing C. And the M'' peak (e), increases significantly and moves to higher frequencies with decreasing C.

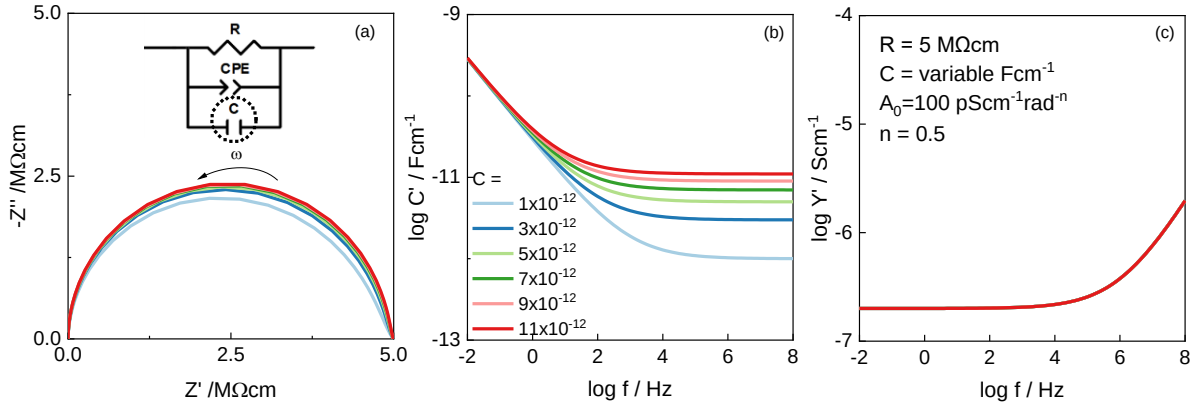

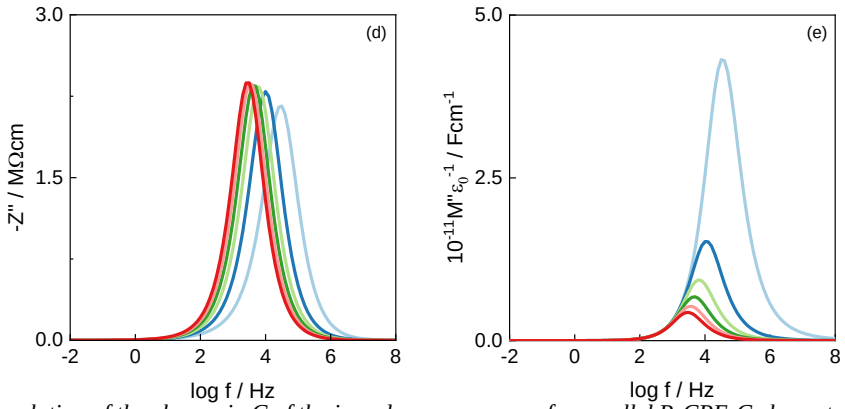

Figure 3.3 *Simulation of the change in C of the impedance response of a parallel R-CPE-C element represented with an (a) impedance complex plane and spectroscopic plots of (b) capacitance, (c) admittance, (d) Z'' and (e) M''.*

The effect of varying the A_0 parameter of the CPE is shown in Figure 3.4. The Z* plane (a) shows that the arc intercepts remain the same, but its height decreases with increasing A_0. The log C' plot (b), shows that all plots reach the same high frequency limiting plateau and the low frequency dispersion keeps the same slope (with a value of n-1), but the intersection of these two regions moves to higher frequencies with increasing A_0. The log Y' plot (c), shows that all plots reach the same low frequency limiting plateau and the high frequency dispersion remains with the same slope (with a value of n), but the transition from one region the other moves to higher frequencies with decreasing A_0. The Z'' peak (d) decreases, broadens and moves to lower frequencies with increasing A_0. And the M'' peak (e), seems to mirror the behaviour of the Z'' peak, as it decreases, broadens but moves to higher frequencies with increasing A_0.

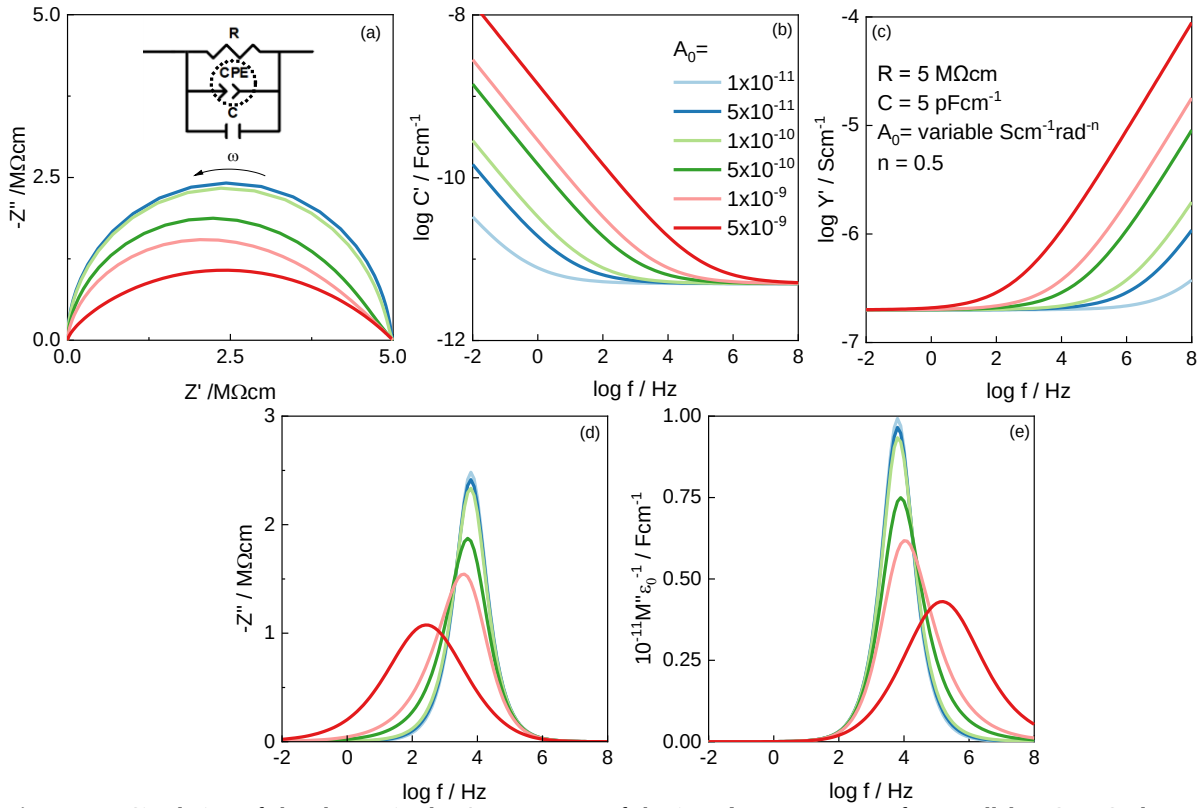

Figure 3.4*. Simulation of the change in the A_0 parameter of the impedance response of a parallel R-CPE-C element represented with an (a) impedance complex plane and spectroscopic plots of (b) capacitance, (c) admittance, (d) Z'' and (e) M''.*

The effect of varying the n parameter of the CPE is shown in Figure 3.5. The Z* plane (a) shows that the arc intercepts remain the same, but its height increases with decreasing n. The log C' plot (b), shows that with increasing n the slope of the low frequency dispersion (with a value of n-1) decreases. The log Y' plot (c), shows that with increasing n, the slope of the high frequency dispersion increases (as it has the value of n) and the low frequency plateau proves to be independent of n. The Z'' peak (d) increases and moves to higher frequencies with decreasing n. And the M'' peak (e) increases and minimally moves to higher frequencies with decreasing n. In addition, at higher frequencies a shoulder seems to appear with increasing n.

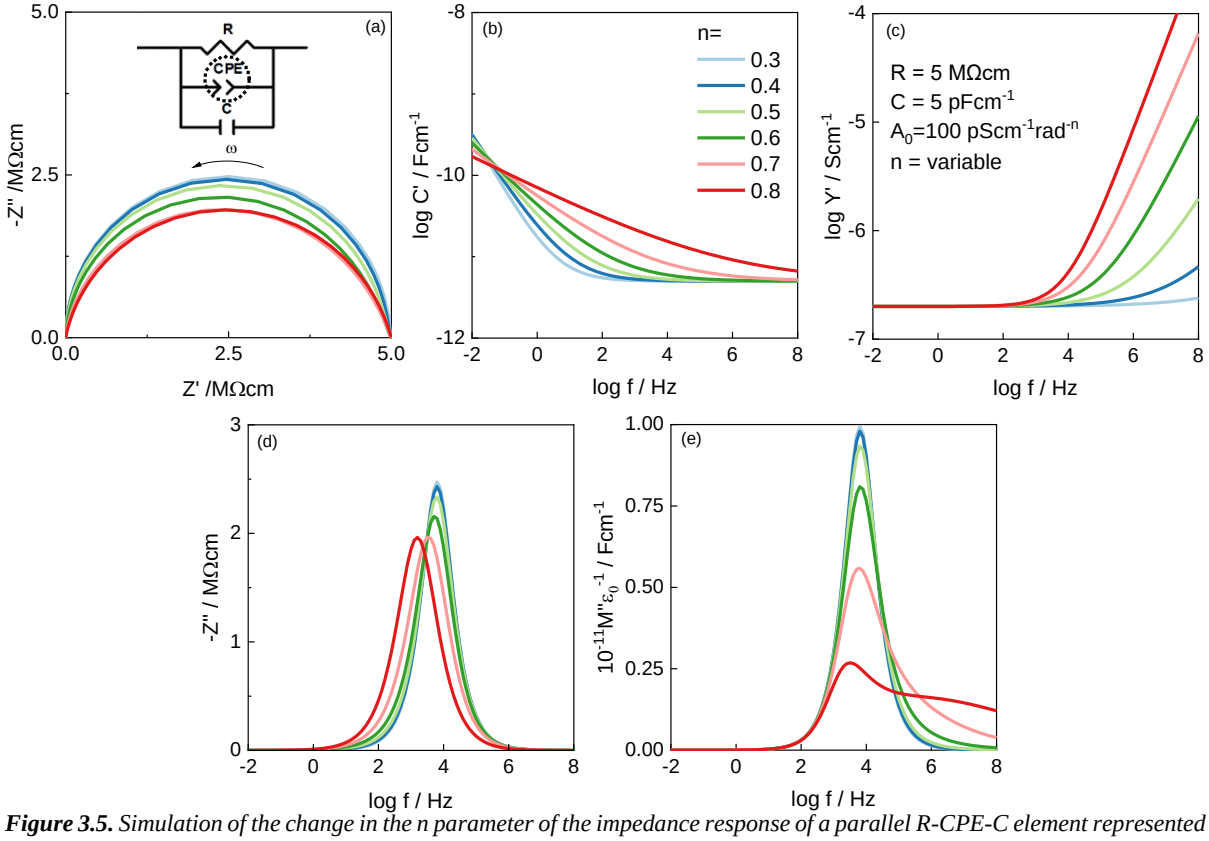

Figure 3.5. *Simulation of the change in the n parameter of the impedance response of a parallel R-CPE-C element represented with an (a) impedance complex plane and spectroscopic plots of (b) capacitance, (c) admittance, (d) Z'' and (e) M''.*

3.7.2.1Derivation of impedance equations for a parallel R-C-CPE element

The admittance of a CPE can be described as,

$$Y^*_{CPE} = A_0\omega^n\left[\cos\left(\frac{n\pi}{2}\right) + j\sin\left(\frac{n\pi}{2}\right)\right] = \mathrm{A}\omega^n + jB\omega^n$$

Therefore, the admittance of a parallel R-C-CPE element would take the form of

$$\mathrm{Y^*} = \frac{1}{\mathrm{R}} + \mathrm{j}\omega\mathrm{C} + \mathrm{A}\omega^{\mathrm{n}} + jB\omega^n$$

The inverse of the admittance will give the impedance

$$\mathrm{Z^*} = \frac{1}{\mathrm{Y^*}} = \frac{1}{\left(\frac{1}{\mathrm{R}} + \mathrm{A}\omega^{\mathrm{n}}\right) + \mathrm{j}(\omega\mathrm{C} + \mathrm{B}\omega^{\mathrm{n}})}$$

Rearrangement of the equation by multiplying it by R/R

$$\mathrm{Z^*} = \frac{\mathrm{R}}{(1 + \mathrm{RA}\omega^{\mathrm{n}}) + \mathrm{j}(\omega\mathrm{RC} + \mathrm{RB}\omega^{\mathrm{n}})}$$

Removing j from the denominator will give an equation that can be separated into its real and imaginary parts

$$Z^* = \frac{R(1 + RA\omega^n) - jR(\omega RC + RB\omega^n)}{(1 + RA\omega^n)^2 + (\omega RC + RB\omega^n)^2}$$

Real part, Z'

$$Z' = \frac{R(1 + RA\omega^n)}{(1 + RA\omega^n)^2 + (\omega RC + RB\omega^n)^2}$$

if $\omega = 0$

$$Z' = R$$

if $\omega \to \infty$

$$Z' = \text{undefined} \therefore 0$$

Imaginary part Z''

$$Z'' = -\frac{R(\omega RC + RB\omega^n)}{(1 + RA\omega^n)^2 + (\omega RC + RB\omega^n)^2}$$

if $\omega = 0$

$$Z'' = 0$$

if $\omega \to \infty$

$$Z'' = \text{undefined} \therefore 0$$

3.7.3 Effect of a dipole in an equivalent circuit

One of the conclusions of Chapter 4 was that a good fit to the bulk response of CSZ x=0.12, 0.15 and 0.18, was obtained by adding a series R-C element in parallel with a parallel R-CPE-C. The effect in the impedance response by changing the values of the capacitor (C_0) and resistor (R_0) of the dielectric element is explored and compared to the impedance response of a parallel R-CPE-C element.

The effect of varying C_0 from 5 to 0.1 pFcm^{-1}, is observed in Figure 3.6. The Z* plane (a) shows that the intercepts of the arc do not change, but its height increases slightly with increasing C_0. The log C' plot (b) shows an intermediate plateau with the presence of the dielectric element at intermediate frequencies. The capacitance of this plateau increases with increasing C_0. The log Y' plot (c) shows the development of a plateau between the frequency-independent region and the high frequency dispersion, which increases with increasing C_0. The Z'' peak (d) minimally increases and shifts to lower frequencies with increasing C_0. The M'' plot (e) shows two peaks at intermediate and high frequencies, related respectively to the R-CPE-C and dielectric element. With increasing C_0, the intermediate frequency peak decreases, while the high frequency peak increases.

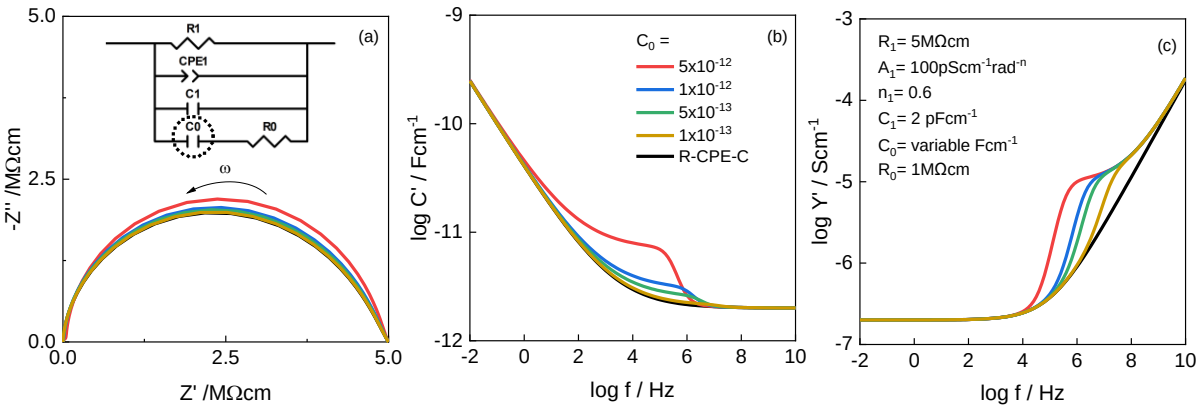

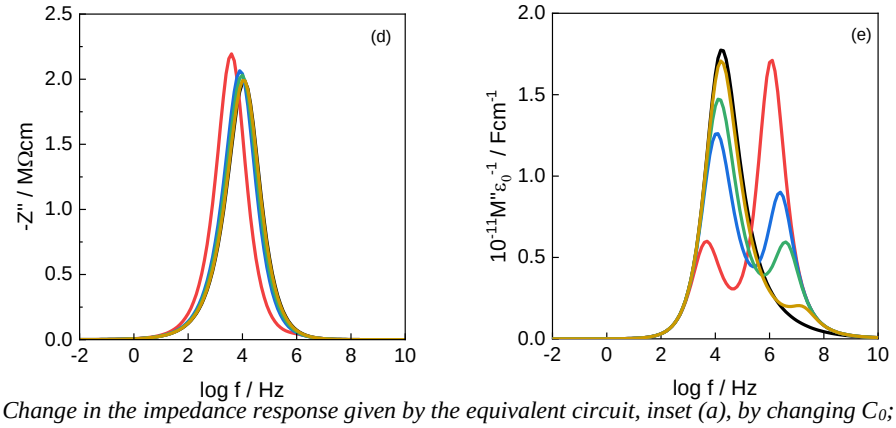

***Figure 3.6**. Change in the impedance response given by the equivalent circuit, inset (a), by changing C_0; (a) impedance complex plane and spectroscopic plots of (b) capacitance, (c) admittance, (d) Z'' and (e) M''.*

The effect of varying R_0 from 0.1 to 100 MΩcm is shown in Figure 3.7. The Z* plane (a) shows that the curvature of the arc changes with R_0, but the intercepts with the real axis remain the same. The log C' plot (b) shows that the intermediate frequency plateau moves to higher frequencies with decreasing R_0. Log Y' (c) shows that the dielectric plateau shifts to higher frequencies and increases its admittance. The height of the Z'' peak (d) fluctuates as with low values of R_0 it increases slightly, but with high values decreases. The M'' plots (e) shows a similar behaviour to the R-CPE-C response with high values of R_0. However, when decreasing R_0 the M'' peak decreases in height and divides in two, with the new peak shifting to higher frequencies. The magnitude of the changes depends on R_0, and can be either diminished or enhanced according to the value of C_0, Figure 3.S1 and 3.S2.

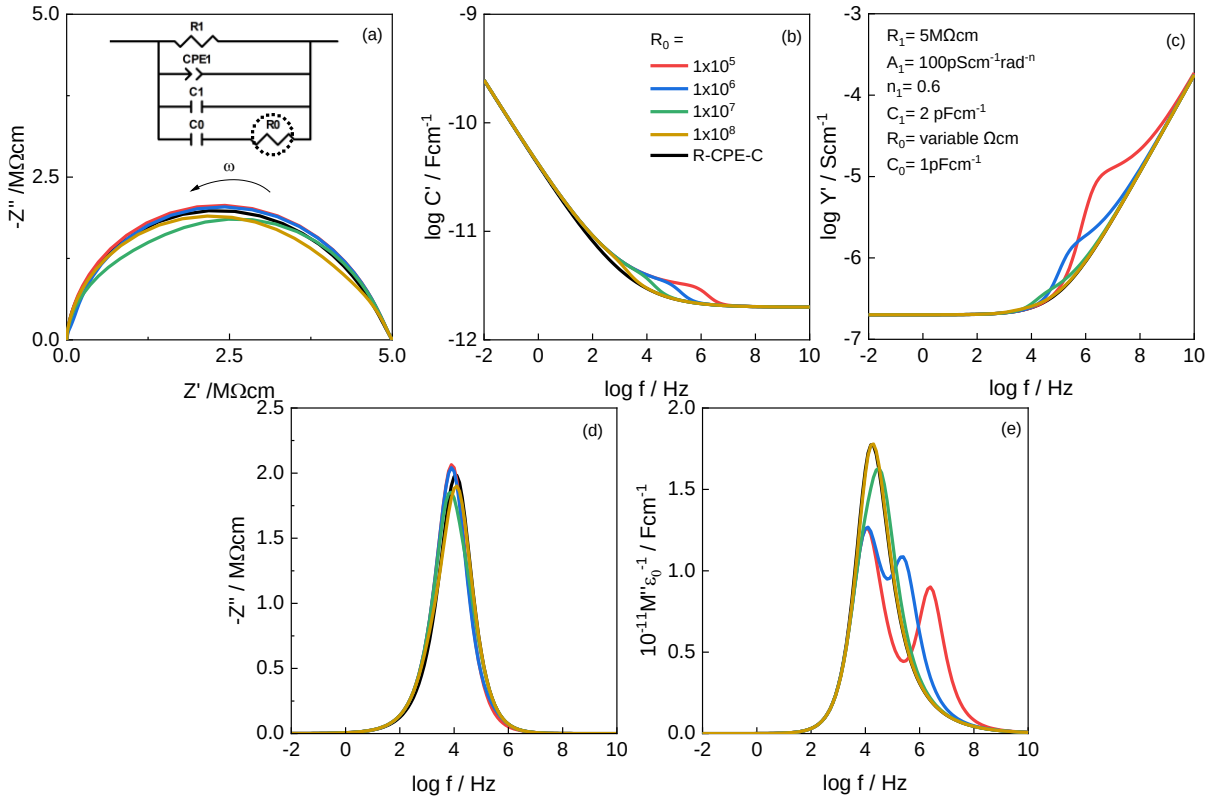

***Figure 3.7**. Change in the impedance response given by the equivalent circuit, inset (a), by changing R_0; a) impedance complex plane and spectroscopic plots of (b) capacitance, (c) admittance, (d) Z'' and (e) M''.*

3.7.3.1 Derivation of impedance equation for a series R_0-C_0 in parallel with a parallel R-C-CPE element

The impedance of series R_0-C_0 can be described as,

$$Z^* = R_0 + \frac{1}{j\omega C_0}$$

The inverse of the admittance will give the impedance

$$Y^* = \frac{1}{Z^*} = \frac{1}{R_0 + \frac{1}{j\omega C_0}}$$

Rearranging

$$Y^* = \frac{j\omega C_0}{1 + j\omega R_0 C_0}$$

Removing j from the denominator

$$Y^* = \frac{(\omega R_0 C_0)^2 + j\omega C_0}{1 + (\omega R_0 C_0)^2}$$

The admittance of the series R_0-C_0 in parallel with a parallel R-CPE-C element will be given by

$$Y^* = \frac{1}{R} + A\omega^n + jB\omega^n + j\omega C + \frac{(\omega R_0 C_0)^2 + j\omega C_0}{1 + (\omega R_0 C_0)^2}$$

Therefore, its impedance will have the form of

$$Z^* = \frac{1}{Y^*} = \frac{1}{\frac{1}{R} + A\omega^n + jB\omega^n + j\omega C + \frac{(\omega R_0 C_0)^2 + j\omega C_0}{1 + (\omega R_0 C_0)^2}}$$

Rearranging, grouping the real and imaginary numbers and passing j to the numerator will give

$$Z^* = \frac{R\left(1 + RA\omega^n + \frac{R(\omega R_0 C_0)^2}{1 + (\omega R_0 C_0)^2}\right) + jR\left(RB\omega^n + \omega RC + \frac{j\omega RC_0}{1 + (\omega R_0 C_0)^2}\right)}{\left(1 + RA\omega^n + \frac{R(\omega R_0 C_0)^2}{1 + (\omega R_0 C_0)^2}\right)^2 + \left(RB\omega^n + \omega RC + \frac{j\omega RC_0}{1 + (\omega R_0 C_0)^2}\right)^2}$$

Real part, Z'

$$Z' = \frac{R\left(1 + RA\omega^n + \frac{R(\omega R_0 C_0)^2}{1 + (\omega R_0 C_0)^2}\right)}{\left(1 + RA\omega^n + \frac{R(\omega R_0 C_0)^2}{1 + (\omega R_0 C_0)^2}\right)^2 + \left(RB\omega^n + \omega RC + \frac{j\omega RC_0}{1 + (\omega R_0 C_0)^2}\right)^2}$$

if $\omega = 0$

$$Z' = R$$

if $\omega \to \infty$

$$Z'' = \text{undefined} \therefore 0$$

Imaginary part, Z''

$$Z'' = \frac{R\left(RB\omega^n + \omega RC + \frac{j\omega RC_0}{1 + (\omega R_0 C_0)^2}\right)}{\left(1 + RA\omega^n + \frac{R(\omega R_0 C_0)^2}{1 + (\omega R_0 C_0)^2}\right)^2 + \left(RB\omega^n + \omega RC + \frac{j\omega RC_0}{1 + (\omega R_0 C_0)^2}\right)^2}$$

if $\omega = 0$

$$Z'' = 0$$

if $\omega \to \infty$ $Z'' = \text{undefined} \therefore 0$

3.7.4 Inductance effect

The effect of including an inductance, in series with a resistor and a parallel R-C/CPE element was studied simulating equivalent circuits (A) and (B) in Figure 3.8. Simulation results of both circuits follows the same trend in most circumstances; therefore, the description applies for both equivalent circuits unless mentioned otherwise. Therefore, figures for circuit (B) are shown within the text and for (A) in the supplementary.

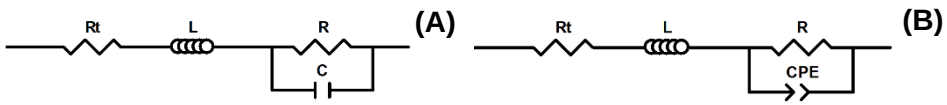

***Figure 3.8**. Equivalent circuits considering inductive effect.*

The characteristic features of the presence of an inductive effect can be identified as a high frequency tail that drops to negative values on the Z* plane, and -Z'' plot. On the log C' plot, the appearance of a disruptive inverted peak, and on the log Y' plot the high frequency positive dispersion, is substituted with a negative dispersion. As the inductive effect usually appears at high temperatures the R values are small. For this reason the M'' peak is out of the frequency range.

The effect of varying R_t from 60 to 140 Ωcm is shown in Figures 3.9 and 3.S3. With increasing R_t the impedance response shifts to the right, on the Z* plane (a) and to lower capacitance (b) and admittance (c) values. The -Z'' plot (d) seems to be independent of R_t. The M'' plot, shows a positive high frequency dispersion, which might be part of a peak; which shifts slightly to lower frequencies with increasing R_t.

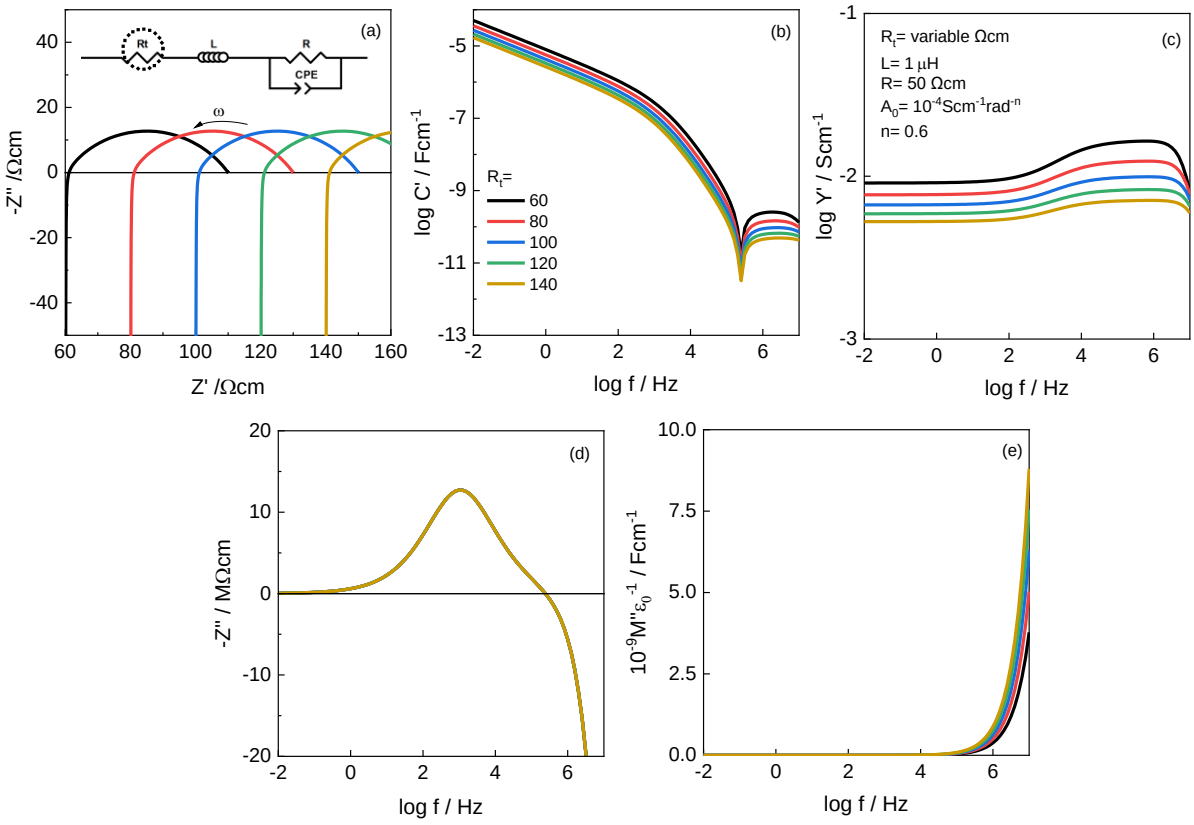

***Figure 3.9**. Change in the impedance response given by the equivalent circuit, inset (a), by changing R_t;(a) impedance complex plane and spectroscopic plots of (b) capacitance, (c) admittance, (d) Z'' and (e) M''.*

The effect of varying L from 10^{-8} to 10^{-4} H is shown in Figures 3.10 and 3.S4. The Z* plane (a) shows that the length of the tails increases by sinking to lower values. In addition, the high frequency intercept with the Z' axis shifts to the right with equivalent circuit 7(b). However, the intercepts of the arc remain the same for equivalent circuit Fig 10.7(a). The log C' plot (b), shows that the disruptive peak moves to lower frequencies with increasing L. The log Y' (c) and -Z''plots (d) show that the high frequency tail shifts to lower frequencies, with increasing L. The M'' peak seems to be independent of L.

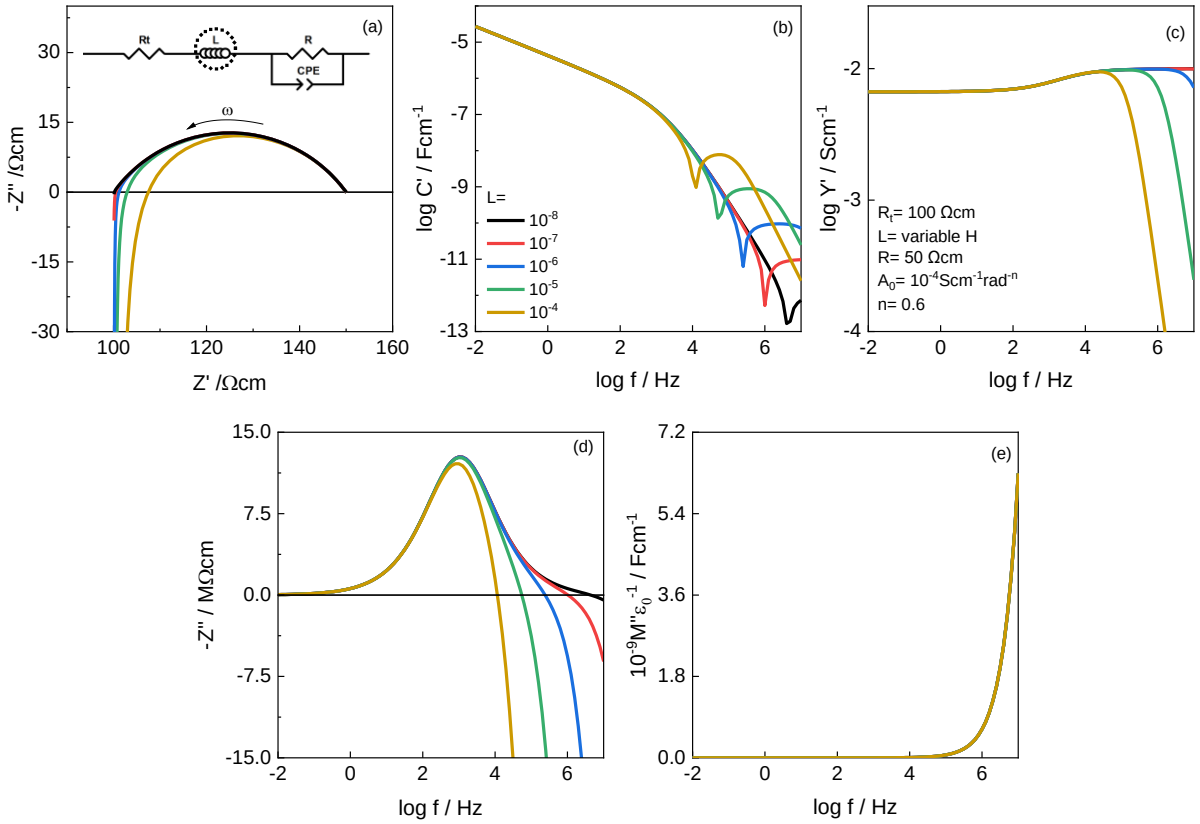

***Figure 3.10**. Change in the impedance response given by the equivalent circuit, inset (a), by changing L;(a) impedance complex plane and spectroscopic plots of (b) capacitance, (c) admittance, (d) Z'' and (e) M''.*

The effect of varying R from 10 to 90 Ωcm, is shown in Figures 3.11 and 3.S5. The Z* plane (a) shows that the arc scales up, preserving the high frequency intercept with the Z' axis, with increasing R. The log C' plot (b) shows that the capacitance of the low frequency dispersion / plateau increases with increasing R. The log Y' plot (c) shows that the admittance of the low frequency plateau decreases with increasing R. The height of the -Z'' peak increases and its position shifts to lower frequencies with increasing R. And the M'' peak seems to be independent of R.

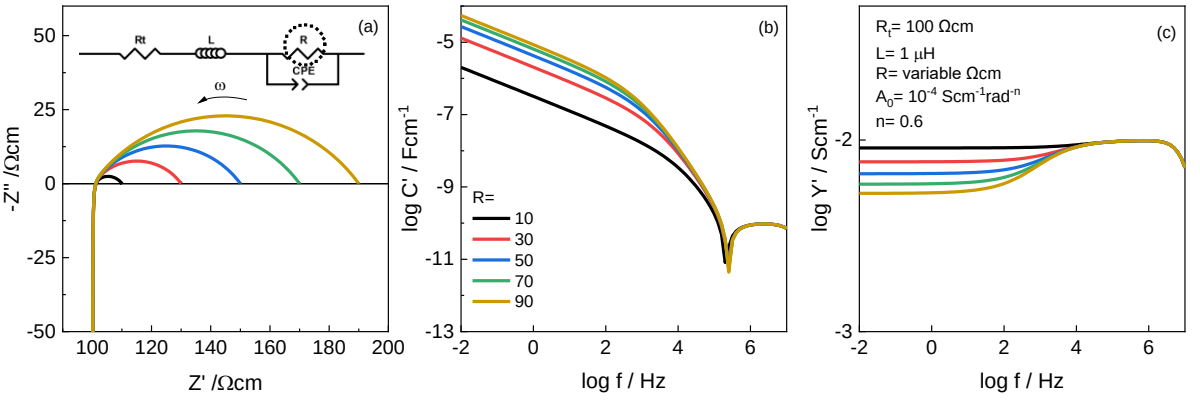

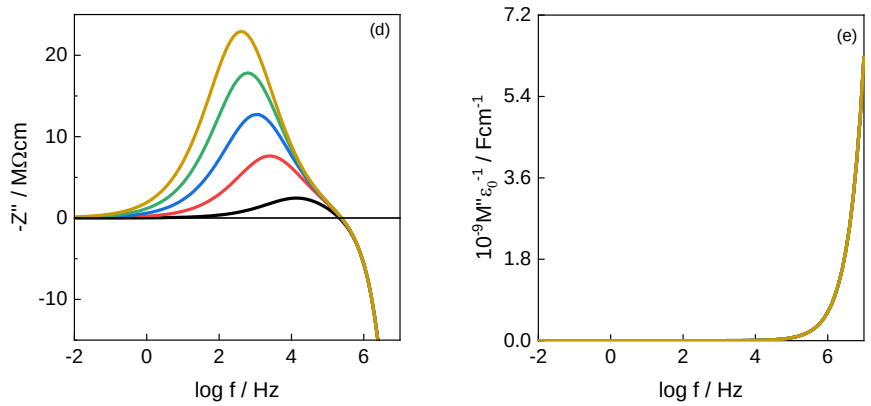

Figure 3.11. *Change in the impedance response given by the equivalent circuit, inset (a), by changing R;(a) impedance complex plane and spectroscopic plots of (b) capacitance, (c) admittance, (d) Z'' and (e) M''.*

The effect of varying the A_0 parameter of the CPE from 10^{-2} to 10^{-6} $Scm^{-1}rad^{-n}$ and C from 10^{-3} to 10^{-9} Fcm^{-1}, is shown in Figures 3.12 and 3.S6. The Z*plane shows that the high frequency intercept with the Z' axis shifts to the right (higher values), but keeping the same low frequency intercept, resulting in the reduction and slight distortion of the arc, with decreasing A_0/C. In addition, the inductance tail changes from vertical at high A_0/C magnitudes to curved at low magnitudes. The log C' plot shows that the capacitance of the low frequency dispersion / plateau decreases and the disruptive peak moves to higher frequencies, with decreasing A_0/C. The log Y' plot (c) shows that the frequency range of the high frequency plateau increases with decreasing A_0/C. The -Z'' peak moves to higher frequencies with decreasing A_0/C, and only at the lowest values of A_0/C it decreases its height. The M'' peak slightly shifts to lower frequencies with decreasing A_0/C.

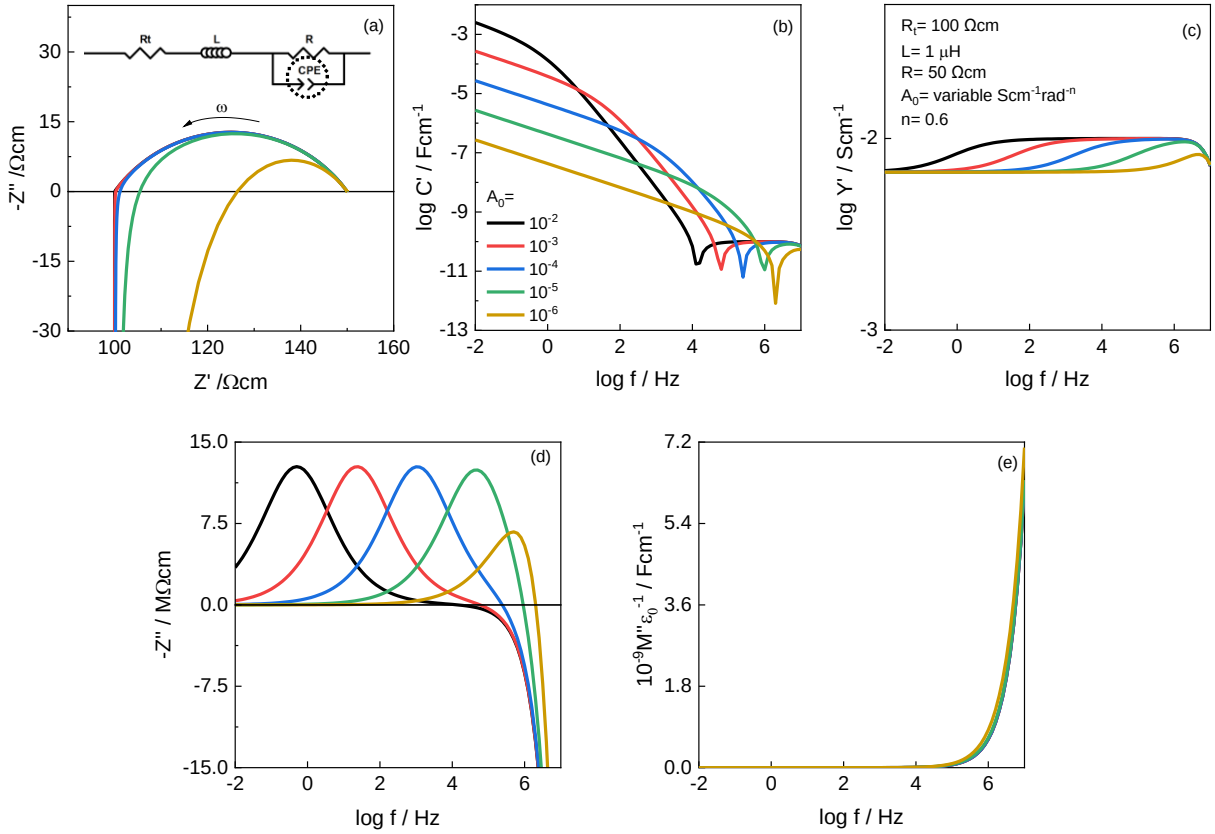

Figure 3.12. *Change in the impedance response given by the equivalent circuit, inset (a), by changing A_0;(a) impedance complex plane and spectroscopic plots of (b) capacitance, (c) admittance, (d) Z'' and (e) M''.*

The effect of varying the n parameter of the CPE from 0.4 to 0.8, is shown in Figure 3.13. A similar effect is observed as with decreasing A_0. The high frequency of the Z' axis (a) shifts to higher values and the arc becomes distorted into the shape of half-drop. The disruptive peak on the log C' plot also shifts to higher frequencies with decreasing n, but the slope of the low frequency dispersion increases with decreasing n. The log Y' plot (c), also shows that the frequency range of the high frequency plateau increases and also the slope changes from the two regions decreases, with decreasing n. The -Z'' peak shifts to lower angles and decreases its height with decreasing n. And the M'' peak minimally shifts to lower frequencies with decreasing n.

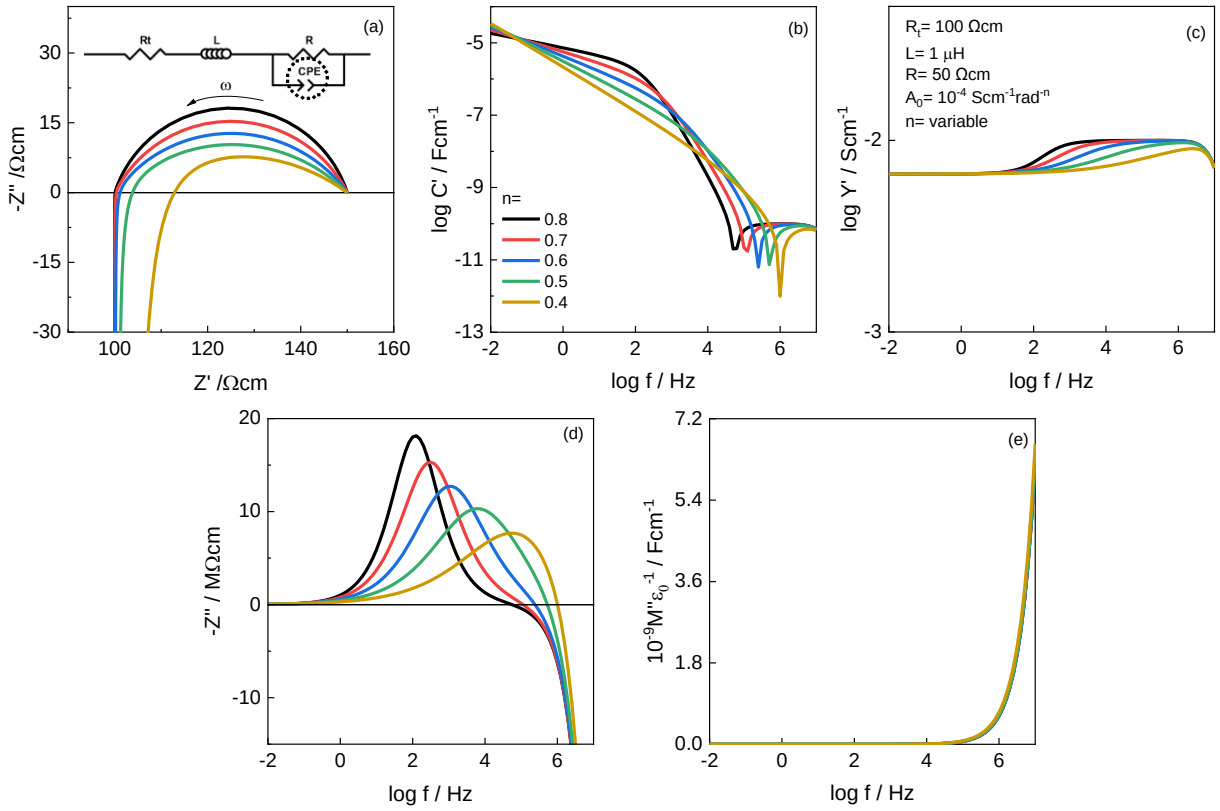

***Figure 3.13**. Change in the impedance response given by the equivalent circuit, inset (a), by changing n;(a) impedance complex plane and spectroscopic plots of (b) capacitance, (c) admittance, (d) Z'' and (e) M''.*

3.7.4.1 Derivation of impedance equation of a parallel RCPE element in series with an inductor and a resistance

(Derivation of impedance equation of a parallel RC element in series with an inductor and a resistance can be found in the supplementary information)

$$Z^* = R_t + j\,\omega L + \frac{1}{\frac{1}{R} + A\omega^n + jB\omega^n}$$

Rearranging

$$Z^* = R_t + j\,\omega L + \frac{R(1 + RA\omega^n) - jR^2B\omega^n}{(1 + RA\omega^n)^2 + (RB\omega^n)^2}$$

Real part, Z'

$$Z' = R_t + \frac{R(1 + RA\omega^n)}{(1 + RA\omega^n)^2 + (RB\omega^n)^2}$$

if $\omega = 0$

$$Z' = R_t + R$$

if $\omega \to \infty$

$$Z' = R_t$$

Imaginary part, Z''

$$Z'' = \omega L - \frac{R^2 B\omega^n}{(1+RA\omega^n)^2+(RB\omega^n)^2}$$

if $\omega = 0$

$$Z'' = 0$$

if $\omega \to \infty$

$$Z'' = \text{undefined} \therefore 0$$

if $Z'' = 0$

$$\omega L = \frac{R^2 B\omega^n}{(1 + RA\omega^n)^2 + (RB\omega^n)^2}$$

3.7.5 Impedance spectra deconvolution

In the following chapters the deconvolution of the impedance spectra has proved to be useful to determine the contribution of individual impedance elements to the overall impedance response. However, it needs to be noted that the data are better represented by spectroscopic plots of the different impedance formalisms, than with the impedance complex plane. This can be observed in Figure 3.14, where two parallel R-CPE-C elements in series were simulated and deconvoluted. The values used for the simulations are approximations of a sample that has been corrected for its overall geometry, but not for the grain boundary (element 2). The times constant (τ) of each element differs by 2 orders of magnitude, as τ_1=1x10^{-6}s and τ_2=5x10^{-4} s. The Z* plane (a) shows that when the individual elements are plotted they share the same origin, therefore if the total impedance response is unknown or unclear, it would be difficult to determine the position of the elements in the Z' axis. Nonetheless, by looking at the collection of the spectroscopic plots (Z' (b), -Z''(c), log C'(d), M''(e) and log Y'(f)), the position of the elements in the frequency range becomes clearer, along with showing that the sum of the elements results in the total impedance response. The criteria to choose which plot/formalism is chosen to represent the impedance spectra deconvolution might consider the information that one wants to highlight in the analysis.

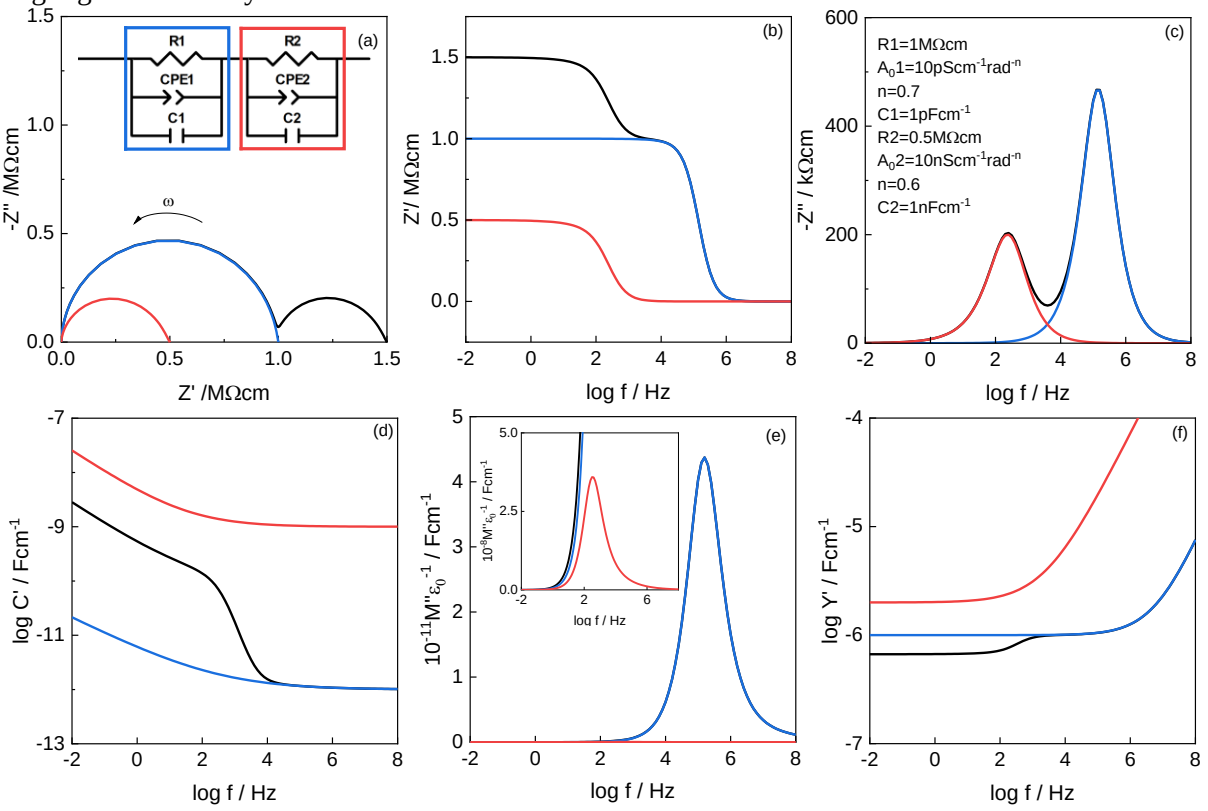

***Figure 3.14**. Deconvolution of impedance response presented in the Z* plane(a) and spectroscopic plots of Z'(b), -Z''(c), log C'(d), M''(e) and log Y'(f). The black line: combine effect of both elements, the blue: element 1 and red: element 2.*

3.7.5.1 Alumina case

The impedance response of a highly resistive alumina sample is shown in Figure 3.15. The impedance complex plane at 900 °C (a), the highest temperature studied, shows part of a single arc. The C' data at 733°C (b) show a high frequency limiting capacitance, $C_1 \sim 0.85$ pFcm^{-1}. However, the M'' spectrum (c) is very broad and indicates significant inhomogeneity in the R and/or C parameters that represent the impedance response.

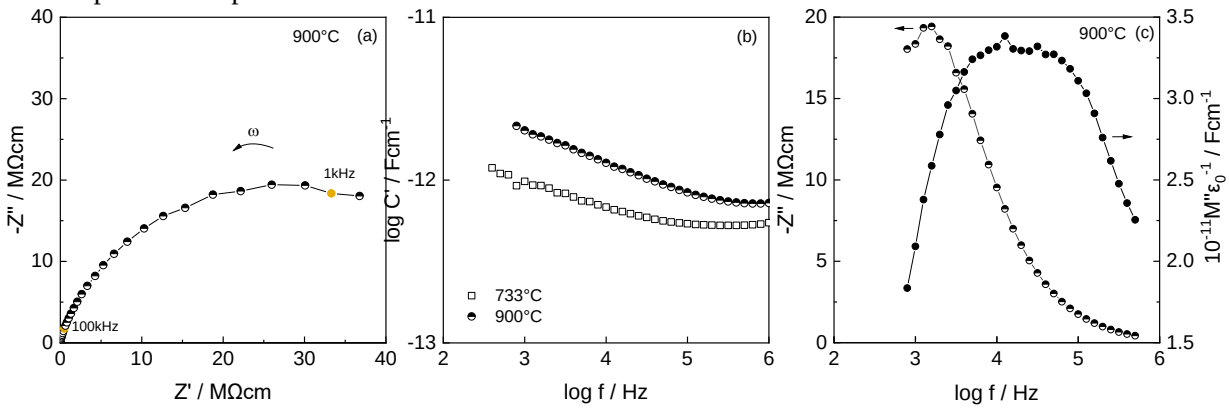

Figure 3.15. *(a) Impedance complex plane plot and spectroscopic plots of (b) capacitance and (c) Z''/M'' at different temperatures for alumina.*

Equivalent circuit analysis was required to deconvolute the impedance data of the alumina sample into its component parts. Starting with the possibility that a combination of two elements in series may represent the overall impedance response, various parameter combinations were tested. Two data points between 10kHz and 100kHz were not taken into account in the fitting process as they were outliner resulting from the experimental setup. An excellent fit was obtained using the circuit shown in Figure 3.16(a), which is a circuit that is frequently used to represent the grain and grain boundary impedances of many materials; fitted parameters for the data set obtained at 900ºC are listed. Regarding the units of element 2, it is important to bear in mind that the measurements were corrected for the total sample's geometry and not for the grain boundary. However, a comparison of the time constants (τ) would be appropriate as it is a geometry independent parameter. In this case, both τ are very proximate to each other, as τ_1=2.81x10^{-6} s and τ_2=2.49x10^{-6} s.

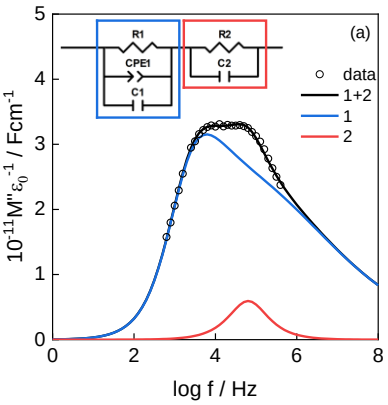

R1	54.69 MΩcm
$A_0$1	22.86 pScm^{-1}rad^{-n}
n1	0.707
C1	0.513 pFcm^{-1}
R2	0.296 MΩcm
C2	8.413 pFcm^{-1}

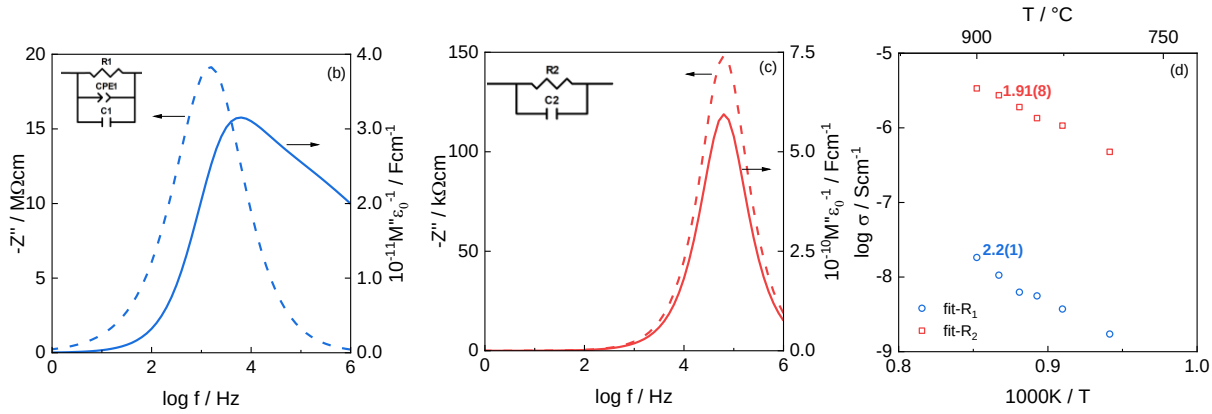

Figure 3.16*. (a) M" data of alumina at 900°C, simulation of complete and deconvoluted equivalent circuit, using fitted results shown. Inset (a) possible equivalent circuit. (b,c) Z"/M" simulations of components 1 and 2. (d) Conductivity Arrhenius plots of the fitted values of alumina*

Since $R_2 << R_1$, resistance R_1 dominates the impedance arc seen in Figure 3.15(a) but component R_2C_2 is clearly evident by deconvolution of the M'' spectrum into the two component elements, 1 and 2, as shown in Figure 3.16(a).

The fitted capacitance values that show $C_1 < C_2$ and therefore, it is clear that element R_1-C_1-CPE_1 represents the bulk and element R_2-C_2 represents the grain boundaries. From the fits, $R_1 >> R_2$, but $C_2 > C_1$. The time constants, τ, given by the RC products are in the sequence $\tau_1 > \tau_2$ and therefore, the approximate frequencies of M'' peak maxima, given by $2\pi f_{max}RC=1$ for a circuit consisting of an ideal RC element, are in the sequence, $f_{max,1} < f_{max,2}$, as observed (a). This leads to the conclusion that the highest frequency peak in the M'' spectrum is NOT the expected bulk peak but is the grain boundary peak whose resistance is much less than the bulk resistance.
It was noted that the shape of the deconvoluted M'' peak for element 1, (a), is non-Debye-like and asymmetric with a high frequency tail. Peak asymmetry of M'' and small displacement in positions of f_{max}, such that $f_{max,\,M''} > f_{max,Z''}$, shown in (b) for element 1, are a direct consequence of the presence of the CPE in the equivalent circuit [9]. Element 2 does not contain a CPE and the M''/Z'' peaks are Debye-like with coincident peak maximum frequencies (c). We tested the effect of adding a second CPE to the circuit, as part of element 2, but the fit residuals were very much worse and a satisfactory refinement was not obtained. An Arrhenius plot for R_1 and R_2 is shown in (d). The conductivity, σ_2 of element 2 is greater than that of element 1, even after taking their different geometries into consideration.

3.7.6 Discussion

3.7.6.1 CPE

Different approaches have been used during the years to analyse and fit the impedance spectroscopy data, mainly divided into the use of distribution of relaxation times (DRT) [10] and equivalent circuit analysis [11], [12]. Some of the most common DRT functions are: the Cole-Cole [13], [14], Williams-Watt [15], Davison-Cole [16], [17], Havriliak-Nagami[18], Jurlewicz-Weron-Stanislavsky [19], [20], Hilfer [21], [22], generalised distribution of relaxation times [23]. These have also been used in combination with the use of Fourier transform [24], statistical model selection [25], weight least squares with optimal experimental design [26], and genetic programming [27], [28].

Typically, the bulk response of materials do not follow the ideal behaviour, frequency independent behaviour, of a parallel R-C element, as they present power law dependencies referred as 'universal dielectric response' (UDR) identified by Jonscher [29]–[32]. These can be observed on the log Y' plot

at high frequencies, of slope n, in addition to the low frequency independent plateau at low frequencies related to the dc conductivity, and on the log C' plot at low frequencies, with slope n-1, in addition to the high frequency plateau, related to the material's permittivity. These power law dependencies can be modeled by a constant phase element (CPE), which can be referred as a parallel combination of a variable frequency resistor and capacitor, where n is the ratio between these two. The presence of a CPE can also be identified by the broadening of the Z'' and M'' peaks and its shift to lower and higher frequencies, respectively, Figure 3.4; compared to the ideal behaviour where both peaks overlap.

Therefore, CPEs are employed in equivalent circuit analysis to deal with the non-ideal behaviour of the materials (Figure 3.4 and 3.5) and to obtain an accurate fit [33]–[35]. However, the physical meaning and/or interpretation of the CPEs are still under study, using Jonscher´s model as a ground base.

The UDR interpretation given by Funke, is that in solid electrolytes arises from the ion hopping process, showing the charge carriers attempted hops caused by the electrostatic interaction between them [36]–[39]. It has also served as a basis to the determination hopping rates and charge carrier concentration in ionic conductors [40]–[42]. It has been also proposed that the UDR results from a random network of interconnected resistors and capacitors, where the n parameter reflects the ratio between these two [43], [44]. The random R-C network has been used to describe the conduction pathways of ionic conductors [45] and the heterogenous microstructure of composites [46]–[49]. Therefore, a CPE can be regarded as a frequency-dependent parallel R-C element that follows a power law behaviour.

3.7.6.2 Dipole

The effect on including a series RC element in parallel combination of a R-CPE-C was shown in Figures 3.6 and 3.7. The simulations and the low frequency limit of Z' (when $\omega \rightarrow 0$), show that the dielectric component does not contribute to the total resistance of the simulated bulk response. Which has been observed in a YSZ single crystal [50] and CSZ ceramics [51].

3.7.6.3 Inductance

The simulations of the equivalent circuits in Figure 3.8(a) and (b), showed that attention needs to be taken when determine the value of Rt. The derivation of the Z' equation of these equivalent circuits showed that when $\omega \rightarrow \infty$ $Z'=R_t$. The high frequency intercept with Z' axis does not have to be taken directly as the value of R_t, without a previous equivalent circuit analysis, as it can be modified by L, A_0, n and C.

3.7.6.4 Impedance spectra deconvolution

The deconvolution of the impedance spectra helps to highlight the induvial contribution of the impedance elements, Figure 3.14. The implementation of these approach on the alumina sample helped to determine the nature of the elements, even when in the position of the time constants was peculiar Figure 3.16.

3.7.7 Conclusions

This section has presented a qualitative representation of the effect of a CPE, a dielectric element, and an inductor, in relationship with specific equivalent circuits. It has been shown how the CPE parameters alter the whole impedance response along the chosen frequency range. The universality of this phenomena and its possible physical interpretations has been discussed. The distortion of the impedance response due to the dipole/dielectric effect was shown. And it was corroborated that it does not contribute to the to the dc conductivity. Regarding the inductive effect, it was noted that the value of R_t, for the equivalent circuit in Figure 3.8, in some cases does not correspond to the high frequency

intercept as the values L, A_0, n and C can modify it. Finally, the deconvolution of the impedance spectra has proven to be useful to show the relative importance of the individual electrical elements to the overall impedance response.

3.8 References

[1] T. Frueh *et al.*, "Powder chemistry effects on the sintering of MgO-doped specialty Al_2O_3," *J. Am. Ceram. Soc.*, vol. 101, no. 7, pp. 2739–2751, 2018.

[2] M. Biesuz, "Flash Sintering of Alumina-based Ceramics," University of Trento, 2017.

[3] S. J. Bennison and M. P. Harmer, "Effect of MgO Solute on the Kinetics of Grain Growth in A12O3," *J. Am. Ceram. Soc.*, vol. 66, no. 5, p. C-90-C-92, 1983.

[4] Struers Inc., "How to select a preparation method," *GRINDING AND POLISHING*. [Online]. Available: https://www.struers.com/en/Knowledge/Grinding-and-polishing#grinding-polishing-how-to.

[5] U. Täffner, V. Carle, and U. Schäfer, "Preparation and Microstructural Analysis of High-Performance Ceramics," in *Metallography and Microstructures*, 2018, pp. 1057–1066.

[6] J. T. S. Irvine, D. C. Sinclair, and A. R. West, "Electroceramics: characterization by impedance spectroscopy," *Adv. Mater.*, vol. 2, no. 3, pp. 132–138, 1990.

[7] D. C. Sinclair, "Characterization of Electro-materials using AC Impedance Spectroscopy," *Bol. la Soc. Esp. Ceram. y Vidr.*, vol. 65, pp. 55–66, 1995.

[8] Scribner Associates Inc., "ZView Operating Manual (version 3.5)." 2016.

[9] D. P. Almond and A. R. West, "Impedance and modulus spectroscopy of 'real' dispersive conductors," *Solid State Ionics*, vol. 11, no. 1, pp. 57–64, 1983.

[10] R. Garrappa, F. Mainardi, and G. Maione, "Models of dielectric relaxation based on completely monotone functions," *Fract. Calc. Appl. Anal.*, vol. 19, no. 5, pp. 1105–1160, 2016.

[11] J. R. Macdonald and L. D. Potter, "A flexible procedure for analyzing impedance spectroscopy results: Description and illustrations," *Solid State Ionics*, vol. 24, no. 1, pp. 61–79, 1987.

[12] J. R. Macdonald, "Impedance Spectroscopy," *Ann. Biomed. Eng.*, vol. 20, pp. 289–305, 1992.

[13] K. S. Cole and R. H. Cole, "Dispersion and absorption in dielectrics I. Arternating current characteristics," *J. Chem. Phys.*, vol. 9, pp. 341–351, 1941.

[14] K. S. Cole and R. H. Cole, "Dispersion and absorption in dielectrics: II. Direct current characteristics," *J. Chem. Phys.*, vol. 10, no. 2, pp. 98–105, 1942.

[15] G. Williams and D. C. Watts, "Non-symmetrical dielectric relaxation behaviour arising from a simple empirical decay function," *Trans. Faraday Soc.*, vol. 66, no. 1, pp. 80–85, 1970.

[16] D. W. Davidson and R. H. Cole, "Dielectric Relaxation in Glycerol, Propylene Glycol, and n-Propanol," *J. Chem. Phys.*, vol. 19, p. 1484, 1951.

[17] D. W. Davidson and R. H. Cole, "Dielectric relaxation in glycerine," *J. Chem. Phys.*, vol. 18, no. 10, p. 1417, 1950.

[18] S. Havriliak and S. Negami, "A complex plane representation of dielectric and mechanical relaxation processes in some polymers," *Polymer (Guildf).*, vol. 8, no. C, pp. 161–210, 1967.

[19] A. Jurlewicz, J. Trzmiel, and K. Weron, "Two-power-law relaxation processes in complex materials," *Acta Phys. Pol. B*, vol. 41, no. 5, pp. 1001–1008, 2010.

[20] A. Stanislavsky, K. Weron, and J. Trzmiel, "Subordination model of anomalous diffusion leading to the two-power-law relaxation responses," *Epl*, vol. 91, no. 4, 2010.

[21] R. Hilfer, "Experimental evidence for fractional time evolution in glass forming materials," *Chem. Phys.*, vol. 284, no. 1–2, pp. 399–408, 2002.

[22] R. Hilfer, "Fitting the excess wing in the dielectric α-relaxation of propylene carbonate," *J. Phys. Condens. Matter*, vol. 14, no. 9, pp. 2297–2301, 2002.

[23] M. A. Danzer, "Generalized distribution of relaxation times analysis for the characterization of impedance spectra," *Batteries*, vol. 5, no. 3, pp. 1–16, 2019.

[24] B. A. Boukamp, "Fourier transform distribution function of relaxation times; application and limitations," *Electrochim. Acta*, vol. 154, pp. 35–46, 2015.

[25] X. Li, M. Ahmadi, L. Collins, and S. V. Kalinin, "Deconvolving distribution of relaxation times, resistances and inductance from electrochemical impedance spectroscopy via statistical model

selection: Exploiting structural-sparsity regularization and data-driven parameter tuning," *Electrochim. Acta*, vol. 313, pp. 570–583, 2019.
[26] F. Ciucci, "Revisiting parameter identification in electrochemical impedance spectroscopy: Weighted least squares and optimal experimental design," *Electrochim. Acta*, vol. 87, pp. 532–545, 2013.
[27] T. Paul, N. Yavo, I. Lubomirsky, and Y. Tsur, "Determination of grain boundary conductivity using distribution function of relaxation times (DFRT) analysis at room temperature in 10 mol% Gd doped ceria: A non-classical electrostrictor," *Solid State Ionics*, vol. 331, no. October 2018, pp. 18–21, 2019.
[28] S. Hershkovitz, S. Baltianski, and Y. Tsur, "Harnessing evolutionary programming for impedance spectroscopy analysis: A case study of mixed ionic-electronic conductors," *Solid State Ionics*, vol. 188, no. 1, pp. 104–109, 2011.
[29] A. K. Jonscher, R. Holloway, and B. N. College, "The 'Universal' Dielectric Response: Part I," *IEEE Electr. Insul. Mag.*, vol. 6, no. 4, pp. 19–24, 1990.
[30] A. K. Jonscher, "The 'Universal' Dielectric Response: Part II," *IEEE Electr. Insul. Mag.*, vol. 6, no. 3, pp. 24–28, 1990.
[31] A. Jonscher, "The 'Universal' Dielectric Reponse: Part III," *IEEE Electr. Insul. Mag.*, vol. 6, no. 4, pp. 19–24, 1990.
[32] A. K. Jonscher, "Dielectric relaxation in solids," *J. Phys. D. Appl. Phys.*, vol. 32, pp. R57–R70, 1999.
[33] M. A. Hernandez, N. Maso, and A. R. West, "On the correct choice of equivalent circuit for fitting bulk impedance data of ionic/electronic conductors," *Appl. Phys. Lett.*, vol. 108, pp. 152901-152901–4, 2016.
[34] E. J. Abram, D. C. Sinclair, and A. R. West, "A Strategy for Analysis and Modelling of Impedance Spectroscopy Data of Electroceramics : Doped Lanthanum Gallate," *J. Electroceramics*, vol. 10, pp. 165–177, 2003.
[35] S. Pandey, D. Kumar, O. Parkash, and L. Pandey, "Equivalent circuit models using CPE for impedance spectroscopy of electronic ceramics," *Integr. Ferroelectr.*, vol. 183, no. 1, pp. 141–162, 2017.
[36] K. Funke, "Debye-Hückel-Tvpe Relaxation Processes in Solid Electrolytes:Complex Conductivity Arcs and Broad Quasielastic Neutron Scattering," *Berichte der Bunsengesellschaft für Phys. Chemie*, vol. 666, pp. 661–666, 1986.
[37] K. Funke and I. Riess, "Solid Conductors," *Zeitschrift für Phys. Chemie*, no. 140, pp. 217–232, 1984.
[38] K. Funke, "Jump relaxation in solid ionic conductors," *Solid State Ionics*, vol. 28–30, no. PART 1, pp. 100–107, 1988.
[39] K. Funke *et al.*, "First and second universalities: Expeditions towards and beyond," *Zeitschrift fur Phys. Chemie*, vol. 224, no. 10–12, pp. 1891–1950, 2010.
[40] D. P. Almond, G. K. Duncan, and A. R. West, "The determination of hopping rates and carrier concentrations in ionic conductors by a new analysis of ac conductivity," *Solid State Ionics*, vol. 8, no. 2, pp. 159–164, 1983.
[41] D. P. Almond and A. R. West, "Mobile ion concentrations in solid electrolytes from an analysis of a.c. conductivity," *Solid State Ionics*, vol. 9–10, no. PART 1, pp. 277–282, 1983.
[42] D. P. Almond, A. R. West, and R. J. Grant, "Temperature dependence of the a.c. conductivity of Na beta-Alumina," *Solid State Communucations*, vol. 44, no. 8, pp. 1277–1280, 1982.
[43] D. P. Almond and B. Vainas, "The dielectric properties of random R-C networks as an explanation of the 'universal' power law dielectric response of solids," *J. Phys. Condens. Matter*, vol. 11, no. 46, pp. 9081–9093, 1999.
[44] R. Bouamrane and D. P. Almond, "The 'emergent scaling' phenomenon and the dielectric properties of random resistor-capacitor networks," *J. Phys. Condens. Matter*, vol. 15, no. 24, pp. 4089–4100, 2003.
[45] B. Vainas, D. P. Almond, J. Luo, and R. Stevens, "An evaluation of random R-C networks for modelling the bulk ac electrical response of ionic conductors," *Solid State Ionics*, vol. 126, no. 1, pp. 65–80, 1999.
[46] C. R. Bowen and D. P. Almond, "Modelling the 'universal' dielectric response in heterogeneous

materials using microstructural electrical networks," *Mater. Sci. Technol.*, vol. 22, no. 6, pp. 719–724, 2006.
[47] D. P. Almond, C. R. Bowen, and D. A. S. Rees, "Composite dielectrics and conductors: Simulation, characterization and design," *J. Phys. D. Appl. Phys.*, vol. 39, no. 7, pp. 1295–1304, 2006.
[48] D. P. Almond and C. R. Bowen, "Anomalous power law dispersions in ac conductivity and permittivity shown to be characteristics of microstructural electrical networks," *Phys. Rev. Lett.*, vol. 92, no. 15, pp. 1–4, 2004.
[49] M. Aouaichia, N. McCullen, C. R. Bowen, D. P. Almond, C. Budd, and R. Bouamrane, "Understanding the anomalous frequency responses of composite materials using very large random resistor-capacitor networks," *Eur. Phys. J. B*, vol. 90, no. 3, pp. 1–16, 2017.
[50] X. Vendrell and A. R. West, "Electrical properties of Yttria-stabilized zirconia, YSZ Single crystal: local AC and long range DC conduction," *J. Electrochem. Soc.*, vol. 165, no. 11, pp. F966–F975, 2018.
[51] J. Ramírez-González and A. R. West, "Electrical properties of calcia-stabilised zirconia ceramics," *J. Eur. Ceram. Soc.*, vol. 40, pp. 5602–5611, 2020.

3.9 Supplementary

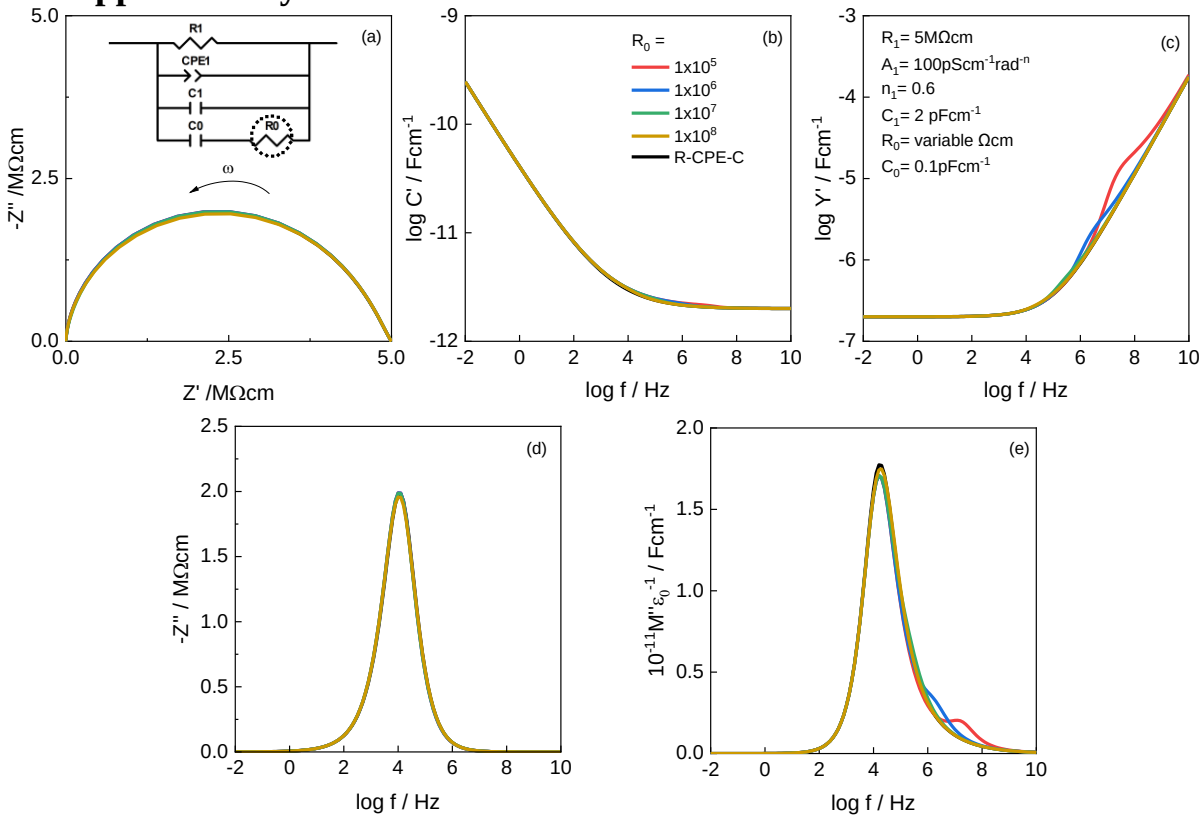

***Figure 3.S1**. Change in the impedance response given by the equivalent circuit, inset (a), by changing R_0 with a low C_0 value; (a) impedance complex plane and spectroscopic plots of (b) capacitance, (c) admittance, (d) Z'' and (e) M''.*

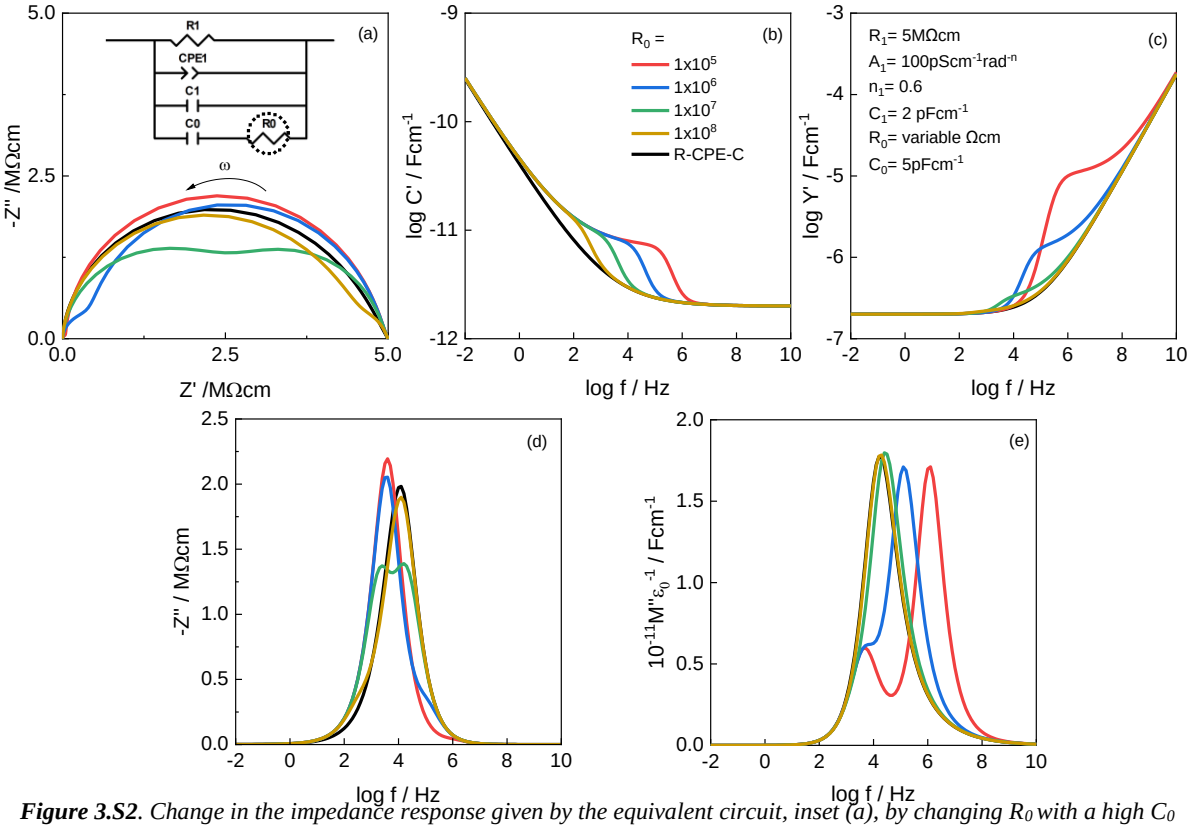

***Figure 3.S2**. Change in the impedance response given by the equivalent circuit, inset (a), by changing R_0 with a high C_0 value; (a) impedance complex plane and spectroscopic plots of (b) capacitance, (c) admittance, (d) Z'' and (e) M''.*

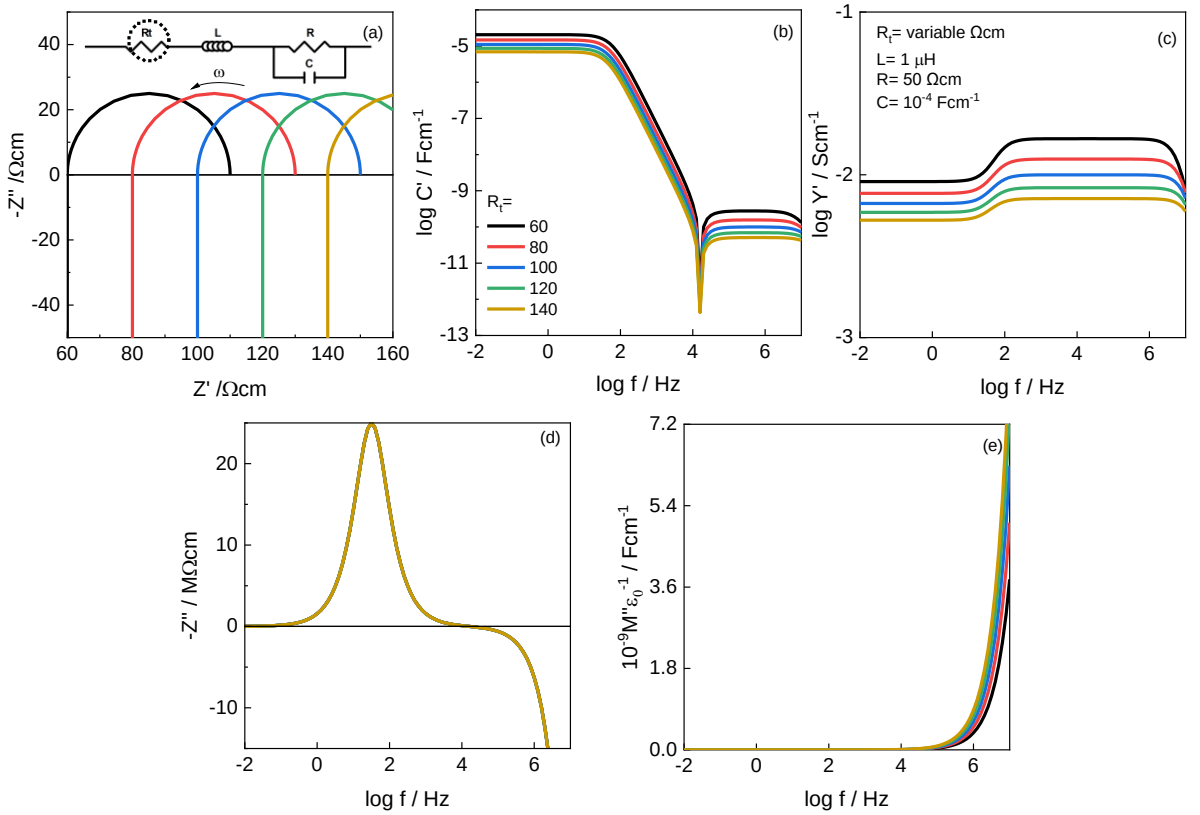

***Figure 3.S3**. Change in the impedance response given by the equivalent circuit, inset (a), by changing R_t; (a) impedance complex plane and spectroscopic plots of (b) capacitance, (c) admittance, (d) Z'' and (e) M''.*

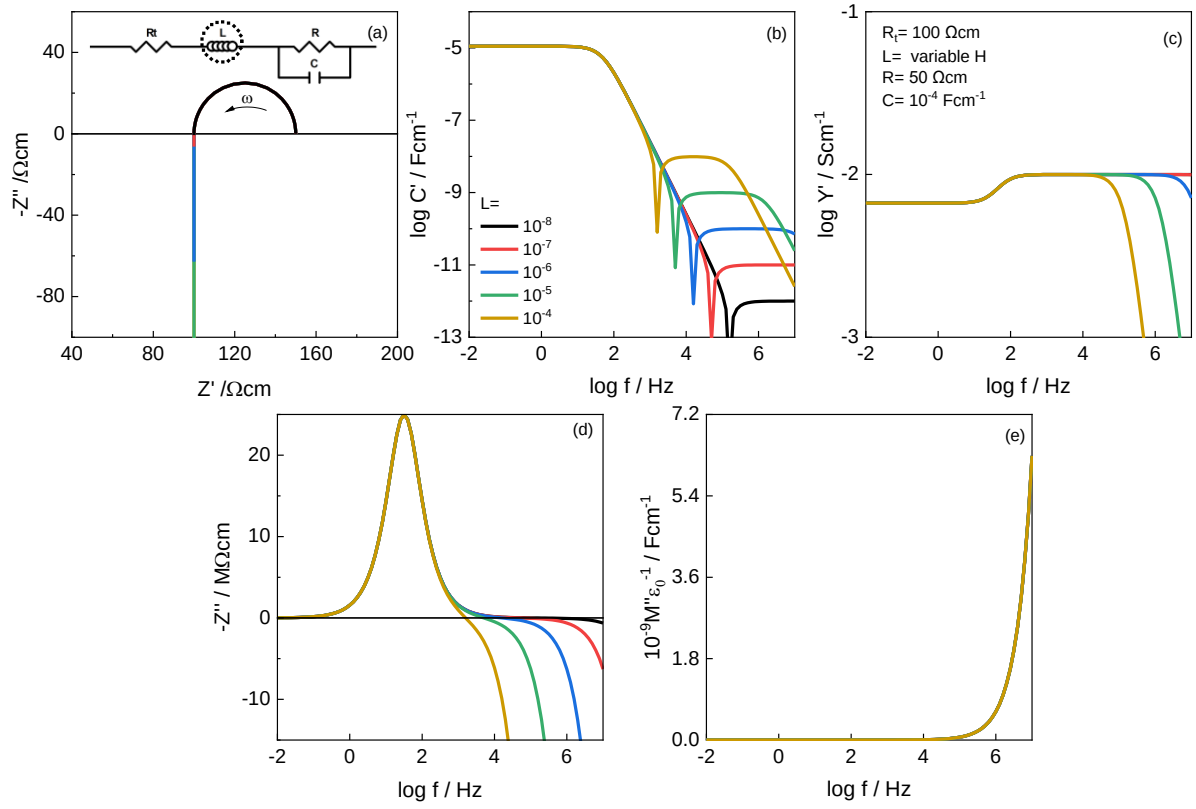

***Figure 3.S4**. Change in the impedance response given by the equivalent circuit, inset (a), by changing L; (a) impedance complex plane and spectroscopic plots of (b) capacitance, (c) admittance, (d) Z'' and (e) M''.*

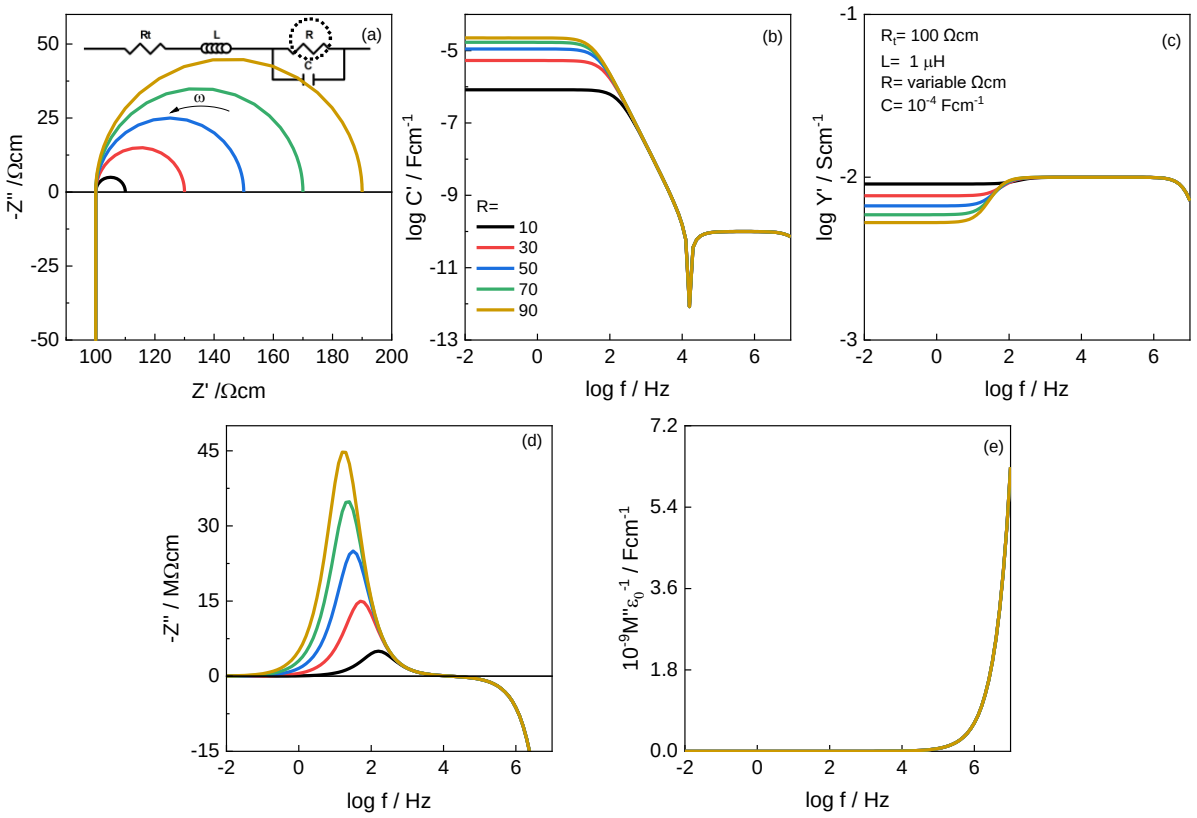

***Figure 3.S5**. Change in the impedance response given by the equivalent circuit, inset (a), by changing R; (a) impedance complex plane and spectroscopic plots of (b) capacitance, (c) admittance, (d) Z'' and (e) M''.*

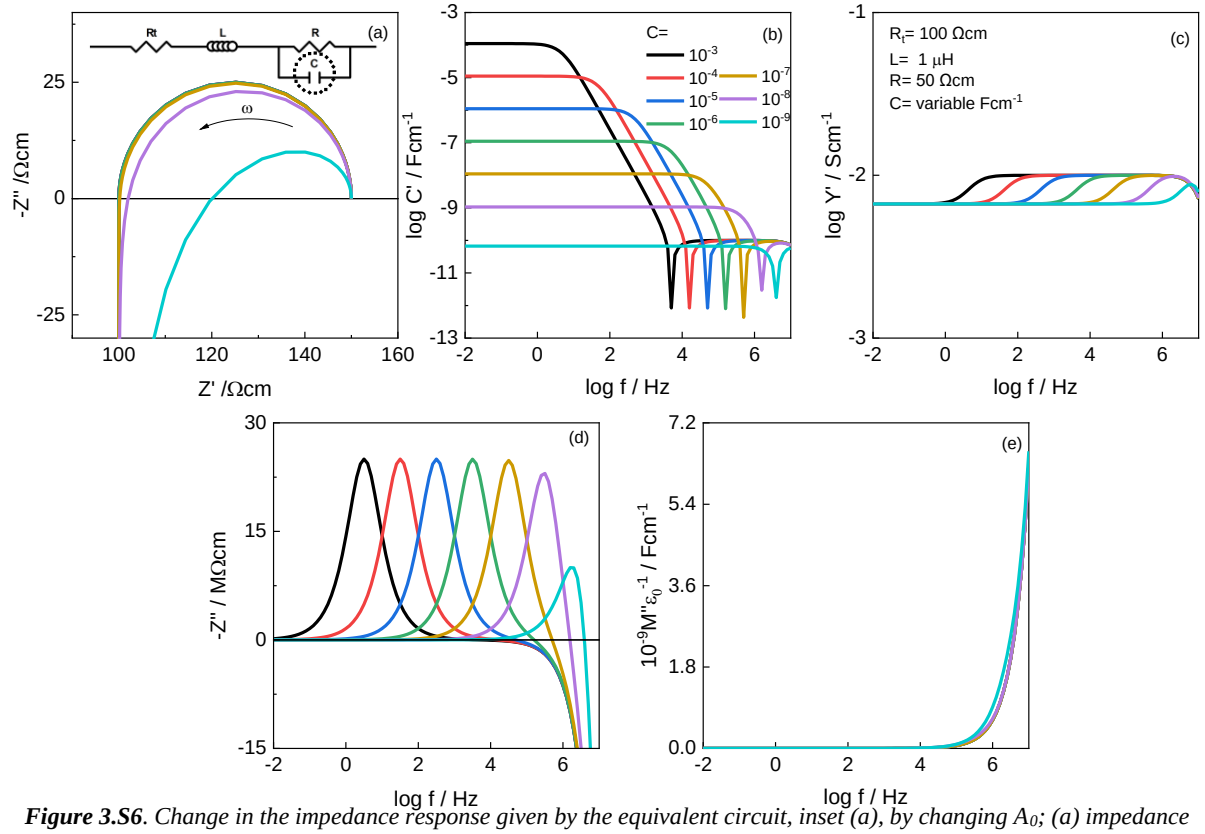

***Figure 3.S6**. Change in the impedance response given by the equivalent circuit, inset (a), by changing A_0; (a) impedance complex plane and spectroscopic plots of (b) capacitance, (c) admittance, (d) Z'' and (e) M''.*

3.9.1 Impedance equation of a parallel RC element in series with an inductor and a resistance

$$Z^* = R_t + j\,\omega\mathrm{L} + \frac{1}{\frac{1}{R} + j\omega\mathrm{C}}$$

Rearranging

$$Z^* = R_t + j\,\omega\mathrm{L} + \frac{R\ -\ j\omega\mathrm{R}^2C}{1 + (\omega\mathrm{RC})^2}$$

Real part, Z'

$$Z' = R_t + \frac{R}{1 + (\omega\mathrm{RC})^2}$$

if $\omega = 0$

$$Z' = R_t + R$$

if $\omega \to \infty$

$$\mathrm{Z'} = R_t$$

Imaginary part, Z''

$$Z'' = \omega\mathrm{L}\ -\ \frac{\omega\mathrm{R}^2C}{1 + (\omega\mathrm{RC})^2}$$

if $\omega = 0$

$$\mathrm{Z''} = 0$$

if $\omega \to \infty$

$$\mathrm{Z''} = \text{undefined} \therefore 0$$

At Debye frequency $\omega\mathrm{RC}=1$

$$Z'' = \omega\mathrm{L}\ -\ \frac{\mathrm{R}}{2}$$

if $\mathrm{Z''} = 0$

$$\omega\mathrm{L}\ =\ \frac{\omega\mathrm{R}^2C}{1 + (\omega\mathrm{RC})^2}$$

Chapter 4
Electrical properties of calcia-stabilised zirconia ceramics

4.1 Introduction

Zirconia-based materials with defect fluorite structures are widely used as solid electrolytes for fuel cell and sensor applications [1]–[4]. To optimise properties, compositional control includes the addition of dopants that stabilise the cubic polymorph: Y is the main dopant for fuel cell electrolytes in yttria-stabilised zirconia, YSZ, but Sc is of interest because of the higher conductivity of Sc-doped materials [5]. The technology of these materials as solid electrolytes is well-developed but numerous scientific issues remain to be clarified which may lead to property improvements.

First, impedance analysis of YSZ ceramics generally shows the common presence of grain boundary impedances in addition to bulk impedances [6], but their origin is not well-understood and they are not readily eliminated by attention to ceramic processing procedures. Second, the commonly-observed curvature of conductivity Arrhenius plots at high temperatures is not well-explained [7]–[13]. Early viewpoints attributed it to a transition from trapped to free oxide ion vacancies, but the reality is now thought to be considerably more complex, especially since the high yttria content of high conductivity materials makes it difficult to envisage how oxygen vacancies can be well-separated from the Y dopant. Third, recent studies on YSZ ceramics and single crystals show that dielectric or dipolar elements contribute to the overall bulk impedance and must be considered in full analysis of impedance data [14]. Fourth, whilst solid electrolyte applications require the absence of any electronic conduction, *p*-type conductivity can be induced in YSZ on application of a small *dc* bias [15] and in yttria-rich YSZ compositions, by simply making impedance measurements in oxygen [16].

There is interest in calcia-stabilised zirconia, $Ca_xZr_{1-x}O_{2-x}$, CSZ, as a model system to investigate some of the above issues and also, as a prelude to using impedance spectroscopy, IS, to study the early stages of flash sintering phenomena, which were discovered using YSZ materials [17]. Early literature, pre-1970, on CSZ, including the stoichiometry range of cubic solid solutions at different temperatures and their electrical properties is fully covered in [18]. Other fluorite-structured solid oxide electrolytes based on ZrO_2, ThO_2, CeO_2 and HfO_2 are also reviewed in [18]. The cubic polymorph of pure zirconia is thermodynamically stable only at very high temperatures, but phase equilibrium studies show that it is stabilised to lower temperatures by numerous aliovalent substituents such as Ca^{2+}, Mg^{2+} and Y^{3+}, in which charge compensation is achieved by oxygen vacancy creation. The advantages of such cubic stabilised materials are that, not only are they very good oxide ion conductors because of the high concentration of oxygen vacancies, but also the disruptive cubic-tetragonal-monoclinic phase changes that are observed on cooling undoped ZrO_2 [19], [20] are not observed.

The most recent CaO-ZrO_2 phase diagram [20], shows an extensive range of cubic solid solutions, $0.14<x<0.18$ at 1300 ^oC which increases to $0.06<x<0.21$ at 2000 ^oC. According to the phase diagram, the cubic solid solutions should decompose below a eutectoid temperature of 1066 ^oC, but the transformation rate is very slow and cubic, single phase materials may be preserved readily, in a metastable state, to lower temperatures. Several papers, summarised in [18], reported development of a superstructure on annealing samples for long times at ~1000 ^0C. This was attributed to vacancy ordering which occurred more readily with increasing Ca content and was not associated with eutectoid decomposition.

CSZ is an oxide ion conductor over the oxygen partial pressure, pO_2 range $1–10^{-22}$ atm [21]; transport measurements show that conduction is entirely anionic, with cation diffusion coefficients that are 5 orders of magnitude less than oxygen diffusion coefficients [18]. Almost all studies on CSZ and other fluorite-structured solid solution materials assume implicitly that oxygen vacancy creation is the

principal charge compensation mechanism on doping with lower-valent cations. However, Diness and Roy, in a little-cited paper [22], showed clear evidence from density measurements of a change from oxygen vacancy compensation to interstitial calcium compensation on heating CSZ samples from 1600 to 1800 ^{o}C. The possible consequences of such a change in defect structure on electrical properties are not known, although it is noted that an early study of the effect of sintering temperature on ceramic microstructure and electrical properties indicated a possible decrease in total conductivity on heating at 2000 ^{o}C compared with heating at 1600 ^{o}C.

The onset of *n*-type conduction that occurs at very low pO_2 has been detected by emf measurements and can be promoted by the addition of donor dopants [23]. The possibility of *p*-type conduction at high pO_2 is envisaged, but was expected to be observed only at extremely high oxygen pressures [24] and has not been observed experimentally. In the absence of Ca doping, however, ZrO_2 does show *p*-type behaviour at high pO_2 [25], [26].

The oxide ion conductivity of fluorite-based oxide ion conductors has received much attention, partly because (i) conductivities pass through a maximum at intermediate oxygen vacancy concentrations and (ii) conductivity Arrhenius plots frequently show a departure from linearity at high temperatures [7]–[10]. A defect-dopant associate model was initially proposed to account for the conductivity maxima [10], [11] and the high temperature curvature widely attributed to the dissociation of defect complexes, thereby allowing values for the defect association and vacancy migration enthalpies to be determined [9]. More recently, however, the validity of the defect dissociation model has been questioned.

Various studies, including neutron and X-ray diffraction and diffuse scattering, neutron quasi-elastic scattering and high temperature neutron diffraction, together with DFT modelling, have led to the suggestion that oxygen vacancies, whether single, paired or aggregated into larger clusters, are key species that influence the composition- and temperature-dependent conductivities of YSZ and scandia-doped zirconia, ScSZ [27]–[30]. Defect structure and diffuse scattering studies of CSZ single crystals with x=0.04, 0.07, 0.10 and 0.15 showed two types of defect in micro-domains based on either a single oxygen vacancy or a pair of vacancies separated by a Ca^{2+} ion in a <111> orientation [31], [32]. Molecular dynamic studies of CSZ showed a dynamic spatial distribution of oxygen vacancies that tend to locate near areas with high density of Ca dopant [33].

There is a greater number of reports in the literature on defect structures in YSZ and ScSZ and it appears that the variety of defect structures may be greater than with CSZ. In addition to oxygen vacancy pairs, there is evidence for tetragonally-distorted defect clusters at low x and larger aggregates of vacancy pairs at high x in YSZ and ScSZ [27]–[30]. However, ionic size mismatch between aliovalent dopant and host (Zr) cations leads to localised strain effects which cause a repulsion between dopant and oxygen vacancies. The resulting defect structures may then represent a compromise between repulsive strain effects and electrostatic attraction between oppositely-charged defect species.

Single crystals and ceramics of CSZ with different composition have been characterised using impedance spectroscopy [34]–[36]. Bulk, grain boundary and sample-electrode responses were identified, although fitting of the impedance data to equivalent circuits was not reported. It was suggested that at high Ca concentrations, the oxygen vacancies may migrate through a continuous network of V_O-Ca_{Zr} defect complexes, without the need to overcome the association energy for the vacancies to escape from the complexes [10].

The main purpose of the present study is to characterise the bulk impedance response of polycrystalline CSZ; this made it necessary to also characterise fully the grain boundary response and the suitability of the Randles circuit [37] to model the sample–electrode response. Further details and discussion of the

sample-electrode response, and the application of IS to study the response of CSZ to a *dc* bias, will be reported subsequently.

4.2 Experimental

Powders with composition $Ca_xZr_{1-x}O_{2-x}$: x= 0.10, 0.12, 0.15, 0.18 and 0.20, were prepared by solid-state reaction of $CaCO_3$ (99%, Fisher) and ZrO_2 (99 %, Aldrich), which were dried overnight at 180 ºC and 1000 ºC respectively prior to weighing. The mixtures were ground manually with acetone using a pestle and mortar, dried and heated in alumina crucibles at 1150 ºC overnight to decarbonate $CaCO_3$ and start the reaction. Subsequently, the powders were re-ground, pellets 10 mm in diameter were uniaxially pressed at around 98 MPa and heated for 10 h. Temperatures depended on the composition; 1720 ºC for x=0.10, 1710 ºC for x=0.12 and 1600 ºC for x=0.15, 0.18 and 0.20. Pellet densities were ~86 %.

Pellets of each composition were crushed and analysed by x-ray powder diffraction with a STOE STADI P diffractometer (Darmstadt, Germany), Cu $K\alpha_1$ radiation. Data were collected from 2θ = 20-80 º and compared to the diffraction pattern of cubic zirconia (PDF card: 01-070-7361) using the JCPDS database. The cubic lattice parameter was determined by least-squares refinement using STOE WinXPOW version 2.25 and Si powder added as internal standard.

The sintered samples were polished metallographically, thermally-etched at 1300 °C for 30 min and sputter-coated with 10 nm of carbon for microstructural analysis. Scanning electron microscopy (SEM) images were taken on a field-emission scanning electron microscope (FEI Inspect F50) using an acceleration voltage of 15 kV and energy-dispersion analysis of X-rays (EDX) from Oxford Instruments using 20 kV.

For impedance measurements, Pt paste electrodes were applied to both faces of the pellets and dried at 900 ºC for 2 h. Electroded pellets were attached to the Pt leads of an in-house conductivity jig with the facility to vary the atmosphere flowing over the pellet. Impedance measurements were made between 190 and 900 ºC using a Solartron SI 1260 (measurement accuracy ±0.1%) impedance analyser over the frequency range 10 mHz – 1 MHz with a nominal *ac* voltage of 100 mV. Two sets of corrections were made to the collected data: (i) a geometric factor concerning pellet thickness and sample-electrode contact area and (ii) jig characteristics consisting of the blank, open circuit capacitance, typically 6 pF and the closed circuit resistance of, primarily, the leads, 1-2 Ω. No corrections were done for the grain boundary response. Data analysis and equivalent circuit fitting was performed using ZVIEW software (ZVIEW-Impedance Software version 2.4 Scribner Associates).

4.3 Results

4.3.1 Materials characterisation

All samples appeared to be single phase and were indexed on a cubic unit cell, space group Fm3m; a representative diffraction pattern is shown in Fig 4.1(a), for x = 0.15. The lattice parameter increased linearly with composition, inset Fig 4.1(a), following Vegard's Law. Therefore, single phase samples belonging to the cubic solid solution, $Ca_xZr_{1-x}O_{2-x}$ had been obtained, consistent with the reported homogeneity range at 1600-1700 ºC [20]; these are referred to here as cubic stabilised zirconia, CSZ.

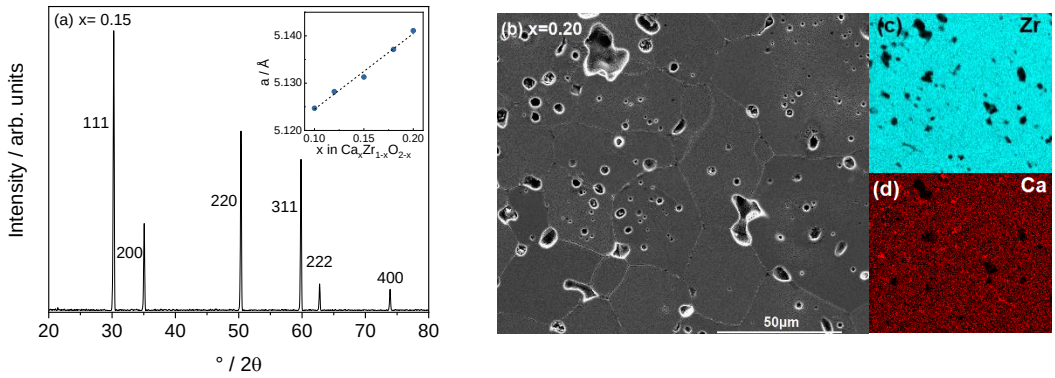

***Figure 4.1**.(a) XRD diffraction pattern of CSZ x=0.15. Inset: Variation in the lattice parameter with x. (b) SEM and (c)(d) EDX images of polished and thermal-etched pellet with composition x=0.20.*

A typical micro-structure of pellet x=0.20, Figure 4.1(b), shows grain sizes in the range 10-60 µm and closed porosity, consistent with the measured density of ~86%. No binder or sintering aids were used so as to avoid possible contamination and modification of the impedance results and therefore, no attempt was made to achieve 100% sintered density. Similar microstructures and grain sizes were observed for all compositions. EDX mapping showed a homogeneous distribution of Zr, with evidence of minor traces of Ca segregation around some pores; Hf impurity was detected and presumably originated from the ZrO_2 reagent (~0.30-0.41 At%, according to the Supplier's composition); it was evenly distributed.

4.3.2 Impedance data

The impedance response of CSZ pellets with composition x = 0.12, 0.15 and 0.18, was measured between 190 and 990 ºC in dry air; similar data sets were obtained for all three compositions. Data for x = 0.15 at selected temperatures are shown in Fig 4.2; data for the other two compositions are shown in Supplementary Figs 4.S1–S2. The impedance complex plane plot for a typical data set at 407 °C, Fig 4.2(a), shows two arcs and a large, low frequency curved spike. The same data replotted as a spectroscopic plot of capacitance against frequency in (c) show three regions of almost constant capacitance at low, intermediate and high frequencies. Z''/M'' spectroscopic plots in (d) show a single peak in M'' that overlaps approximately with the high frequency peak in Z'' and is attributed to the bulk response. Finally, the same data replotted as log Y' vs frequency in (e) show plateaux at two intermediate frequencies.

Some additional impedance features are seen at both higher and lower temperatures. First, impedance complex plane plots at higher temperature show that the low frequency curved spike in (a) becomes a broad arc, as shown at 697 ºC in (b), that terminates in a 'tail' extending slightly along the Z' axis at lowest frequencies. Second, the C' data at higher temperatures, eg 936 ºC in (c), show a poorly resolved plateau around 10^{-5}-10^{-4} Fcm^{-1} attributed to the sample-electrode response which becomes a rising dispersion at lowest frequencies. Third, at lower temperatures, eg 199 ºC, (c), the C' data level off at high frequencies to give a clear, frequency-independent plateau around $2x10^{-12}$ Fcm^{-1}, attributable to the frequency-independent, high frequency permittivity, ε' with a value of ~22.6 given by $\varepsilon' = C'/e_0$ where e_0 is the permittivity of free space, $8.854x10^{-14}$ Fcm^{-1}.

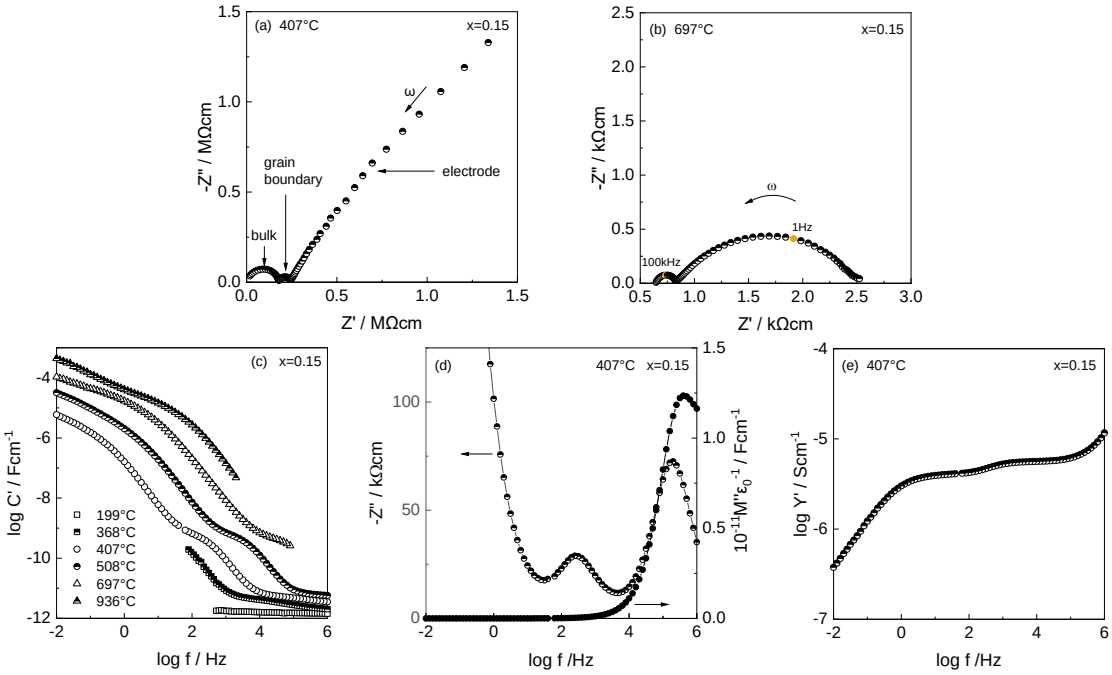

Figure 4.2. *(a)-(b) Impedance complex plane plots and spectroscopic plots of (c) capacitance, (d) Z''/M'' and (e) admittance at different temperatures for x=0.15; ω =2πf.*

Consideration of all these plots and characteristic features together leads to the initial conclusion that the data may be represented by an equivalent circuit that contains three impedance elements connected in series. The arcs shown in (a) and (b) are attributed to, with decreasing frequency, bulk, b, grain boundary, gb and electrode-sample contact, el, impedances. Resistance values were estimated from the intercepts of the arcs on the Z' axis and are shown as conductivity Arrhenius plots in Fig 4.3(a,b).

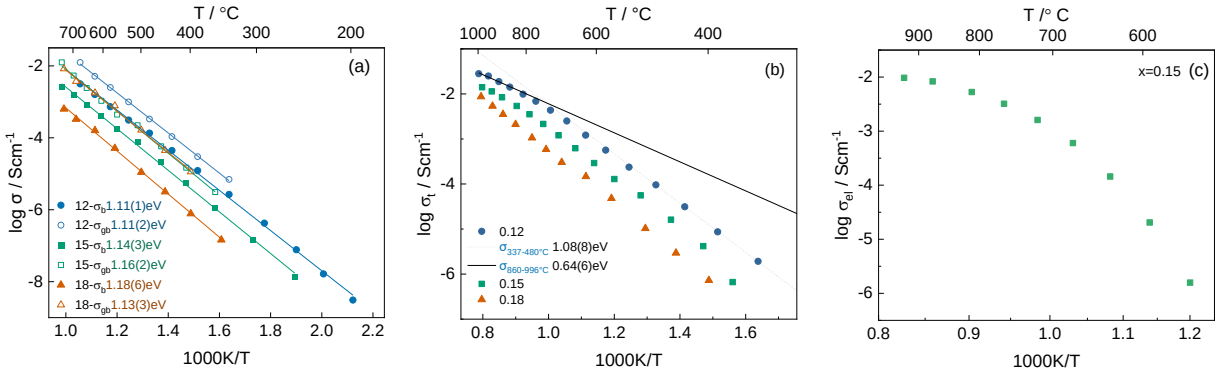

Figure 4.3. *Conductivity Arrhenius plots of (a) bulk and grain boundary, (b) total and (c) electrode resistances.*

In (a), separate plots for grain and grain boundary conductivities are shown at ~200 – 720 °C over which range, both values could be obtained. Activation energy values were estimated assuming linear plots, as shown, although close inspection shows a small amount of curvature in some of the plots. Three general observations may be made. First, all data sets are approximately parallel over this temperature range. Second, both bulk and grain boundary conductivities decrease systematically with increasing Ca content, x. Third, for each composition, although the grain boundary conductivities appear to be higher than the bulk conductivities, the grain boundary values have been corrected only for the overall pellet geometry. The true grain boundary conductivities, after correcting for grain boundary geometry, would

be approximately two orders of magnitude smaller and therefore, true grain boundary conductivities are significantly smaller than the bulk conductivities.

At temperatures above 720 ^{o}C, only the total sample resistances could be measured and are presented in Fig 4.3(b) as total conductivities, σ_t. It is clear that these Arrhenius plots show significant curvature at high temperatures, especially for the compositions with highest conductivity. In this sense, the data are similar to those that are well-established for yttria-stabilised zirconia, YSZ, which also show curvature and a systematic decrease in conductivity with higher Y content. Data obtained at high temperatures for the overall conductivity of the sample-electrode impedance, σ_{el}, are shown in (c) and give very non-linear Arrhenius plots with a high activation energy at low temperatures, ≥ 3.0 eV, that levels off to a much smaller value at highest temperatures. Again, the σ_{el} data are corrected only for the overall sample geometry and not for the geometry of the sample-electrode contact**.**

4.3.3 Equivalent circuits

In order to quantify further the analysis and interpretation of impedance data, the next step is to find the equivalent circuit that gives the best fits to the data and therefore, establish the correct equations to be used to quantify impedance parameters, leading to a description of the behaviour and electrical make-up of the sample. To a first approximation, the impedance data, Fig 4.2(a,b) indicate an equivalent circuit that contains three impedances, b, gb and el, connected in series. Low temperature data are considered first. These should be, at least partially, free from grain boundary and electrode impedances, thus allowing the bulk response to be examined separately and with fewer parameters to be refined. Knowledge of the bulk parameter values and their temperature dependence should also help subsequent fitting to more complex circuits, with more variables, at higher temperatures.

4.3.3.1 Bulk impedance

A number of equivalent circuits that possibly could be used to represent the bulk response are shown in Figs 4.4 and 4.5, together with the residuals between experimental and fitted impedance data for one representative composition, x = 0.15 and temperature, 304 ^{0}C in Fig 4.5; for other compositions and temperatures results are given in Figs 4.S3 and 4.S4. Justification for considering these circuits is as follows. In all cases, the simplest possibility, a resistor, R and capacitor, C in parallel, Fig 4.4, is considered as the starting point. R would represent the sample resistance and C its capacitance or polarizability. One useful 'thought process' which clarifies why R and C should be placed in parallel is to regard samples as leaky dielectrics; R represents a conduction pathway through the sample that is in parallel with its polarizability.

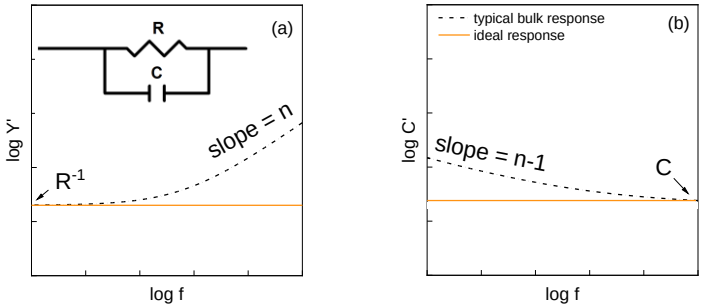

Figure 4.4*. Schematic representation of typical bulk response compared with the ideal response given by a parallel RC element.*

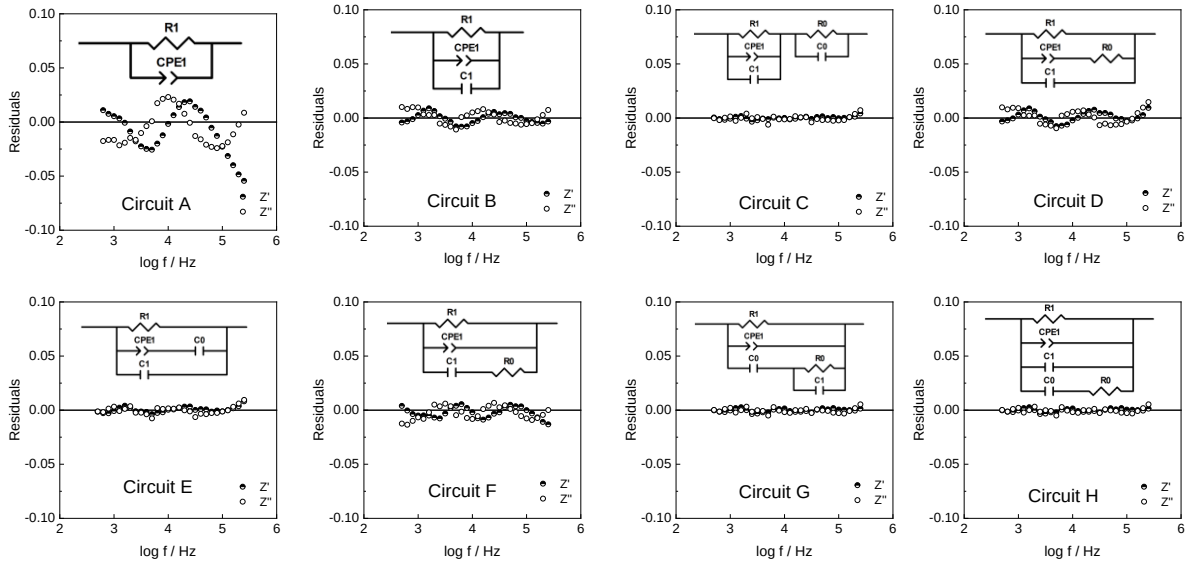

***Figure 4.5**. Fitting residuals of the bulk response from 8 possible equivalent circuits for x=0.15 at 304°C.*

For the parallel RC element, Fig 4.4, R and C are single-valued and the parameters Y' and C' are frequency-independent, as shown schematically by the horizontal lines in Fig 4.4. In practice, Y' and C' are rarely frequency-independent. Instead, Y' data for a bulk response typically show a frequency-independent plateau at lower frequencies which is the *dc* or bulk conductivity plateau, together with an additional high frequency power law dispersion, of slope n when plotted on logarithmic scales, attributed to the ubiquitous Jonscher Law behaviour, Fig 4.4(a). The onset of a power law response is seen for frequencies > 10^4 Hz in Fig 4.2(e). As part of the same Jonscher Law behaviour, C' data show a dispersion towards increasing C' values at lower frequencies, below that of the high frequency permittivity plateau, Fig 4.4(b) and with slope (n-1) on logarithmic scales. This is seen for frequencies over the range 10^4-10^6 Hz in Fig 4.2(c).

Two circuits are commonly used in the literature to account for non-ideality in equivalent circuits. Both involve inclusion of a constant phase element, CPE, whose admittance is given by $Y^* = A\omega^n + jB\omega^n$. One circuit, A, Fig 4.5 has a CPE instead of capacitance C. The other, B, has a CPE in addition to, and in parallel with the RC element. Although circuit A is often used to represent impedance data over a limited frequency range [38], [39] and indeed, is included in the widely-used circuit fitting software package [40], it ignores the frequency-independent permittivity shown in many data sets, such as Fig 4.2(c), particularly at high frequencies and low temperatures. Consequently, fitted values of the CPE parameters obtained using circuit A may be incorrect, especially if the onset of the high frequency capacitance plateau is apparent in the data.

Circuit C, Fig 4.5, has two impedances connected in series and is the circuit that is used very frequently to represent materials that have both bulk and grain boundary impedances. Depending on the time constants, τ, of the two circuits, given ideally by the magnitude of their RC products, separate arcs may be seen in impedance complex plane plots, as in Fig 4.2(a) and an intermediate frequency plateau in C' spectroscopic plots, as in Fig 4.2(c). If the time constants are more similar, then single distorted or asymmetric arcs may be seen in impedance complex plane plots.

Until recently, circuit B has been considered to represent adequately the bulk impedance response of many ionically-conducting materials. However, studies on YSZ ceramics [41] and single crystals [14]

showed the need for an additional circuit element to adequately represent the bulk response which was different from the addition of a second RC element in series, as in circuit C. The element that was considered most suitable is shown in circuit H and is considered, together with other similar possible circuits, D-G, to model the CSZ data obtained here. All the circuits, D-H, include the possibility of a series-connected RC element in parallel with the bulk conduction element.

This series RC element, considered in isolation, Fig 4.6, is the element that is regarded to represent dielectric relaxation phenomena, such as dipole reorientation, in materials that show no *dc* conductivity. R_0 represents the resistive component of short range motions involved in the relaxation process; C_0 is viewed as either a blocking capacitance that prevents long range conduction, or as the charge stored by alignment of the dipoles. It is not clear from the literature whether there is a preferred or optimised equivalent circuit to represent such series relaxation processes. Three 'ideal' possibilities are shown in Fig 4.6; additional possibilities that involve non-ideal behaviour could involve replacement of either capacitance, C_0 or resistance, R_0 by a CPE, but were not found necessary to model the data reported here.

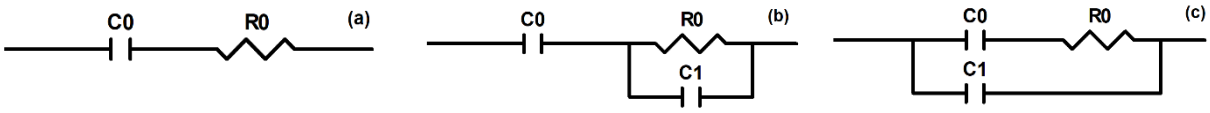

***Figure 4.6**. Possible equivalent circuits to represent dielectric relaxation phenomena.*

In previous studies of the bulk impedance of YSZ single crystals [14], it was clear that circuit B gave only an approximate fit with rather high residuals between experimental and fitted impedances. Circuit C also did not fit the single crystal data well and anyway, should be inappropriate for a single crystal sample. Circuit H gave a good fit and was justified as being the circuit that represented a combination of the bulk conducting component, circuit B and the simple dielectric element, Fig 4.6(a). Therefore, the initial assumption that circuit H may represent the bulk impedance data of the present CSZ ceramics was made.

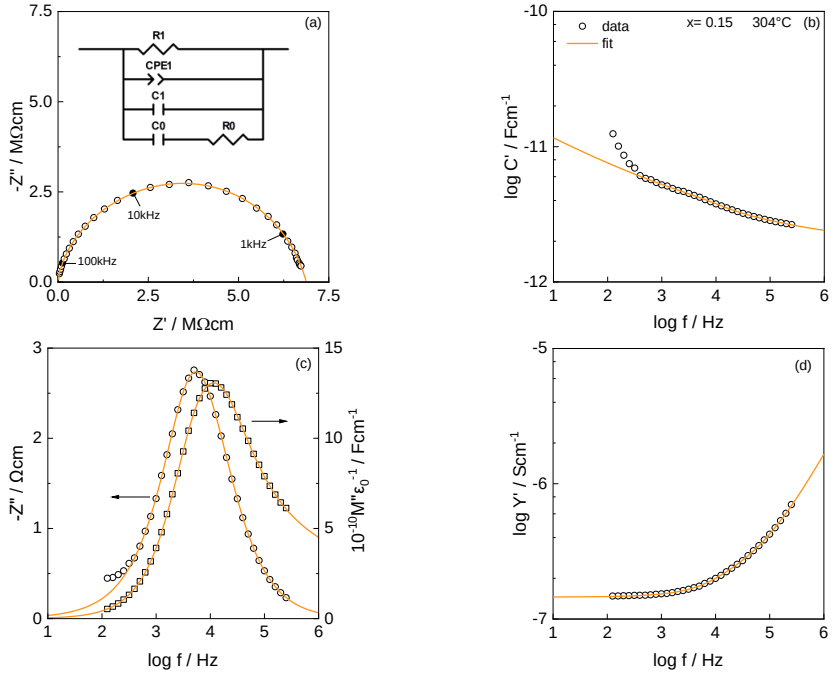

***Figure 4.7**. The bulk impedance response of x=0.15 at 304°C, fitted to equivalent circuit H.*

Fits to circuit H for all four impedance formalisms are shown for one temperature and composition in Fig 4.7; impedance residuals are shown for the same data set in Fig 4.5(h). Fits for other compositions are shown in Fig 4.S5-S6, and fitted parameter values in Tables 4.S1-S3. Excellent agreement between experimental and fitted data is obtained for frequencies above 10^2-10^3 Hz and the residuals are as low as those of any of the other circuits that were tested, and certainly better than those for circuit B. At lowest frequencies, an additional circuit element representing the grain boundary impedance is required to fit the data, especially the C' data, Fig 4.7, as discussed later. The residuals in Fig 4.5 show a good fit also for circuit G, which differs from H only in the location of capacitance C_1. The fit for circuit E is slightly less good than for H, but does have one fewer refineable parameter, ie R_1. The fits for circuits A, B, D and F are significantly worse than the other fits.

It was concluded that circuit H is the preferred circuit for two reasons. First, it has the parallel combination of conducting and dielectric elements, which intuitively, seems to be the most logical circuit. Second, together with closely related circuit G, it has the smallest fit residuals. Circuit C also has low fit residuals, but it was excluded since it would represent a series combination of two impedance components and imply that the sample was electrically inhomogeneous. This circuit was excluded from consideration of fits to single crystal YSZ [14].

Conductivity data for σ_1 (ie R_1^{-1}) have already been given in Fig 4.3(a) and are reproduced in Fig 4.8(b), together with data for the dielectric component, σ_0 (ie R_0^{-1}). Two observations may be made. First, as stated previously, σ_1 *(ie* σ_b*)* decreases with increasing x but its activation energy is unchanged. The conductivity of a material with hopping charge carriers is given by:

$$\sigma = n\, e\, \mu \qquad (4.1)$$

where n, e and μ are the number, charge and mobility of the carriers. Since the activation energy is unchanged with composition, it is likely that the conductivity activation energy is the same as that for migration, or mobility. Therefore, n is temperature-independent for a particular data set but decreases with increasing x; the conductivity reduction is attributed to a reduction in number of mobile oxygen vacancies.

Second, the activation energies for σ_0 and σ_1 are the same for x = 0.12 but that for σ_0 increases with x. This means that, with increasing x, the processes responsible for σ_0 are increasingly different from those responsible for *dc* conduction, σ_1. In particular, the oxygen vacancy hops responsible for the dielectric component or dipole reorientation become more difficult with increasing x.

Fitted data for the dipole or dielectric capacitance, C_0 are shown in Fig 4.8(a). Two effects are seen:
(i) C_0 values decrease with increasing x. This is consistent with the decrease in σ_0 shown in (b): the dipoles show smaller polarizability or capacitance at the same time as their ease of reorientation, given by σ_0, decreases with x
(ii) C_0 values increase with increasing temperature, (a) and at the same time, σ_0 increases, (b). Again, there is a correlation between increased local conductivity and increased polarizability of the local environment around the hopping oxide ions.

The bulk polarisation, represented by C_1, remain between 1.45pFcm^{-1} to 1.57 pFcm^{-1} for x=0.12, 1.72 pFcm^{-1}to 1.90 pFcm^{-1} for x=0.15 and 1.88 pFcm^{-1} to 1.91 pFcm^{-1} for x=0.18, within the corresponding temperature range of Fig 4.8.

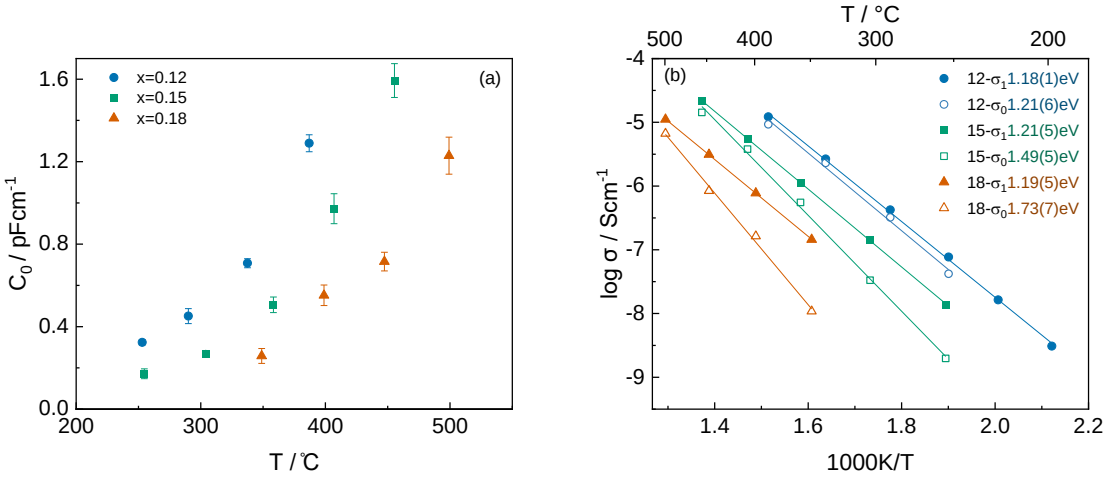

***Figure 4.8**. Temperature and composition dependence of dipolar relaxation parameters (a) C_0 and (b) σ_0 ($\equiv R_0^{-1}$) for x=0.12,0.15 and 0.18. Data for σ_1 are included in (b) for comparison.*

4.3.3.2 Grain boundary impedance

The next step in circuit analysis was to consider the grain boundary data. It was found that addition of the parallel element R_2CPE_2 to circuit H gave good fits, as shown for x = 0.15 at 455 °C in Fig 4.9 and for other compositions and temperatures in Figs 4.S7 and 4.S8. Tables of the fitted parameters are shown on tables 4.S4-S6 The presence of CPE_2 was required to obtain a good fit, but it was not found necessary to add an additional parallel capacitance C_2 to the circuit. Arrhenius plots for the grain boundary conductivity, σ_{gb} (ie σ_2), are given in Fig 4.3(a). Within errors, the values obtained were the same as those estimated manually from intercepts of the grain boundary arc, such as seen in Fig 4.2(a), on the Z' axis. From the similarity in activation energies, it was concluded that the grain boundary material is essentially the same as the bulk CSZ, but the concentration of mobile carriers is different, perhaps due to partial segregation of Ca towards / away from the grain boundaries.

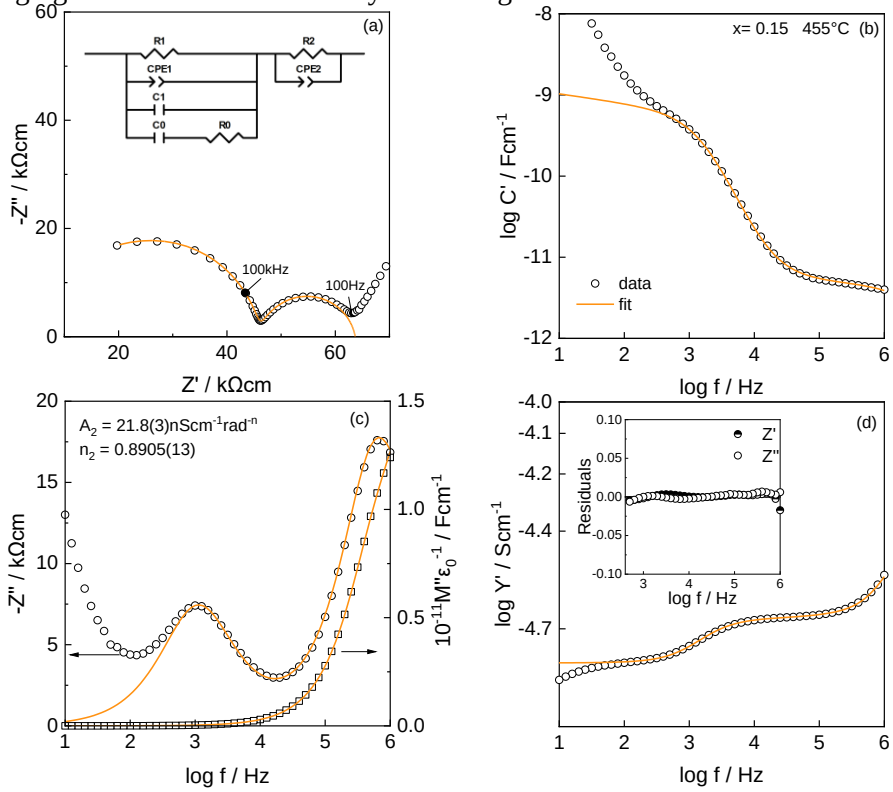

***Figure 4.9**. Fitting results and residuals of circuit H in series with a parallel R-CPE element that together, represent bulk and grain boundary response of x=0.15 at 455°C.*

4.3.3.3 Sample-electrode impedance

The final step in circuit analysis was to consider the sample-electrode response. Typical data, Figs 4.2(a) at 407 ºC and 2(b) at 697 ºC, show a high impedance effect that dominates the overall response at these temperatures and is characterised by a broad asymmetric arc that appears to have a linear component at the highest frequencies. Various circuits, including the Randles circuit, are considered in the literature and include the possibility of two impedance contributions: (i) a parallel RC element (ideally) in which R represents charge transfer of oxygen species / electrons and is in parallel with a double layer capacitance at the sample-electrode interface; (ii) a Warburg diffusion element that represents oxygen molecules moving towards / away from the interface and involves diffusion through the electrode.

Various circuits that may represent these possibilities were tested for one typical data set and are shown in Fig 4.10, together with the fit residuals that were obtained. Fitted parameter values are given in Table 4.S7. Due to frequency limitations of the data at high temperatures, the only components of the sample impedance that could be included in the fits were the bulk resistance, R_1 and the grain boundary impedance, R_2CPE_2. The most satisfactory fit for the sample-electrode response is shown in (c) and has components R_3C_3 that appear to represent the charge transfer impedance and R_4CPE_4 that represents the Warburg; this is a finite Warburg which is limited at low frequencies by the parallel resistance, R_4 and probably, is a characteristic of the electrode material and its microstructure. The fitted impedance response for x=0.15 at 697°C is shown in Fig 4.S9.

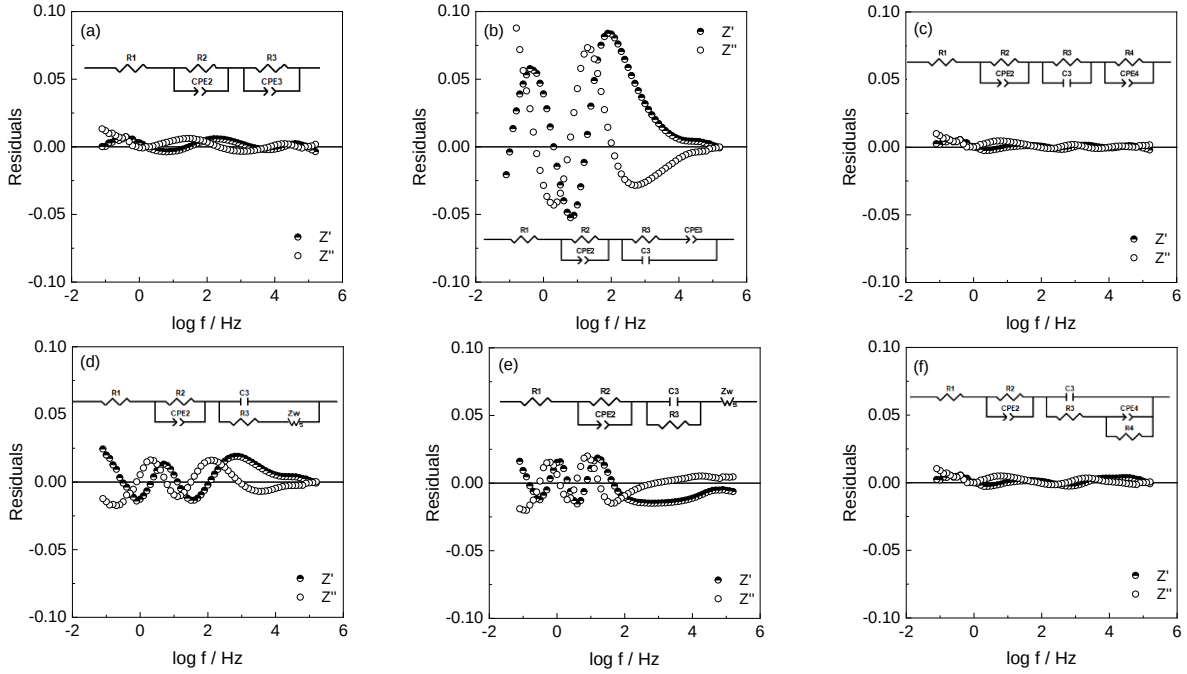

Figure 4.10. *Fitting residuals from 6 possible equivalent circuits to represent the bulk, grain boundary and electrode response of x=0.15 at 697°C.*

4.4 Discussion

4.4.1 Conduction mechanism in CSZ grains and grain boundaries

The decrease in bulk conductivity with increasing x, reported here for compositions in the range 0.12 to 0.18, is consistent with literature reports that show a maximum conductivity around x=0.12 to 0.13 [10], [18], which is just inside the compositional range of the cubic stabilised solid solutions. Comparison of activation energy values with those in the early literature is not straightforward, however, due to (i) the possible contribution of grain boundary impedances to total conductivity data in the early literature, (ii) the effect of curvature in Arrhenius plots at high temperatures and (iii) the

possibility of order-disorder phenomena associated with differences in sample history and annealing temperature. Nevertheless, since all Arrhenius plots are essentially parallel, the implication is that the conductivity differences are attributable entirely to differences in mobile carrier concentration; a single conduction mechanism is responsible for the temperatures and compositions studied, as well as for both grain and grain boundary regions.

The reduction in bulk conductivity, and therefore, mobile oxygen vacancy concentration, between compositions 12 and 18% CaO, Fig 4.8(b), is by a factor of about 20-25. As a consequence of the charge compensation mechanism half of the dopant concentration creates oxygen vacancies, as shown in equation 4.2, therefore the total vacancy concentration increases by 50%.

$$CaO \xrightarrow{ZrO_2} Ca''_{Zr} + V_O^{\bullet\bullet} + O_O^x \qquad (4.2)$$

As the difference between 18% and 12% is 6%, this means that the *effective* mobile carrier concentration in 18% CaO is only about 3% of that in 12% CaO and indeed, it is by no means certain that all vacancies in 12% CaO are mobile. CSZ may, therefore, be regarded as a *weak electrolyte* [42], [43] in which only a small number of the potential current carriers are dissociated, or mobile. The conclusion that mobile carrier concentration is independent of temperature in the lower temperature region of linear Arrhenius behaviour agrees with similar conclusions in [44], but disagrees with the conclusion in [44] that all oxygen vacancies are mobile.

The bulk and grain boundary conductivities in the linear, low temperature region have activation energy, 1.15(6) eV, independent of x over the range 0.12 to 0.18. Grain boundary conductivities are apparently ½ to 1 order of magnitude higher than the bulk conductivities, Fig 4.3(a), but are not corrected for the geometry of the grain boundary regions. Capacitance data, Fig 4.2(c), show plateaux around 0.1-1 nF that are two orders of magnitude larger than the bulk plateaux. Making the assumption that grain boundary thickness is inversely proportional to grain boundary capacitance [45], the grain boundary resistivities may be up to one order of magnitude larger than grain resistivities. This may reflect a reduction in mobile carrier concentration in the grain boundary regions, possibly due to partial segregation of Ca, and oxygen vacancies away from the grain boundaries. However, similarity of grain and grain boundary activation energies indicates a similarity in structure of the two regions and therefore, that the grain boundary has the character of a constriction resistance [46], associated either with incomplete densification of the ceramics or segregation of Ca.

There has been much interest in the literature in the mechanism of conduction by oxygen vacancies in CSZ and in other fluorite-structured materials, especially YSZ. Dopants such as Ca and Y carry different charge to neutral Zr and the oxygen vacancies are also charged, leading to strong electrostatic interactions between dopants and the current carrying species. An early defect structure model was developed [10] that predicted a change in the composition dependence of the conductivity of CSZ which passed through a maximum at a similar composition, x=0.125, to that seen experimentally by several authors. The model was subsequently applied to YSZ compositions [11] to account for experimental data. Nakamura and Wagner [10], [11], suggested that oxide ion conductivity takes place through the dopant-$V_O^{\bullet\bullet}$ path but involves more than one level of dopant-defect association, taking into consideration that every cation has 8-first and 24-second nearest anion neighbour sites. The essence of the model is that vacancy conduction is facilitated best when each substitutional Ca has one of its eight nearest neighbour oxygen sites vacant, in what was described as a 'one-fold dopant-defect associate' or complex involving interactions such as Ca_{Zr}''-$V_O^{\bullet\bullet}$ in CSZ or Y_{Zr}'-$V_O^{\bullet\bullet}$ in YSZ. At composition x = 0.125, these complexes overlap to cover the entire structure which means that long range oxygen vacancy hopping could occur inside the complexes and therefore, the complexes would act to facilitate rather than hinder conduction.

In the Nakamura / Wagner model, migration of un-associated oxygen vacancies requires extra energy compared with that for migration within the complexes and is regarded as the reason for reduced conductivity at smaller x values where the complexes do not link to form a continuous network. At higher x values, more than one oxygen vacancy / Ca is associated with each complex leading to trimers such as Ca_{Zr}''- $V_O^{\bullet\bullet}$ - Ca_{Zr}''. These were thought to bind the oxygen vacancies more strongly, thereby

reducing the carrier concentration but also, blocking partially the vacancy migration pathway. Consequently, the conductivity decreases at higher x values. This viewpoint is, however, significantly different from that of many subsequent authors who treated the complexes as instead, traps that require an additional enthalpy of dissociation to liberate 'free' oxygen vacancies.
Various models for defect formation, interaction and association in YSZ and ScSZ have been evaluated in a definitive series of papers by Hull *et al* [27]–[29]. They used a combination of conductivity measurements, diffraction studies, including diffuse scattering, quasielastic scattering and molecular dynamics simulations and were able to investigate the significance of various defect combinations. To summarise briefly the main conclusions:

1.Oxygen vacancies are associated preferentially with Zr rather than with Y, Sc;

2.Cation–oxygen vacancy interactions are mainly responsible for differences in conductivity with different dopants;

3.Oxygen vacancy–oxygen vacancy pairs in the <111> orientation are important in determining the composition–dependence of conductivity for a given dopant;

4.The decrease in conductivity that is generally observed at higher dopant concentrations is attributed to immobilisation of the oxygen vacancy pairs into aggregates with a <112> orientation. Interestingly, these aggregates resemble the oxygen vacancy order in $Zr_3Y_4O_{12}$ and raise the possibility of premonitory segregation of ordered regions within an otherwise-homogeneous solid solution.

The defect structure in CSZ [33] appears to be different from that in YSZ and ScSZ and is limited to single oxygen vacancies and vacancy pairs [27], [31], [32], without evidence for either larger defect aggregates or tetragonal distortions. In all three cases, however, it appears that defect clusters are responsible for reduced conductivity at high x, but is less clear whether single oxygen vacancies or vacancy pairs are responsible for the high conductivity at low x. The role of the acceptor dopant appears not to be dominant in optimising conductivity at low x since the conductivity in all systems decreases with dopant concentration at higher x. For ScSZ, the composition with maximum conductivity varies with measurement temperature and so, in this system at least, there is not a specific composition at which the conductivity is maximised [29].

4.4.2 Curvature of Arrhenius plots

Early models of the widely-observed curvature in conductivity Arrhenius plots at high temperatures [7]–[13] assumed that dissociation of trapped vacancies was responsible, which would reduce even further the mobile vacancy concentration at lower temperatures. This model may be correct in principle, but alternatively, the carriers may be trapped as oxygen vacancy pairs or larger aggregates that may, or may not, involve cations. There may also be oxygen vacancy pairs that have different separation in <111>, <110> and <100> orientations. Evidence from MD simulations on YSZ and ScSZ indicates that the numbers of pairs of these three types is temperature-dependent [28].

4.4.3 Dielectric contribution to the bulk impedance

No direct experimental evidence was found for the possible effect of dipoles on electrical properties has been presented previously. Some authors report dielectric measurements with data presented in tan δ format [9], [47]; however, tan δ peaks are not necessarily evidence of dipole re-orientation but can arise simply from series R-C connections that form part of a larger equivalent circuit. The features of the experimental results that need explanation are:

1.At the lowest x value studied, x=0.12, the activation energies for dielectric relaxation or dipole reorientation and bulk conductivity are similar, 1.21 eV, Fig 4.8(b).
2.With increasing x, the activation energy for the dielectric component is increasingly greater than that for bulk conduction, eg 1.73(7) eV compared with 1.19(5) eV for x=0.18.
3.The dipole capacitance, C_o, increases with temperature but decreases with x, Fig 4.8(a).

In order to detect dipolar processes in impedance data, it is essential that the processes are (i) localised, (ii) constrained by a series capacitance, C_o and (iii) do not contribute to long range conduction. The logical origin of dipoles would be the association of oppositely-charged oxygen vacancies and calcium dopants, ie $V_o^{\bullet\bullet}$-Ca_{Zr}'', although it is clear that strain effects associated with size mismatch can act to moderate the strength of electrostatic interactions [29]. The results of diffuse scattering measurements on single crystals of CSZ with different composition [31], [32] were interpreted in terms of two types of defect, single oxygen vacancies with relaxed neighbouring ions and oxygen vacancy pairs. These results show the composition independence of the bulk activation energy and the decrease in conductivity with x, taken together, indicate that the species responsible for bulk conduction are likely to be isolated oxygen vacancies whose number decreases with increasing x at the same time as the number of oxygen vacancy pairs increases.

The dipoles may correspond to oxygen vacancies that form pairs to either side of a Ca^{2+} ion, oriented in the <111> directions. Dipole reorientation may involve vacancies that hop in either <100> or <110> directions although in both cases, this results in an increase in separation of the Ca_{Zr} and V_O species that form the dipoles. The activation energy for dipole reorientation, σ_0, increases with x, either because their reorientation becomes more difficult with an increase in number of pairs, or because the pairs begin to coalesce into larger aggregates. With increasing temperature, the increase in permittivity, ε', is attributed to increased thermal motion of the dipole components, but with increasing x, ε' decreases due to the increase in dipole cluster strength.

For a structure such as CSZ that contains both short range dielectric and long range conductivity components, there appears to be no *a priori* reason why the local process should have either higher or lower activation energy than long range conduction. From these results on CSZ, the short range conduction has either similar (x=0.12) or greater (x=0.15, 0.18) activation energy, whereas for YSZ single crystal [14], its value was less. The similarity in activation energy for x=0.12 could indicate that the first hop is the same for both long range conduction and short range dielectric processes, but the distinction arises over the possibility of second, and subsequent hops; clearly in the dielectric case, follow-on hops are blocked.

4.5 Conclusions

The bulk conductivity of CSZ ceramics decreases with increasing x but the activation energy is unchanged. This means that the activation energy is controlled by the activation energy for migration, or hopping, of oxygen vacancies.

The magnitude of the conductivity is controlled by the number of *mobile* oxygen vacancies which decreases greatly with x. The number of oxygen vacancies that are mobile is small, ≤3% at high x, indicating that CSZ may be regarded as a weak electrolyte. The number of mobile vacancies is temperature-independent for 12, 15 and 18% CaO, at least in the lower temperature region of linear Arrhenius behaviour.

The mechanism responsible for increased immobilisation of the oxygen vacancies with increasing x is tentatively attributed to the formation of oxygen vacancy pairs and/or larger aggregates, similar to those that have been identified in YSZ and ScSZ.

The impedance data show the presence of a local dielectric loss or conductivity in addition to long range conduction. The logical explanation for this is that local hops occur but without the possibility of follow-on hops. It is difficult to see how oxygen vacancy pairs alone could lead to dipoles. These are therefore attributed to Ca_{Zr} – V_o pairs or larger defect groupings.

Although oxygen vacancy pairs and defect dipoles are both in evidence, the precise factors that control the ionic conductivity, its activation energy and high temperature curvature in Arrhenius plots are still not fully resolved. The species that are responsible for long range conduction appear to involve a

minority of the potentially mobile oxygen vacancies, which complicates their study by most characterisation techniques.

The presence of local conduction processes such as dipole reorientation, in parallel with long range conduction, does not affect the value of the sample bulk conductivity but is apparent on fitting impedance data to the most appropriate equivalent circuit.

4.6 References

[1] B. C. H. Steele, "Oxygen ion conductors and their technological applications," *Mater. Sci. Eng. B*, vol. 13, no. 2, pp. 79–87, 1992.

[2] A. B. Stambouli and E. Traversa, "Solid oxide fuel cells (SOFCs): a review of an environmentally clean and efficient source of energy," *Renew. Sustain. Energy Rev.*, vol. 6, pp. 433–455, 2002.

[3] S. A. Sternbergh and W. M. Hickam, "Flight Type Oxygen Partial Pressure Sensor," Pittsburgh, Pa., 1966.

[4] J. W. Fergus, "Doping and defect association in oxides for use in oxygen sensors," *J. Mater. Sci.*, vol. 38, no. 21, pp. 4259–4270, 2003.

[5] S. J. Skinner and J. A. Kilner, "Oxygen ion conductors," *Mater. Today*, vol. 6, no. 3, pp. 30–37, 2003.

[6] M. C. Steil, F. Thevenot, and M. Kleitz, "Densification of yttria - stabilized zirconia impedance spectroscopy analysis," *J. Electrochem. Soc.*, vol. 144, no. 1, pp. 390–398, 1997.

[7] T. Y. Tien and E. C. Subbarao, "X-ray and electrical conductivity study of the fluorite phase in the system ZrO_2 –CaO," *J. Chem. Phys.*, vol. 39, pp. 1041–1047, 1963.

[8] M. Asadikiya and Y. Zhong, "Oxygen ion mobility and conductivity prediction in cubic yttria-stabilized zirconia single crystals," *J. Mater. Sci.*, vol. 53, no. 3, pp. 1699–1709, 2018.

[9] S. Komine and F. Munakata, "Dielectric relaxation analysis for 8 mol% YSZ single crystal," *J. Mater. Sci.*, vol. 40, no. 15, pp. 3887–3890, 2005.

[10] A. Nakamura and J. B. Wagner, "Defect structure, ionic conductivity, and diffusion in calcia-stabilized zirconia," *J. Electrochem. Soc.*, vol. 127, no. 11, pp. 2325–2333, 1980.

[11] A. Nakamura and J. B. Wagner, "Defect structure, ionic conductivity, and diffusion in yttria stabilized zirconia and related oxide electrolytes with fluorite structure," *J. Electrochem. Soc.*, vol. 133, no. 8, p. 1542, 1986.

[12] J. A. Kilner and R. J. Brook, "A study of oxygen ion conductivity in doped non-stoichiometric oxides," *Solid State Ionics*, vol. 6, no. 3, pp. 237–252, 1982.

[13] D. K. Honke, "Ionic conduction in doped zirconia," in *Fast Ion Transport in Solids, Electrodes and Electrolytes*, 1979, pp. 669–672.

[14] X. Vendrell and A. R. West, "Electrical properties of Yttria-stabilized zirconia, YSZ Single crystal: local AC and long range DC conduction," *J. Electrochem. Soc.*, vol. 165, no. 11, pp. F966–F975, 2018.

[15] N. Masó and A. R. West, "Electronic conductivity in Yttria-stabilized zirconia under a small dc bias," *Chem. Mater.*, vol. 27, no. 5, pp. 1552–1558, 2015.

[16] M. Jovaní, H. Beltrán-Mir, E. Cordoncillo, and A. R. West, "Atmosphere- and voltage-dependent electronic conductivity of oxide-ion-conducting $Zr_{1-x}Y_xO_{2-x/2}$ ceramics," *Inorg. Chem.*, vol. 56, no. 12, pp. 7081–7088, 2017.

[17] M. Cologna, B. Rashkova, and R. Raj, "Flash sintering of nanograin zirconia in < 5s at 850°C," *J. Am. Ceram. Soc.*, vol. 93, no. 11, pp. 3556–3559, 2010.

[18] T. H. Etsell and S. N. Flengas, "The electrical properties of solid oxide electrolytes," *Chem. Rev.*, vol. 70, no. 3, pp. 339–376, 1970.

[19] R. Terki, G. Bertrand, H. Aourag, and C. Coddet, "Structural and electronic properties of zirconia phases: a FP-LAPW investigations," *Mater. Sci. Semicond. Process.*, vol. 9, no. 6, pp. 1006–1013, 2006.

[20] S. Y. Kwon and I. H. Jung, "Critical evaluation and thermodynamic optimization of the CaO-ZrO_2 and SiO_2-ZrO_2 systems," *J. Eur. Ceram. Soc.*, vol. 37, no. 3, pp. 1105–1116, 2017.

[21] K. Kiukkola and C. Wagner, "Measurements on galvanic cells involving solid electrolytes," *J.*

Electrochem. Soc., vol. 104, no. 6, pp. 379–387, 1957.
[22] A. M. Diness and R. Roy, "Experimental confirmation of major change of defect type with temperature and composition in ionic solids," *Solid State Commun.*, vol. 3, no. 6, pp. 123–125, 1965.
[23] T. H. Etsell and S. N. Flengas, "N-type conductivity in stabilized zirconia solid electrolytes," *J. Electrochem. Soc.*, vol. 119, no. 1, pp. 1–7, 1972.
[24] F. A. Kröger, "Electronic conductivity of calcia-stabilized zirconia," *J. Am. Ceram. Soc.*, vol. 49, no. 4, pp. 215–218, 1966.
[25] J. Rudolph, "Mechanism of conduction in oxide semiconductors at high temperatures," *Zeitschrift für Naturforsch.*, vol. 14, no. 8, pp. 727–737, 1959.
[26] R. W. Vest, N. M. Tallan, and W. C. Tripp, "Electrical properties and defect structure of zirconia: I, monoclinic phase," *J. Am. Ceram. Soc.*, vol. 47, no. 12, pp. 635–640, Dec. 1964.
[27] J. P. Goff, W. Hayes, S. Hull, M. T. Hutchings, and K. N. Clausen, "Defect structure of yttria-stabilized zirconia and its influence on the ionic conductivity at elevated temperatures," *Phys. Rev. B - Condens. Matter Mater. Phys.*, vol. 59, no. 22, pp. 14202–14219, 1999.
[28] S. T. Norberg *et al.*, "Structural disorder in doped zirconias, part I: the $Zr_{0.8}Sc_{0.2-x}Y_xO_{1.9}$ ($0.0 \leq x \leq 0.2$) System," *Chem. Mater.*, vol. 23, no. 6, pp. 1356–1364, 2011.
[29] D. Marrocchelli, P. A. Madden, S. T. Norberg, and S. Hull, "Structural disorder in doped zirconias, part II: vacancy ordering effects and the conductivity maximum.," *Chem. Mater.*, vol. 23, no. 6, pp. 1365–1373, 2011.
[30] A. Bogicevic and C. Wolverton, "Nature and strength of defect interactions in cubic stabilized zirconia," *Phys. Rev. B - Condens. Matter Mater. Phys.*, vol. 67, no. 2, 2003.
[31] T. Proffen, R. B. Neder, F. Frey, and W. Assmus, "Defect structure and diffuse scattering of zirconia single crystals doped with 7 mol% CaO," *Acta Crystallogr. Sect. B*, vol. 49, no. 4, pp. 599–604, 1993.
[32] T. Proffen, R. B. Neder, F. Frey, D. A. Keen, and C. M. E. Zeyen, "Defect structure and diffuse scattering of zirconia single crystals with 10 and 15 mol% CaO at temperatures up to 1750 K," *Acta Crystallogr. Sect. B*, vol. 49, no. 4, pp. 605–610, 1993.
[33] S. Jing-ze and W. Yu-ming, "Diffusion in fast-ion conductor calcia-stabilized zirconia: a molecular dynamics study," *Chinese Phys. Lett.*, vol. 15, no. 10, p. 727, 1998.
[34] S. Kazlauskas, A. Kežionis, T. Šalkus, and A. F. Orliukas, "Electrical properties of YSZ and CaSZ single crystals," *Solid State Ionics*, vol. 231, pp. 37–42, 2013.
[35] O. Y. Kurapova, O. V Glumov, M. M. Pivovarov, S. N. Golubev, and V. G. Konakov, "Structure and conductivity of calcia stabilized zirconia ceramics, manufactured from freeze-dried nanopowder," *Rev. Adv. Mater. Sci.*, vol. 52, no. 1–2, pp. 134–141, 2017.
[36] C. Schwandt and W. Weppner, "Electrode reactions at oxygen, noble metal / stabilized zirconia interfaces," *Ionics (Kiel).*, vol. 2, no. 2, pp. 113–122, 1996.
[37] J. E. B. Randles, "Kinetics of rapid electrode reactions," *Faraday Discuss.*, vol. 1, pp. 11–19, 1947.
[38] S. Pandey, D. Kumar, O. Parkash, and L. Pandey, "Equivalent circuit models using CPE for impedance spectroscopy of electronic ceramics," *Integr. Ferroelectr.*, vol. 183, no. 1, pp. 141–162, 2017.
[39] N. H. Perry, T. C. Yeh, and T. O. Mason, "Temperature dependence of effective grain core/single crystal dielectric constants for acceptor-doped oxygen ion conductors," *J. Am. Ceram. Soc.*, vol. 94, no. 2, pp. 508–515, 2011.
[40] Scribner Associates Inc., "ZView Operating Manual (version 3.5)." 2016.
[41] M. A. Hernandez and A. R. West, "Dipolar relaxation and impedance of an yttria-stabilised zirconia ceramic electrolyte," *J. Mater. Chem. A*, vol. 4, no. 4, pp. 1298–1305, 2016.
[42] M. D. Ingram, C. T. Moynihan, and A. V. Lesikar, "Ionic conductivity and the weak electrolyte theory of glass," *J. Non. Cryst. Solids*, vol. 38–39, no. Part 1, pp. 371–376, 1980.
[43] J. L. Souquet and W. G. Perera, "Thermodynamics applied to ionic transport in glasses," *Solid State Ionics*, vol. 40/41, pp. 595–604, 1990.
[44] A. Orliukas, P. Bohac, K. Sasaki, and L. Gauckler, "Relaxation dispersion of ionic conductivity in a $Zr_{0.85}Ca_{0.15}O_{1.85}$ single crystal," *J. Eur. Ceram. Soc.*, vol. 12, no. 2, pp. 87–96, 1993.
[45] J. T. S. Irvine, D. C. Sinclair, and A. R. West, "Electroceramics: characterization by impedance

spectroscopy," *Adv. Mater.*, vol. 2, no. 3, pp. 132–138, 1990.
[46] P. G. Bruce and A. R. West, "The A-C Conductivity of Polycrystalline LISICON, $Li_{2+2x}Zn_{1-x}GeO_4$, and a Model for Intergranular Constriction Resistances," *J. Electrochem. Soc.*, vol. 130, no. 3, p. 662, 1983.
[47] H. Yamamura, Y. Yagi, and K. Kakinuma, "Dielectric relaxations of Y-Doped ZrO_2 single crystal," *J. Ceram. Soc. Japan*, vol. 115, no. 1345, pp. 546–550, 2007.

4.7 Supplementary

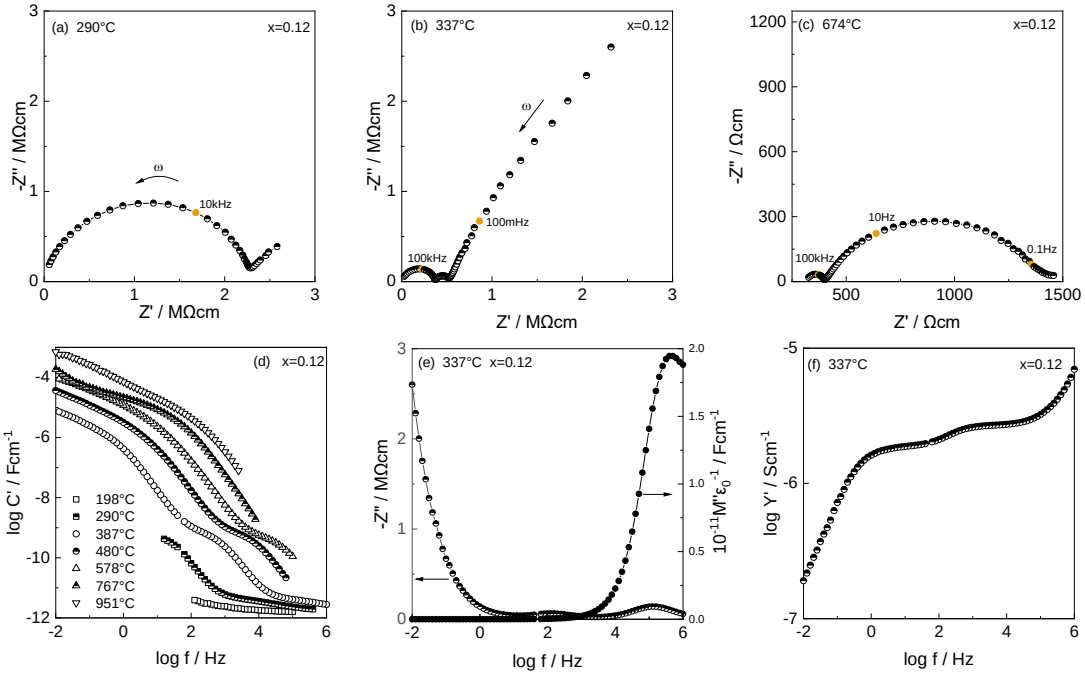

***Figure 4.S1**. (a)-(c) Impedance complex plane plots and spectroscopic plots of (d) capacitance, (e) Z''/M'' and (f) admittance at different temperatures for x=0.12; ω =2πf.*

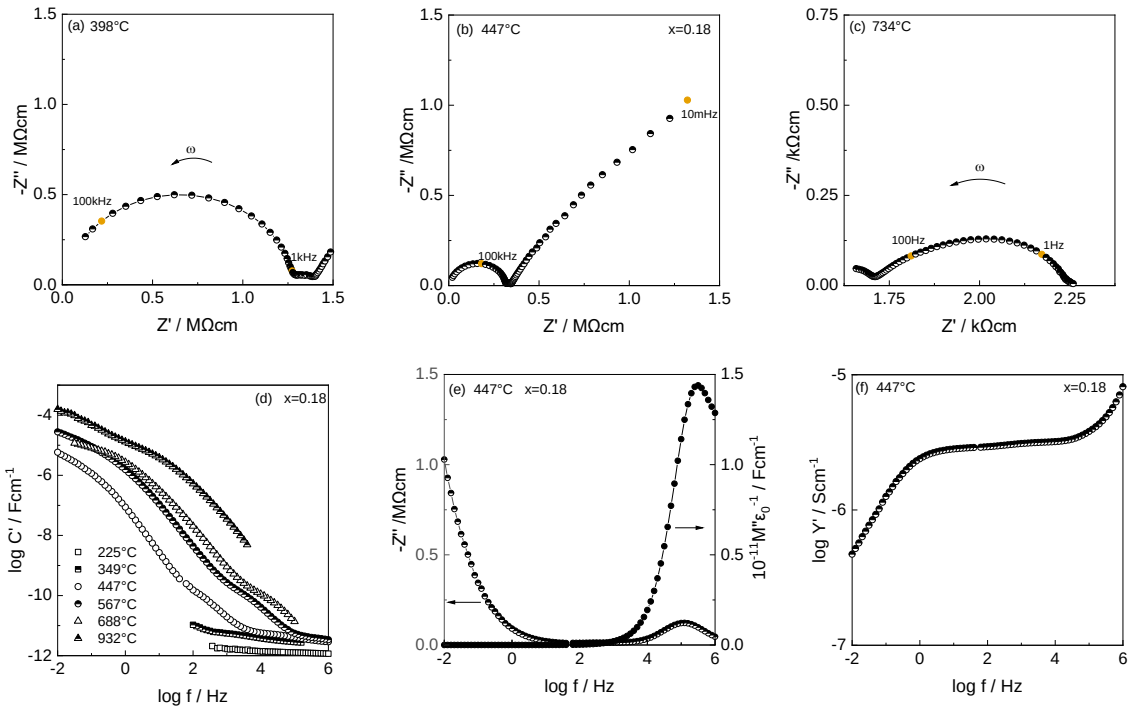

***Figure 4.S2**. (a)-(c) Impedance complex plane plots and spectroscopic plots of (d) capacitance, (e) Z''/M'' and (f) admittance spectroscopic plots at different temperatures for x=0.18; ω =2πf.*

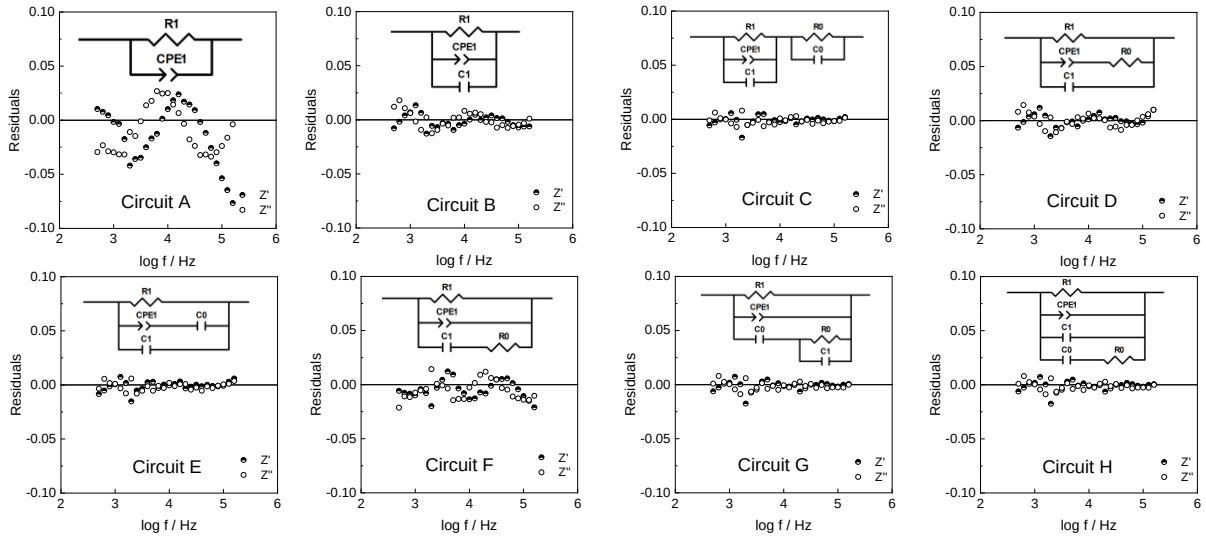

Figure 4.S3*. Fitting residuals of the bulk response from 8 possible equivalent circuits for x=0.12 at 253°C.*

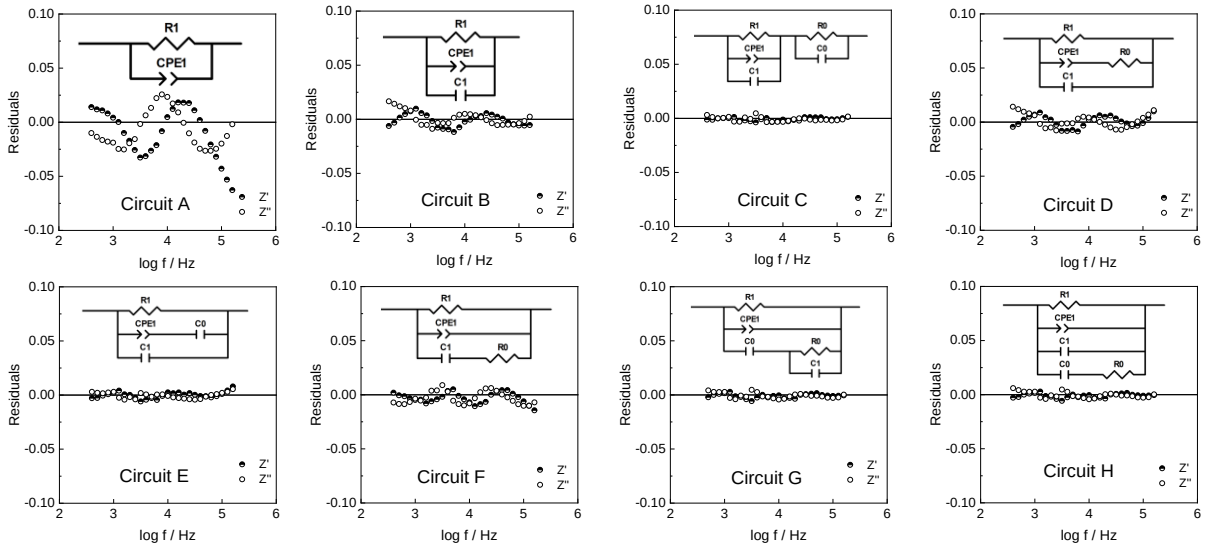

Figure 4.S4*. Fitting residuals of the bulk response from 8 possible equivalent circuits for x=0.18 at 349°C.*

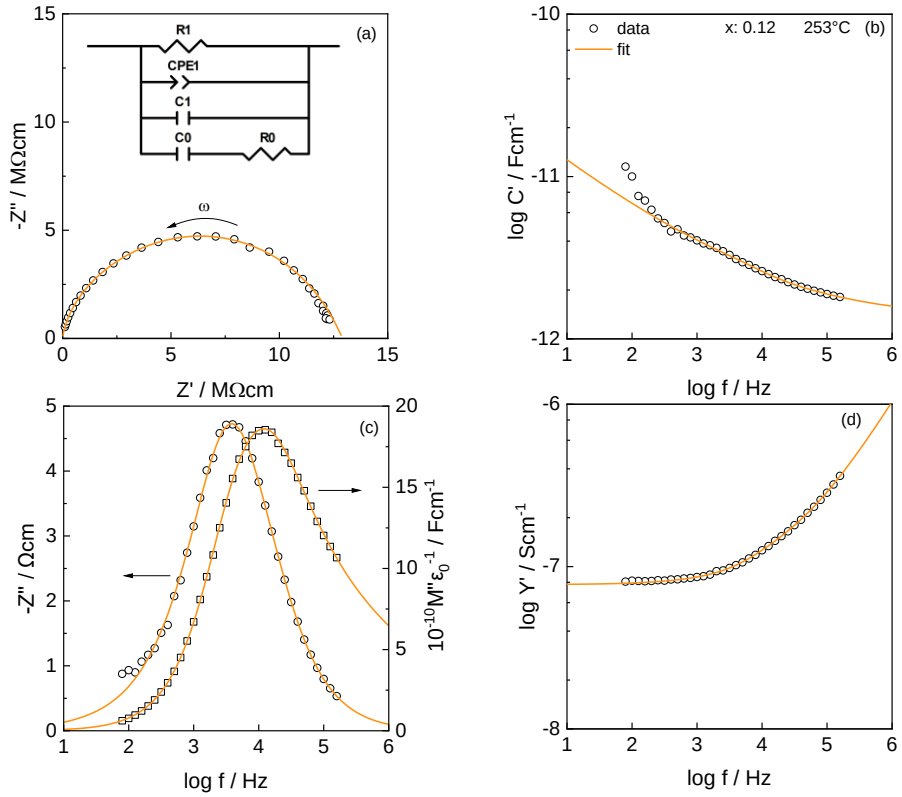

Figure 4.S5*. The bulk impedance response of x=0.12 at 253°C, fitted to equivalent circuit H.*

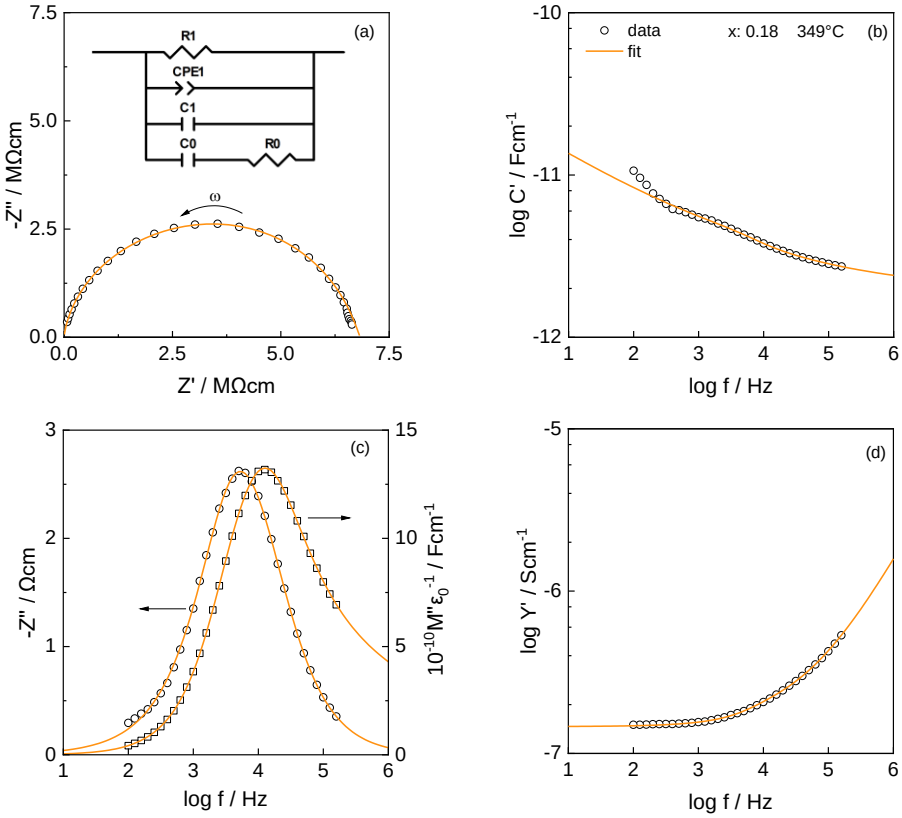

Figure 4.S6*. The bulk impedance response of x=0.18 at 349°C, fitted to equivalent circuit H.*

***Table 4.S1**. Fitted parameters of the different circuits tested for the bulk response, x=0.15 at 304°C.*

Circuit	R_1 (MΩcm)	R_0 (MΩcm)	A_1 ($pScm^{-1}rad^{-n}$)	n_1	C_1 ($pFcm^{-1}$)	C_0 ($pFcm^{-1}$)	X^2 ($x10^{-5}$)	Weighted Sum of Squares ($x10^{-3}$)
A	6.7(5)	–	13.7(5)	0.884(3)	–	–	128	65
B	7.02(2)	–	48(3)	0.715(7)	1.89(3)	–	11	5.5
C	5.3(8)	1.6(8)	73(6)	0.688(7)	2.16(3)	2.7(2)	1.6	0.8
D	7.03(5)	0.8(1)	59(4)	0.677(6)	2.41(2)	–	12	6.3
E	6.8(2)	–	29(4)	0.56(1)	2.18(2)	5.7(4)	3.6	1.8
F	6.7(2)	26(2)	9.1(2)	0.913(2)	7.8(4)	–	14	6.9
G	6.8(1)	1.0(1)	28(1)	0.759(5)	12.2(9)	2.12(2)	1.4	0.7
H	6.8(1)	47(3)	28(1)	0.759(5)	1.81(3)	0.31(2)	1.4	0.7

***Table 4.S2**. Fitted parameters of the different circuits tested for the bulk response, x=0.12 at 253°C.*

Circuit	R_1 (MΩcm)	R_0 (MΩcm)	A_1 ($pScm^{-1}rad^{-n}$)	n_1	C_1 ($pFcm^{-1}$)	C_0 ($pFcm^{-1}$)	X^2 ($x10^{-5}$)	Weighted Sum of Squares ($x10^{-3}$)
A	12.1(2)	–	13.5(7)	0.854(4)	–	–	222.4	108.9
B	13.3(7)	–	71(5)	0.650(7)	1.32(2)	–	14.4	6.909
C	10.7(3)	2.3(2)	103(14)	0.62(1)	1.46(3)	27(3)	5.4	2.471
D	13.1(7)	1.7(2)	67.(5)	0.645(7)	1.64(2)	–	11.6	5.455
E	12.5(5)	–	323(43)	0.52(1)	1.48(1)	5.3(4)	5.7	2.671
F	12.3(6)	40(3)	7.7(3)	0.895(3)	0.84(5)	–	32.7	15.387
G	12.9(6)	1.8(4)	48(5)	0.58(1)	9(1)	1.54(3)	6.0	2.776
H	12.9(6)	23(3)	107(5)	0.58(1)	1.56(2)	0.32(1)	6.0	2.776

***Table 4.S5**. Fitted parameters of the circuit fitted to the bulk and grain boundary response, x=0.15 at 455°C.*

R_1 (kΩcm)	R_0 (kΩcm)	A_1 ($nScm^{-1}rad^{-n}$)	n_1	C_1 ($pFcm^{-1}$)	C_0 ($pFcm^{-1}$)	R_2 (kΩcm)	A_2 ($nScm^{-1}rad^{-n}$)	n_2	X^2 ($x10^{-5}$)	Weight Sum of Squares ($x10^{-3}$)
46.3(7)	72(3)	0.118(7)	0.69(2)	1.90(3)	1.49(1)	15.2(5)	21.8(3)	0.890(1)	18.5	11.6

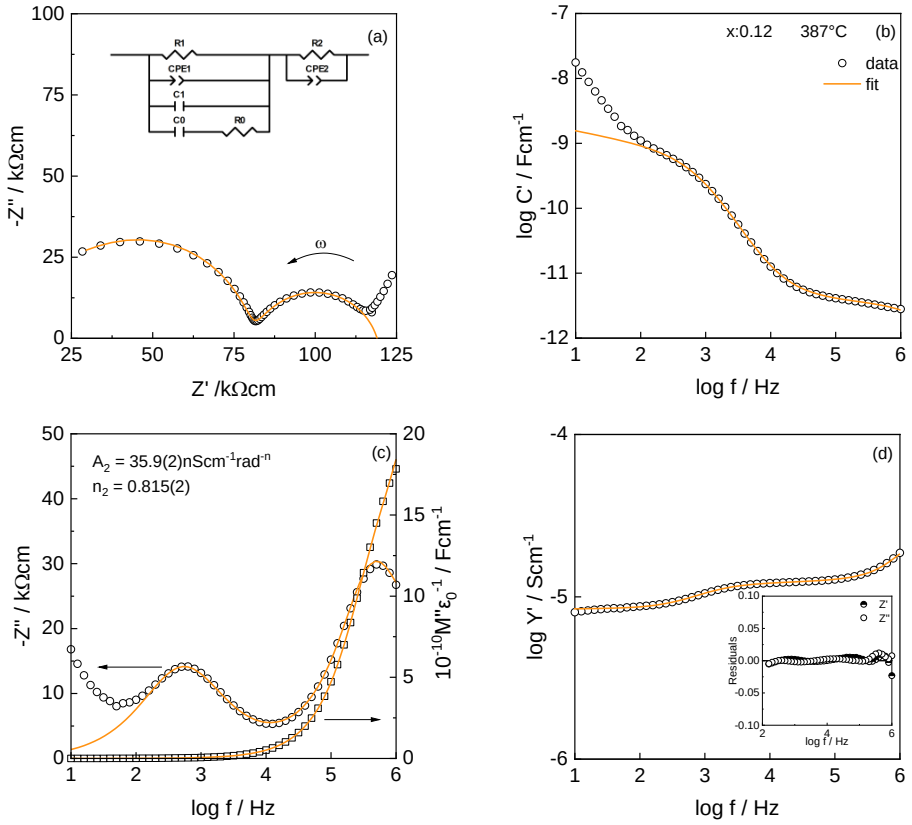

Figure 4.S7. *Fitting results and residuals of circuit H in series with a parallel R-CPE element that together, represent bulk and grain boundary response of x=0.12 at 387°C.*

Table 4.S5. *Fitted parameters of the circuit fitted to the bulk and grain boundary response, x=0.12 at 387°C.*

R_1 (kΩcm)	R_0 (kΩcm)	A_1 ($nScm^{-1}rad^{-n}$)	n_1	C_1 ($pFcm^{-1}$)	C_0 ($pFcm^{-1}$)	R_2 (kΩcm)	A_2 ($nScm^{-1}rad^{-n}$)	n_2	X^2 ($x10^{-5}$)	Weight Sum of Squares ($x10^{-3}$)
82.0(1)	107(3)	0.517(2)	0.56(1)	1.53(2)	1.28(4)	37.0(3)	35.9(5)	0.82(3)	14.6	10.5

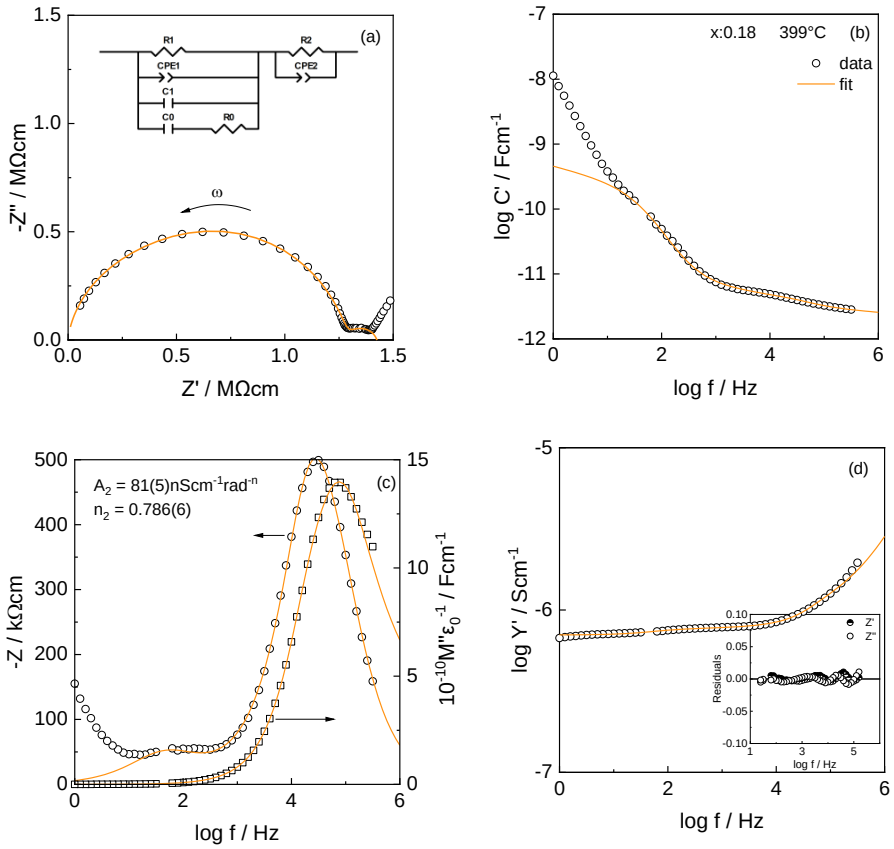

Figure 4. S8*. Fitting results and residuals of circuit H in series with a parallel R-CPE element that together, represent bulk and grain boundary response of x=0.18 at 399°C.*

Table 4.S5*. Fitted parameters of the circuit fitted to the bulk and grain boundary response, x=0.18 at 399°C.*

R_1 (kΩcm)	R_0 (kΩcm)	A_1 ($pScm^{-1}rad^{-n}$)	n_1	C_1 ($pFcm^{-1}$)	C_0 ($pFcm^{-1}$)	R_2 (kΩcm)	A_2 ($nScm^{-1}rad^{-n}$)	n_2	X^2 ($x10^{-5}$)	Weight Sum of Squares ($x10^{-3}$)
90.0(5)	150(15)	90(2)	0.695(6)	1.88(2)	1.23(9)	88(2)	81(5)	0.786(6)	6.09	2.2

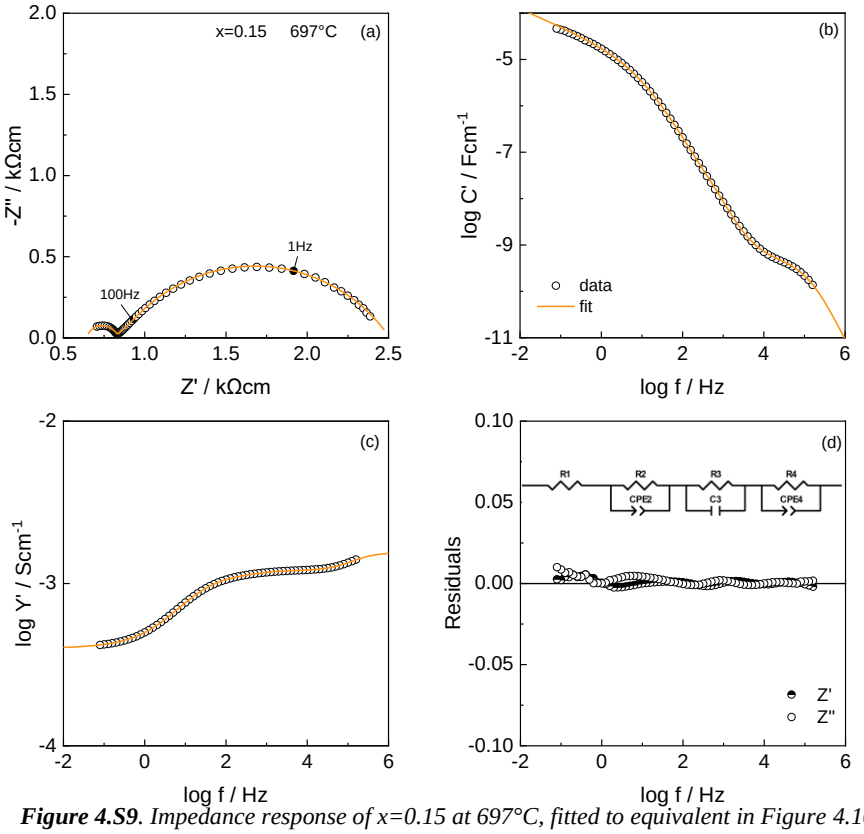

***Figure 4.S9**. Impedance response of x=0.15 at 697°C, fitted to equivalent in Figure 4.10(c).*

***Table 4.S7.** Fitted parameters of the different circuits tested for the electrode response, x=0.15 at 697°C.*

Circuit	R_3 (Ωcm)	$R_{4/ZWs}$ (Ωcm)	A_3 ($mScm^{-1}rad^{-n}$)	n_3	$A_{4/ZWs}$ ($mScm^{-1}rad^{-n}$)	$n_{4/ZWs}$	C_3 (μFcm^{-1})	X^2 ($x10^{-5}$)	Weighted Sum of Squares ($x10^{-3}$)
1.R3CPE3	1705(6)	-	0.125(1)	0.603(2)	-	-	-	15.76	127.7
2.(CPE3-R3)C3	$2.1x10^{-6}$(4)	-	0.67(2)	0.16(1)	-	-	11.8(9)	1963.9	1610.4
3.(R3C3)-(R4CPE4)	15.4(2)	1671(5)	-	-	$121.4x10^{-3}$(9)	0.618(2)	1.26(6)	1.93	1.35
4. (Zw_s-R3)C3	$1.6x10^{-5}$(7)	1552(12)	-	-	274(9)	0.275(9)	3.1(2)	114.85	141.27
5.(R3C3)-Zw_s	626(20)	906(22)	-	-	72(4)	0.072(4)	376(3)	114.68	141.05
6.(R-(CPER4))C3	39(2)	1650(5)	-	-	$142.6x10^{-3}$(8)	0.611(2)	1.60(8)	8.75	10.76

Chapter 5
Electrical properties of calcia-stabilised zirconia ceramics: pO_2 dependence and electrode response

5.1 Introduction

The dependence of conductivity on oxygen partial pressure, pO_2 is a useful parameter for determining whether an oxide ion conductor is in the electrolytic domain or has started to become electronically conducting by losing or gaining oxygen. The following equilibria:

$$O_O^x \rightarrow 1/2O_2 + V_O^{\bullet\bullet} + 2e' \quad (5.1)$$

$$1/2O_2 + V_O^{\bullet\bullet} \rightarrow O_O^x + 2h^{\bullet} \quad (5.2)$$

results in the presence of n- or p-type conductivity, respectively [1].

Cubic calcia-stabilised zirconia (CSZ) is a well-known oxide ion conductor [2] [3]. The limits of its electrolytic domain have been studied: evidence of n-type conduction at low pO_2 was detected [4] [5] by emf measurements, and the possibility of p-type conduction has been predicted theoretically at very high pO_2, but without experimental confirmation [6].

The Randles equivalent circuit and its modifications have been used to interpret the impedance response of the sample-electrode interface in many systems [7]-[18]. What these equivalent circuits have in common is the presence of a double layer capacitance, modelled by either a capacitor, $C_{dl,}$ or a constant phase element, CPE_{dl}, that is in parallel with a charge transfer resistance, R_{ct}, and in series with a diffusion process, modelled with either a Warburg impedance, Z_W or a constant phase element, CPE_{diff}.

This study aims to investigate the pO_2 dependence of the impedance response of CSZ and to further investigate the electrode response by equivalent circuit analysis.

5.2 Experimental

Electroded pellets with composition $Ca_xZr_{1-x}O_{2-x}$: x= 0.12, 0.15, 0.18 and densities ~86%, were prepared following the procedure described in Chapter 4. Impedance measurements were taken between 390 and 930 °C using a Modulab XM MTS impedance analyser (measurement accuracy ±0.1%) frequency range 100 mHz-1 MHz, with a nominal *ac* voltage of 100 mV in both cases. Pellets were attached to the Pt leads of a conductivity jig which allowed the flow of gas over the pellet.

Two sets of corrections were made to the collected data: (i) a geometric factor consisting of pellet thickness and sample-electrode contact area and (ii) jig impedance characteristics consisting of the blank, open circuit capacitance, typically 6 pF and the closed circuit resistance of, primarily, the leads, 1-2 Ω. Data analysis was performed using ZVIEW software (ZVIEW-Impedance Software version 2.4 Scribner Associates).

5.3 Results

Samples with x= 0.12, 0.15 and 0.18 were measured sequentially in N_2, air, O_2, air and N_2 or in a similar sequence but commencing with O_2, at a fixed temperature. Prior to each set of measurements, samples were allowed to equilibrate with the new atmosphere for 5-15 min; separate measurements after different times

showed that this length of time was sufficient for samples to equilibrate. Previous impedance analysis at ~ 400 °C of similar samples identified the presence of bulk, grain boundary and electrode responses with decreasing frequency. Initially, the effect of pO_2 was studied around this temperature, but the impedance responses in for example, the Z* plane, Figure 5.1 or the log C' spectroscopic plot, Figure 5.2 did not show any variation with pO_2, indicating that at this temperature and pO_2 values, the samples were in the electrolytic domain.

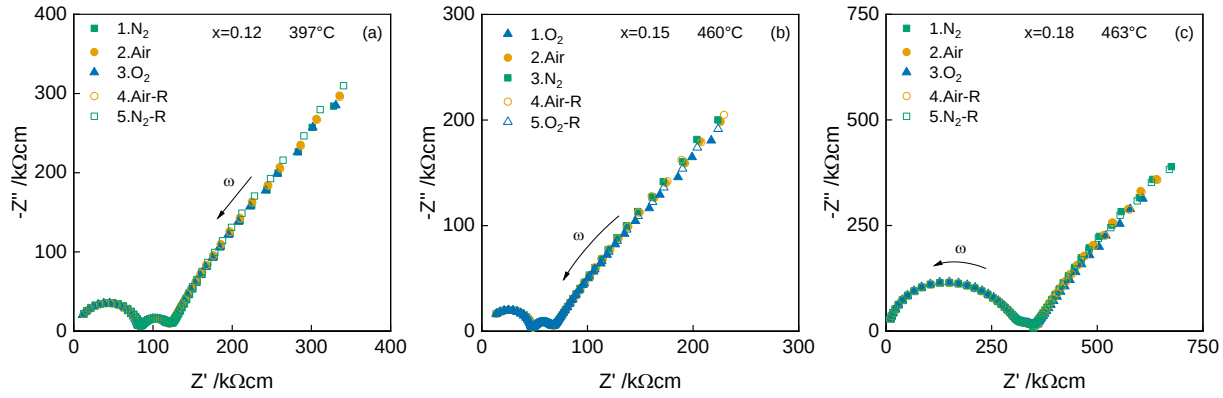

Figure 5.1. *Z* plane showing impedance response of CSZ x=0.12 (a), 0.15(b) and 0.18 (c) under different pO_2 at ~ 400 °C.*

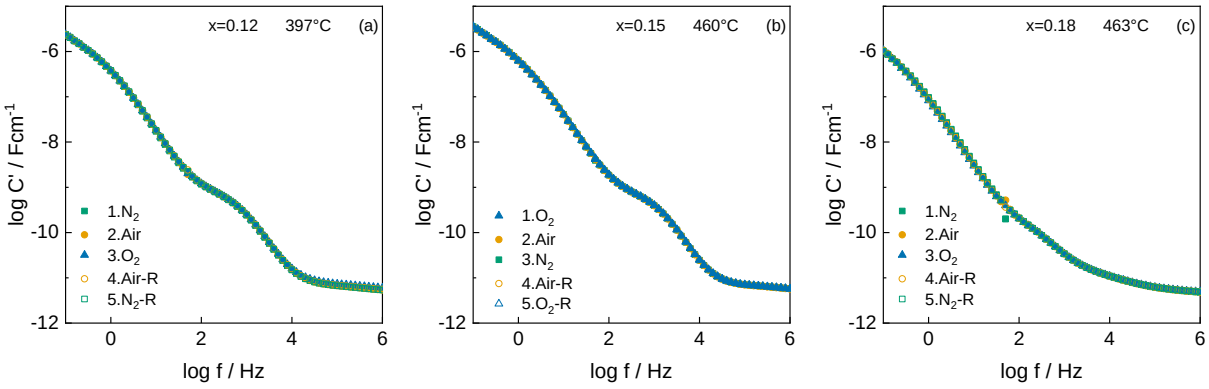

Figure 5.2. *Log C' spectroscopic for the data shown in Figure 5.1.*

To assess whether there was any change with temperature, similar impedance data sets were recorded at ~ 892-928 °C. At these temperatures, only the low frequency electrode response was seen, as a rather distorted arc, but the impedance data had two additional features at the frequency extremes, shown for one example in Fig 5.3. At the highest frequencies, an inductive effect was apparent, highlighted in blue, in both Z'' and C' data. At the lowest frequencies, the Z* plane showed an additional, poorly-resolved component, highlighted in green; this appeared as an additional dispersion in the log C' plot above 10^{-5} Fcm^{-1}.

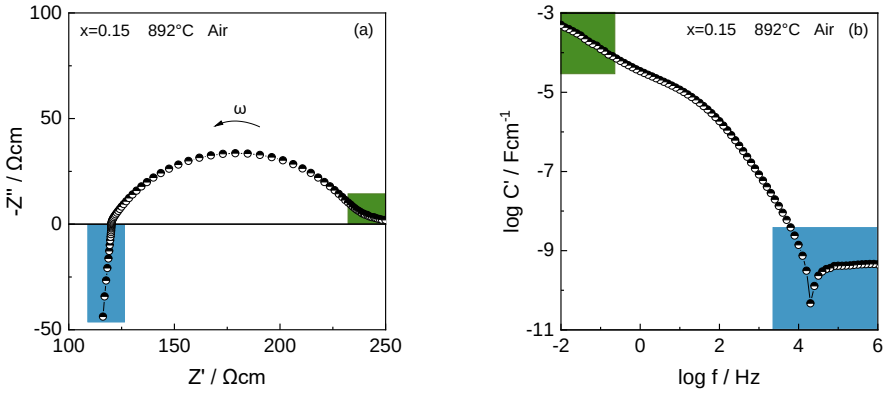

Figure 5.3. *Impedance response of CSZ x=0.15 at 892°C, showing inductive (blue) and possible electrochemical reactions (green) effects, which are out of the scope if this study.*

In addition to the extra effects at these temperatures, the electrode response was pO_2 dependent, Figure 5.4. The sample-electrode resistance increased with decreasing pO_2 for all three compositions, (a-c). However, the high frequency intercept with the real axis, related to the sample total resistance ($R_t = R_{bulk} + R_{grain\ boundary}$), had more complex pO_2 dependence, shown on expanded scale in (d-f). For x=0.12, the intercept shifted slightly to lower resistance with decreasing pO_2; with x=0.15, it remained essentially the same; with x=0.18, it shifted to higher resistance with decreasing pO_2. The log C' plots at this temperature, Figure 5.5, show that the capacitance of x= 0.12 and 0.18 decreased slightly with increasing pO_2 whereas that for x= 0.15 remained almost the same. As only one sample per composition was run at this temperature, repetition would be beneficial to confirm this behaviour.

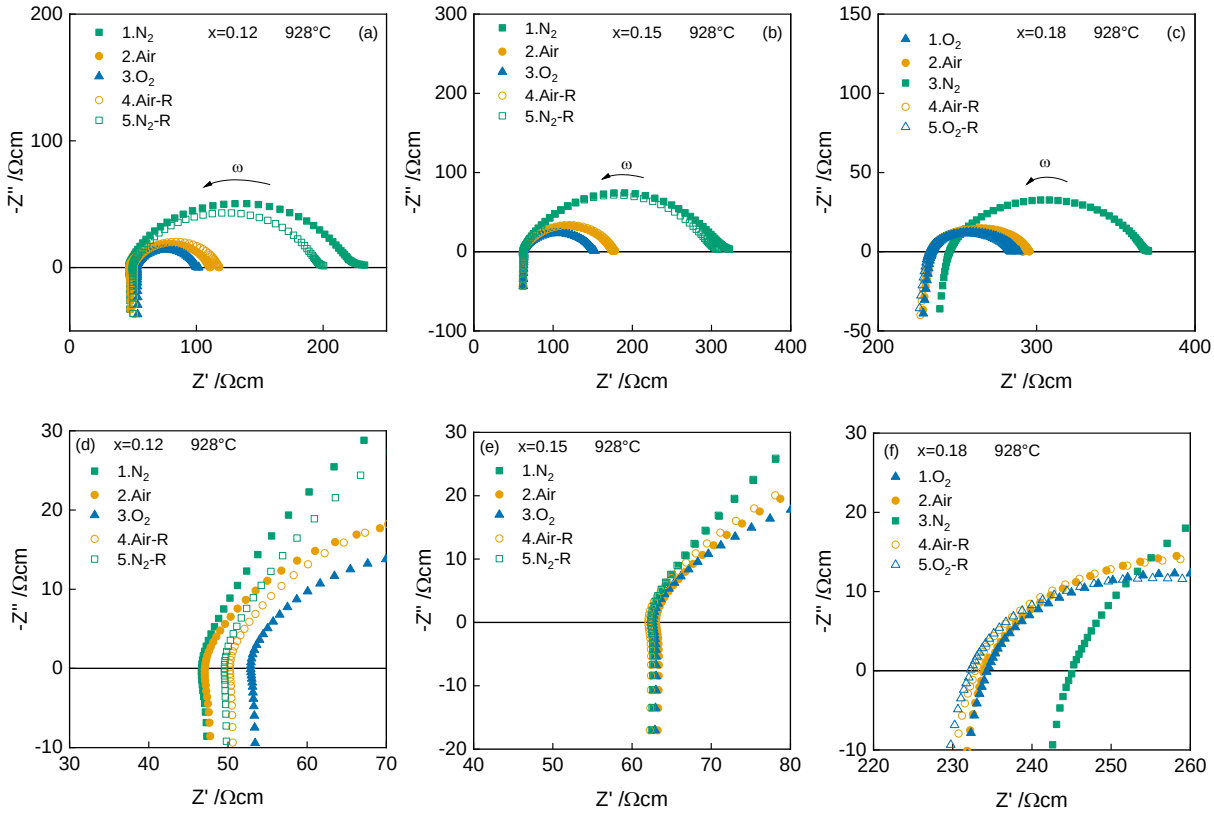

Figure 5.4. *Z* plane for x=0.12 (a)(d), 0.15(b)(e) and 0.18 (c)(f) under different pO_2 at ~ 930°C.*

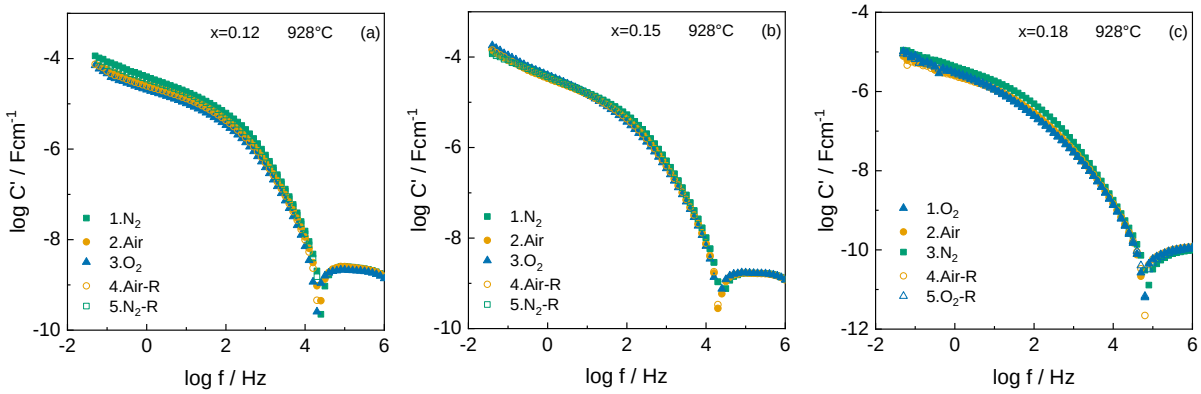

Figure 5.5. *Log C' plots for x=0.12 (a), 0.15(b) and 0.18 (c) under different pO_2 at ~ 930°C.*

The sample-electrode impedance response of x= 0.15 was fitted to several equivalent circuits in the previous chapter. The best fit was given by parallel element R_3C_3 in series with parallel element R_4CPE_4, inset Figure 5.6(a). In order to further investigate the effects of pO_2 and the inductance, equivalent circuit analysis was performed on the 928°C datasets, Figures 5.6, 5.7 and 5.8 for all three compositions. The values of the fitted circuit parameters are shown in Tables 5.1,5.2 and 5.3. The data points highlighted in green in Figure 5.3, were excluded from the fitting analysis as they appear to be related to electrochemical reactions which are beyond the scope of this project.

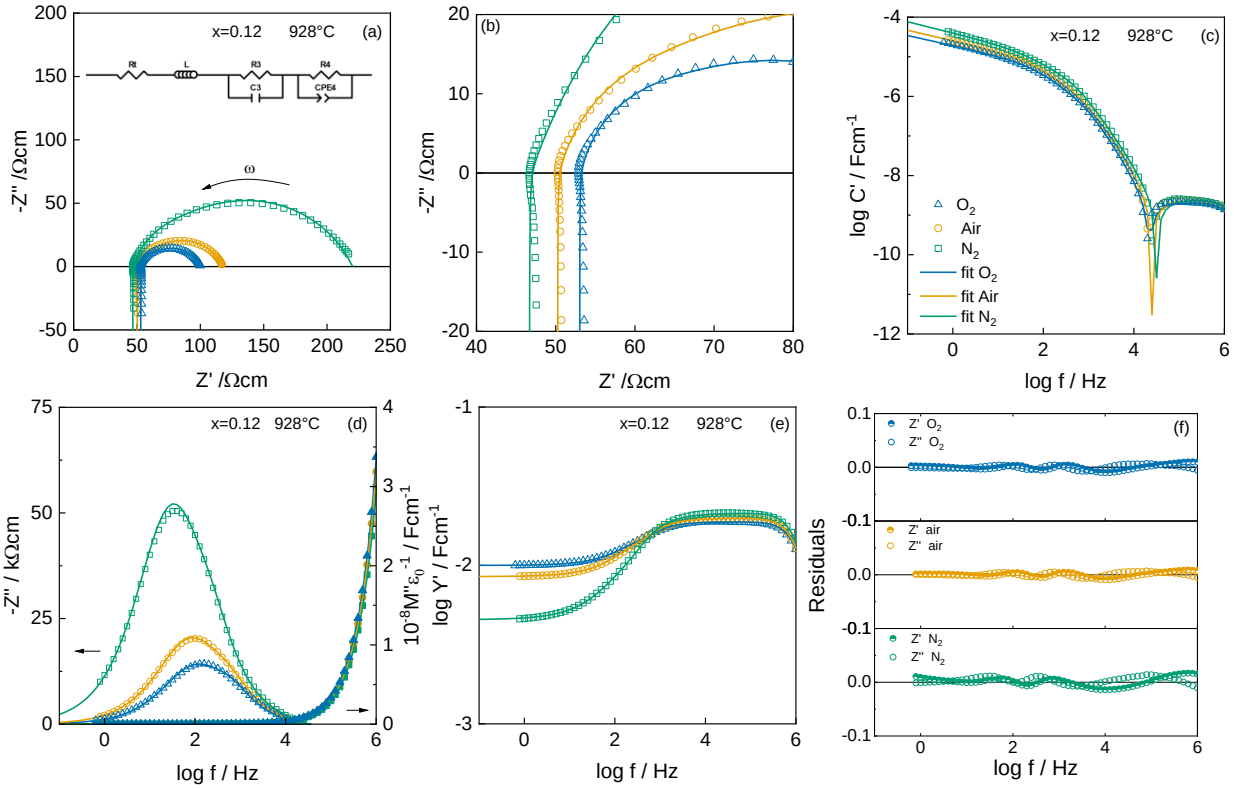

Figure 5.6. (a-e) *Impedance data (symbols) and fits (solid lines) for x=0.12 at 928°C under different atmospheres. (f) Residuals.*

Table 5.1. *Fitted impedance values for x=0.12 at 928°C, Figure 5.6a.*

ATM	Rt (Ωcm)	L (μHcm^{-1})	R_3=R_{ct} (Ωcm)	R_4 =R_{diff} (Ωcm)	C_3=C_{dl} (μFcm^{-1})	A_{04} = Z_W ($\mu Scm^{-1}rad^{-n}$)	n_4	$X^2(x10^{-5})$
O_2	53.01(6)	5.93(3)	8.1(7)	38.8(7)	30(3)	219(9)	0.747(8)	32.6
Air	50.22(5)	5.92(2)	8.1(6)	59.(7)	33(2)	177(5)	0.738(5)	23.7
N_2	46.65(8)	5.33(4)	15(1)	158(1)	42(3)	143(5)	0.720(5)	51.3

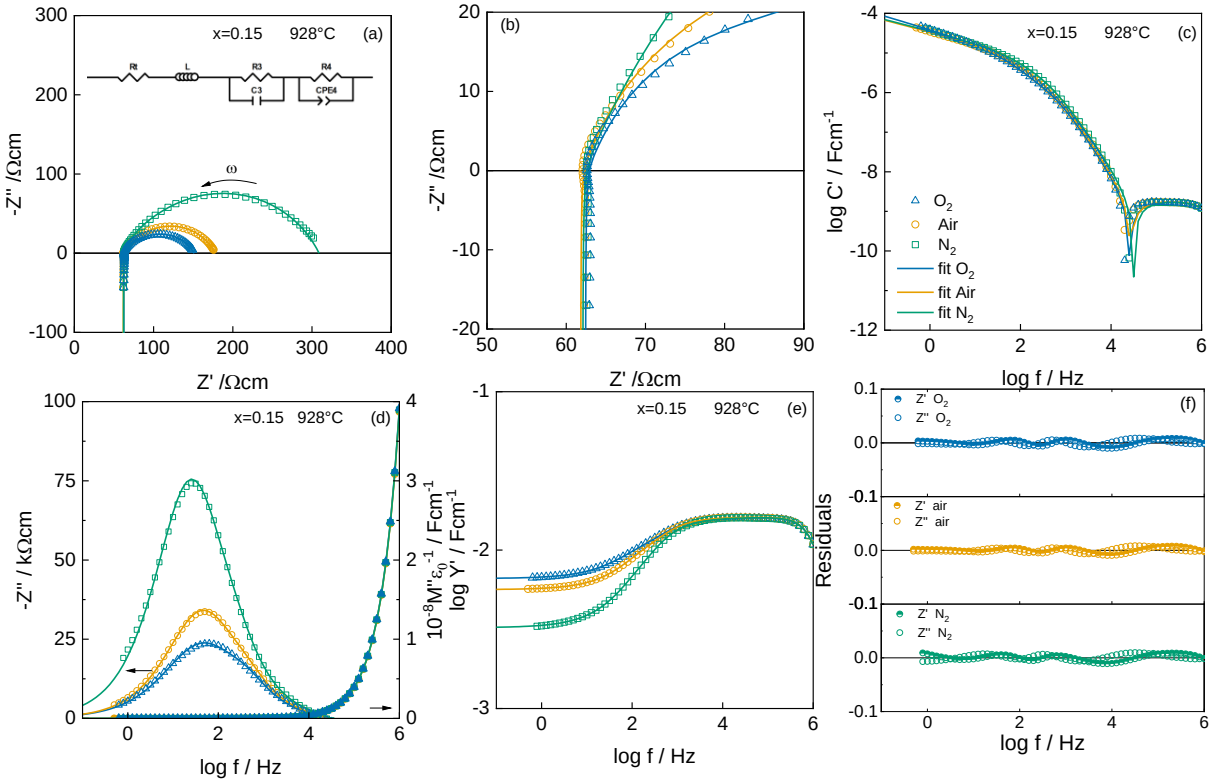

Figure 5.7. (a-e) *Impedance data (symbols) and fits (solid lines) for x=0.15 at 928°C under different atmospheres. (f) Residuals.*

Table 5.2. *Fitted impedance values for x=0.15 at 928°C, Figure 5.7a.*

ATM	Rt (Ωcm)	L (μHcm^{-1})	R_3=R_{ct} (Ωcm)	R_4 =R_{diff} (Ωcm)	C_3=C_{dl} (μFcm^{-1})	A_{04} = Z_W ($\mu Scm^{-1}rad^{-n}$)	n_4	X^2(x10^{-5})
O_2	62.37(7)	6.89(3)	9.2(6)	79.6(8)	38(3)	304(9)	0.665(5)	27.5
Air	61.78(6)	6.89(3)	7.5(6)	108.3(7)	46(4)	176(3)	0.703(4)	19.8
N_2	62.02(8)	6.92(4)	8.0(9)	238(1)	75(9)	113(2)	0.712(3)	24.1

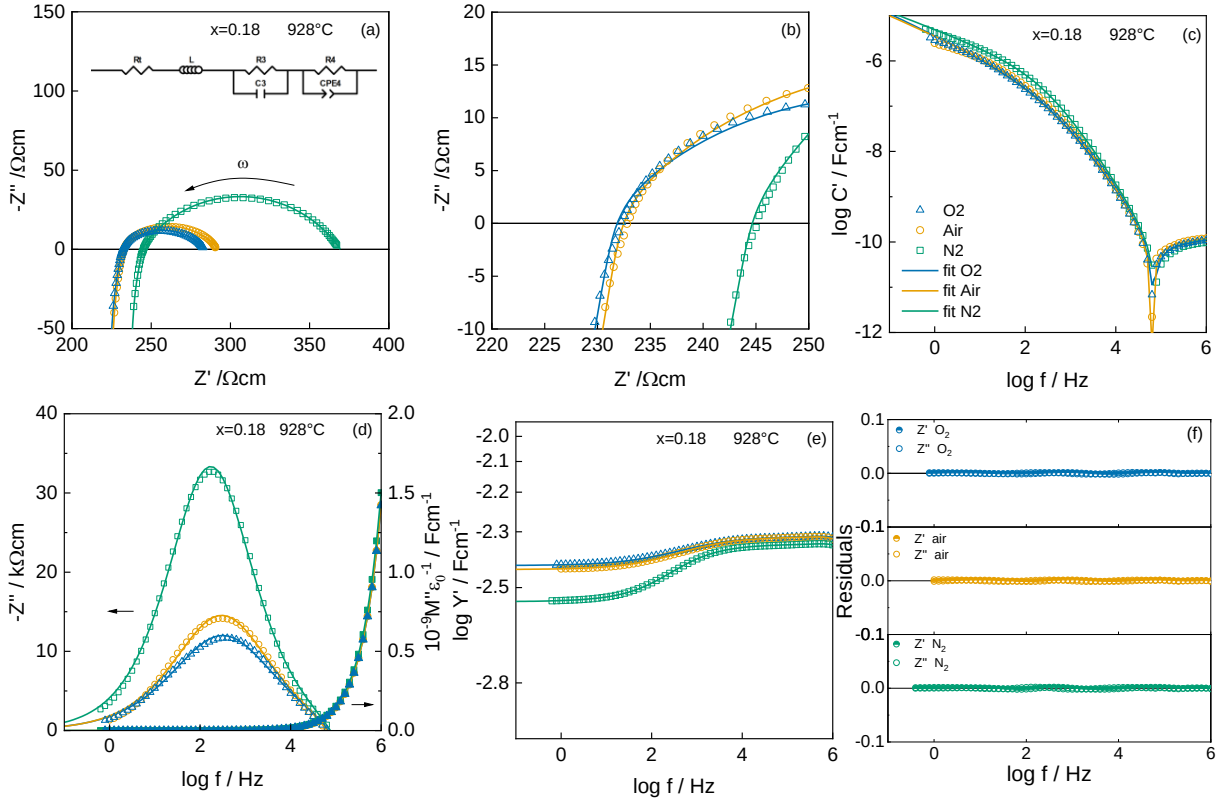

Figure 5.8. (a-e) *Impedance data (symbols) and fits (solid lines) for x=0.18 at 928°C under different atmospheres. (f) Residuals.*

Table 5.3. *Fitted impedance values for x=0.18 at 928°C, Figure 5.8a.*

ATM	Rt (Ωcm)	L (μHcm^{-1})	R_3=R_{ct} (Ωcm)	R_4 =R_{diff} (Ωcm)	C_3=C_{dl} ($nFcm^{-1}$)	A_{04} = Z_W ($\mu Scm^{-1}rad^{-n}$)	n_4	$X^2(x10^{-5})$
O_2	222(1)	6.37(8)	7.27(0.97)	54.2(2)	25(6)	330(6)	0.529(2)	4.67
Air	223.7(1)	7.01(3)	6.8(1)	61.96(17)	29(5)	237(4)	0.559(2)	4.65
N_2	236.2(9)	6.38(9)	6.8(9)	126.4(2)	30(7)	105(1)	0.618(1)	4.28

The main results from these fits are summarised as follows:
1.For all compositions, R_4 and C_3 increased and A_{04} decreased with decreasing pO_2.
2.With decreasing pO_2, R_3 increased for x=0.12, decreased for x=0.15 and remained the same for x=0.18.
3.The inductance, L, remained approximately the same with changing pO_2 for each composition.
4.With decreasing pO_2, R_t decreased for x=0.12, remained similar for x=0.15 and increased for x=0.18.

The sample-electrode impedance fitted an equivalent circuit with two elements, 3 and 4, in series, *ie* R_3C_3 and R_4CPE_4. Deconvolution of the fit for the Z" parameter of these two components is shown in Figure 5.9 (a) for x=0.12 at 928°C under O_2. Experimental data are shown together with the overall fit and the two components using the data in Table 5.1. This deconvolution allows comparison of the effect of pO_2 effect on element 3, (b) and 4, (c). The Z" peaks of both decrease in magnitude and shift to higher frequencies, illustrating the reduction in R_3 and R_4 with increasing pO_2.

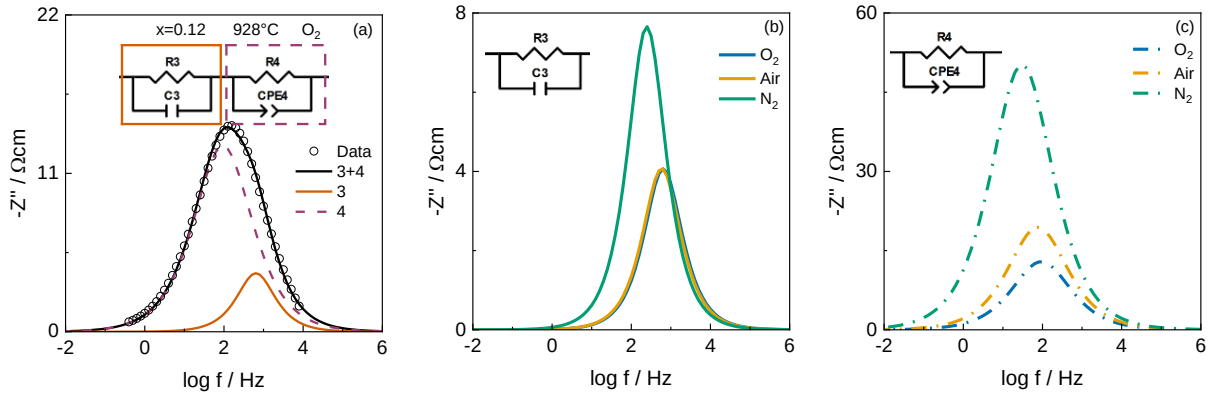

Figure 9. *Simulations using equivalent circuit in inset and fitting results from Table 5.1, presented as spectroscopic plots of -Z", showing the combined and deconvoluted response of component 3 and 4 (a), and the change of component 3(b) and 4(c) with pO_2.*

5.4 Discussion

5.4.1 pO_2 dependence

When the conductivity of an oxide ion conductor is independent of pO_2, it can be regarded to be in the electrolytic domain [1]. Therefore, in agreement with the literature [3], all three compositions near 400°C are in the electrolytic domain, as no change in the overall impedance response was observed with changing pO_2.

At higher temperature, above 900°C, the impedance response did vary with pO_2. The electrode-sample component is extrinsic to the overall measured impedance, as the interfacial roughness and electrode

porosity and thickness will generally vary from sample to sample, independent of sample composition. Although it was not possible to compare meaningfully the individual electrode responses of pellets with different composition, it was possible to compare the high frequency intercept on the Z' axis which is related to the sample total resistance, R_t, which it is related to the sum of the bulk and grain boundary.

Consequently, x= 0.12 shows the presence of n-type conductivity, as with higher pO_2, R_t increased, x=0.15 seems to be in the electrolytic domain, as R_t remained in the same position and x=0.18 showed introduction of p-type conductivity as R_t decreased with increasing pO_2. As previously mentioned, repetition of these experiments would benefit the confirmation of the results, and therefore their interpretation. However, in the spirit of an open discussion these results relate to the previously-reported *n*-type conductivity detection by emf [5] and the prediction of *p*-type conductivity in this system [6]. In addition, there is a similarity with yttria-stabilised zirconia, in the sense that for $Y_xZ_{1-x}O_{2-x/2}$ (YSZ), the conductivity of x=0.08 is pO_2 independent [19], but higher yttria content YSZ, x=0.4-0.7, shows *p*-type conductivity [20]. However, *n*-type conductivity is seen in YSZ only under strongly reducing conditions.

Thus, these results suggest that the upper and lower limits of the electrolytic domain of CSZ are dependent on both composition and temperature. With lower x, n-type conduction is promoted by oxygen loss following Eq 5.1. At higher x, p-type conduction arises by oxygen uptake, following Eq 5.2. The width of the electrolytic domain contracts markedly with increasing temperature and is essentially non-existent at 928ºC.

The holes in the *p*-type region are assumed to be localised on under-bonded oxygen ions near sample surfaces and in the vicinity of acceptor dopants. They form as the first step in dissociation of lattice oxide ions during oxygen uptake [21], similarly to the mechanism proposed in the case of high yttria content YSZ [22].

5.4.2 Electrode-sample response

The electrode-sample response was successfully fitted to the equivalent circuit shown in Figure 5.6(a), where R_3 is attributed to the charge transfer resistance (R_{ct}), C_3 to the double layer capacitance (C_{dl}), CPE_4 to a Warburg impedance (Z_W) representing diffusion of oxygen molecules towards and away from the sample-electrode interface and R_4 to the finite resistance of the Warburg impedance (R_{diff}).

With decreasing pO_2, the amount of oxygen in the atmosphere available to participate in charge transfer at the negative electrode decreases. As a result, the values of R_{ct} and and R_{diff} increase, as shown in Table 5.1. The double layer capacitance, C_{dl}, remains similar within errors under the three atmospheres, which indicates that the geometry of the region, was not altered by the change in pO_2. The microstructure of Pt electrodes over YSZ and its effects on interfacial impedance were investigated by impedance spectroscopy [12].

In this work, R_{ct} is lower than R_{diff}. This relationship has been observed previously where it was concluded that the rate limiting step in the electrode process was surface diffusion of dissociated oxygen molecules adsorbed on the platinum electrode towards the electrochemical reaction sites (ers) [7], [8]. The electrode conductivity arises from the electric current generated by Eq 5.3

$$1/2O_{2\,(ers)} + V_O^{\bullet\bullet}{}_{(YSZ)} + 2e'_{(Pt)} \rightarrow O_O^x{}_{(YSZ)} \qquad (5.3)$$

When the electrode conductivity was plotted as a function of pO_2, Figure 5.10, it was observed that at 900°C the conductivity increased with pO_2, but with decreasing the temperature, the curve increased up to a maximum, followed by a decrease, with increasing pO_2. In addition, these maxima shifted to lower pO_2,

with decreasing temperature. Equation 5.1 and 5.2, might occurred simultaneously, however these results might suggest that when the electrode conductivity increases, equation 5.1 dominates and when it decreases equation 5.2 becomes dominant. Which could confirm the possibility of the presence of n- or p-type conduction in addition to the oxide ion and its interaction with the electrode response.

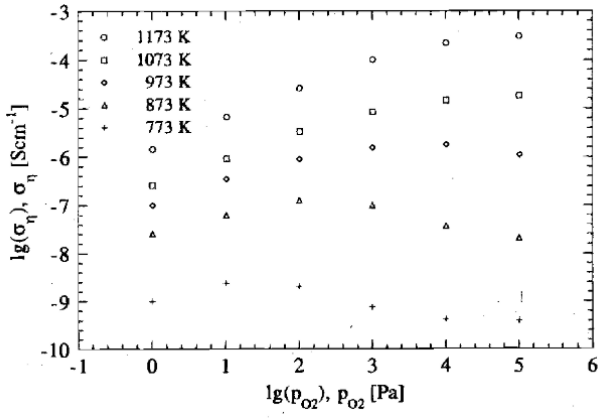

Figure 5.10. *Electrode conductivity of O_2\|Pt\|YSZ as function of pO_2 at different temperatures. From Fig 5 in ref* [7].

5.5 Conclusions

The pO_2 dependence of CSZ ceramics with composition x=0.12, 0.15 and 0.18 was analysed by impedance spectroscopy. The resistance of all the compositions remain independent of pO_2 around 400°C, indicating that with those conditions they remain within the electrolytic domain. At higher temperatures, near 930°C, CSZ x=0.12 showed introduction of n-type conduction, x=0.18 of p-type and x=0.15 did not show pO_2 dependence. These preliminary results might lead to the conclusion that the limits of the electrolytic domain vary with temperature and composition.

The electrode response was fitted to a parallel R_{ct}-C_{dl} element in series with a parallel R_{diff}-CPE_{zw} element. Representing the charge transfer resistance (R_{ct}), double layer capacitance (C_{dl}), diffusion processes model as a Warburg impedance using a CPE (CPE_{zw}) with a finite resistance (R_{diff}). R_{ct} and R_{diff} were deconvoluted from the total electrode response, and it was found that $R_{ct} << R_{diff}$.

Regarding the pO_2 dependence of the electrode response both R_{ct} and R_{diff} increase with decreasing pO_2, presumably related with the reduction in availability of molecular oxygen to take part in charge transfer reactions.

5.6 References

[1] A. R. West, *Solid State Chemistry and its Applications*, Second Edi. Wiley, 2014.

[2] F. Hund, "Die Fluoritphase im System ZrO_2—CaO," *Zeitschrift für Phys. Chemie*, vol. 199, no. 1, p. 142, 1952.

[3] K. Kiukkola and C. Wagner, "Measurements on galvanic cells involving solid electrolytes," *J. Electrochem. Soc.*, vol. 104, no. 6, pp. 379–387, 1957.

[4] T. H. Etsell and S. N. Flengas, "The electrical properties of solid oxide electrolytes," *Chem. Rev.*, vol. 70, no. 3, pp. 339–376, 1970.

[5] T. H. Etsell and S. N. Flengas, "N-type conductivity in stabilized zirconia solid electrolytes," *J. Electrochem. Soc.*, vol. 119, no. 1, pp. 1–7, 1972.

[6] F. A. Kröger, “Electronic conductivity of calcia-stabilized zirconia,” *J. Am. Ceram. Soc.*, vol. 49, no. 4, pp. 215–218, 1966.

[7] C. Schwandt and W. Weppner, “Electrode reactions at oxygen, noble metal / stabilized zirconia interfaces,” *Ionics (Kiel).*, vol. 2, no. 2, pp. 113–122, 1996.

[8] C. Schwandt and W. Weppner, “Kinetics of oxygen, platinum/stabilized zirconia and oxygen, gold/stabilized zirconia electrodes under equilibrium conditions,” *J. Electrochem. Soc.*, vol. 144, no. 11, pp. 3728–3738, 1997.

[9] A. Nasser-Eddine, B. Huard, J. D. Gabano, and T. Poinot, “A two steps method for electrochemical impedance modeling using fractional order system in time and frequency domains,” *Control Eng. Pract.*, vol. 86, pp. 96–104, May 2019.

[10] T. Q. Nguyen and C. Breitkopf, “Determination of Diffusion Coefficients Using Impedance Spectroscopy Data,” *J. Electrochem. Soc.*, vol. 165, no. 14, pp. E826–E831, 2018.

[11] C. Schwandt and W. Weppner, “Variation of the oxygen exchange rate of zirconia-based electrodes by electrochemical pretreatment,” *Solid State Ionics*, vol. 112, no. 3–4, pp. 229–236, 1998.

[12] K. Sakurai, H. Nagamoto, and H. Inoue, “Microstructure of Pt electrodes over solid-electrolyte and its effects on interfacial impedance,” *Solid State Ionics*, vol. 35, no. 3–4, pp. 405–410, 1989.

[13] N. Nakagawa, C. Kuroda, and M. Ishida, “A new equivalent circuit for Pt/YSZ of a solid oxide electrolyte fuel cell: Relation between the model parameters and the interface characteristics,” *Solid State Ionics*, vol. 40–41, no. PART 1, pp. 411–414, 1990.

[14] P. Tomczyk and M. Mosialek, “Investigation of the oxygen electrode reaction in basic molten carbonates using electrochemical impedance spectroscopy,” *Electrochim. Acta*, vol. 46, no. 19, pp. 3023–3032, 2001.

[15] A. Sacco, “Electrochemical impedance spectroscopy as a tool to investigate the electroreduction of carbon dioxide: A short review,” *J. CO_2 Util.*, vol. 27, pp. 22–31, Oct. 2018.

[16] A. A. Moya, “Identification of characteristic time constants in the initial dynamic response of electric double layer capacitors from high-frequency electrochemical impedance,” *J. Power Sources*, vol. 397, pp. 124–133, Sep. 2018.

[17] A. Lasia, “Impedance of porous electrodes,” *J. Electroanal. Chem.*, vol. 397, no. 1–2, pp. 27–33, 1995.

[18] P. Kurzweil and H. J. Fischle, “A new monitoring method for electrochemical aggregates by impedance spectroscopy,” *J. Power Sources*, vol. 127, no. 1–2, pp. 331–340, 2004.

[19] J.-H. Park and R. N. Blumenthal, “Electronic Transport in 8 Mole Percent Y_2O_3-ZrO_2,” *J. Electrochem. Soc.*, vol. 136, no. 10, p. 2867, 1989.

[20] M. Jovaní, H. Beltrán-Mir, E. Cordoncillo, and A. R. West, “Atmosphere- and voltage-dependent electronic conductivity of oxide-ion-conducting $Zr_{1-x}Y_xO_{2-x/2}$ ceramics,” *Inorg. Chem.*, vol. 56, no. 12, pp. 7081–7088, 2017.

[21] R. A. De Souza, “A universal empirical expression for the isotope surface exchange coefficients (k*) of acceptor-doped perovskite and fluorite oxides,” *Phys. Chem. Chem. Phys.*, vol. 8, no. 7, p. 890, 2006.

[22] X. Vendrell and A. R. West, “Induced p-type semiconductivity in yttria-stabilized zirconia,” *J. Am. Ceram. Soc.*, vol. 102, no. 10, pp. 6100–6106, Oct. 2019.

CHAPTER 6
Electrical properties of calcia-stabilised zirconia ceramics: *dc* bias effect

6.1 Introduction

Cubic calcia-stabilised zirconia (CSZ) is a well-known oxide ion conductor [1]. The limits of its electrolytic domain have been studied, evidence of n-type conduction at low pO_2 was detected [2] by emf measurements, and the possibility of p-type conduction has been theoretically predicted at very high pO_2 [3]. The previous chapter showed an attempt to present experimental evidence of these transitions.

The transition from ionic to mixed electronic-ionic conduction in cubic zirconias has being explored by changing the measurement conditions. Samples of 8mol% yttria-stabilised zirconia (YSZ) showed a decrease in resistance, correlated with the decrease in ionic transport number, with the application of a small *dc* bias (1-20V or 5-100Vcm^{-1}) across the sample at 566°C [4]. High yttria content zirconia ($Zr_{1-x}Y_xO_{2-x/2}$; x=0.4-0.7) has shown pO_2- and *dc*- bias dependence with decreasing resistance under high pO_2 and increasing voltage, around 750°C and 800°C [5]. Later, it was confirmed that the increase in conductivity was related to introduction of p-type conductivity [6] by the application of voltage under different atmospheres, as the decrease in resistance was more pronounced with increasing voltage under oxygen than under nitrogen. The creation of a *p-n* junction was detected in 10mol% YSZ [7] by using N_2/Ag and air/Pt electrodes and applying less than 2.23V between 700 to 900°C and also in $Y_{0.5}Zr_{0.5-x}Mg_xO_{1.75-x}$, with x = 0.01 [8] by applying more than 2V under N_2 at 800°C. In addition, the possible reactions and charged species leading to the formation of a *p-i-n* junction as a consequence of the application of a *dc* bias to YSZ between blocking electrodes has been explored [9].

The resistance of CSZ has also been shown to be voltage-dependent. Samples with composition $Ca_{0.15}Zr_{0.85}O_{1.85}$ in a symmetrical cell set-up with oxygen pressures ranging from 1 to 10−20 atm, under the application of voltages from 0-6V at 560°C showed two regimes, attributed to different rate-limiting steps [10] . Below 2V the resistance varied with pO_2, associated with the oxygen diffusion through the Pt electrode. At higher voltages, above 2V, no pO_2 dependence was observed. Blackening from cathode to anode on glass-encapsulated 10mol% CSZ samples, was detected during the application of 10 to 500 V at 500°C [11]. The blackened front moved faster with increasing voltage and was attributed to electrochemical reduction. It was also observed that the blackened zirconia showed higher conductivity than the original.

A sudden increase in conductivity is also characteristic of flash sintering [12]–[14]. This technique allows the densification of a green body within less than a minute, combining the application of an electric field with heat. Prior to the "flash event", which is characterised by the presence of densification, luminescence and an abrupt increase in conductivity, an incubation time is required. It has been envisaged that this time, which might depend on the length of the sample and the magnitude of the applied electric field, is required to change the concentration of charged species generated and/or consumed by internal reactions [15]. Also, the transition from blocking to non-blocking Pt electrodes on a single crystal YSZ sample, was observed during the incubation time of flash sintering between 300 to 700°C [16]. These results imply the introduction of electronic conductivity during this period.

Regarding the electrical properties of flash sintered samples, 8 mol% YSZ showed an increase in ionic conductivity, after flash and removal of the applied voltage [17]. Flashed samples with different current density limits were compared to conventional sintered samples. An increment in the bulk and grain boundary conductivity was observed with increasing current density limit. The enhanced ionic conductivity was attributed to an unknown change in the defect structure of the material, leading to an increase in the concentration of mobile charges, and not associated with microstructural changes.

Voltage effects in oxide ion conductors are in need of further study. Therefore, the work reported in this chapter analyses the impedance response of CSZ samples during and after the application a range of electric fields. The temperature, voltage hold time and cooling rate were used as variables to identify changes in the electrical properties of the samples.

6.2 Experimental

Electroded pellets with composition $Ca_xZr_{1-x}O_{2-x}$: x= 0.12, 0.15, 0.18 and densities ~93%, were prepared following the procedure described in chapter 4. Impedance measurements were taken between 350 and 850°C using two impedance analysers: a Modulab XM MTS (measurement accuracy ±0.1%) frequency range 100mHz-1MHz and an Agilent Agilent 4294A (measurement accuracy ±0.08%) frequency range 40Hz-1MHz, with a nominal ac voltage of 100 mV in both cases. In some cases, a *dc* bias in the range 0.5-42.5 V was applied across samples, at the same time as impedance data were recorded.

For the *dc* bias and temperature cut-off, two profiles were used, Figure 6.1. The aim of profile 1 was to register the recovery of the sample after the application of voltage. Therefore, impedance measurements were taken after the voltage cut off, keeping a constant temperature. Profile 2 aimed to freeze the sample state during the voltage application. Thus, the sample was taken out of the furnace and compressed air at room temperature was purged directly to the sample, whilst the voltage was still applied. After this the voltage was turned off.

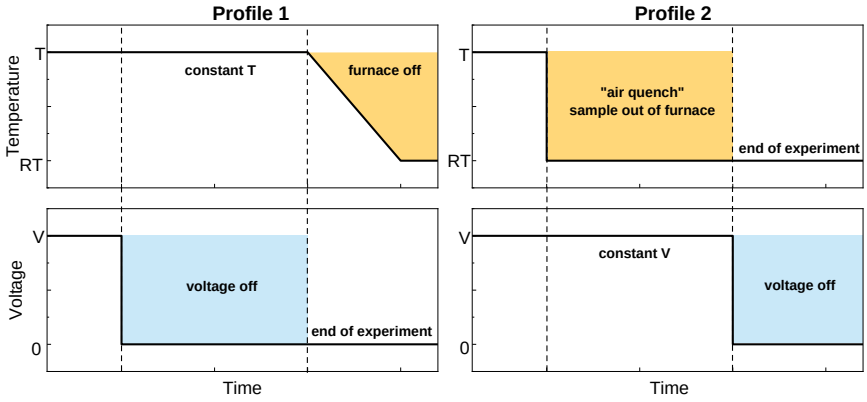

Figure 6.1. *Temperature and dc bias cut-off profiles.*

Two sets of corrections were made to the collected data: (i) a geometric factor consisting of pellet thickness and sample-electrode contact area and (ii) jig impedance characteristics consisting of the blank, open circuit capacitance, typically 6 pF and the closed circuit resistance of, primarily, the leads, 1-2 Ω. Data analysis was performed using ZVIEW software (ZVIEW-Impedance Software version 2.4 Scribner Associates).

6.3 Results

6.3.1 Comparison of the 3 compositions

Based on chapter 4, it was established that the bulk, grain boundary and sample-electrode interface impedance responses are visible in the frequency range 100mHz-1MHz between 350-440°C, for $Ca_xZr_{1-x}O_{2-x}$: x= 0.12, 0.15, 0.18. Therefore, this temperature range was chosen to compare the response of the three compositions to *dc* bias. Prior to voltage application, and to be able to observe changes in conductivity, a similar value for the total resistance R_t (R_b + R_{gb}) was chosen as ~ 780kΩcm. As a result, the temperature required to reach this value was 358°C for x=0.12, 391°C for x=0.15 and 436°C for x=0.18.

A comparison of the impedance response of x= 0.12, 0.15 and 0.18 during the application of 0.5 to 8 V, is shown in Figure 6.2. The bulk response was not altered by the *dc* bias, in any of the three cases, as its resistance, capacitance and M'' peak did not change. The grain boundary resistance decreased with increasing voltage. The change in size of the Z'' peak with *dc* bias appears to be least for x=0.15.

The largest change in the overall impedance response was given by the sample-electrode interface for all three samples. Nevertheless, it is not possible to make a quantitative compositional comparison of the electrode response as its properties are extrinsic to the material. The porosity, roughness and thickness of the interface varies from sample to sample, which may be reflected in the shape and magnitude of the arc in the Z* plane. However, a similar trend is observed in the three samples with increasing voltage and can be related to be the effect of *dc* bias. In particular, the decrease of R_{el} is substantial at 8V it was no longer visible in the Z* plane, and a decrease of the low frequency dispersion from 10^{-7} to 10^{-9} Fcm^{-1} is seen in the log C' plot. From this analysis it was concluded that the overall dc resistance of the sample decreases due to decrease of R_{el}.

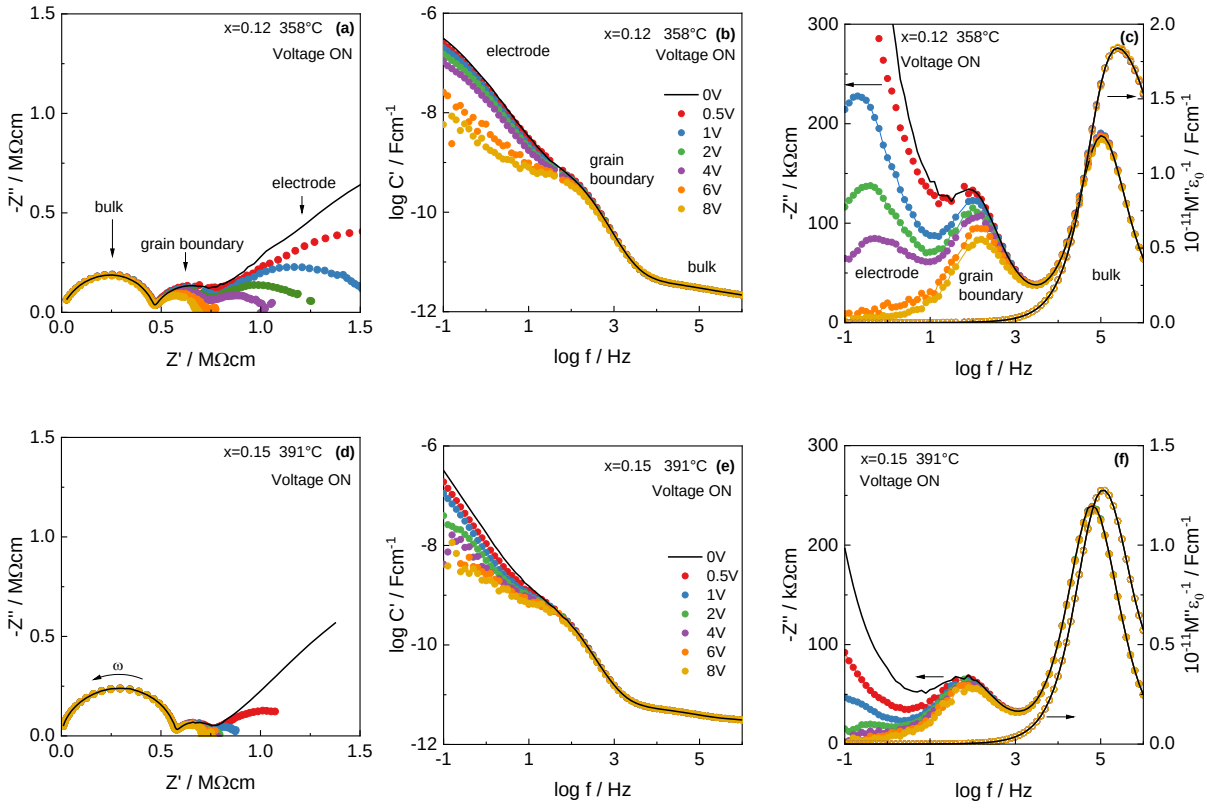

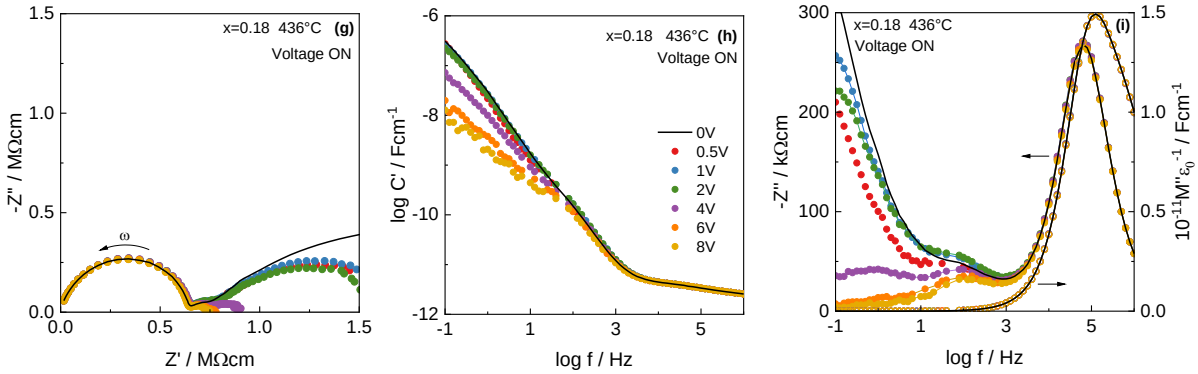

Figure 6.2. *Change in the impedance response under the application of 0.5-8 V on CSZ x=0.12 (a-c), 0.15 (d-f) and 0.18 (g-i); corresponding sample thickness of 1.02mm, 1.03mm and 1.13mm.*

To find out if the *dc* bias effect was reversible, 3 impedance responses at 0V were compared: (i) the initial impedance before the voltage steps, (ii) the final impedance right after the voltage cut off, and (iii)10 minutes after the voltage cut off, Figure 6.3. The Z* plot (a) shows that the grain boundary resistance recovered the initial state after 10 minutes of the voltage cut off, and the log C' plot (b) shows that the initial capacitance was recovered right after the voltage cut off. The impedance of the sample-electrode interface, moved towards the initial state upon removing the voltage; however, longer times were required to recover the initial state completely.

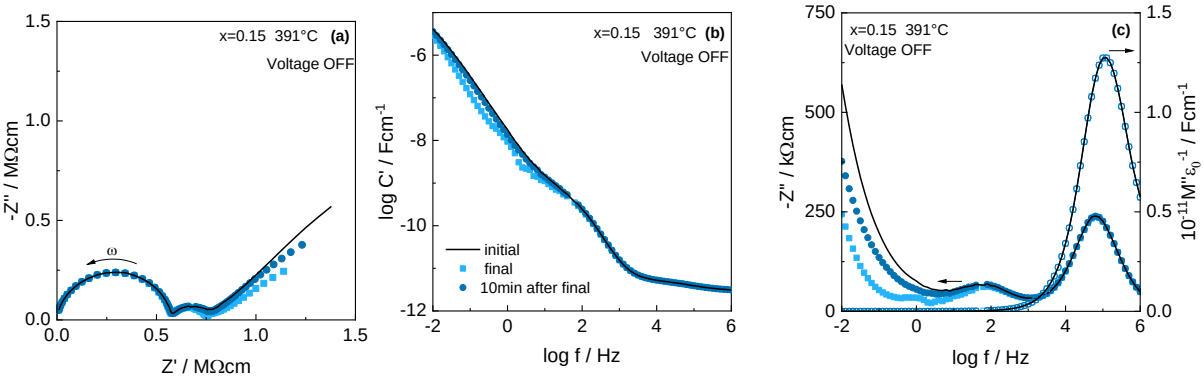

Figure 6.3. *Impedance response of x=0.5 at 0V, before and after the voltage application.*

6.3.2 CSZ x=0.15 at intermediate temperatures and bias voltages

A different impedance analyser was used for this study; as a consequence, the frequency range changed due to the instrument limitations. A sequence of 30 minutes of applied voltage followed by 30 minutes of recovery at 0V, with voltage steps from 4.1 to 16.5 V (corresponding to 25 to 100 Vcm^{-1}) at 518°C was applied, Figure 6.4. The Z* plane (a) shows that R_b, R_{gb} and R_{el} all decreased with *dc* bias. The log C' plot (b) shows that C_b and C_{gb} do not changed, but C_{el} dropped with V increasing from 0 to 25V/cm. Figure 6.4 (d), that changes to R_t were reversible after a recovery of 30 min.

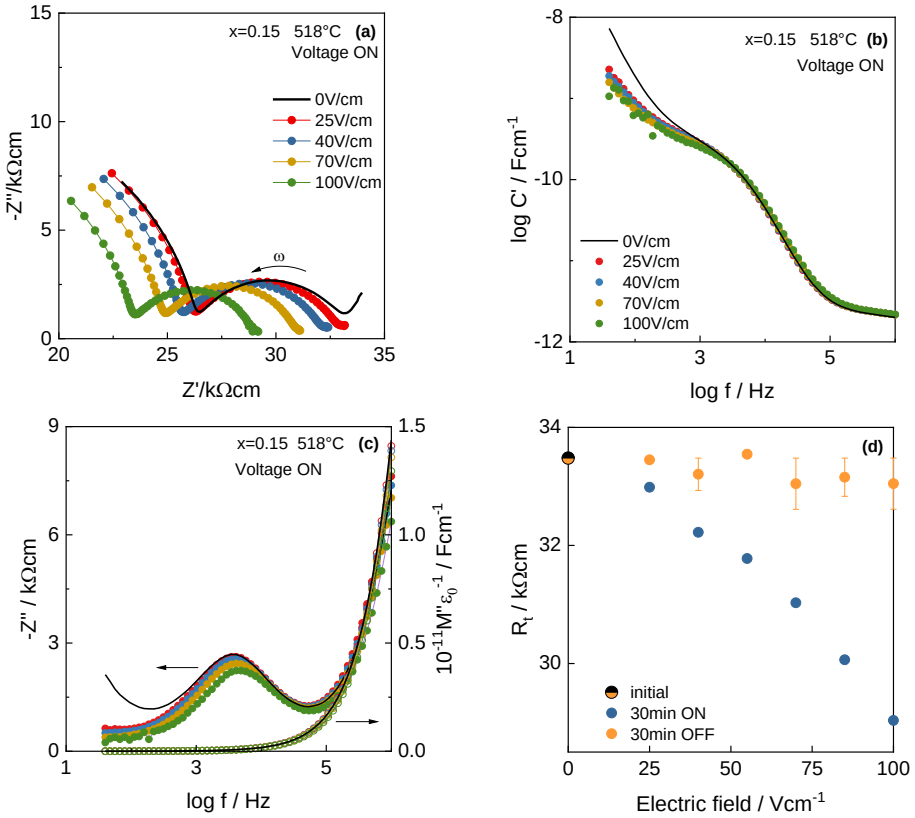

Figure 6.4. *(a-c) Impedance response of x=0.15 at 518°C after 30 minutes of applied voltage sample. (d) Total resistance as function of electric field, after 30 minutes of applied voltage and from voltage cut off. Sample thickness: 1.65mm*

On voltage application and removal, the main changes occurred within the first minute. Figure 6.5 shows the impedance evolution of x=0.15 under 55Vcm^{-1}, ON (a)-(c), and OFF (d)-(f). During the ON state R_t decreased by ~2kΩcm after 1 minute and by an additional ~300Ωcm after 30 minutes. The log C' (b) and M'' (c) plots did not show any change after the first minute of applied voltage. Similar behaviour was observed during the OFF state.

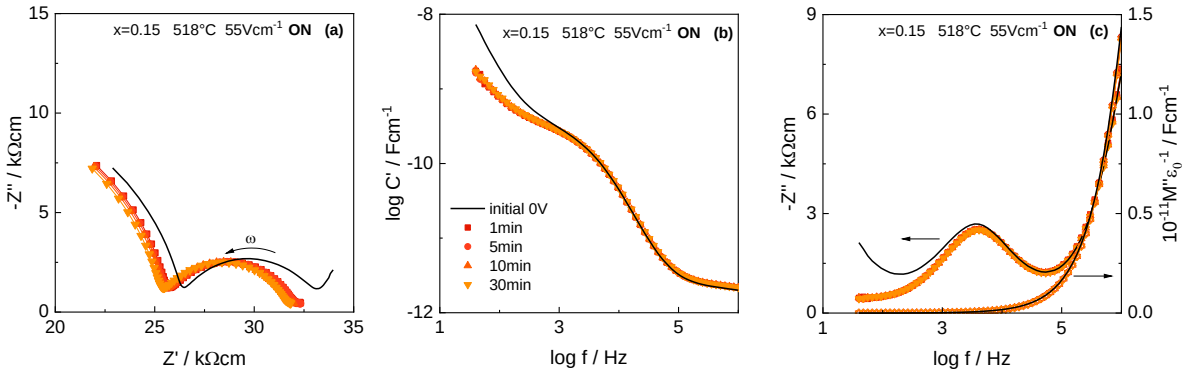

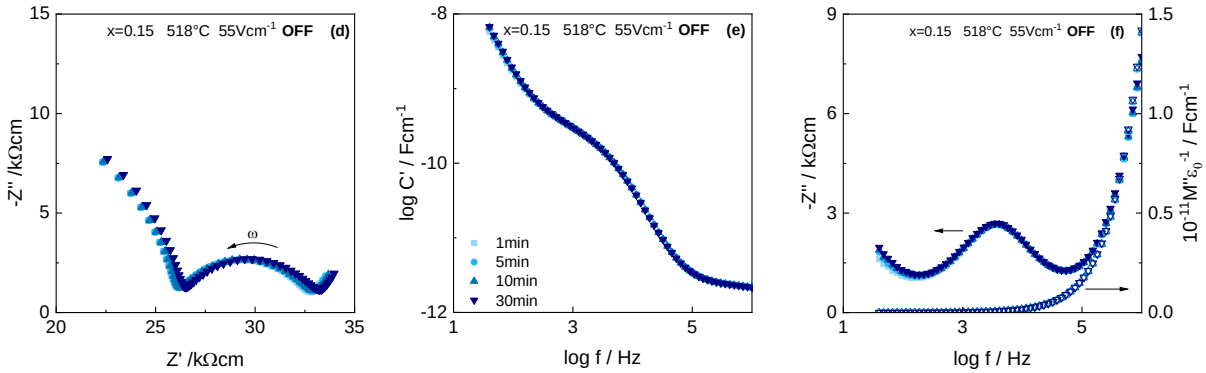

Figure 6.5. *Time dependence of the impedance response of x=0.15 at 518°C during the application (a-c) and removal (d-f) of 55Vcm^{-1}. Sample thickness 1.65mm.*

6.3.3 Combined effect of pO_2 and voltage

In order to find out if the *dc* bias effect is dependent on pO_2, N_2, dry air and O_2 were purged over a sample with x=0.15 during the application of 0 to 25V. Prior to the voltage application, preliminary impedance measurements were taken under different atmospheres with the furnace temperature fixed. However, the temperature reading from the thermocouple placed near the sample varied by a couple of degrees depending on the purge gas. This might be related to the location of the gas tanks and their exposure to weather conditions and/or to the manual adjustment of the flow rate and gas pressure. To eliminate any effect due to variation of temperature, the initial value of R_t at 0V was subtracted from all of the measurements; therefore Figure 6.6 shows the normalised change of R_t, in blue. From these plots it can be observed that the voltage effect is independent of pO_2 for this composition.

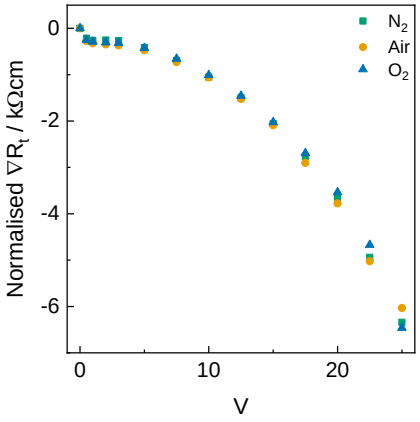

Figure 6.6. *Normalised change in total resistance of CSZ x=0.15 with voltage application at ~ 600°C. Sample thickness 1.03mm.*

6.3.4 Change in impedance depending on the time of exposure to a large voltage at high temperature

A sample of composition x=0.15 was subjected to an "ON (25V) and OFF (0V)" cycle at 721°C, Figure 6.7. The "ON" state dwell times at 25V were: 10s, 30s, 1 min, 10 min, 30min, 1h and 2h, and impedance measurements were taken during voltage application after the completion of each time segment. The "OFF" state at 0V were 6 min after the short "ON" states and 12 min after the long "ON" state; impedance measurements were taken every minute during these recovery segments.

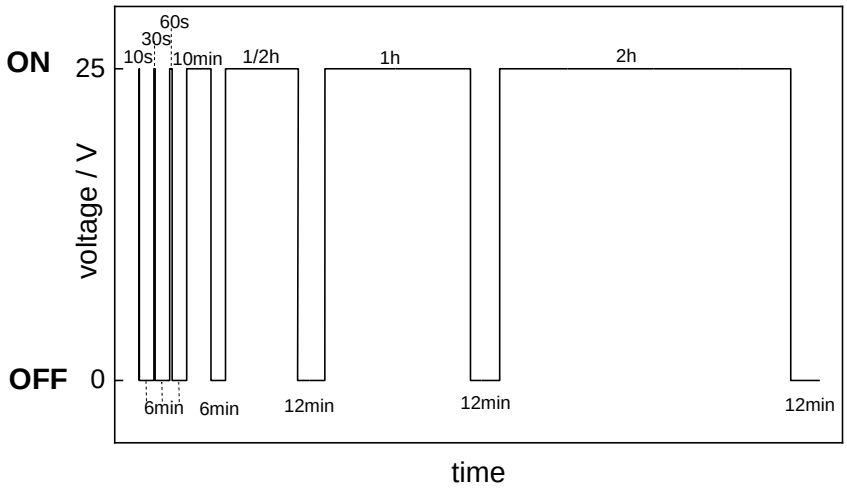

Figure 6.7. *Voltage application profile for sample x=0.15 at 721°C.*

Figure 6.8 shows a comparison of 5 impedance responses at 721°C. The response during the application of 25V after 30 min and 2h, with their corresponding response after 12min of voltage cut off is shown. As reference, the initial impedance response at 0V is shown as a black line. Before describing the voltage effect, note that above 700°C the impedance response shows an inductive effect at high frequencies. This is shown on the Z* plane (a) as a tail that drops to negative values and on the log C' plot (b) as a disruptive inverted peak.

The initial response at 0V shows, from high to low frequencies, in the C' plot (b), an inductive effect, grain boundary and electrode response. On application of 25V for 30min and 2h, the Z* plane (a) shows that the impedance is lowest after 30min of voltage application, and the log C' plot (b) shows that the response is dominated by the inductive effect. On removal of the voltage after 30 min, Z* and C' plots (a,b) showed recovery of the initial state. After 2h with an applied voltage, the resistance in the "ON" state increased from ~200 to ~300Ωcm. During the "OFF" state, Z* (a) shows part of an arc with a resistance of ~15M Ωcm, which is ~ 4 orders of magnitude larger than the initial state, and the log C' plot a high frequency plateau of a couple of pFcm^{-1}; which resembles the bulk response at low temperatures (~ 300°C).

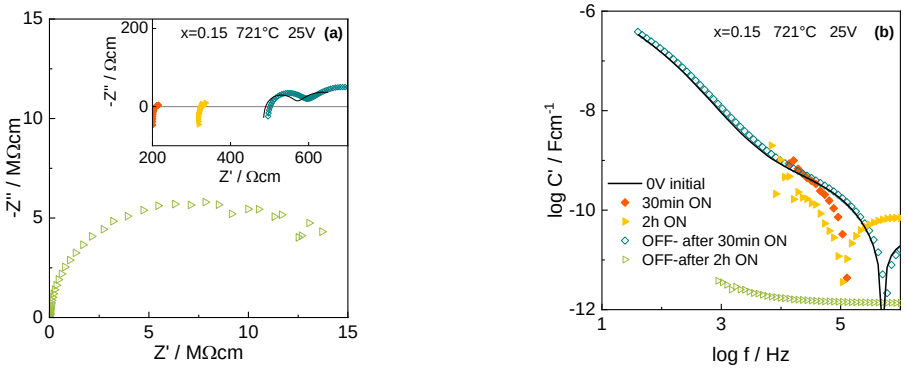

Figure 6.8. *Impedance response of x=0.15 at 721°C, during the application of 25V for 30 min (orange) and 2h (yellow), and after the 30 minutes from the voltage cut off, from 30min (aqua) and 2h (green)of voltage application. Sample thickness 1.03mm.*

Two new pellets with composition x=0.15, were used as sacrificial samples to observe the microstructure near the positive and negative electrodes after applying 25V for 30min and 2h at 720°C. Figure 6.9 (a)-(b) shows the fracture surfaces and EDX mapping, after 30min of applied voltage, and (c)-(d) after 2h. A good sample-electrode contact can be observed for both electrodes after 30min of voltage application, (a)-(b), and in the negative electrode after 2h of voltage application (d). However, the positive electrode presents delamination (c) and Figure 6.S1. For all cases, EDX maps showed an even distribution of Zr, minor traces of Ca segregation around some pores, and the location of the Pt paste.

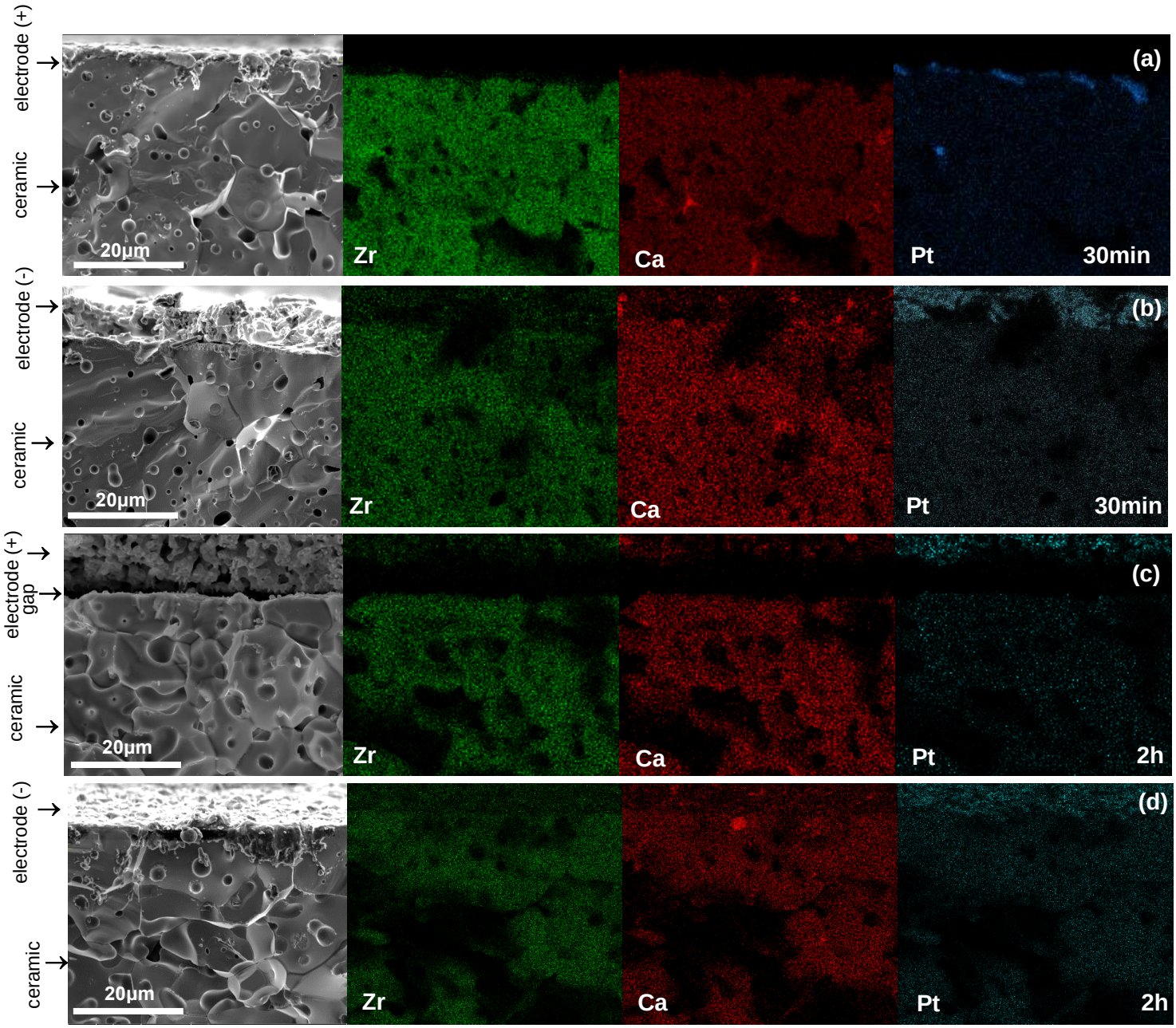

Figure 6.9. *Micrographs of fracture surface near the electrodes of sacrificial samples of CSZ x=0.15 after being subjected to 25V for 30 min and 2h at 720°C*

An impedance summary of the sample with composition x=0.15 that was subjected to the "ON and OFF" cycling of Figure 6.7 and 6.8, is shown in Figure 6.10. Figure 6.10 (a) shows the initial total resistance R_t at 0V, and how it changes during the voltage application under the different dwell times. R_t decreases with increasing time up to 30min, but then starts to increase (a). The response of R_t during each "OFF" state is shown in Figure 6.10 (b) on a logarithmic scale and a zoom of the dotted region is presented in (c) on a linear scale. Figure 6.10 (b) shows that R_t increased by ~2 orders of magnitude after holding 25V for 1h, and ~ 4 orders of magnitude after 2h. Figure 6.10 (c) shows that after the voltage cut off of applying 25V for 10s, 30s and 1 minute, R_t approximates the initial resistance with time, but with dwell voltages longer than 10 min the resistance exceeded the initial resistance.

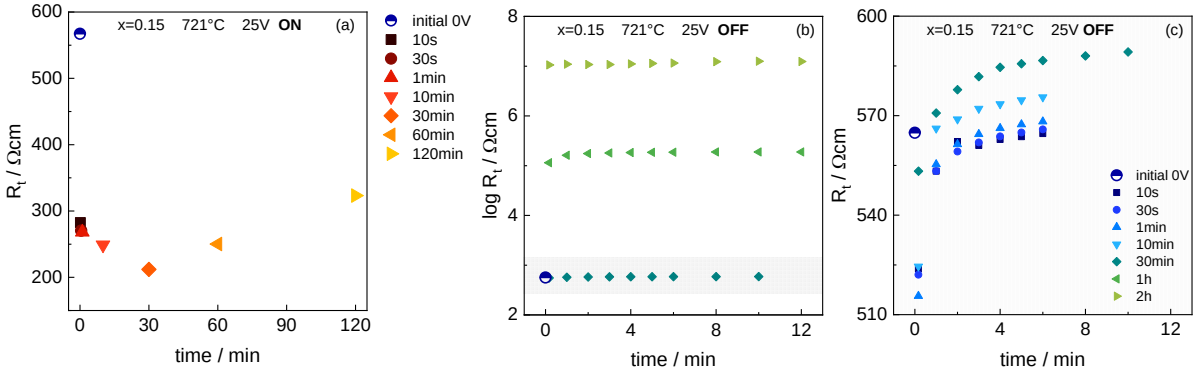

Figure 6.10. *(a)Total resistance R_t (R_1+R_2), of x=0.15 at 721°C, during the application of 25 V under different dwell times. (b) time dependence of R_t after the removal of 25V from the different dwell times. (c)Zoom in of dotted region on (b). Sample thickness 1.03mm.*

6.3.5 Air quench during voltage application

The purpose of this set of experiments was to freeze in any changes that occur during the voltage application, using profile 2 of Figure 6.1, that might disappear if the sample is slow cooled by using profile 1 of Figure 6.1. The experiment sequence is shown in Figure 6.11. First, impedance measurements of a sample with composition x=0.15 were taken in the temperature range from 300 to 850°C, in order to register the sample's original behaviour. Then, the temperature was set to 750°C and 250V/cm were applied for 30min. After 30min the sample was taken out of the furnace, without removing the *dc* bias, and compressed air was purged directly onto the sample; after ~ 1 min the *dc* bias was removed. Then, a second set of impedance measurements was taken over the temperature range 300 to 850°C (in order to find out if there any changes). This same process was repeated on a new sample of the same composition, with the difference of applying the voltage for 2h.

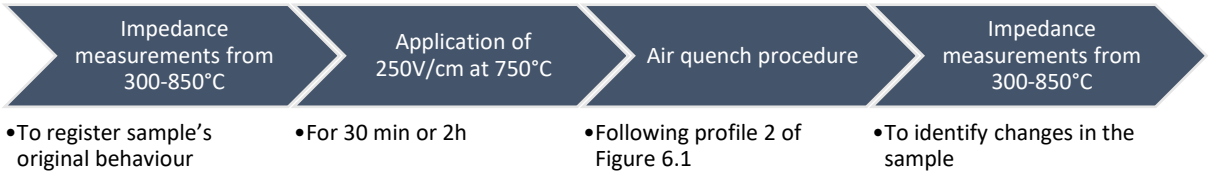

Figure 6.11. *Voltage-air quench experimental procedure.*

6.3.5.1 Air quench after 30min of 250V/cm at 750°C

The impedance response at 373°C before and after air quenching from 250V/cm for 30min, is shown in Figure 6.12. The Z* plane (a) shows that the overall impedance reduces after the voltage treatment. The log C' plot (b) based on the analysis of chapter 4, shows that the dipole plateau and the grain boundary are no longer well defined. The Z" plot (c) shows a decrease in the bulk and electrode peak, with the grain boundary peak not visible. And the M" plot (c) shows that the high frequency peak shifted to higher frequencies.

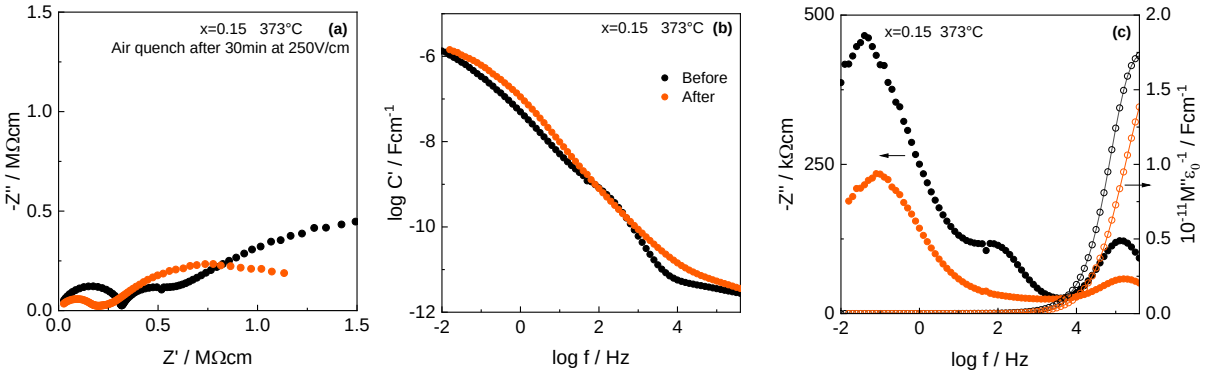

Figure 6.12. *Impedance response of x=0.15 at 373°C before and after applying 30 min of 250V/cm followed by air quenching with applied voltage. Sample thickness 1.43mm.*

To gain further information, the impedance responses before and after the voltage-quench treatment were successfully fitted to an equivalent circuit consisting of a parallel R-CPE-C in parallel with a series C-R for the bulk (1) response, which together are in series with two parallel R-CPE elements, corresponding to the grain boundary (2) and electrode (3) responses. Figure 6.13 shows the circuit and fit results for the 30 min-250V/cm quenched response at 373°C, Table 6.1 the list the values of the fitted results.

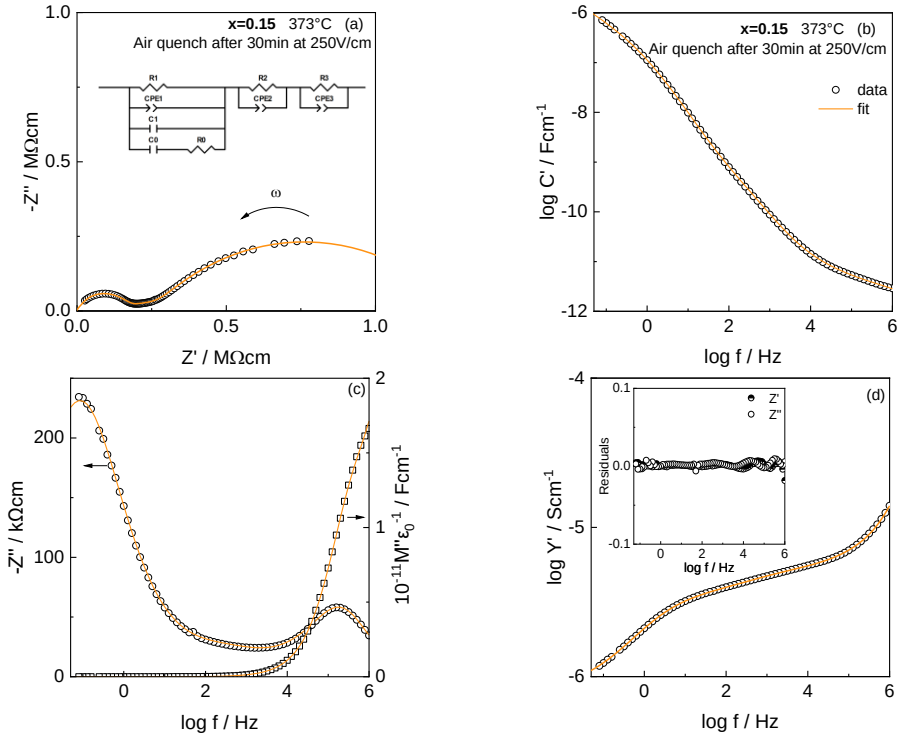

Figure 6.13. *Impedance response of x=0.15 at 373°C, after applying 30 min of 250V/cm followed by air quenching with applied voltage, fitted to the equivalent circuit inset (a). Inset (d) residuals. Sample thickness 1.43mm.*

Table 6.1. *Fitting results from fitting equivalent circuit Figure 6.13(a) to the impedance response of x=0.15 at 373°C, before and after the 30 min voltage-air quench treatment.*

Parameter	R1	$A_0$1	n1	C1	C0	R0	R2	$A_0$2	n2
Before	320(1) kΩcm	0.244(14) nScm^{-1}rad^{-n}	0.596(4)	1.90(4) pFcm^{-1}	0.86(4) pFcm^{-1}	633(38) kΩcm	290(8) kΩcm	16(1) nScm^{-1}rad^{-n}	0.83(1)
After	185.2(5) kΩcm	1.450(5) nScm^{-1}rad^{-n}	0.571(5)	0.97(3)pFcm^{-1}	0.73(5) pFcm^{-1}	119(9) kΩcm	74(2) kΩcm	238(20) nScm^{-1}rad^{-n}	0.53(1)

Simulations of the impedance response resulting from the equivalent circuit (excluding electrode element) and the values of Table 6.1, are plotted in Figure 6.14 as spectroscopic plots of Z' (a, b) and -Z" (c). It can be observed that after the voltage-air treatment the overall impedance response decreased, with the grain boundary having the larger reduction. In addition, Table 6.1 shows that the dipole parameters (C0 and R0) have decreased.

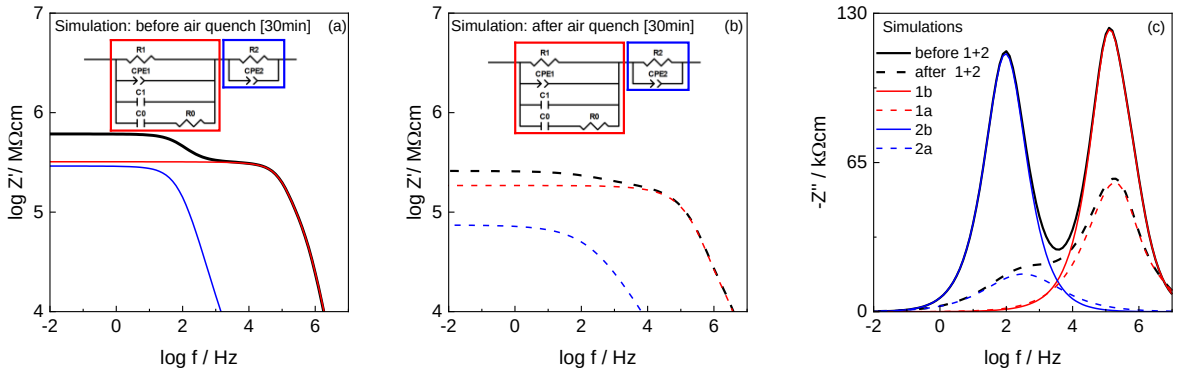

Figure 6.14. *Simulations using equivalent circuit in inset and fitting results from Table 6.1, presented as spectroscopic plots of Z'(a)(b) and -Z" (c), showing the change of the total and deconvoluted impedance response before and after the 30 min voltage-air quench treatment.*

Figure 6.15 shows the resistance values of R_1, R_2 (a) and R_t (b) before and after the voltage-air treatment as conductivity Arrhenius plots. After the voltage-air treatment the conductivity of R_1 and R_2 at low temperatures increased, and the activation energy of R_t decreased from 1.128(8) to 0.87(4) eV.

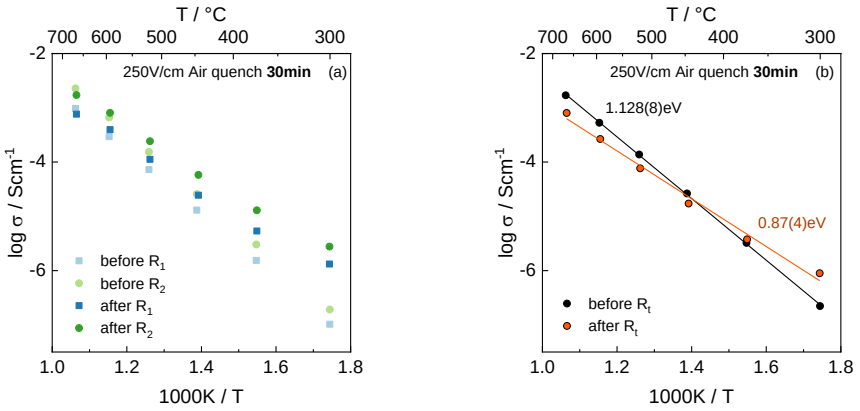

Figure 6.15. *Conductivity Arrhenius plots of R_1 and R_2 (a) and R_t (b), before and after the 30 min voltage-air quench treatment.*

6.3.5.2 Air quench after 2h of 250V/cm at 750°C

The impedance response at 371°C before and after the application of 250V/cm for 2 hours, is shown in Figure 6.16. The Z* plane (a) shows that the overall impedance increased after the voltage-quench treatment. The log C' plot (b) shows similar capacitive response as that after the 30 minutes voltage-quench treatment, with no defined dipole nor grain boundary response. The Z" plot (c) shows one peak

from high to intermediate frequencies and a low frequency dispersion. And the M" plot (c) shows that the high frequency peak did not change.

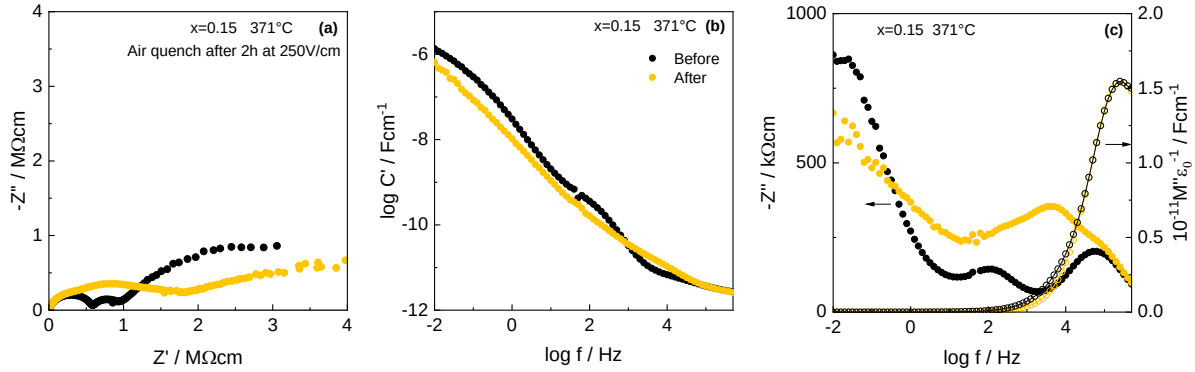

Figure 6.16. *Impedance response of x=0.15 at 371°C before and after applying 2h of 250V/cm followed by air quenching with applied voltage. Sample thickness 1.70mm.*

A good fit was obtained to a parallel R-CPE-C in parallel with a series C-R for the bulk (1) response, in series with three parallel R-CPE, corresponding to an unidentified response (x), the grain boundary (2) and electrode elements (3) responses. Figure 6.17 shows the fit results, and Table 6.2 the values of the fitted results.

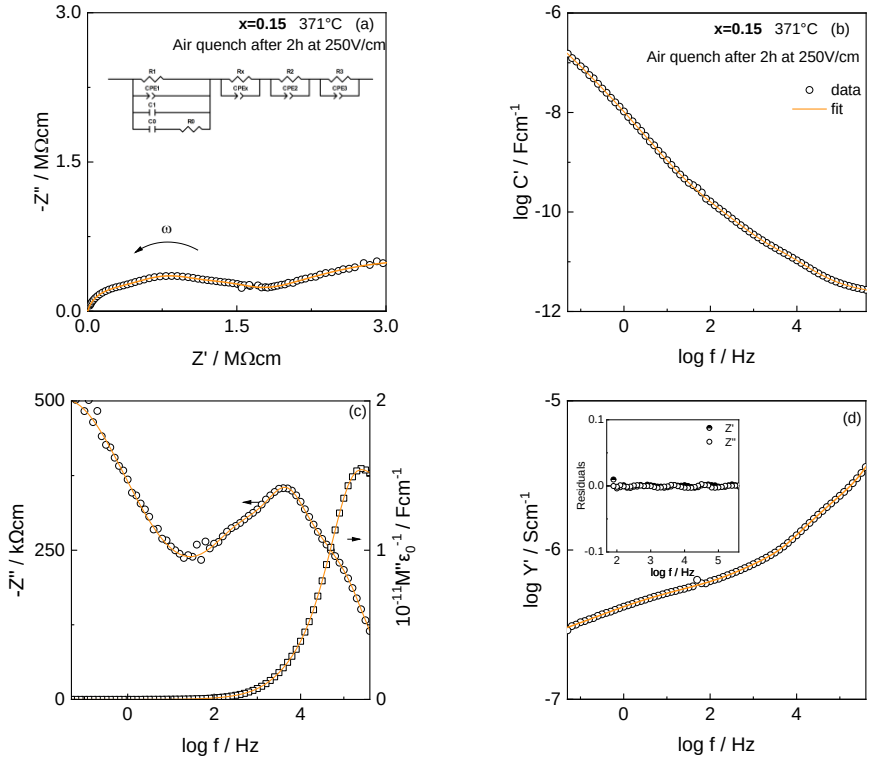

Figure 6.17. *Impedance response of x=0.15 at 371°C, after applying 2h of 250V/cm followed by air quenching with applied voltage, fitted to the equivalent circuit inset (a). Inset (d) residuals. Sample thickness 1.70mm.*

Table 6.2. *Fitting results from fitting equivalent circuit Figure 6.17(a) to the impedance response of x=0.15 at 373°C, before and after the 2h voltage-air quench treatment.*

Parameter	R1	$A_0$1	n1	C1	C0	R0	R2	$A_0$2	n2	Rx	A_0x	nx
Before	599(3)kΩcm	0.31(4)nScm^{-1}rad^{-n}	0.618(8)	1.83(3)pFcm^{-1}	0.78(7)pFcm^{-1}	2.5(2)MΩcm	369(11)kΩcm	13(1)nScm^{-1}rad^{-n}	0.82(2)			
After	445(39) kΩcm	0.293(2)nScm^{-1}rad^{-n}	0.635(8)	2.4(1)pFcm^{-1}	0.98(4)pFcm^{-1}	3.5(1)MΩcm	1.1(1)MΩcm	20(1)nScm^{-1}rad^{-n}	0.525(3)	453(20)kΩcm	0.30(3)nScm^{-1}rad^{-n}	0.86(1)

Simulations of the impedance response resulting from the equivalent circuit (excluding electrode element) and the values of Table 6.2, are plotted in Figure 6.18 as spectroscopic plots of Z' (a, b) and -Z" (c). After the voltage-air treatment the overall impedance response increased. The individual contribution from the bulk decreased, from the grain boundary increased and an additional impedance element is observed. Table 6.2 shows that the values of C0 and R0 increased.

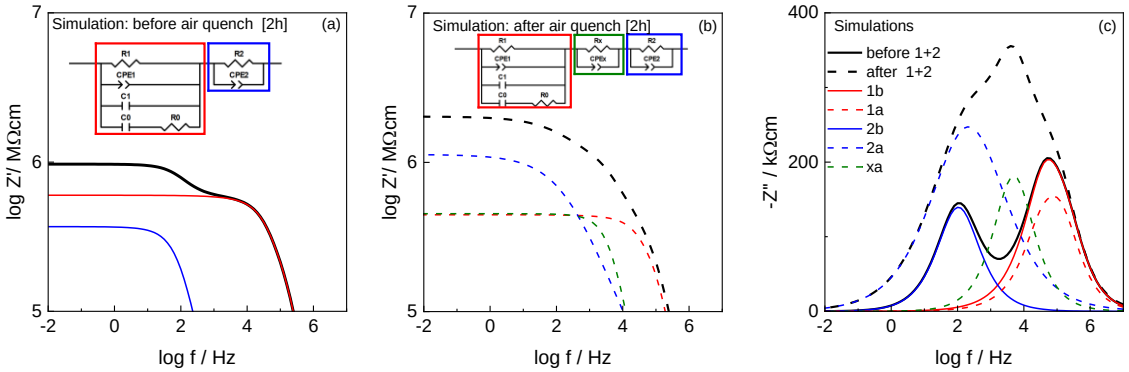

Figure 6.18. *Simulations using equivalent circuit in inset and fitting results from Table 6.2, presented as spectroscopic plots of Z' and -Z", showing the change of the total and deconvoluted impedance response before and after the 2h voltage-air quench treatment.*

With increasing temperature, for 2h voltage-quenched sample only the high frequency intercept with the Z' axis of the electrode response was clear, which was taken as R_t. A comparison of R_t before and after the voltage-quench treatment is shown in Figure 6.19. Similarly to the 30min voltage-quench sample, the activation energy decreased to some extent as the values match within errors.

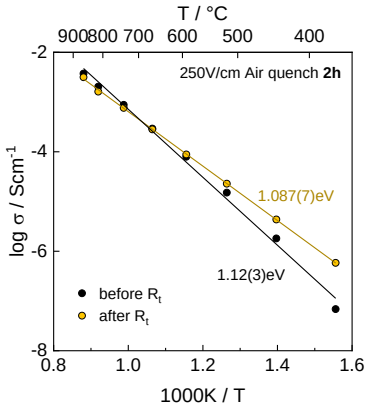

Figure 6.19. *Conductivity Arrhenius plots of R_t, before and after the 2h min voltage-air quench treatment.*

6.4 Discussion

The observed decrease in resistance with applied voltage may be explained by the introduction of electronic conductivity, resulting in a mixed ionic-electronic conduction pathway. The nature of the electronic conductivity could be p-type, by merging the pO_2 dependence results of chapter 5 and a comparison with other systems [4]–[8]. In this case, the electron holes might be located on under-bonded oxygen ions near the surface and/or close to an acceptor dopant. In the presence of a *dc* bias under-bonded oxygen ions might give up an electron to the positive electrode, following equation 6.1 from left to right

$$O_O^x \leftrightarrow O_O^\bullet + e' \qquad (6.1)$$

This process seems to be gradual, starting at the sample-electrode interface, by showing the collapse of its impedance, which might be related to the readiness of a charge transfer process and/or the diffusion of oxygen in-and-out the sample, Figure 6.2. After that, it might continue through the grain boundaries, where resistance decreases with applied voltage, showing sensitivity to composition. Finally, it reaches the bulk, which is only evident when high voltages are applied, as shown in Figure 6.4.

A sample of composition CSZ x=0.15 was tested under the combined effect of pO_2 and voltage. This test confirmed that such composition did not present impedance variations with the effect of pO_2 during voltage application. However, it needs to be noted that this behaviour might change with variations in temperature or composition, as from chapter 5 it was established that the limits of the electrolytic window may vary with temperature and composition.

The sections 6.3.4 and 6.3.5 of this chapter explore the effect of applying high voltage, temperature and different dwell times, as well as, the effect of air-quenching. The results presented in these sections leave some open questions. What happens during the application of high voltage for a long time at high temperature? , why does the resistance start to increase after 1-2 hours of applying 25V when the trend during the first 30min was the opposite? , why does the resistance increase by 4 orders of magnitude after applying 25V for 2h followed by a voltage cut-off?, what is the nature of the unidentified element found in the fittings in the sample that was subjected to the voltage-quench treatment of 2h at 250V/cm?

Here an attempt to address these points is made, in the spirit of an open discussion.

The initial increase in resistance shown in Figure 6.10 (a), might be due to oxygen loss, according to:

$$O_O^x \leftrightarrow 1/2O_2 + V_O^{\bullet\bullet} + 2e' \qquad (6.2)$$

This effect could have three consequences: (i) Oxygen gas is pumped out of the ceramic which may damage the sample-electrode interface, resulting in delamination, as observed in Figure 6.9 and 6.S1. (ii) Creation of free electrons that may be injected to the sample through the negative electrode, filling the electron holes, and increasing the resistance. (iii) Formation of a passive/surface layer which obstructs, prevents or limits the formation of electron holes, either because all the under-bonded oxygens have been ionised, oxygen loss has left an oxygen-depleted region, or the oxygen diffusion rate at each electrode differs from each other. All of these consequences may be related to the highly resistive element identified by the equivalent circuit analysis of the sample, shown in section 6.3.5.2.

The Arrhenius plots, in Figures 6.15 and 6.19, show a decrease in activation energy after the voltage-air quench experiment. This could be due to an increase in charge carrier mobility, resulting from the formation of new conduction pathways during the voltage application.

6.5 Conclusions

The bulk, grain boundary and electrode response of CSZ ceramics was analysed by impedance spectroscopy under the application of a range of *dc* bias. The general trend was a decrease in resistance with increasing voltage at short times, with an enhanced effect at higher temperatures. The main conclusion of this study, is to relate this behaviour to the introduction of p-type conductivity, attributed to localised holes in under-bonded oxygen ions.

Out of the 3 electrical components (bulk, grain boundary and electrode) the electrode response was the most sensitive to voltage. This indicates that the electrode processes, charge transfer and/or oxygen diffusion resistance, get facilitated under voltage application. Then, the change in grain boundary response proved to be dependent on composition. Finally, the bulk response showed *dc* bias dependence under higher voltages and temperatures.

The impedance of a sample with composition x=0.15 was measured under the combined effect of voltage and pO_2. It was concluded that this composition did not present pO_2 dependence under the application up to 25V at ~ 600°C. The application of extreme conditions (250V/cm for 2h at 750°C), resulted in an increased of resistance ~ 4 order of magnitude larger than the original state.

6.6 References

[1] F. Hund, "Die Fluoritphase im System ZrO_2-CaO," *Zeitschrift für Phys. Chemie*, vol. 199, no. 1, p. 142, 1952.

[2] T. H. Etsell and S. N. Flengas, "The electrical properties of solid oxide electrolytes," *Chem. Rev.*, vol. 70, no. 3, pp. 339–376, 1970.

[3] F. A. Kröger, "Electronic conductivity of calcia-stabilized zirconia," *J. Am. Ceram. Soc.*, vol. 49, no. 4, pp. 215–218, 1966.

[4] N. Masó and A. R. West, "Electronic conductivity in Yttria-stabilized zirconia under a small dc bias," *Chem. Mater.*, vol. 27, no. 5, pp. 1552–1558, 2015.

[5] M. Jovaní, H. Beltrán-Mir, E. Cordoncillo, and A. R. West, "Atmosphere- and voltage-dependent electronic conductivity of oxide-ion-conducting $Zr_{1-x}Y_xO_{2-x/2}$ ceramics," *Inorg. Chem.*, vol. 56, no. 12, pp. 7081–7088, 2017.

[6] X. Vendrell and A. R. West, "Induced p-type semiconductivity in yttria-stabilized zirconia," *J. Am. Ceram. Soc.*, vol. 102, no. 10, pp. 6100–6106, 2019.

[7] W. Weppner, "Electronic transport properties and electrically induced p-n junction in ZrO_2 + 10 mol% Y_2O_3," *J. Solid State Chem.*, vol. 20, no. 3, pp. 305–314, 1977.

[8] M. Jovaní, H. Beltrán-Mir, E. Cordoncillo, and A. R. West, "Field-induced p-n transition in yttria-stabilized zirconia," *Sci. Rep.*, vol. 9, 2019.

[9] R. Kirchheim, "On the mixed ionic and electronic conductivity in polarized yttria stabilized zirconia," *Solid State Ionics*, vol. 320, pp. 239–258, Jul. 2018.

[10] H. Yanagida, R. J. Brook, and F. a. Kröger, "Direct Current-Voltage Characteristics of Calcia Stabilized Zirconia with Porous Platinum Electrodes," *J. Electrochem. Soc.*, vol. 117, no. 5, p. 593, 1970.

[11] J. Janek and C. Korte, "Electrochemical blackening of yttria-stabilized zirconia - Morphological instability of the moving reaction front," *Solid State Ionics*, vol. 116, no. 3–4, pp. 181–195, 1999.

[12] M. Yu, S. Grasso, R. Mckinnon, T. Saunders, and M. J. Reece, "Review of flash sintering: materials, mechanisms and modelling," *Adv. Appl. Ceram.*, vol. 116, no. 1, pp. 24–60, 2017.

[13] C. E. J. Dancer, "Flash sintering of ceramic materials," *Mater. Res. Express*, vol. 3, no. 10, 2016.

[14] M. Biesuz and V. M. Sglavo, "Flash sintering of ceramics," *J. Eur. Ceram. Soc.*, vol. 39, no. May 2018, pp. 115–143, 2018.

[15] R. Kirchheim, "Incubation time for flash sintering as caused by internal reactions, exemplified for yttria stabilized zirconia," *Acta Mater.*, vol. 175, pp. 361–375, 2019.

[16] S. Jo and R. Raj, "Transition to electronic conduction at the onset of flash in cubic zirconia," *Scr. Mater.*, vol. 174, pp. 29–32, Jan. 2020.

[17] X. Vendrell, D. Yadav, R. Raj, and A. R. West, "Influence of flash sintering on the ionic conductivity of 8 mol% yttria stabilized zirconia," *J. Eur. Ceram. Soc.*, vol. 39, no. 4, pp. 1352–1358, Apr. 2019.

6.7 Supplementary

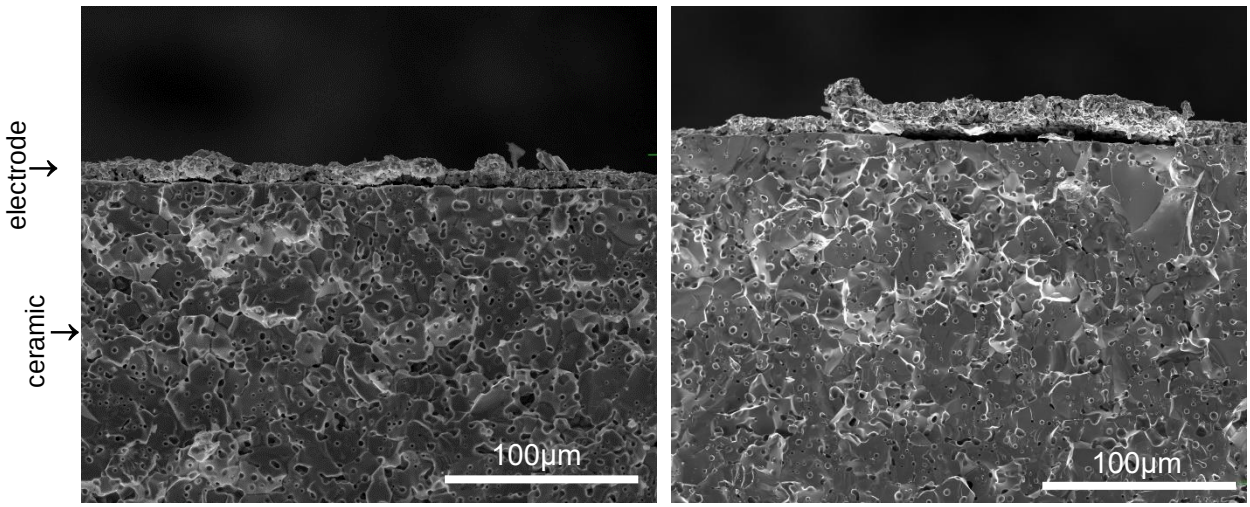

Figure 6.S1. *Micrographs of fracture surface near the positive electrode of a sacrificial sample of CSZ x=0.15 after being subjected to 25V for 2h at 720°C.*

Chapter 7
Flash phenomena in lime-stabilised zirconia oxide ion conductor

7.1 Introduction

In recent decades, different sintering techniques have been developed to reduce the energy consumption during sintering of ceramics; among them, the electric current assisted/activated sintering techniques also aim to reduce the processing time [1]. Flash sintering, which belongs to this category, is able to sinter samples in less than a minute, after reaching an onset temperature (T_{onset}) during the application of an electric field [2]. The shrinkage process is accompanied by power dissipation, non-linear increase in conductivity and emission of light; therefore, this stage of the process is known as the "*flash-event*".

The first material to be flash sintered was the oxide ion conductor 3 mol% yttria stabilised zirconia (3YSZ) by Cologna *et al.* [3]. The furnace temperature was reduced from 1450°C to ~900°C and the densification duration from hours to seconds, in comparison with conventional sintering, by applying 100V/cm during heating.

Calcia-stabilised zirconia (CSZ) is also an oxide ion conductor [4], and was chosen over YSZ is in the former the number of cations needed to obtain the same number of defects in the crystal structure is halved [5], as shown in equations 7.1 and 7.2.

$$CaO \xrightarrow{ZrO_2} Ca''_{Zr} + O_O^x + V_O^{\bullet\bullet} \quad (7.1)$$

$$Y_2O_3 \xrightarrow{ZrO_2} 2Y'_{Zr} + 3O_O^x + V_O^{\bullet\bullet} \quad (7.2)$$

The aim of this work is to find out whether CSZ behaves in a similar manner to YSZ during the flash sintering process.

7.2 Methodology

Powder with composition $Ca_xZr_{1-x}O_{2-x}$; x: 0.15, was prepared by solid-state reaction using $CaCO_3$ (99%, Fisher Chemical) and ZrO_2 (99%, Aldrich Chemistry), which were dried overnight at 180°C and 1000°C, respectively prior to weighing. The mixture was manually ground with acetone using a pestle and mortar, then fired to decarbonate and start the reaction at 1150°C. Subsequently, the powder was re-ground and heated at 1500°C for 8h.

The resulting product was analysed by X-ray powder diffraction using a Stoe Stadi P diffractometer (Darmstadt, Germany) using Cu $K\alpha_1$ radiation. Data were collected from 2θ=20 to 80° and compared to the diffraction pattern of cubic zirconia (PDF card:01-070-7361) using the JCPDS database.

7.2.1 Conventional sintering

Pellets of 10 mm diameter were uni-axially pressed at around 98MPa, and sintered at 1600°C for 10h. To ensure a good electrical contact, Pt paste electrodes were applied on both sides and dried at 900°C for 2h. Pellet densities were ~86%.

Electrical measurements from 350 to 650°C were performed on conventional-sintered samples using an impedance analyzer Solatron SI 1260 (measurement accuracy ± 0.1%) over the frequency range 10mHz-1MHz with an ac voltage of 100mV. Measurements were corrected for the geometry of the

pellets and for the blank cell capacitance, more commonly known as jig correction. ZVIEW software (ZVIEW-Impedance Software version 2.4 Scribner Associates) was used to analyse the results.

7.2.2 Flash sintering

Dog bone-shaped samples with 5wt% of PVA as binder, were pressed using a uniaxial press, applying 1ton. To burn out the binder, the samples were taken to 550°C for 2h with a heating rate of 2°C/min, and pre-sintered at 1300°C 1400°C and 1500°C for 2h; this step was used to allow the density changes during the subsequent flash process to be measured. As with conventional-sintered samples, Pt electrodes were painted inside the holes of the dog-bones and dried at 900°C for 2h. The samples were suspended inside a tube furnace using Pt wires and heated from room temperature at a heating rate of 10°C/min; a constant electric field was applied, 100V/cm, with a current density limit set at 100mA/mm^2. Relative density values were calculated by comparing theoretical and measured density.

7.3 Results and Discussion

Synthesized powder appeared to be single phase and was indexed on a cubic unit cell, space group $Fm3m$, Figure 7.1. Therefore, the cubic phase of zirconia was stabilised by adding 15mol% of CaO, consistent with the reported phase diagram for the CaO-ZrO_2 system [6].

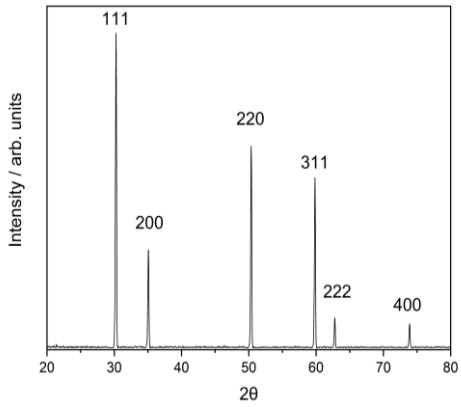

***Figure 7.1**. XRD pattern of CSZ*

A representative set of impedance data, recorded at 456°C, is shown in Figure 7.2. The impedance complex plane plot (a) shows three components: one semicircle at high frequencies, another at intermediate frequencies and a spike at low frequencies. The capacitance spectroscopic plot (b) shows 2 plateaus with values of ~1pF/cm at high frequencies and ~0.6nF/cm at intermediate frequencies. These values are typical of bulk and grain boundary responses. At low frequency the capacitance dispersion reaches a value of ~20 μF/cm, which can be related to the sample-electrode interfaces, due to ionic species creating a double layer capacitance at the electrodes. Therefore, from these capacitance values, the three components on the impedance complex plane can be identified [7].

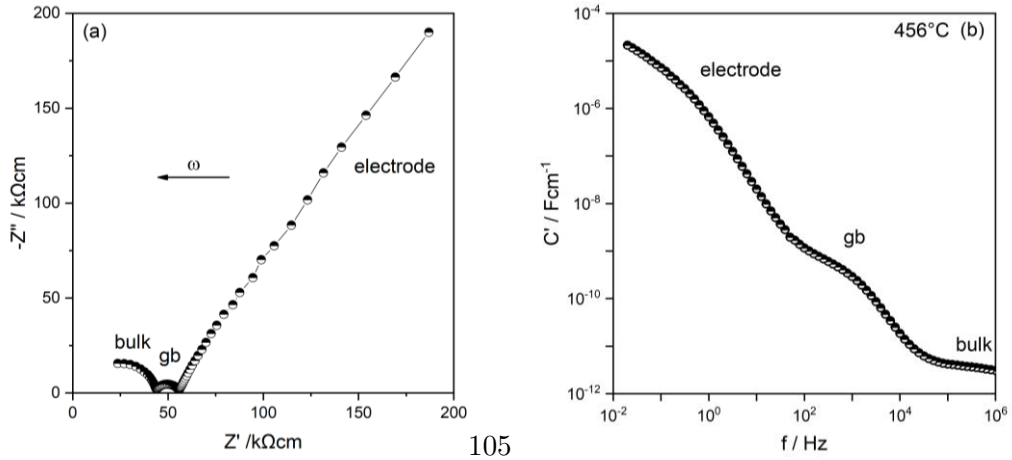

***Figure 7.2.** Impedance complex plane plot (a) and capacitance spectroscopic plot (b) of CSZ x:0.15 at 456°C, ω = 2πf.*

From the impedance plots at different temperatures, the total resistances (bulk + grain boundary) were extracted from the intercepts with the Z' axis and are shown as a conductivity Arrhenius plot, Figure 7.3. The activation energy was calculated from the slope with a value of ~1.2 eV, in agreement with values reported [8] for oxide ion conduction in CSZ, although there was evidence for curvature of the Arrhenius plot at high temperatures, similar to that seen for YSZ [9].

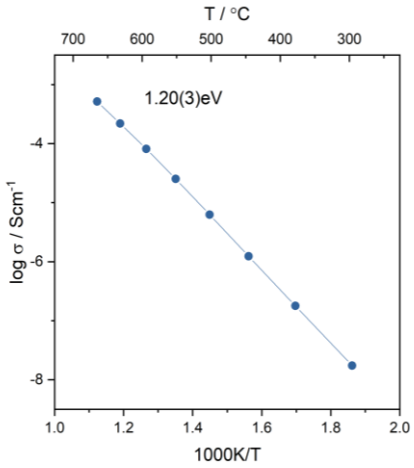

Figure 7.3. *Arrhenius plot of the total conductivity of CSZ.*

From these results, it was confirmed that the powder used for the flash sintering experiments was single phase and had the expected ionic conduction.

The samples subjected to the flash experiment showed a few of the characteristics of the "*flash event*" but not all. The conductivity increased, light was emitted, but an increase in density was not observed. The sudden increment in the conductivity is shown in Figure 7.4; the current density passing through the samples increased after reaching the flash onset temperature (T_{onset}). As the samples were heated at a constant rate, time and temperature are proportional; in this case, the results are plotted as function of time. Two types of control were used. During heating, the power supply operated in voltage control and applied a constant voltage. Once the rise in conductivity occurred, the power supply switched to current control. The samples were held between one and two minutes before turning off the power supply.

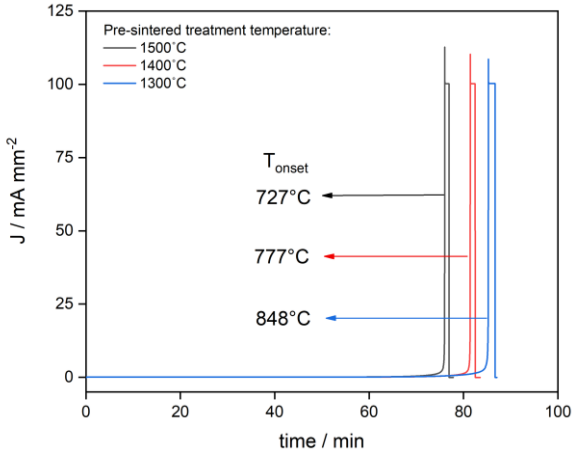

Figure 7.4*. Current density as a function of time during the flash sintering experiment, showing the increase in conductivity and the onset temperatures for the samples pre-sintered at different temperatures.*

The onset temperature varied according to the pre-sintering heat treatment; with higher heat treatment temperatures, T_{onset} decreased. This might be due to the lower porosity achieved at higher pre-sintering temperatures, allowing the current to find more easily a conduction pathway.

Emission of light was also present in all three cases during the *flash event* and remained during the subsequent current control stage, Figure 7.5.

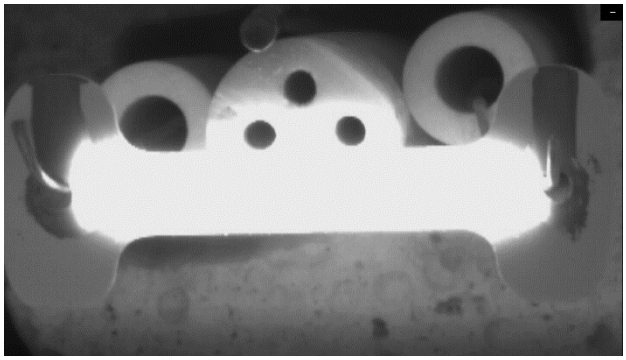

Figure 7.5*. Sample pre-sintered at 1500°C during current control.*

The relative densities of the samples after flash were less than 60%, as shown in Table 7.1. These were significantly less than those achieved during conventional sintering.

Table 7.1. *Final densities of the samples subjected to the flash experiment.*

Pre-sintering heat treatment temperature (°*C*)	Relative density (*%*) after flash
1300	53
1400	54
1500	59

The origins of densification and the emission of light are still unclear; different mechanisms that relate one to the other have been suggested by different authors. In the case of densification, Joule heating was proposed by Du *et al*. [10], formation of Frenkel pairs by Naik *et al*. [11], local overheating at grain boundaries and the interaction between electric field and space charge by Cologna *et al*. [12]. For the emission of light, electroluminescence, related to formation of defects, was proposed by Terauds *et al*. [13] and incandescence, related to Joule heating, by Biesuz *et al*. [14]

The results presented in this work indicate that the phenomena surrounding the *flash event* could be of different nature and that densification may be decoupled from the emission of light.

Some results in the literature could support this suggestion. Fully dense samples were flashed by Lebrun and Raj [15], in order to study the conductivity and photoemission relationship. They observed both increased conductivity and luminescence and proposed that the rise in conductivity was due to the creation of e-h pairs and the emission of light resulted from the recombination of these two electronic species. Composites of non-polar ($SrTiO_3$) and polar (0-25vol% $KNbO_3$) ceramics were flashed sintered by Naik *et al*. [10]. They observed that on increasing the amount of $KNbO_3$, little or no densification was achieved and the luminescence intensity decreased. The hypothesis was that defects (vacancies and interstitials), which were thought to be responsible for the densification, originated within the grains and migrated to the grain boundaries. For this reason, in pure $SrTiO_3$, full densification was achieved as the defect concentration was generated in the entire volume of the ceramic, whereas in the composites not enough defects were generated, due to the presence of the metallic interphases.
As the material used in the present study was single phase and not fully dense prior to the flash experiments, it provides a clear example of the possible decoupling of the densification and emission of light, referred to as "*flash-sans sintering*" by Raj [16].

7.4 Conclusions

The cubic phase of zirconia can be stabilised at room temperature by adding 15 mol% of CaO. Conventional-sintered samples showed three electrical components bulk, grain boundary and sample-electrode interface, and ionic conduction with an activation energy of ~1.2eV.

Samples subjected to the flash experiment showed an abrupt increase in conductivity and emission of light at an onset temperature between 720°C and 850°C depending on the temperature of pre-sintering heat treatment; nevertheless, densification did not occur. The implication of these results is that the sintering process can be separated from the emission of light.

Further work using different experimental conditions is planned in order to gain a better understanding of the origins of the *flash event*.

7.5 References

[1] S. Grasso, Y. Sakka, and G. Maizza, "Electric current activated/assisted sintering (ECAS): A review of patents 1906-2008," *Sci. Technol. Adv. Mater.*, vol. 10, no. 5, pp. 53001–24, 2009.

[2] M. Yu, S. Grasso, R. Mckinnon, T. Saunders, and M. J. Reece, "Review of flash sintering: materials, mechanisms and modelling," *Adv. Appl. Ceram.*, vol. 116, no. 1, pp. 24–60, 2017.

[3] M. Cologna, B. Rashkova, and R. Raj, "Flash sintering of nanograin zirconia in < 5s at 850°C," *J. Am. Ceram. Soc.*, vol. 93, no. 11, pp. 3556–3559, 2010.

[4] S. Jing-ze and W. Yu-ming, "Diffusion in fast-ion conductor calcia-stabilized zirconia: a molecular dynamics study," *Chinese Phys. Lett.*, vol. 15, no. 10, p. 727, 1998.

[5] T. H. Etsell and S. N. Flengas, "The electrical properties of solid oxide electrolytes," *Chem. Rev.*, vol. 70, no. 3, pp. 339–376, 1970.

[6] S. Y. Kwon and I. H. Jung, "Critical evaluation and thermodynamic optimization of the CaO-ZrO_2 and SiO_2-ZrO_2 systems," *J. Eur. Ceram. Soc.*, vol. 37, no. 3, pp. 1105–1116, 2017.

[7] J. T. S. Irvine, D. C. Sinclair, and A. R. West, "Electroceramics: characterization by impedance spectroscopy," *Adv. Mater.*, vol. 2, no. 3, pp. 132–138, 1990.

[8] A. Nakamura and J. B. Wagner, "Defect structure, ionic conductivity, and diffusion in calcia-stabilized zirconia," *J. Electrochem. Soc.*, vol. 127, no. 11, pp. 2325–2333, 1980.

[9] S. Komine and F. Munakata, "Dielectric relaxation analysis for 8 mol% YSZ single crystal," *J. Mater. Sci.*, vol. 40, no. 15, pp. 3887–3890, 2005.

[10] Y. Du, A. J. Stevenson, D. Vernat, M. Diaz, and D. Marinha, "Estimating Joule heating and ionic conductivity during flash sintering of 8YSZ," *J. Eur. Ceram. Soc.*, vol. 36, no. 3, pp. 749–759, 2016.

[11] K. Naik, S. K. Jha, and R. Raj, "Correlations between conductivity, electroluminescence and flash sintering," *Scr. Mater.*, vol. 118, pp. 1–4, 2016.

[12] M. Cologna, J. S. C. Francis, and R. Raj, "Field assisted and flash sintering of alumina and its relationship to conductivity and MgO-doping," *J. Eur. Ceram. Soc.*, vol. 31, no. 15, pp. 2827–2837, 2011.

[13] K. Terauds *et al.*, "Electroluminescence and the measurement of temperature during Stage III of flash sintering experiments," *J. Eur. Ceram. Soc.*, vol. 35, no. 11, pp. 3195–3199, 2015.

[14] M. Biesuz, P. Luchi, A. Quaranta, A. Martucci, and V. M. Sglavo, "Photoemission during flash sintering: An interpretation based on thermal radiation," *J. Eur. Ceram. Soc.*, vol. 37, no. 9, pp. 3125–3130, 2017.

[15] J. M. Lebrun and R. Raj, "A first report of photoemission in experiments related to flash sintering," *J. Am. Ceram. Soc.*, vol. 97, no. 8, pp. 2427–2430, 2014.

[16] R. Raj, Personal communication, 2019.

Chapter 8
Electrical properties of Mg-doped alumina

8.1 Introduction

The defect structure and electrical properties of pure and doped Al_2O_3 have been the focus of many studies since 1960 [1]. Extensive reviews on the diffusion of oxygen and aluminium have been written [2][3][4] which reflect the continuing debate and unresolved questions on this topic.

The defects responsible for conductivity and/or diffusion were considered variously to be aluminium vacancies ($V_{Al}^{'''}$), aluminium interstitials ($Al_i^{\bullet\bullet\bullet}$), oxygen vacancies ($V_O^{\bullet\bullet}$) and oxygen interstitials ($O_i^{''}$) [5]–[17]. The intrinsic Schottky, anion Frenkel and cation Frenkel defect reactions are shown in equations 8.1-8.3

$$2Al_{Al}^{x} + 3O_O^x \rightarrow 2V'''_{Al} + 3V_O^{\bullet\bullet} \quad (8.1)$$

$$O_O^x \rightarrow O_i'' + V_O^{\bullet\bullet} \quad (8.2)$$

$$Al_{Al}^x \rightarrow V_{Al}''' + Al_i^{\bullet\bullet\bullet} \quad (8.3)$$

These were suggested from a wide range of diffusion experiments, *dc* and *ac* conductivity measurements, consideration of the thermodynamics of defect equilibria including the energetics of formation of Schottky and Frenkel defects, molecular dynamic and atomic scale simulations. Difficulties in identifying the intrinsic defects in alumina arise from the similarity in formation energies of oxygen Frenkel and Schottky defects [16], [17] and their sensitivity to impurities: a few ppm may create defects whose consequences overshadow the effects of intrinsic defect concentrations [17].

The possible defects created as compensation mechanisms for doping with divalent cations (D), equations 8.4-8.6,

$$2DO \xrightarrow{Al_2O_3} 2D'_{Al} + 2O_O^x + D_i^{\bullet\bullet} \quad (8.4)$$

$$3DO \xrightarrow{Al_2O_3} 3D'_{Al} + 3O_O^x + Al_i^{\bullet\bullet\bullet} \quad (8.5)$$

$$2DO \xrightarrow{Al_2O_3} 2D'_{Al} + 2O_O^x + V_O^{\bullet\bullet} \quad (8.6)$$

and tetravalent (T) cations, equations 8.7-8.8,

$$2TO_2 \xrightarrow{Al_2O_3} 2T_{Al}^{\bullet} + 4O_O^x + O''_i \quad (8.7)$$

$$3TO_2 \xrightarrow{Al_2O_3} 3T_{Al}^{\bullet} + 6O_O^x + V'''_{Al} \quad (8.8)$$

have been mentioned in studies involving a wide range of dopants [7][16]. It was suggested that for doping with divalent ions $V_O^{\bullet\bullet}$ would be created more readily and $V_{Al}^{'''}$ for doping with tetravalent ions [7][16]. However, it was also suggested that if Frenkel defects predominate, divalent cations are compensated by $Al_i^{\bullet\bullet\bullet}$ [7] and $O_i^{''}$ species compensate for the dissolution of Ti^{4+}, rather than $V_{Al}^{'''}$[15]. There is general agreement that oxygen diffusion increases with Mg-doping and decreases with Ti-doping; it was concluded that oxygen diffusion occurs via $V_O^{\bullet\bullet}$ in the former and $O_i^{''}$ in the latter and that $V_O^{\bullet\bullet}$ diffusion is 2-2.5 times faster than that of $O_i^{''}$ [2]. Nevertheless, aluminium diffusion, as either vacancies or interstitials, was also considered possible, with the conclusion that $Al_i^{\bullet\bullet\bullet}$ dominates in the presence of Mg^{2+} and $V_{Al}^{'''}$ in the presence of Ti^{4+} [2]. When comparing aluminium and oxygen diffusion, $Al_i^{\bullet\bullet\bullet}$ diffuses 10^3-10^4 times faster than $V_O^{\bullet\bullet}$ [2] and the presence of Si increases the amount of $V_{Al}^{'''}$ [12].

Conductivity measurements at 1650°C showed a large variation with pO_2. The electronic conductivity increased in either reducing or oxidizing atmospheres and was separated by an electrolytic domain that became increasingly broadened as temperature decreased to 1200°C [11]. Due to the resistive nature of the material, long times were necessary to reach equilibrium below 1200°C [12]. Depending on stoichiometry and experimental conditions, especially temperature and oxygen partial pressure, pO_2, Al_2O_3 could present both electronic (*n*- or *p*-type) and/or ionic conductivity. Consistent with this observation, thermoelectric emf experiments showed that the hot junction on a single crystal of Al_2O_3 was positive under pure oxygen and negative under low pO_2 ($\sim 10^{-10}$ atm) [5]. Other factors to be considered in rationalising knowledge of defect concentrations and equilibria with conductivity and diffusion data include the distinction between continuous, long range conduction and short range hops over barriers that have the lowest energy, the possibility of defect-defect interactions and the formation of charged or neutral clusters; these appear to be ignored in most cases [4].

Alumina-based ceramics have found use in a wide range of commercial applications due to their many key properties. Exceptionally high electrical resistivity, high mechanical strength, corrosion resistance and thermal stability well above 1000 °C, as well as biological inertness, combine to allow extensive utilisation of Al_2O_3.[18] The cost of manufacturing Al_2O_3 ceramic components is highly dependent on the purity and processing routes used, which in turn influence the microstructure and final properties. A balance in both cost and final properties must be reached depending on the final application. For example, a small grain size (< 2 μm) and high purity (> 99 %) are desired in demanding mechanical and chemically corrosive applications, but can be costly. There is also a necessity for the addition of a sintering aid, commonly MgO, which enables the Al_2O_3 ceramic to sinter to near full density, whilst controlling grain growth [19].

Often, a secondary glass phase is used as a processing aid, despite potentially lowering the ceramic's mechanical strength. As an electrical insulator, Al_2O_3 ceramics can benefit from a glass phase through improved bonding strength to metallisation inks used for metal assemblies. The use of a glassy secondary phase also aids sintering, with rates of mass transport increased at relatively lower firing temperatures, allowing for the use of a larger starting particle size Al_2O_3, reducing the overall cost of production [20]. For electrically insulating applications, such as electrical feedthrough or high voltage power tubes, it is important that the addition of a sintering aid does not diminish the electrical resistivity of the Al_2O_3. Understanding the electrical resistance behaviour of an Al_2O_3 ceramic can aid in understanding why some grades perform better in specific applications, whilst directing the future development of new grades.

The main purpose of this study has been to use impedance spectroscopy to measure the electrical properties of doped alumina ceramics at much lower temperatures, ~ 500-900 °C, than those used to evaluate defect equilibria, usually in single crystal materials, at very high temperatures, > ~ 1400 °C. The objective is to identify and understand the main factors and principal defects that control the conductivity of doped ceramics, whether ionic or electronic. Although the materials are unlikely to be in thermodynamic equilibrium with the atmosphere at these relatively low temperatures, the properties should nevertheless be dominated by the defects and their concentrations that have been frozen in from higher temperatures. The materials may, therefore, exhibit kinetic stability and associated metastable equilibria that have a controlling effect on electrical properties at lower temperatures. Two types of Mg-doped alumina ceramics have been studied, both with and without the addition of silica. It was of interest to see whether the addition of silica led to the presence of a separate glassy phase or whether it could dissolve in the alumina lattice. The results demonstrate particularly well the sensitivity of electrical conductivity to the charge compensation mechanism associated with aliovalent dopants.

8.2 Experimental

Samples with compositions 0.05wt%MgO-Al_2O_3 (Mg0.05) and 0.5wt%(MgO/SiO_2)-Al_2O_3 were provided by an industrial contact. These are typically prepared from reagent grade (> 99%) Al_2O_3, $Mg(NO_3)_2{\cdot}4H_2O$ and $Si(OC_2H_5)_4$ [21]–[23], which were combined and mixed with inorganic additives and organic binders in an aqueous slurry before spray drying. Dried powders were uniaxially pressed using a 20 mm pellet die at 150 MPa before debinding and sintering sintering at typically 1550°C for 8 h in. The final fired density of each of the pellets was 3.94 and 3.86 g/cm^3 for Mg0.05 and Mg0.5, respectively. Mg0.05 had an average grain size of 2 μm, while Mg0.5 had an average of 20 μm. Platinum paste electrodes were applied to opposite pellet faces and dried at 900°C for 2 h. For impedance measurements, pellets were attached to the Pt leads of a conductivity jig which allowed the flow of gas over the pellet.

Sintered samples were polished metallographically, thermally etched at 1350°C for 20 min and sputter-coated with 10 nm of carbon. Ceramic microstructures were determined by secondary electron (SE) images taken on a field-emission scanning electron microscope (FEI Inspect F50) using an acceleration voltage of 15 kV and energy-dispersion analysis of x-rays (EDS) from Oxford Instruments using 20 kV.

For impedance measurements, Pt paste electrodes were applied to opposite pellet faces and dried at 900°C for 2 h. Electroded pellets were attached to the Pt leads of a conductivity jig which allowed the flow of gas. Isothermal impedance measurements were taken after 30 min of flowing N_2, O_2 and dried air at 101.325 kPa, over the temperature range 400-950 °C. Two impedance analysers were used: a Solartron SI 1260 (measurement accuracy ±0.1%), frequency range 10 mHz-1 MHz and an Agilent Agilent 4294A (measurement accuracy ±0.08%), frequency range 40 Hz-1 MHz, with a nominal *ac* voltage of 100 mV in both cases.

Two sets of corrections were made to the collected data: (i) a geometric factor consisting of pellet thickness and sample-electrode contact area and (ii) jig impedance characteristics consisting of the blank, open circuit capacitance, typically 6 pF and the closed circuit resistance of, primarily, the leads, 1-2 Ω. The reported values for bulk resistances, R_1, correspond approximately to their resistivities; grain boundary resistances, R_2, are not resistivities as they were not corrected for grain boundary geometries, although they are reported also in units of ohm cm. Data analysis was performed using ZVIEW software (ZVIEW-Impedance Software version 2.4 Scribner Associates).

8.3 Results

8.3.1 Mg0.05 gave a typical impedance complex plane response characterised by 3 electrical components, Figure 8.1(a-c). At 433°C (a), part of a poorly-resolved semicircular arc with resistance R_1 is observed at high frequencies (schematic fit is shown, dashed, as a visual aid) and at lower frequencies, a spike. The spike becomes the high frequency tail of a second arc with resistance R_2 at higher temperatures, as shown in (b). The same data plotted as a capacitance, C' spectroscopic plot (d), show a high frequency plateau, $C_1 \sim 0.54$ pFcm^{-1}, that is attributed to the bulk response and corresponds to a relative permittivity of ~ 6.04, given by:

$$\varepsilon' = C'/\varepsilon_0 \qquad (8.9)$$

where ε_0 is the permittivity of free space, 8.854x10^{-14} Fcm^{-1}. Further evidence of the bulk response is given in the spectroscopic M" plot (e); this shows a Debye-like peak in the same frequency range as the poorly-resolved, high frequency arc in Z*. Because the largest peak in an M" spectrum is dominated

by the component with the smallest capacitance [24], M" spectra provide a very useful, visual way to identify the bulk response of a sample.

The second arc and resistance R_2 dominates the impedance complex plane at 762°C (b); at 923 °C (c) a third, low frequency arc with resistance (extrapolated) R_3 is seen. The capacitance data at 762 °C (d) show a plateau, C_2 around 10 pFcm^{-1} at similar intermediate frequencies to the second impedance arc. At 923 ^{0}C, a low frequency dispersion in C' with values above 10 μFcm^{-1} is observed (d) at similar frequencies to the low frequency arc. From the magnitudes of their capacitances, these three impedance elements were attributed tentatively, with decreasing frequency, to the bulk effect (R_1), grain boundary or minor second phase (R_2) and sample-electrode interface (R_3). Values for the resistances R_1 and R_2 were estimated directly from the intercepts of semicircles with the Z' axis and are shown as conductivity Arrhenius plots in (f). R_1 has activation energy 0.92(4) eV and, as discussed later, is associated primarily with bulk oxide ion conduction whereas R_2 is more resistive, with high activation energy, 2.29(2) eV, and is attributed to a grain boundary whose conductivity is mainly electronic.

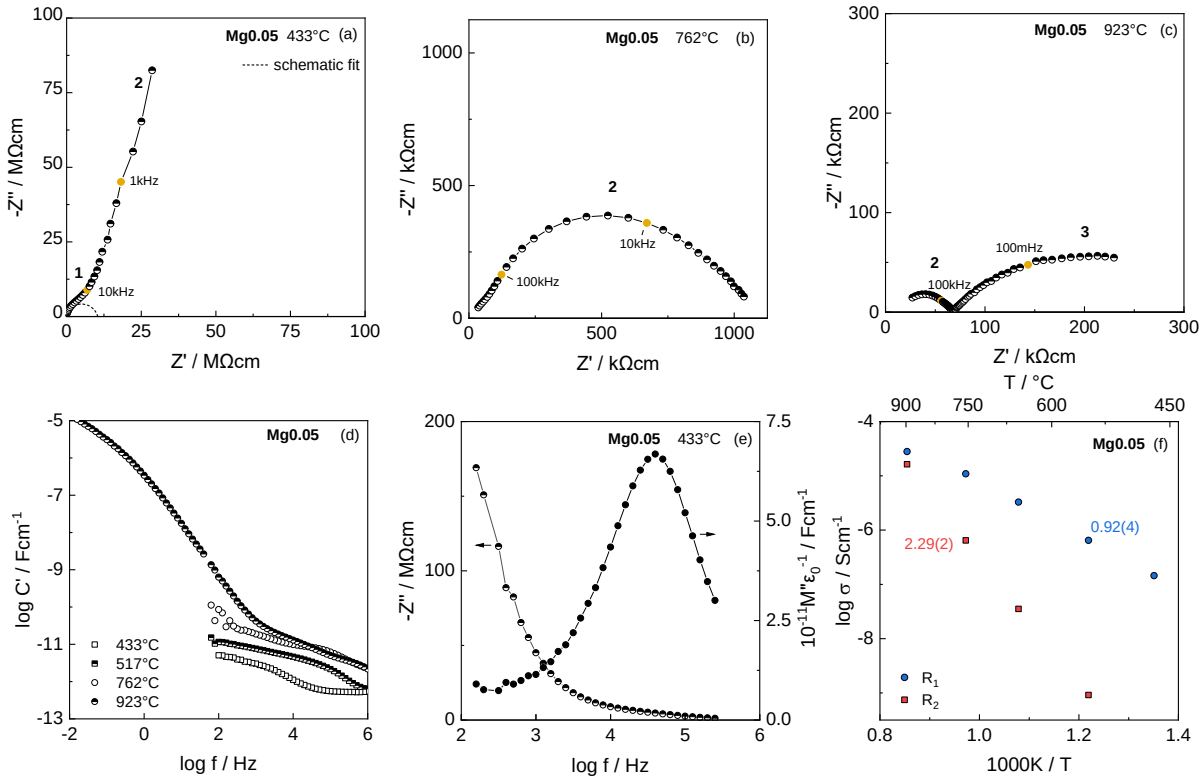

***Figure 1**. (a)-(c) Impedance complex plane plots and spectroscopic plots of (d) capacitance and (e) Z''/M'' at different temperatures for Mg0.05; (f) Conductivity Arrhenius plot of bulk, R_1 and grain boundary, R_2 impedances*

8.3.2 Mg0.5 also gave typical impedance data sets with three electrical components, Figure 8.2. The impedance complex plane at 909°C (a) shows two arcs of similar size at high frequencies and a broad depressed arc at low frequencies. The C' data at this temperature (b) show, similarly, a low frequency dispersion approaching 0.62 μFcm^{-1}, an intermediate plateau around ~ 15 pFcm^{-1} and a high frequency limiting capacitance ~ 0.88 pFcm^{-1}, which is seen more clearly at lower temperature, 708°C (b) and corresponds to a bulk relative permittivity of ~ 9.9. The Z''/M'' plots at 909°C, (c), show that the highest frequency Z'' peak and impedance complex plane arc (a) correspond to the component with the lowest capacitance, C_1 that is responsible for the M'' peak.

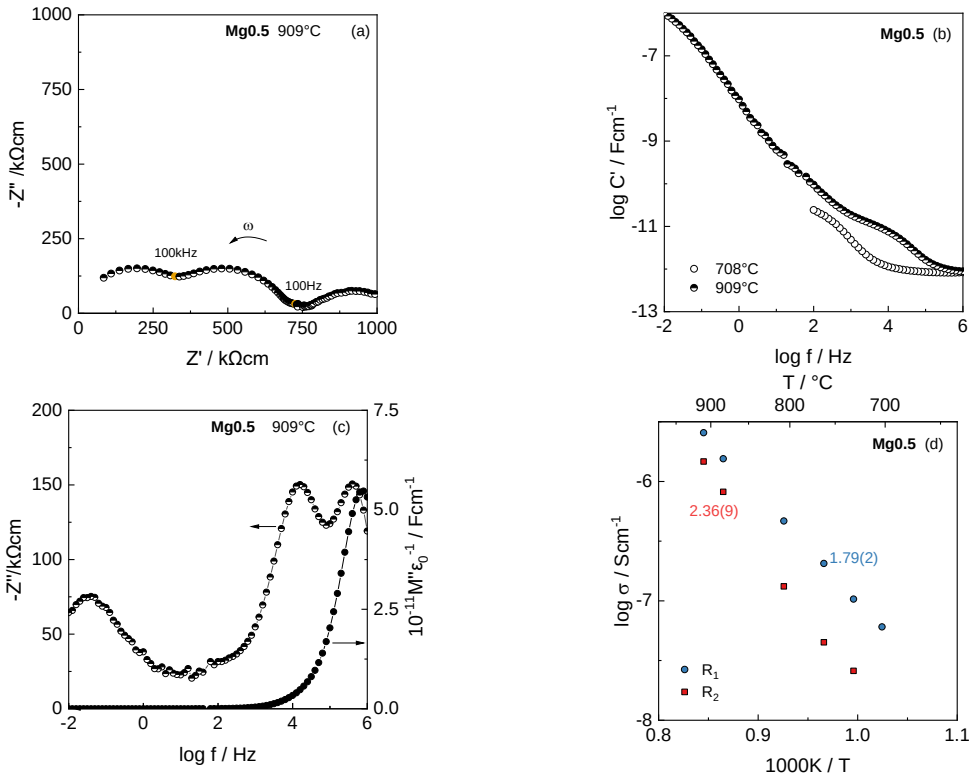

***Figure 8.2**. (a) Impedance complex plane plot and spectroscopic plots of (b) capacitance and (c) Z''/M'' at different temperatures for Mg0.5; (d) Conductivity Arrhenius plot of bulk, R_1 and grain boundary, R_2 impedances*

The main difference between Mg0.05 and Mg0.5 datasets is that, although both have impedance components of similar geometric dimensions from the values of C_1 and C_2, the values of resistances R_1, R_2 and R_3 are comparable for Mg0.5 whereas for Mg0.05, R_1 is relatively, much smaller than the other two resistances. Arrhenius plots for Mg0.5, Fig 8.2(d), show that there is not the same dramatic difference between R_1 and R_2 that is seen with Mg0.05, Fig 8.1(f); we attribute this difference to the reduced level of oxide ion conduction in Mg0.5, discussed later.

Arrhenius plots for both samples are collected in Figure 8.3 where they are separated into (a) bulk and (b) grain boundary components. The bulk conductivities, σ_1 decrease with increasing amount of dopant, in the sequence Mg0.05 > Mg0.5. However, the grain boundary conductivities, σ_2 have similar activation energy and differ by only one order of magnitude in conductivity.

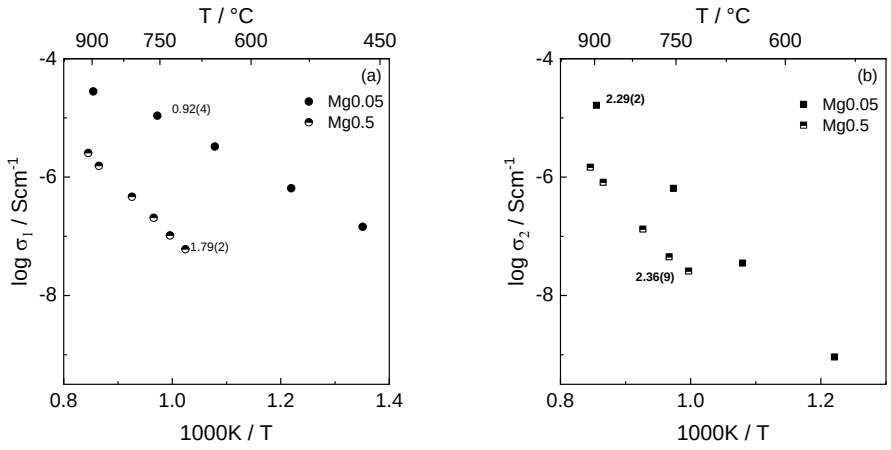

***Figure 8.3**. Comparison of conductivity Arrhenius plots of (a) bulk and (b)grain boundary conductivities*

Both samples showed dependence of conductivity on oxygen partial pressure, pO_2 at~900 ^{0}C, as shown in Figure 8.4(a-b), but not at lower temperature (c-d). In each case, at~900 ^{0}C the total resistance of the samples, as well as the three individual resistance components for both Mg0.05 and Mg0.5, decreased with increasing pO_2. This behaviour suggests a *p*-type electronic contribution to the conductivity at higher temperatures since the following idealised equilibrium at the sample surfaces is displaced to the right with increasing pO_2:

$$1/2O_2 + V_O^{\bullet\bullet} \leftrightarrow O_o^x + 2h^{\bullet} \qquad (8.10)$$

At lower temperatures, the absence of any pO_2 dependence suggests that under these conditions (c,d), the samples are within the electrolytic domain and any *p*-type conductivity is too small to detect in the presence of the oxide ion conductivity.

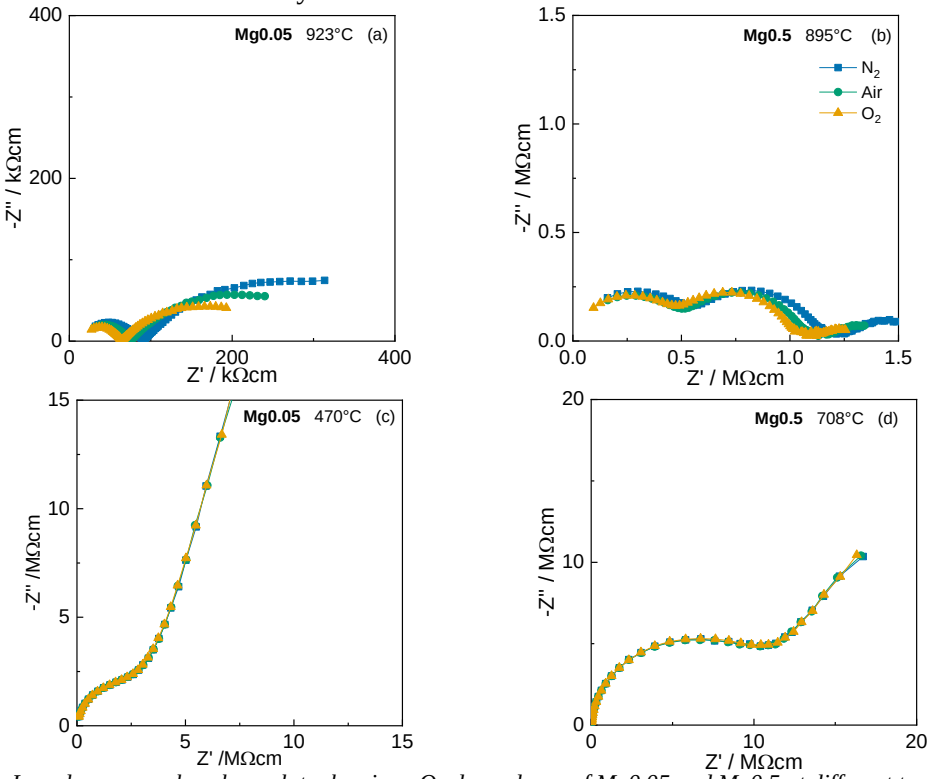

Figure 8.4. *Impedance complex plane plots showing pO_2-dependence of Mg0.05 and Mg0.5 at different temperatures.*

8.3.3 SEM/EDS results are shown in Figures 8.5 and 8.6. Secondary electron, SE, images, 5(a), for Mg0.05 show a small amount of closed porosity and grain sizes in the range 0.7-5 μm with an average of~2 μm; EDS images, 5(b,c), show a homogeneous distribution of Al and Mg. For Mg0.5, SE images, 6(a), show a wider range of grain sizes, 0.7-40 μm with an average of~15 μm and slightly more closed porosity; EDS maps, 6(b-d), show a homogeneous distribution of Al, Mg and Si through the grains with minor amounts of isolated Si segregation.

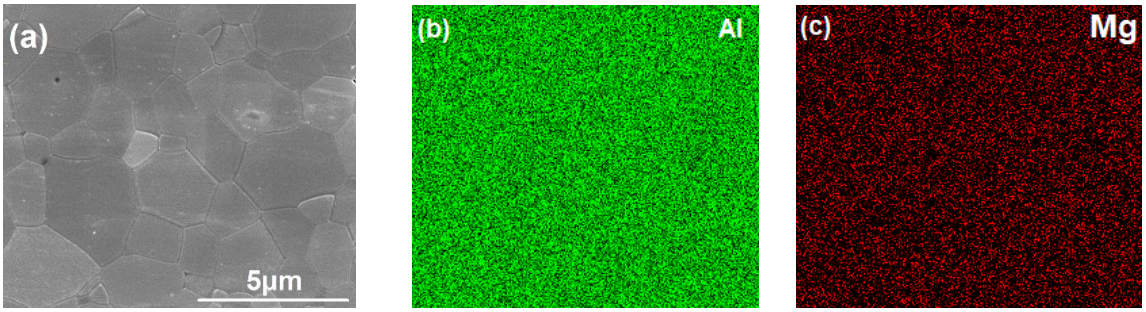

Figure 8.5. *(a) SE and (b,c) EDS images of polished and thermal-etched pellet of Mg0.05.*

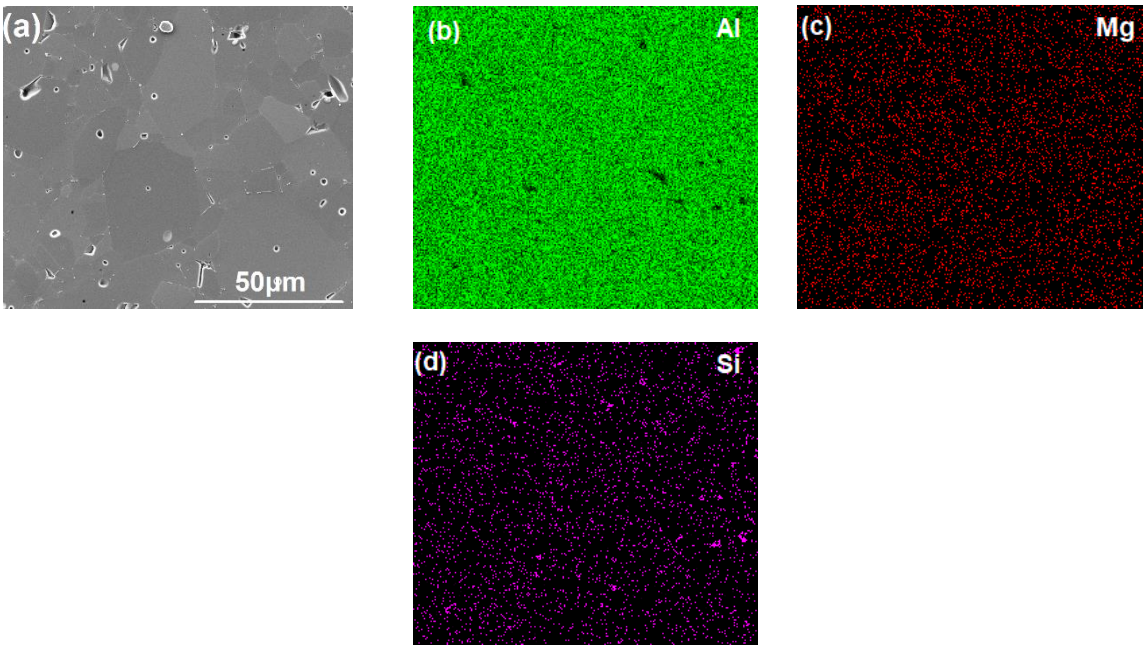

Figure 8.6*. (a) SE and (b-d) EDS images of polished and thermal-etched pellet of Mg0.5.*

8.4 Discussion

The impedance data for both Mg0.05 and Mg0.5 show three components which indicate an equivalent circuit consisting, to a first approximation, of three parallel RC elements in series. Resistance values were obtained readily from the intercepts, or extrapolated intercepts, of arcs on the Z' axis of impedance complex plane plots. However, the impedance arcs were broadened from an ideal semi-circular shape; detailed circuit analysis and fitting would require inclusion of constant phase elements in the equivalent circuit but was not deemed necessary since resistance values were obtained directly from Z* plots. Resistance data gave linear Arrhenius plots and activation energies in the range 0.92(4) to 2.36(9) eV.

Capacitance values were estimated from plateaux in spectroscopic plots of log C'. Using the relation:

$$C = e_0\varepsilon' Ad^{-1} \qquad (8.11)$$

where A and d represent the area and thickness of regions responsible for a particular impedance effect, the capacitance values were assigned as follows: C_1 - sample bulk; C_2 - grain boundaries; C_3 - sample-electrode interface. Permittivity values calculated from C_1 were in the range 6-10, consistent with values expected for dielectric Al_2O_3. Values for C_2, around 10^{-11} Fcm^{-1}, indicated that the thickness of the grain boundary regions was approximately 5-10 % that of the bulk grains, assuming a simple model in which $C \alpha d^{-1}$, equation (8.11). It should be emphasised that these capacitance values and relative thicknesses refer to the ***electrical*** microstructure of the samples, which is not necessarily the same as the microstructure determined by direct microscopic observation. Limiting values of C_3 at 10^{-2} Hz were, for Mg0.5, $>10^{-6}$ Fcm^{-1} and for Mg0.05, $>10^{-5}$ Fcm^{-1}, which clearly correspond to the sample-electrode contact impedances.

Information on the nature of the current carriers responsible for the conductivity data was obtained from a combination of impedance measurements at different frequencies and in atmospheres of different pO_2. The results taken together indicate a temperature- and composition-dependent combination of oxide ion conduction and *p*-type electronic conduction.

8.4.1 Ionic conduction is indicated by a high value of sample-electrode capacitance at low frequencies: double layer capacitances of $\sim 10^{-5}$ Fcm^{-1} are typical of ion blocking at sample-electrode interfaces. Experimental values obtained here, $>3x10^{-5}$ Fcm^{-1} at 10^{-2} Hz for Mg0.05, are attributed to oxide ions as the conducting species responsible, consistent with a charge compensation mechanism of oxygen vacancy creation on doping alumina with Mg^{2+}. For Mg0.5, the alumina appeared to be double-doped with self-compensating Mg^{2+} and Si^{4+}, which greatly reduced the need for oxygen vacancy creation; the smaller value of the capacitance, 10^{-6} Hz at 10^{-2} Hz, is consistent with a reduced level of oxide ion conductivity.

The impedance response of oxide ion conductivity may also be sensitive to pO_2 for two possible reasons. First, redox transfer of oxygen usually occurs across the sample-electrode interfaces and can be represented by a charge transfer resistance, R_{CT}, in parallel with a blocking double layer capacitance, C_{DL}. The effect of R_{CT} is to transform an 'electrode spike' into a low frequency impedance arc whose magnitude may depend on pO_2 in the surrounding atmosphere. The oxygen redox reaction, given ideally by:

$$1/2O_2 + V_O^{\bullet\bullet} + 2e' \leftrightarrow O_O^x \qquad (8.12)$$

occurs in opposite directions at the two electrodes, one of which, either the oxygen evolution reaction, OER, or the oxygen reduction reaction, ORR, is likely to control the overall impedance and measured R_{CT} value.

Second, permeation of oxygen molecules, either towards or away from the sample-electrode interface may be a rate-limiting step in the overall impedance. To represent this, a Warburg impedance, Z_W, is usually placed in series with the rest of the equivalent circuit and becomes the limiting, zero frequency impedance of the measuring system. Both of these effects, R_{CT} and Z_W, may therefore make a contribution to the value of R_3. Although the electrode response, R_3C_3 of oxide ion conductors may be sensitive to pO_2, the sample resistances themselves, R_1 and R_2 do not change because the effect of pO_2 on oxide ion vacancy concentration is very small. As discussed later, a small uptake of oxygen may occur at sample surfaces and interfaces with increasing pO_2, which is compensated by the onset of *p*-type electronic conductivity, but the overall change in oxygen vacancy concentration is too small to influence the level of oxide ion conductivity.

8.4.2 Electronic conduction can also be studied by measurements in atmospheres of different pO_2 which in particular, can provide information concerning the nature of electronic charge carriers, as shown in the data obtained at ~900 ^oC, Figure 4. For materials that are conductors of oxide ions alone, as indicated above, the bulk and grain boundary conductivities should not be sensitive to pO_2. For materials that are low level electronic semiconductors, however, measurements in different pO_2 allow distinction between *n*- and *p*- type carriers. From equations (8.10) and (8.12), the effect of increasing pO_2 is either to decrease the number of *n*-type carriers (8.12) or to increase the number of *p*-type carriers (8.10). Results obtained here with both samples showed enhanced conductivity with increased pO_2 and therefore, *p*-type extrinsic conductivity. This must occur in parallel with any oxide ion conductivity and therefore, the materials are mixed conductors.

At this stage, we have no information on the relative transport numbers of holes and oxide ions, but clearly both are significant and the electronic transport numbers are not fixed but vary with pO_2. The bulk conductivity of Mg0.05 is 1-2 orders of magnitude higher than that of Mg0.5 and also has a much lower bulk activation energy, whose value, 0.92(4) eV is typical of oxide ion conductors such as yttria-stabilised zirconia, YSZ [25]. Therefore, it is suggested that Mg0.05 is primarily an oxide ion conductor whereas Mg0.5 is primarily an electronic conductor.

In our experience of sample-electrode contacts in materials that are electronically conducting, a contact impedance is commonly observed (ie contacts may be non-ohmic) but is not double layer in nature. Since there is no capacitive charge build-up, the interface behaves effectively as a parallel RC element in which the capacitance represents an, often poor, contact between rough surfaces of the sample and metal electrode and typically, has much smaller capacitance values. The smaller value of the low frequency capacitance for Mg0.5 compared with that for Mg0.05 is consistent with electronic conductivity but also a certain amount of oxide ion conductivity.

The possible mechanism(s) for incorporating Mg and Si dopants into the alumina samples were next considered. The SEM/EDS results give two important conclusions. First, in composition Mg0.05, the Mg is distributed homogeneously through the alumina grains with no indication of any segregation. Second, in Mg0.5, both Mg and Si are distributed homogeneously through the alumina lattice.

Mg^{2+} and Al^{3+} are similar-sized ions with similar bonding character and are able to substitute readily for each other in crystal structures, as shown by the variable stoichiometry of $MgAl_2O_4$ spinel in the MgO-Al_2O_3 phase diagram. Addition of MgO to Al_2O_3 could, in principle, involve two possible ionic charge compensation mechanisms. The general formulae that arise, as well as use of Kröger-Vink notation to describe the reactions, are as follows:

1.Creation of oxygen vacancies in $Al_{2-x}Mg_xO_{3-\frac{x}{2}}$

$$2MgO \xrightarrow{Al_2O_3} 2Mg'_{Al} + V_O^{\bullet\bullet} + 2O_O^x \qquad (8.13)$$

2.Creation of interstitial cations in $Al_{2-2x}Mg_{3x}O_3$:

$$3MgO \xrightarrow{Al_2O_3} 2Mg'_{Al} + Mg_i^{\bullet\bullet} + 3O_O^x \qquad (8.14)$$

A related possibility is that the interstitial Mg^{2+} ions may change places with lattice Al^{3+} ions to give interstitial Al^{3+} ions, consistent with a Frenkel defect model for alumina.

3.Creation of holes. An electronic charge compensation mechanism requires the creation of holes, but neither Mg^{2+} or Al^{3+} are possible as locations of holes due to their very high subsequent ionisation potentials. The observed, thermally-activated *p*-type conductivity at high temperatures and its dependence on pO_2, is therefore attributed to creation of holes on oxygen to give, $Al_{2-x}Mg_xO_{3-(x/2)+\delta}$:

$$1/2O_2 + V_o^{\bullet\bullet} + O_o^x \leftrightarrow 2O_o^{\bullet} \qquad (8.15)$$

In this mechanism, O_2 molecules from the surrounding atmosphere absorb on the sample surface, dissociate, pick up electrons from neighbouring under-bonded oxide ions which ionise singly and occupy oxygen vacancies as O^- ions.

In summary, only mechanism 1, equation (8.13), involves oxygen vacancy creation and therefore, readily accounts for the observed oxide ion conduction. Mechanism 2 could conceivably give rise to conduction by interstitial Mg^{2+} or Al^{3+} ions but not to hole conduction. Mechanism 3 accounts for hole conduction and the ready variation in *p*-type conductivity with changing pO_2, but not oxide ion conduction. Both ionic and electronic mechanisms are generally involved, therefore and the relative importance of each depends on experimental conditions, especially temperature and pO_2.

The sizes of Si^{4+} and Al^{3+} are also similar and many examples of mixed site occupancy exist in the large family of aluminosilicate minerals and their synthetic analogues. In these, Si occupies tetrahedral sites exclusively. It is rare, but not unknown, for Si to occupy octahedral sites, as in glassy and crystalline Si phosphates [26]. In Mg0.5, the SEM / EDS results support a mechanism by which Al_2O_3 is co-doped with both Mg^{2+} and Si^{4+}:

$$MgO + SiO_2 \xrightarrow{Al_2O_3} Mg'_{Al} + Si^{\bullet}_{Al} + 3O_o^x \qquad (8.16)$$

Further work is required to determine whether both Si and Mg occupy octahedral sites or whether Si occupies tetrahedral sites. However, a direct consequence of the co-doping mechanism, irrespective of the details concerning the location of Si, is that creation of oxygen vacancies is not necessary to compensate for equal amounts of Mg and Si dopants.

The requirements for *p*-type conductivity in the doped aluminas were considered. Equation (8.15) appears to be the mechanism responsible and in particular, requires (i) the availability of oxygen vacancies to absorb oxygen with increasing pO_2 and (ii) the availability of underbonded oxide ions which can ionise readily, transferring one electron to an incoming oxygen atom and thereby generating two singly charged O^- ions. Under-bonded oxide ions may be regarded as those in the vicinity of Mg^{2+} dopant ions, also regarded as acceptor dopants, since such oxide ions are not surrounded exclusively by Al^{3+} ions and do not experience a full quota of positive charge, 2+.

The bulk conductivity of Mg0.5 is significantly lower than that of Mg0.05 although it contains 10x more Mg than Mg0.05, but nevertheless, it is still a modest mixed hole/oxide ion conductor. A ready explanation of this based on the results was found in which the concentration of both oxygen vacancies and electron holes is reduced and also in the literature on sintering and microstructural studies of doped alumina ceramics [22][27][28]: a key result was that the solubility of Mg in alumina is greatly enhanced by co-doping with Si. The sintering studies also showed that the initial location of dopants at grain boundaries (as expected by the in-diffusion mechanism associated with dopant incorporation) was followed by a gradual incorporation of Mg and Si into the grain interiors after, for example, heating at 1525 ^oC for 3 hours.

Literature data on well-sintered ceramics [22][27][28] show well-defined, thin grain boundaries, typically 1 nm thick, with segregation of dopants, at least in the early stages of sintering. Electrical microstructure results presented here on the well-sintered samples indicate that electrically, the grain boundary regions are very much thicker, even though the SE images show clear microstructures with narrow and pore-free contacts between grains. There is an apparent conflict, therefore, between the two types of microstructure, determined either directly by microscopy [22][27][28]or indirectly by impedance spectroscopy. Possibly, there are two types of grain boundary, thin ones seen by high resolution electron microscopy [22][27][28] which do not impact on the electrical properties and thick ones detected indirectly by impedance spectroscopy but for which there is no direct microscopic evidence. The grain boundary regions seen in the impedance data are more resistive than the bulk regions; they have higher activation energy and therefore, the concentration of mobile oxygen vacancies is less. The EDS results do not show any significant variation in Mg distribution throughout the grains. Possibly, a different mechanism of charge compensation exists in the grain boundary regions, such as the creation of either interstitial Mg^{2+} ions, equation (8.14), or O^- ions, equation (8.15) both of which avoid the creation of oxygen vacancies. Further studies, including high resolution TEM would be required to determine whether there is any cation segregation at the thin grain boundaries; from the

impedance results, however, there is no evidence of any additional impedance associated with thin grain boundary regions.

The results reported here, showing high temperature conductivity properties that range from oxide ion conduction to *p*-type electronic conduction, depending on composition, pO_2 and temperature, are consistent with early measurements on the *dc* conductivity of pure and Mg-doped alumina single crystals and polycrystals [6], [10]. Direct comparison with the literature is difficult, however, since our *ac* results show that grain boundary resistances dominate the impedance at lower temperatures whereas the higher activation energy of grain boundary resistances means that bulk resistances may dominate their impedance at temperatures $\geq 900^{o}C$, beyond the present measuring range and assuming linear Arrhenius behaviour.

Nevertheless, it is clear from [6], [10] that the materials are essentially *p*-type conductors at high temperature and increasingly, show a broad, pO_2-dependent electrolytic domain with ionic conductivity at lower temperatures. The general behaviour of Mg-doped polycrystalline Al_2O_3 [6] was reported to be similar to that of single crystal samples but the transition to electronic conduction occurred at lower temperatures and lower pO_2; possibly, this was because the higher oxygen vacancy concentration in the samples promoted an increase in *p*-type conduction. The activation energies for conductivity reported in [6] were in the range 2.5 to 3.5 eV; these are not inconsistent with our grain boundary activation energies in the range 2.29-2.36 eV. Our much lower bulk activation energy of 0.92 eV for Mg0.05 would not have been observed in *dc* measurements because of (i) the high grain boundary activation energy at lower temperatures and (ii) a switch to electronic conductivity at high temperatures.

It was not possible to solve the conundrum of the discrepancy between experimental and calculated diffusion parameters highlighted in [2]–[4] , but are able to suggest some additional factors that may merit consideration. From our results and the early literature on electrical properties, it is clear that for conductivity measurements in air or O_2, of both nominally pure and doped Al_2O_3, the materials are mixed conductors ranging from mainly oxide ion conduction at lower temperatures to *p*-type semi-conduction at the high temperatures, ~1600 ^{o}C, that are typically used in diffusion measurements. The *p*-type conductivity is likely to be a hopping conductivity which means that the holes are localised on an atomic species, for which the only realistic possibility is oxygen. Holes on oxygen equate to lower valence O^- ions instead of the ubiquitous O^{2-} ions. The structures therefore contain mixed anions, O^- and O^{2-}, as well as showing mixed ionic and electronic conductivity. Since O^- ions and the associated holes appear to be the dominant defects that control conductivity at $1600^{o}C$, their role in diffusion processes, of both Al and O, may be significant.

Clear evidence for two ionic charge compensation mechanisms have been showed here, leading to either oxygen vacancies or self-compensation of aliovalent cations, with the possibility under certain circumstances of a third mechanism involving either interstitial Mg^{2+} ions or O^- ions that fill available oxygen vacancies. Each of these compensation mechanisms may impact differently on the measurement of diffusion coefficients.

8.5 Conclusions

Some general conclusions can be drawn concerning the electrical properties of alumina ceramics, based on samples prepared with different doping schedules that were studied here.

The main charge compensation mechanism for incorporation of Mg^{2+} ions as a single dopant into the alumina lattice appears to involve oxygen vacancy creation. This is responsible for the observed oxide

ion conduction, for which evidence is provided by the presence of double layer capacitance effects in low frequency impedance data.

In the presence of Si, literature data suggest that dissolution of Mg is enhanced by a double substitution mechanism in which charge balance is achieved without oxygen vacancy creation. This is confirmed by the EDS results showing a uniform distribution of both Mg and Si dopants through the alumina grains and accounts for the much reduced oxide ion conductivity associated with a reduced oxygen vacancy concentration observed in composition Mg0.5 compared with Mg0.05.

The Mg-doped samples are mixed conductors of both oxide ions and holes. The level of hole conductivity is sensitive to oxygen partial pressure in the surrounding atmosphere. This sensitivity indicates rapid oxygen exchange between the surrounding atmosphere and sample surfaces at ~900 ^{o}C and is probably facilitated by the presence of oxygen vacancies in Mg-doped alumina.

The easy creation of holes on oxygen, as O^- ions, is attributed to the under-bonding of certain oxide ions associated with the acceptor dopant Mg^{2+}. Absorption of O_2 molecules and creation of holes may be represented ideally by equation (8.10), similar to what was proposed to account for the occurrence of *p*-type conductivity in acceptor-doped Ba and Sr titanate perovskites [28].

Although Al_2O_3 is regarded as a 'classic' ionic oxide, at high temperatures it is a *p*-type electronic semiconductor with holes located on oxygen. This means that, to achieve charge balance of O^- ions, a slight excess of oxygen, beyond that of the Al_2O_3 stoichiometry, may be required and especially, be facilitated by the availability of oxygen vacancies in Mg-doped alumina. In contrast to ceramic oxides such as TiO_2 and $BaTiO_3$, that lose a small amount of oxygen at high temperature by oxidation of some near-surface lattice O^{2-} ions and exhibit *n*-type semiconductivity, Mg-doped alumina shows only partial oxidation of O^{2-} ions, by reaction with O_2, giving rise to *p*-type semiconductivity associated with the resulting O^- ions.

8.6 References

[1] Y. Oishi and W. D. Kingery, "Self-Diffusion of Oxygen in Single Crystal and Polycrystalline Aluminum Oxide," *J. Chem. Phys.*, vol. 33, pp. 480–486, 1960.

[2] A. H. Heuer and K. P. D. Lagerlof, "Oxygen self-diffusion in corundum (α-Al_2O_3): A conundrum," *Philos. Mag. Lett.*, vol. 79, no. 8, pp. 619–627, 1999.

[3] A. H. Heuer, "Oxygen and aluminum diffusion in α-Al_2O_3: How much do we really understand?," *J. Eur. Ceram. Soc.*, vol. 28, no. 7, pp. 1495–1507, 2008.

[4] J. H. Harding, K. J. W. Atkinson, and R. W. Grimes, "Experiment and Theory of Diffusion in Alumina," *J. Am. Ceram. Soc.*, vol. 86, no. 4, pp. 554–59, Apr. 2003.

[5] J. Pappis and W. D. Kingery, "Electrical Properties of Single-Crystal and Polycrystalline Alumina at High Temperatures," *J. Am. Ceram. Soc.*, vol. 44, no. 9, pp. 459–464, Sep. 1961.

[6] N. M. Tallan and H. C. Graham, "Interfacial Polarization and Electrical Conductivity in Sapphire," *J. Am. Ceram. Soc.*, vol. 48, no. 10, pp. 512–516, 1965.

[7] K. J. W. Atkinson, R. W. Grimes, M. R. Levy, Z. L. Coull, and T. English, "Accommodation of impurities in α-Al_2O_3, α-Cr_2O_3 and α-Fe_2O_3," *J. Eur. Ceram. Soc.*, vol. 23, no. 16, pp. 3059–3070, 2003.

[8] J. Pan, J. Öijerholm, A. B. Belonoshko, A. Rosengren, and C. Leygraf, "Self-diffusion activation energies in α-Al_2O_3 below 1000°C - Measurements and molecular dynamics calculation," *Philos. Mag. Lett.*, vol. 84, no. 12, pp. 781–789, 2004.

[9] J. Öijerholm, "Ionic transport of α -alumina below 1000°C An in-situ impedance spectroscopy study," RoyalInstitute of Technology, Stockholm, Sweden, 2004.

[10] R. J. Brook, J. Yee, and F. A. Kröger, “Electrochemical Cells and Electrical Conduction of Pure and Doped Al_2O_3,” *J. Am. Ceram. Soc.*, vol. 54, no. 9, pp. 444–451, 1971.
[11] K. Kitazawa and R. L. Coble, “Electrical Conduction in Single-Crystal and Polycrystalline Al_2O_3 at High Temperatures,” *J. Am. Ceram. Soc.*, vol. 57, no. 6, pp. 245–250, 1974.
[12] H. P. R. Frederikse and W. R. Holser, *High Temperature Electrical Conductivity of Aluminum Oxide*, vol. 9. Boston, 1975.
[13] S. K. Mohapatra and F. A. Kröger, “Defect Structure of α-Al_2O_3 Doped with Magnesium,” *J. Am. Ceram. Soc.*, vol. 60, no. 3–4, pp. 141–148, 1977.
[14] H. A. Wang and F. A. Kröger, “Chemical Diffusion in Polycrystalline Al_2O_3,” *J. Am. Ceram. Soc.*, vol. 63, no. 11–12, pp. 613–619, Nov. 1980.
[15] D. S. Phillips, T. E. Mitchell, and A. H. Heuer, “Precipitation in star sapphire III. Chemical effects accompanying precipitation,” *Philos. Mag. A Phys. Condens. Matter, Struct. Defects Mech. Prop.*, vol. 42, no. 3, pp. 417–432, 1980.
[16] P. W. M. Jacobs and E. A. Kotomin, “Defect energies for pure corundum and for corundum doped with transition metal ions,” *Philos. Mag. A Phys. Condens. Matter, Struct. Defects Mech. Prop.*, vol. 68, no. 4, pp. 695–709, 1993.
[17] K. P. D. Lagerlöf and R. W. Grimes, “The defect chemistry of sapphire (α-Al_2O_3),” *Acta Mater.*, vol. 46, no. 16, pp. 5689–5700, Oct. 1998.
[18] A. J. Ruys, *Alumina Ceramics: Biomedical and Clinical Applications*. Woodhead Publishing, 2018.
[19] R. L. Coble, “Sintering Crystalline Solids. II. Experimental Test of Diffusion Models in Powder Compacts,” *J. Appl. Phys.*, vol. 32, no. 5, pp. 793–799, 1961.
[20] R. M. German, P. Suri, and S. J. Park, “Review: liquid phase sintering,” *J. Mater. Sci.*, vol. 44, no. 1, pp. 1–39, 2009.
[21] S. J. Bennison and M. P. Harmer, “Effect of MgO Solute on the Kinetics of Grain Growth in Al_2O_3,” *J. Am. Ceram. Soc.*, vol. 66, no. 5, p. C-90-C-92, 1983.
[22] T. Frueh *et al.*, “Powder chemistry effects on the sintering of MgO-doped specialty Al_2O_3,” *J. Am. Ceram. Soc.*, vol. 101, no. 7, pp. 2739–2751, 2018.
[23] M. Biesuz, “Flash Sintering of Alumina-based Ceramics,” University of Trento, 2017.
[24] D. P. Almond and A. R. West, “Impedance and modulus spectroscopy of ‘real’ dispersive conductors,” *Solid State Ionics*, vol. 11, no. 1, pp. 57–64, 1983.
[25] X. Vendrell and A. R. West, “Electrical properties of Yttria-stabilized zirconia, YSZ Single crystal: local AC and long range DC conduction,” *J. Electrochem. Soc.*, vol. 165, no. 11, pp. F966–F975, 2018.
[26] T. L. Weeding, B. H. W. S. de Jong, W. S. Veeman, and B. G. Aitken, “Silicon coordination changes from 4-fold to 6-fold on devitrification of silicon phosphate glass,” *Nature*, vol. 318, pp. 352–353, 1985.
[27] C. A. Handwerker, P. A. Morris, and R. L. Coble, “Effects of Chemical Inhomogeneities on Grain Growth and Microstructure in Al_2O_3,” *J. Am. Ceram. Soc.*, vol. 72, no. 1, pp. 130–136, 1989.
[28] K. L. Gavrilov, S. J. Bennison, K. R. Mikeska, J. M. Chabala, and R. Levi-Setti, “Silica and magnesia dopant distributions in alumina by high-resolution scanning secondary ion mass spectrometry,” *J. Am. Ceram. Soc.*, vol. 82, no. 4, pp. 1001–1008, 1999.
[29] M. Guo, N. Maso, Y. Liu, and A. R. West, “Electrical Properties and Oxygen Stoichiometry of Ba_{1-x} $Sr_xTiO_{3-\delta}$ Ceramics,” *Inorg. Chem.*, vol. 57, pp. 64–71, 2018.
[30] University of Baylon, “Phase diagrams.” [Online]. Available: http://www.uobabylon.edu.iq/eprints/publication_12_16142_5018.pdf.

8.7 Supplementary

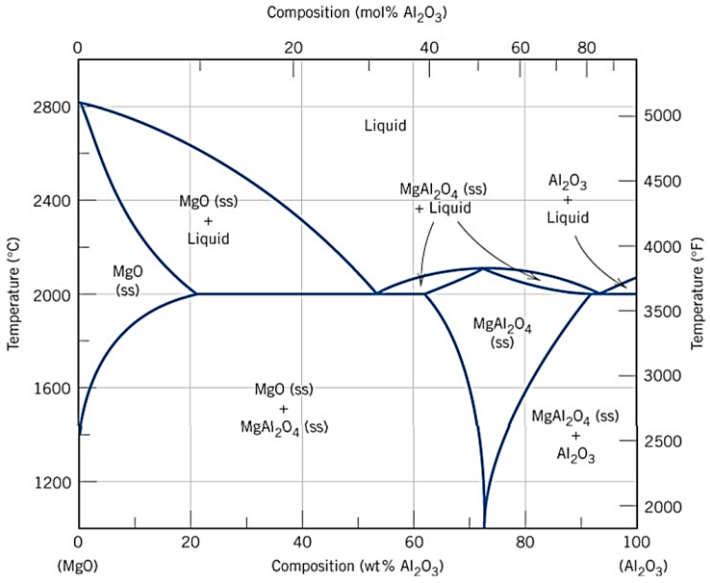

Figure 8.S1. *MgO-Al_2O_3 phase diagram* [30].

Chapter 9
Electrical properties of Mg-doped alumina: effect of *dc* bias

9.1 Introduction

Alumina (Al_2O_3) is a well-known dielectric [1]. A large range of applications rely on its electrically insulating properties. Therefore, it is of great interest to understand the dielectric breakdown conditions. The effect of MgO and SiO_2 on the dielectric strength of alumina has been studied [2] indicating that it increases when SiO_2 is the major impurity and decreases when MgO is added. In a different field of study, flash sintering, a sudden increase in conductivity is observed, along with densification and luminescence, when a large voltage is applied across a sample [3]. Mg-doped alumina has being flash sintered [4]. Similarity between flash sintering and electrical breakdown strength in dielectrics, has been pointed out [5] [6]. These two processes present a transition from insulating to conducting behaviour, need an incubation time which decreases with applied field, and are sensitive to sample geometry.

To gain insight into the early stages of these two processes, this work studies changes to the impedance of Mg-doped alumina during application of lower voltages than those used in flash sintering and dielectric breakdown. In addition, measurements involving a combination of applied voltage and change in oxygen partial pressure (pO_2) give further information about the nature of the mobile species.

9.2 Experimental

Impedance measurements of the same electroded samples that were used for chapter 8 (Mg0.5 and Mg0.05) were made at around 900°C using a conductivity jig which allowed flow of a gas over the pellet. An Agilent 4294A was used as impedance analyser (measurement accuracy ±0.08%), frequency range 40 Hz-3 MHz, with a nominal *ac* voltage of 100 mV. In some cases, a *dc* bias in the range 1-35 V was applied across samples, at the same time as impedance data were recorded. Two experiment profiles were used for application of the voltage, Figure 9.1. Profile **A** applied 15 minutes of voltage followed by 15 minutes of recovery at 0 V, with an electric field range from 5 to 75 Vcm^{-1}. Profile **B** applied 1 hour of voltage, electric field range 75 to 175 Vcm^{-1}, followed by voltage removal and impedance measurements over the time required to obtain a similar impedance response to that of the original state.

Two sets of corrections were made to the collected data: (i) a geometric factor consisting of pellet thickness and sample-electrode contact area and (ii) jig impedance characteristics consisting of the blank, open circuit capacitance, typically 6 pF and the closed circuit resistance of, primarily, the leads, 1-2 Ω. Data analysis was performed using ZVIEW software (ZVIEW-Impedance Software version 2.4 Scribner Associates).

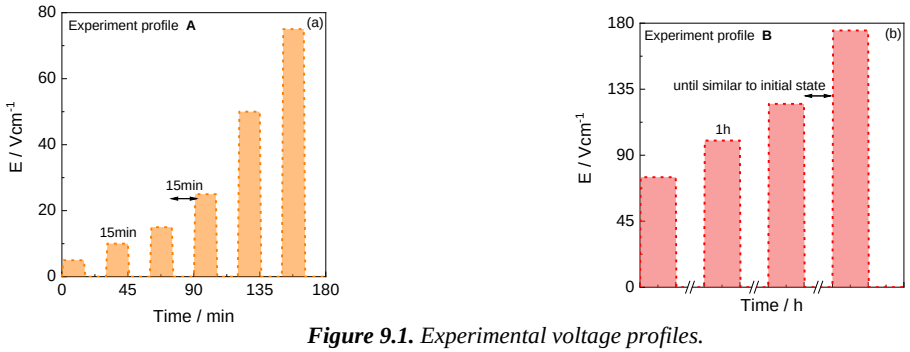

Figure 9.1. *Experimental voltage profiles.*

9.3 Results

9.3.1 Mg0.5

The impedance response of Mg0.5 at 909 °C, measured during and after application of an electric field ranging from 0 to 75 Vcm^{-1} for 15 mins, is shown in Figure 9.2. At 0 Vcm^{-1} the Z* plane (a) shows two arcs of similar size, labelled as R_1 and R_2 with decreasing frequency, which give a total resistance R_t (R_1+R_2) of ~ 1 MΩcm at 0 Vcm^{-1}, increasing to ~ 4 MΩcm at 75 Vcm^{-1}. The corresponding capacitances are shown in (b) with C_1~ 1 $pFcm^{-1}$ and C_2~ 10 $pFcm^{-1}$, in addition to the onset of a low frequency dispersion related to the sample-electrode interface. From the capacitance values, element 1 corresponds to the bulk response and element 2 to either the grain boundary, surface layer or shell of a core-shell structure. The increase in resistance with applied voltage was, however, time-dependent, as shown in (c). For each voltage, the resistance increased gradually and had not reached a steady state, even after 15 min. On removal of the bias, all of the resistances decreased gradually but also, had not recovered the initial value after 15 mins. The time evolution of the impedance response during the application, and after removal, of 75 Vcm^{-1}, is shown in Supplementary Figure 9.S1.

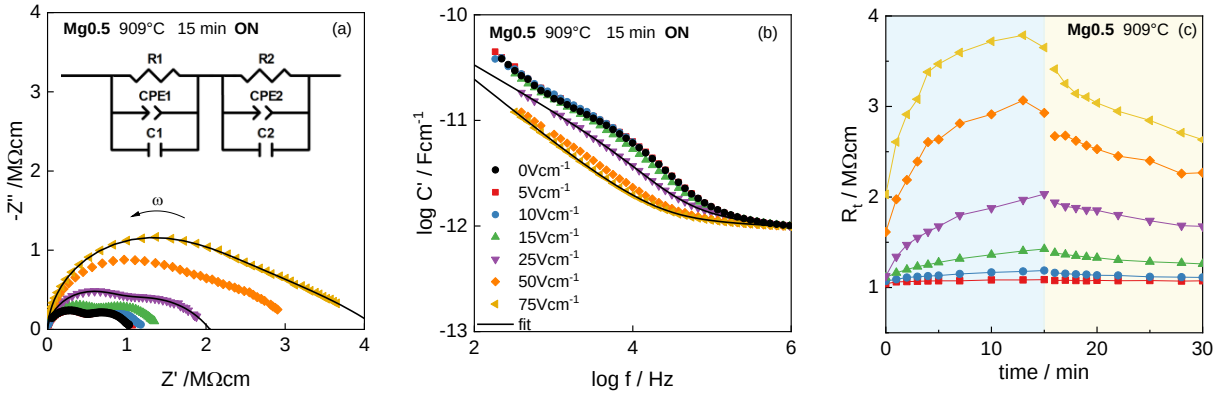

Figure 9.2. *(a)-(b) Impedance response after 15 minutes of applied voltage at 909°C. Inset (a) possible equivalent circuit. Continuous lines are fitted results. (c)Time dependence of Rt during and after the application of voltage using profile A, Figure 9.1.*

In order to further understand the effect of voltage and extract accurate resistance and capacitance values for the bulk and grain boundary impedances, equivalent circuit analysis was carried out. Two circuits were tested to fit Mg0.5 data at 0 Vcm^{-1}. The first consisted of two parallel R-CPE-C elements in series, Figure 9.3a, and the second included a series R-C element in parallel with the existing R-CPE-C bulk element, Figure 9.S3a. Addition of the series R-C element would represent a dielectric/dipole response, similar to that seen recently in yttria- and calcia-stabilised zirconia samples [7], [8]. In general, both circuits gave successful fits, Figures 9.S2, 9.S3, with the difference that, at high frequencies the residuals of the second circuit were lower. As the objective here was to extract the resistance and capacitance values, and both circuits gave similar values for these, the simpler circuit was used to fit the data with applied voltages in the range 5-75 Vcm^{-1}. The possibility of an additional dielectric component in the overall response was not further investigated here.

Examples of the fits (black lines) for 25 and 75 Vcm^{-1} are given in Figure 9.2(a,b). A more detailed presentation of the fit with 75 Vcm^{-1} is given in Figure 9.S4, where the residuals are shown and the contribution of individual bulk and grain boundary components is deconvoluted from the overall response.

The extracted resistance and capacitance values for the bulk and grain boundary as a function of voltage are summarised in Figure 9.3. Resistance values were taken from fits to the 15 min datasets although, as shown in Fig 9.2(c), these had not reached a steady state. Both R_1 and R_2 showed voltage dependence (a); however, R_1 showed a delayed response at lower voltages compared to R_2, but from 25 Vcm^{-1} a similar trend was followed in both. C_2 showed a consistent decrease in capacitance from 8.6(5) to 4(3) $pFcm^{-1}$ with increasing voltage (b). By contrast, C_1 appeared to show a slight increase from 0.93(1) to 1.1(2) $pFcm^{-1}$. This could be interpreted as a change in size of the two regions with voltage: the grain boundary is getting thicker as C_2 decreases and therefore, to compensate, the bulk is getting thinner as C_1 increases. As a note, one possible reason for the increased errors shown for R and C values at the higher voltages is the increased similarity of C_1 and C_2 values leading to more uncertainty in their refined values.

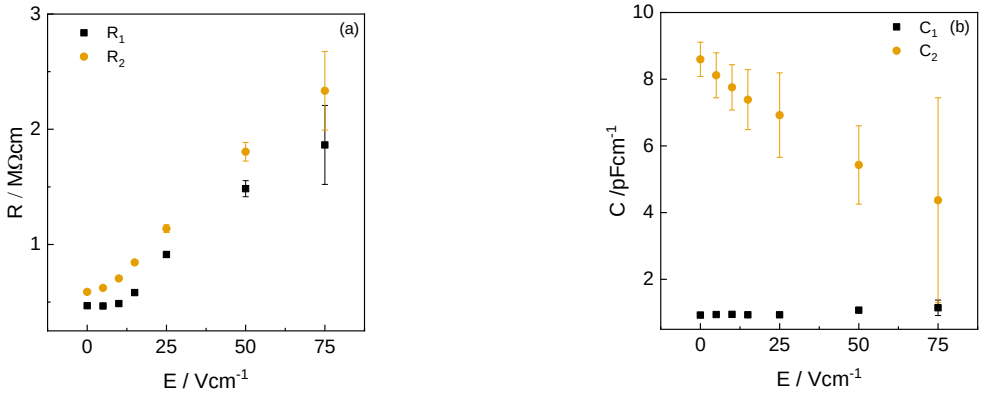

Figure 9.3. *Electric field dependence of fitted results of Mg0.5 at 909°C, resistances (a) and capacitances (b).*

9.3.2 Mg0.05

It was shown in chapter 8 that at 0 V, pellet Mg0.05 showed two impedance components, attributed to bulk and grain boundary elements and a low frequency spike that was evidence of a significant contribution of oxide ion conduction to the overall conductivity. For measurements with an applied bias, different impedance instrumentation was used that had a more limited frequency range, with a lower limit of 100 Hz, compared with 0.01 Hz for the zero bias studies. This meant that a full coverage of the low frequency impedance response was not available. In addition, the bulk impedance component was concealed under the high frequency wing of the distorted impedance arc dominated by the grain boundary impedance. Partly for this reason, the following results focus on the total resistance R_t only, where $R_t = R_1 + R_2$. At higher voltages and with increasing times, the low frequency spike changed into a curved arc from which an additional resistance R_3 was apparent.

The impedance response with and without applying 75 to 175 Vcm^{-1} for 1 hour at 914 °C is given in Figure 9.4. At 0 V, the Z* plane shows part of an arc with resistance R_t (a, inset). The log C' plot shows an intermediate frequency plateau (C_2 ~6 $pFcm^{-1}$) corresponding to the grain boundary and a low frequency dispersion representing the electrode contact impedance (b), as discussed in chapter 8.

With increasing voltage, the Z* plane (a) shows that R_t increases. The spike seen at 0 Vcm^{-1} (a inset), evolves into a large semicircle with resistance R_3 (eg R_3 ~ 6 MΩcm at 175 Vcm^{-1}). The log C' plot (b) shows that C_2 decreases to a similar value of ~ 0.93 $pFcm^{-1}$ at all voltages and an additional, poorly-resolved plateau forms of value ~20 $pFcm^{-1}$ at low frequencies, which is attributed to the new element, C_3.

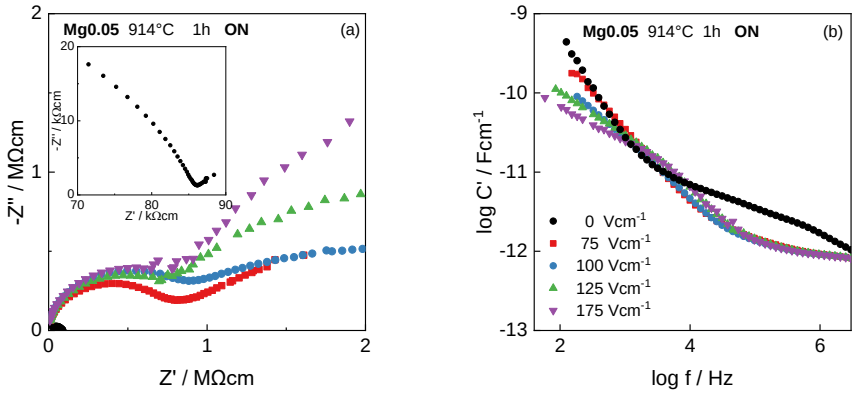

Figure 9.4. *Impedance response of Mg0.05 at 914°C, after 1 hour of applied voltage.*

These results are a snapshot taken after 1 hour of voltage application, but to reach this state there was a gradual change in the impedance response. A representative time dependence under 175 Vcm^{-1} is shown in Figure 9.5. In the first minute, R_t rises rapidly and C_2 appears to decrease. With time, R_t continues to increase but passes through a maximum around 7 minutes and then decreases. At the same time, R_3 appears and continues to increase with time, while R_t decreases.

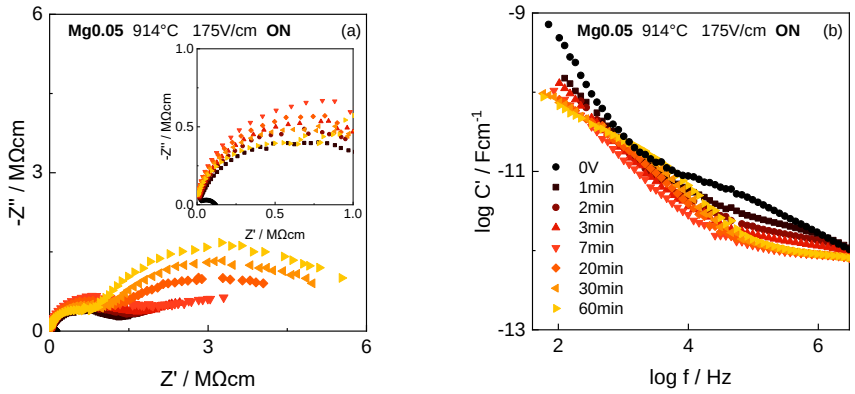

Figure 9.5. *Change in the impedance response of Mg0.05 at 914 °C with time, during the application of 175 Vcm^{-1}.*

On removal of the *dc* bias, the Z* and log C' plots, Figure 9.6, show that the time required to recover the initial state after application of 5 Vcm^{-1}, 15 min, and 150 Vcm^{-1}, 1h was both time- and voltage- dependent; ie after applying 5 Vcm^{-1} around 15 min of recovery was enough, but over 50 h recovery was required after applying 150 Vcm^{-1}.

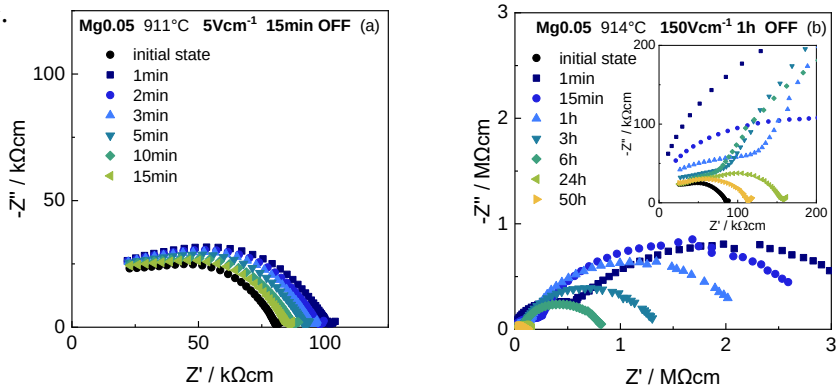

Figure 9.6. *Change in the impedance response of Mg0.05 with time, after the voltage cut off after applying 5 to 50 Vcm^{-1} for 15 min, and 150 Vcm^{-1} for 1 h.*

The effect of pO_2 on the impedance response under a *dc* bias, 175 Vcm^{-1} at 920 °C, is shown in Figure 9.7. The evolution with time is shown in N_2 (a,c) and O_2 (b,d). The Z* plane shows that R_t is larger under N_2 than O_2. With time under N_2, (a) R_3 and/or R_t increases and then gradually evolves into a spike at lowest frequencies. Under O_2 (b), R_3/R_t also increases, but remains as part of an arc. The log C' plots show that under N_2 (c), C_2 decreases faster than under O_2 (d).

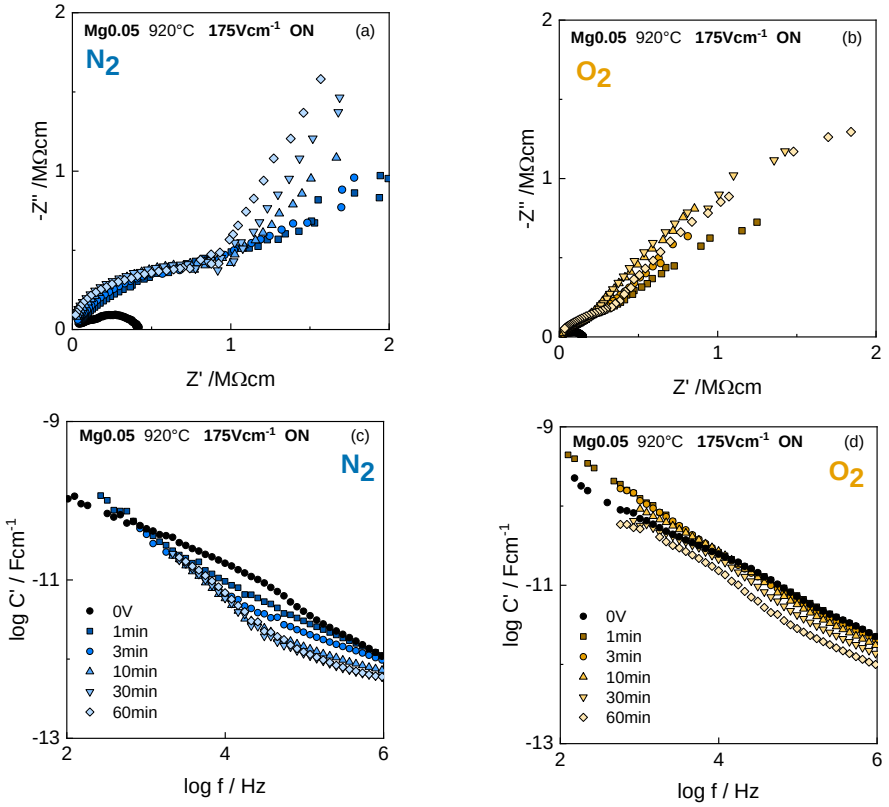

Figure 9.7. *Impedance response of Mg0.05 at 920 °C, during the application of 175 Vcm^{-1} under N_2 (a)(c) and O_2 (b)(d).*

The overall effect on R_t of both applying and subsequently removing electric fields up to 175 Vcm^{-1} is summarised in Fig 9.8(a,b) and of a field of 175 Vcm^{-1} in different pO_2 in Fig 9.8(c). Two regimes can be identified: ≤50 Vcm^{-1} and ≥75Vcm^{-1}. In the first, (a), R_t increased rapidly and reached a steady state with time. In the second, (b), R_t increased rapidly, reached a peak and then decreased gradually to a steady state. The magnitude of the peak increased with voltage.

When comparing the effect of *dc* bias in different atmospheres, Fig 9.8(c), the same trend was observed in N_2 and air, but R_t was slightly larger in N_2. In O_2, R_t did not pass through a maximum but instead, increased slowly and steadily. However, all three plots seem to converge with time, to give a similar steady state R_t value.

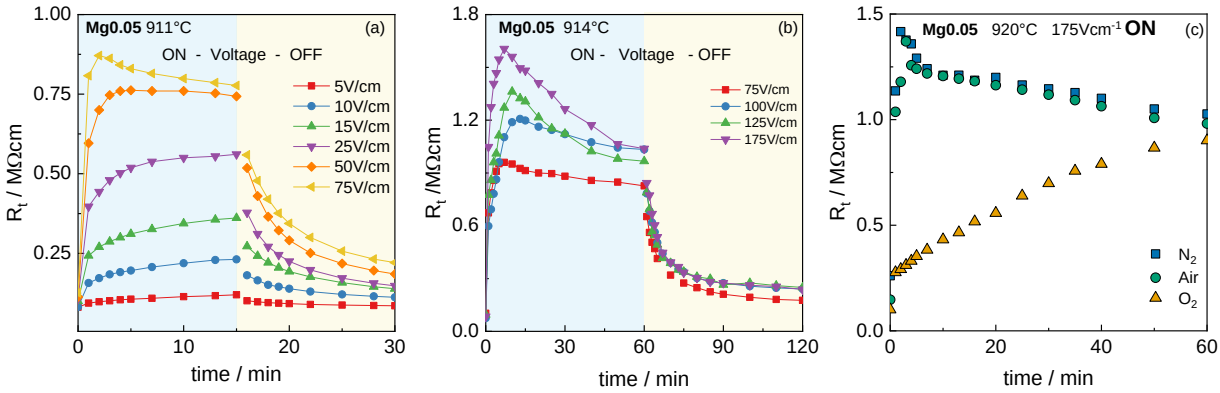

Figure 9.8. *Time dependence of Rt for Mg0.05 during application of voltage with (a) profile A at 911°C, (b) profile B at 914°C, (c) with 175 V/cm under N_2, air and O_2.*

9.4 Discussion

The data for Mg0.5 show that: (i) both resistances R_1 and R_2 increase with (a) increasing bias voltage, Fig 9.2(a) and (b) increasing time, Fig 9.2(c); (ii) on removal of the bias voltage, both resistances gradually reduce and may recover their original values after sufficient time, Fig 9.2(c); (iii) data for C_1 and C_2 show that the apparent grain boundary regions thicken with applied bias whereas the bulk becomes thinner, Fig 9.3(b); (iv) there is an induction period before R_1 starts to increase with applied bias, but this is not observed with R_2, Fig 9.3(a).

To account for these observations, we assume that the changes seen in the impedance results are associated entirely with the level of electronic *p*-type conductivity and that any effect of changes to possible oxide ion conductivity is negligibly small. We also note that, unusually, the electronic conductivity is *p*-type, which is the opposite of that expected for many materials which start to lose a little oxygen at high sintering temperatures, leading to *n*-type behaviour. *p*-type behaviour in a hopping conductor requires the holes to be located on a specific atomic species, which we believe is oxygen and leads to the unavoidable conclusion that O^- ions are responsible. Further, since the hole concentration increases with pO_2 (as judged by an increase in conductivity), oxygen from the atmosphere must be involved in creation of O^- ions. The only possible source of the necessary electrons to form O^- ions on dissociation of O_2 molecules, is pre-existing O^{2-} ions within /at the surface of the alumina lattice, Figure 9.9. In particular, these appear to be O^{2-} ions that are under-bonded and are associated with lower valence Mg^{2+} ions that substitute for Al^{3+} ions in the alumina crystal structure. Hence, the overall equation for the creation of holes is, ideally:

$$1/2O_2 + V_O^{\bullet\bullet} + O_O^x \leftrightarrow 2O_O^{\bullet} \qquad (9.1)$$

in which $O_O^{\bullet}$ is Kroger-Vink notation for an O^- ion.

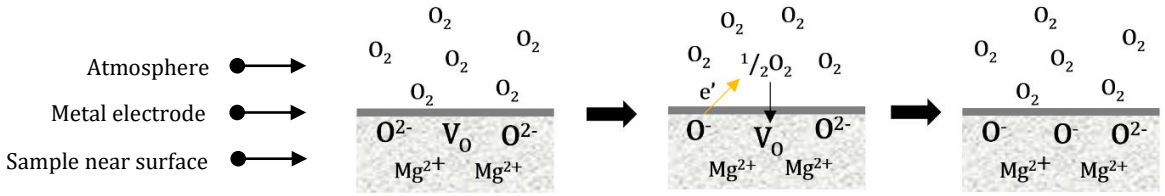

Figure 9.9. *Schematic diagram showing the creation of holes by donation of electrons from under-bonded lattice oxide ions to incoming oxygen molecules which dissociate and occupy oxide ion vacancies as O^- ions.*

The effect of either an applied bias, or reduction of pO_2 is to drive equation (9.1) to the left, although the exact mechanistic details associated with the effect of an applied bias are not fully resolved. In practice, the grain boundary resistance R_2 responds first to changing pO_2 or applied bias and this accounts for the induction period seen with R_1, *ie* the surface/grain boundary regions represented by R_2 respond to an external stimulus more quickly than the grain cores. The reduction in C_2 with increasing bias shows that the effective grain boundary regions thicken as O_2 is evolved from increasingly deeper regions of the alumina ceramic, leading also to a corresponding gradual reduction in thickness of the grain cores, or bulk regions. We do not understand the precise compositional / microstructural reasons why the grain boundaries are different from the grains but are able to comment on their electrical properties and changing dimensions. The diffusion of oxygen molecules / ions through the ceramic is likely to be very slow, which accounts for the time dependence of the resistance changes, which are particularly slow in the forward direction of equation (9.1) that requires the in-diffusion of oxygen.

The data for Mg0.05 present a more complex voltage response, in particular associated with the appearance of a third impedance element at high voltages. We were unable to deconvolute the contributions of R_1 and R_2 at the measuring temperature, ~ 900 ^oC and therefore, report data for R_t, although the data for R_t were probably dominated by R_2. R_t shows a complex time dependence, passing through a maximum after a few minutes under bias, especially at voltages above 50 Vcm^{-1}. At approximately the same time, the low frequency electrode spike becomes obscured by the appearance of a third impedance element, R_3C_3.

The impedance changes under bias depend strongly on pO_2 in the surrounding atmosphere, which confirms the controlling importance of oxygen exchange reactions at the sample surface on the overall electrical properties. The effect of changing pO_2 in isolation can be interpreted in terms of equation 9.1, but with an applied bias it is necessary to consider that different reactions or phenomena may be present at the two electrodes, both of which may contribute to the overall impedance response. At the positive electrode, O_2 gas may be released according to the ideal equation (9.2):

$$O^{2-} \rightarrow 1/2O_2 + 2e \qquad (9.2)$$

and the released electrons annihilate the holes responsible for the *p*-type conductivity, Figure 9.10(a), leading to the observed resistance increases under bias. At low voltages, there appears to be no evidence from the impedance data of any reactions at the negative electrode, but at high voltages, resistance decreases are observed at longer times that may indicate the onset of electron injection at the negative electrode, Figure 9.10 (b).

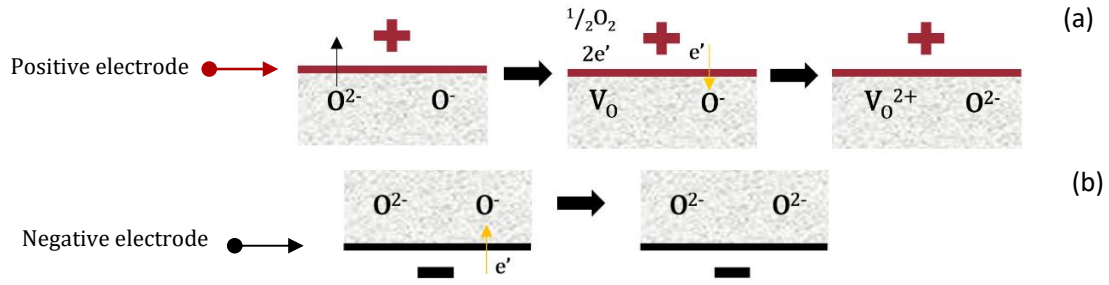

Figure 9.10. *Schematic diagram showing electron holes filled by electrons coming from oxygen loss at the anode/positive electrode(a) and electron injection at the cathode/negative electrode (b).*

The onset of resistance R_3 at high voltages indicates the creation of an additional high resistance component that may involve sample decomposition leading to loss of oxide ion conductivity. Since oxide ion vacancies

are created by the incorporation of Mg^{2+} ions into the alumina lattice, R_3 may result from decomposition of the solid solution and segregation of insulating Al_2O_3 and/or MgO components.

9.4.1 Comparison with, and comments on the Literature

Very many reports appear in the early literature on the electrical properties of pure and doped alumina ceramics and single crystals, from which, no clear picture has emerged. As stated in [9], 'all authors agree on the magnitude of the conductivity data ≥1400 °C, but there is a wide range of interpretation of these data'. We agree with several reports that, (i) at lower temperatures, materials are in the electrolytic domain and exhibit oxide ion conduction and (ii) at higher temperatures, materials exhibit primarily *p*-type electronic conduction, especially in atmospheres of high pO_2 [10-12].

Very few impedance measurements are reported in the early literature, other than a significant paper on dielectric measurements [13] which considers both dipolar processes and interfacial polarisation as the origin of tan δ peaks. A key conclusion, with which we strongly agree, is that a 'surface layer whose conductivity is different from that of the bulk appears, whose thickness depends on temperature and time of annealing treatment'; this is what we observe with resistances R_2 and R_3. Dielectric relaxation experiments between 700 and 1200°C, found a capacitance dispersion sensitive to pO_2, which vary its conductivity and thickness from 5 to 50 μm [13]. These results were interpreted by the interfacial polarization model and attributed to a surface layer or an internal interface. The formation of this layer was suggested to be a consequence of the time required to attain equilibrium by the moving species. Also, the possibility of second phase distributed as spheres or spheroids throughout the crystal could not be ruled out. In addition, the surface layer had a higher resistance than the bulk. Therefore, there is the possibility that R_3 and C_3 are associated with the formation of a second / surface layer product or a gradient of mobile species within the sample.

Very few *dc* bias studies have been reported, but in one, an alumina tube at 1537°C under vacuum, showed a decrease in conductivity with an applied electric field, ranging from 0 to 40 Vcm^{-1}[9], Figure 9.11. The behaviour of electrodes was established as non-blocking, allowing oxygen diffusion through the porous electrode (Pt-film). Thus, it was concluded that purely electronic or ionic conduction could not account for the magnitude of the observed conductivity. Figure 9.11, was adapted from Fig.1 ref [9], and the conductivity values were calculated using the following relationship:

$$J=\sigma E \qquad (9.3)$$

where J represents the current density and E the electric field.

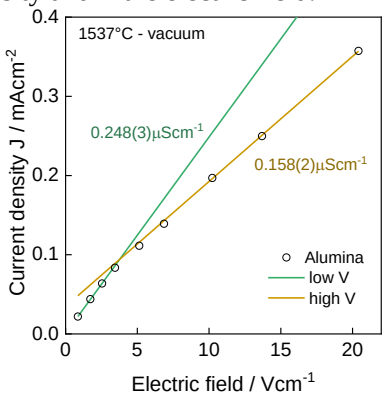

Figure 9.11. *Current density as function of applied voltage of an alumina tube under vacuum. Adapted from Fig 1 ref* [9].

9.5 Conclusions

The effect of a dc bias in the range 1-35 V at~900 °C on the impedance of two Mg-doped alumina ceramics has been studied, with very different results in the materials. Sample Mg0.5 showed a bias-dependent and time-dependent increase in both the bulk, R_1 and grain boundary/surface layer/shell, R_2 resistances. R_1 showed an induction period before the resistance rise which points to a mechanism involving oxygen loss that commences at the sample surface. The response of Mg0.05 was more complex; at higher voltages, the total resistance R_t (which ~ = R_2) passed through a maximum after a few minutes and again, O_2 loss appears to be the controlling parameter. The changes to R_1 and R_2 were reversible over longer timescales on removing the dc bias. The increase in resistances with a dc bias is attributed to electron-hole recombination and the loss of p-type conductivity associated with oxygen loss.

9.6 References

[1] K. Z. Rajab *et al.*, "Broadband dielectric characterization of aluminum oxide (Al_2O_3)," *J. Microelectron. Electron. Packag.*, vol. 5, no. 1, pp. 2–7, 2008.

[2] K. Zarbout *et al.*, "Consequences of Silicon Segregation on the Dielectric Properties of Sintered Alumina," *Defect Diffus. Forum*, vol. 249, pp. 281–285, 2006.

[3] C. E. J. Dancer, "Flash sintering of ceramic materials," *Mater. Res. Express*, vol. 3, no. 10, 2016.

[4] M. Cologna, J. S. C. Francis, and R. Raj, "Field assisted and flash sintering of alumina and its relationship to conductivity and MgO-doping," *J. Eur. Ceram. Soc.*, vol. 31, no. 15, pp. 2827–2837, 2011.

[5] M. Biesuz, "Flash Sintering of Alumina-based Ceramics," University of Trento, 2017.

[6] M. Biesuz, P. Luchi, A. Quaranta, and V. M. Sglavo, "Theoretical and phenomenological analogies between flash sintering and dielectric breakdown in α-alumina," *J. Appl. Phys.*, vol. 120, no. 14, 2016.

[7] X. Vendrell and A. R. West, "Electrical properties of Yttria-stabilized zirconia, YSZ Single crystal: local AC and long range DC conduction," *J. Electrochem. Soc.*, vol. 165, no. 11, pp. F966–F975, 2018.

[8] J. Ramírez-González and A. R. West, "Electrical properties of calcia-stabilised zirconia ceramics," *J. Eur. Ceram. Soc.*, in press, 2020.

[9] H. P. R. Frederikse and W. R. Holser, *High Temperature Electrical Conductivity of Aluminum Oxide*, vol. 9. Boston, 1975.

[10] R. J. Brook, J. Yee, and F. A. Kröger, "Electrochemical Cells and Electrical Conduction of Pure and Doped Al_2O_3," *J. Am. Ceram. Soc.*, vol. 54, no. 9, pp. 444–451, 1971.

[11] K. Kitazawa and R. L. Coble, "Electrical Conduction in Single-Crystal and Polycrystalline Al_2O_3 at High Temperatures," *J. Am. Ceram. Soc.*, vol. 57, no. 6, pp. 245–250, 1974.

[12] J. Pappis and W. D. Kingery, "Electrical Properties of Single-Crystal and Polycrystalline Alumina at High Temperatures," *J. Am. Ceram. Soc.*, vol. 44, no. 9, pp. 459–464, Sep. 1961.

[13] N. M. Tallan and H. C. Graham, "Interfacial Polarization and Electrical Conductivity in Sapphire," *J. Am. Ceram. Soc.*, vol. 48, no. 10, pp. 512–516, 1965.

9.7 Supplementary Figures

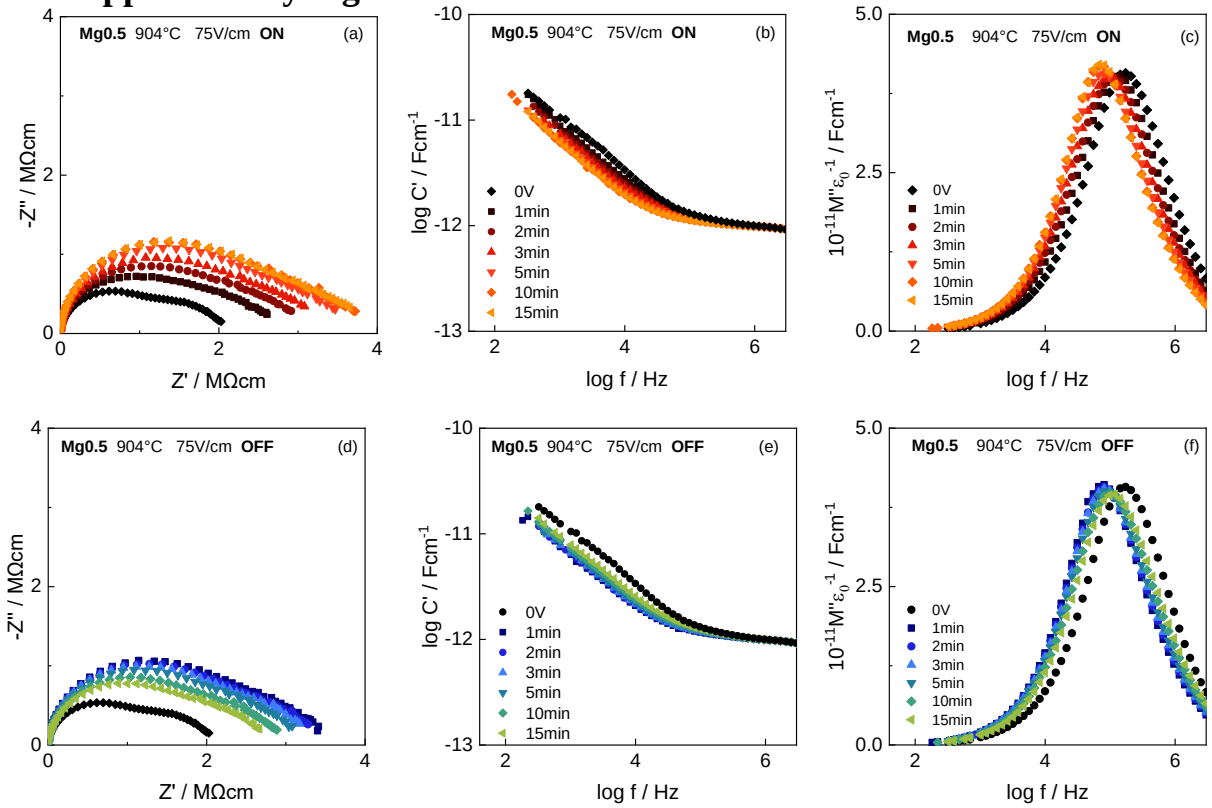

Figure 9.S1. *Impedance response of Mg0.5 at 904°C, during and after the application of 75Vcm^{-1}.*

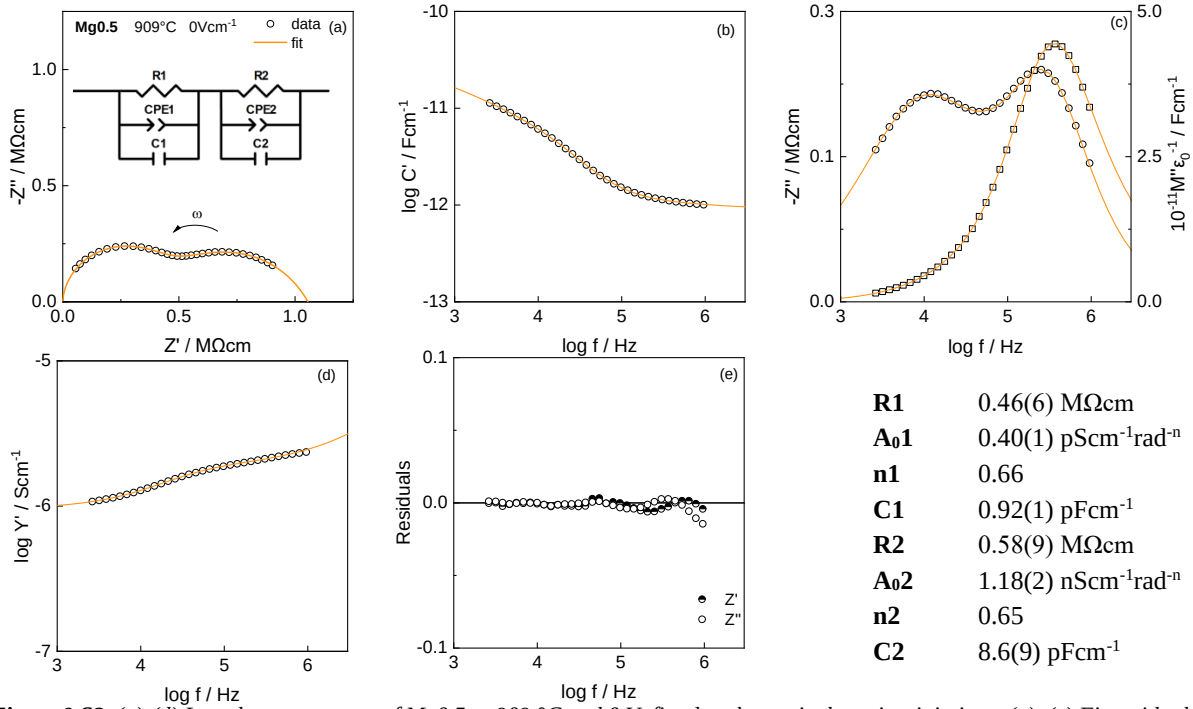

R1	0.46(6) MΩcm
$A_0$1	0.40(1) pScm^{-1}rad^{-n}
n1	0.66
C1	0.92(1) pFcm^{-1}
R2	0.58(9) MΩcm
$A_0$2	1.18(2) nScm^{-1}rad^{-n}
n2	0.65
C2	8.6(9) pFcm^{-1}

Figure 9.S2. *(a)-(d) Impedance response of Mg0.5 at 909 °C and 0 V, fitted to the equivalent circuit in inset (a). (e) Fit residuals and list of fit results for each circuit parameter.*

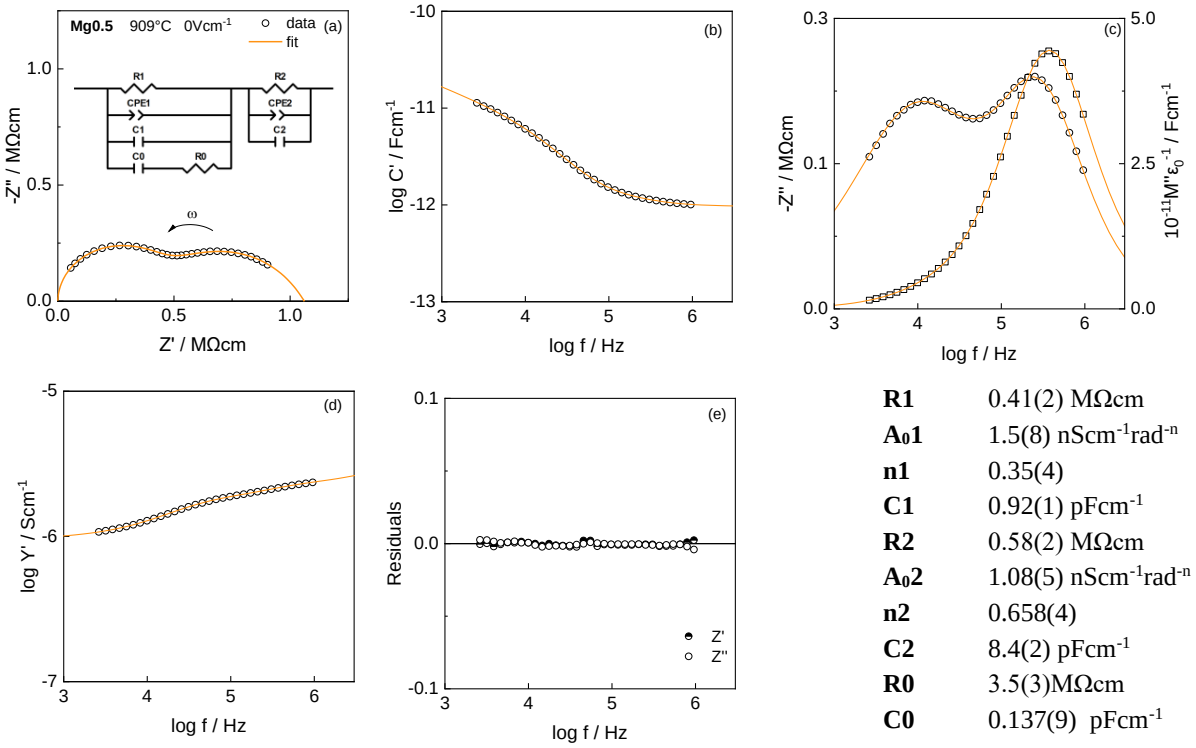

R1	0.41(2) MΩcm
$A_0$1	1.5(8) nScm^{-1}rad^{-n}
n1	0.35(4)
C1	0.92(1) pFcm^{-1}
R2	0.58(2) MΩcm
$A_0$2	1.08(5) nScm^{-1}rad^{-n}
n2	0.658(4)
C2	8.4(2) pFcm^{-1}
R0	3.5(3)MΩcm
C0	0.137(9) pFcm^{-1}

Figure 9.S3. *(a)-(d) Impedance response of Mg0.5 at 909 °C and 0 V, fitted to the equivalent circuit in inset (a), which includes a dipole element as part of the bulk response. (e) Fit residuals and list of fit results for each circuit parameter.*

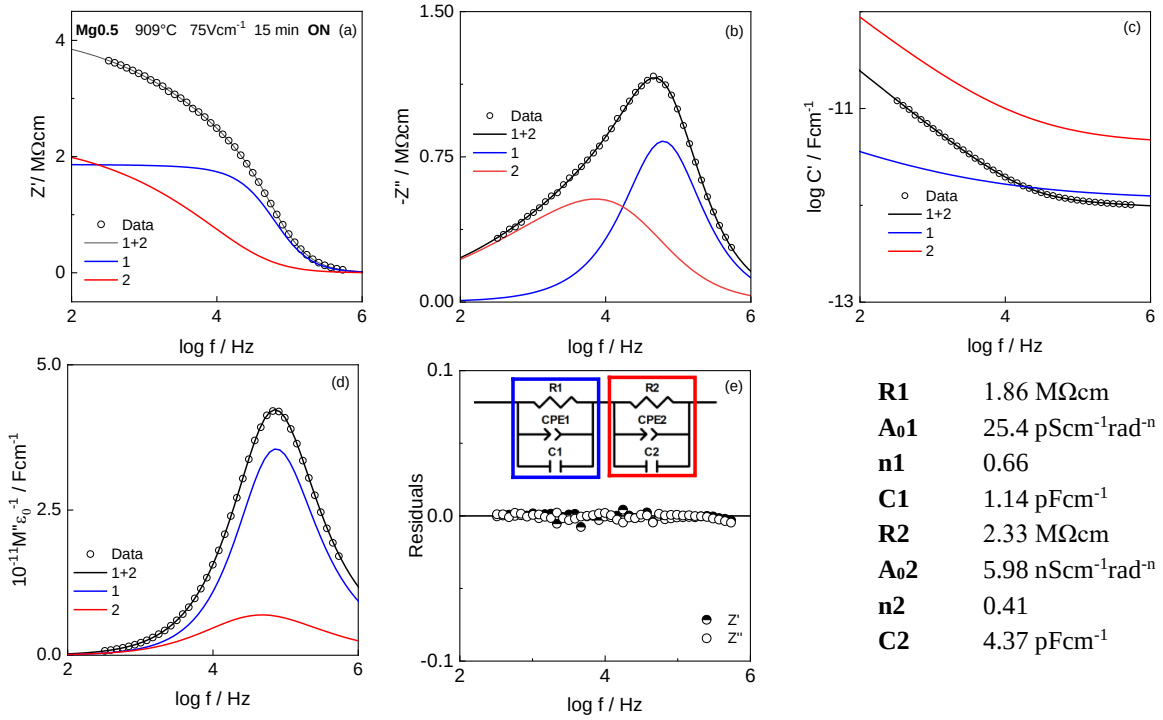

R1	1.86 MΩcm
$A_0$1	25.4 pScm^{-1}rad^{-n}
n1	0.66
C1	1.14 pFcm^{-1}
R2	2.33 MΩcm
$A_0$2	5.98 nScm^{-1}rad^{-n}
n2	0.41
C2	4.37 pFcm^{-1}

Figure 9.S4. *(a)-(d) Impedance response of Mg0.5 after 15 min of applying 75Vcm^{-1} and simulation of the response of the complete and deconvoluted equivalent circuit (e). (e) Fit residuals and list of fit results for each circuit parameter.*

Chapter 10
Conclusions

Flash sintering can reduce the sintering time from hours to ≤ 1 minute [1]. The onset mechanisms of this technique are still under debate. Therefore, the aim of this study was to gain further understanding of the early stages of this process. The approach was to (i) choose a material (calcia-stabilised zirconia and Mg-doped alumina), (ii) identify its electrical properties using impedance spectroscopy and (iii) observe how they change as function of temperature, oxygen partial pressure (pO_2) and applied voltage. This allowed to observe how the electrical microstructure of these materials changed at the pre-monitored region of the *flash event*.

10.1 Calcia-stabilised zirconia

Calcia-stabilised zirconia ceramics with composition CSZ ($Ca_xZr_{1-x}O_{2-x}$:$0.10 \leq x \leq 0.20$) were synthesised by solid state reaction. Single phase samples belonging to the cubic solution were obtained. The lattice parameter increased linearly with composition, following Vegard's Law. Detailed impedance analysis of compositions $0.12 \leq x \leq 0.18$ in the temperature range 190-900°C showed the presence of bulk (R_b), grain boundary (R_{gb}) and sample-electrode (R_{el}) responses, as well as an inductive effect above 600°C.

Conductivity Arrhenius plots presented a decrease in conductivity with increasing *x*. A similar effect has been observed in Scandia-, Yttria- and other Calcia-stabilised zirconias. This was attributed to aggregates of $V_O^{\cdot\cdot}$- $V_O^{\cdot\cdot}$ pairs [2][3] or Ca_{Zr}''-$V_O^{\cdot\cdot}$-Ca_{Zr}'' trimers [4][5]. The calculated bulk and grain boundary activation energies were ~1.1eV, indicating the migration or hopping of oxygen ions. The total conductivity ($\sigma_t \equiv R_t^{-1}$; $R_t = R_b + R_{gb}$) showed curvature at the highest temperatures. This behaviour may be explained by dissociation of trapped $V_O^{\cdot\cdot}$, as the number of $V_O^{\cdot\cdot}$- $V_O^{\cdot\cdot}$ pairs is temperature dependent, demonstrated by molecular dynamic simulations [3]. However, the origin of the curvature remains an open question.

A good fit to the bulk response was obtained when a series R-C element was added in parallel to a parallel R-C-CPE element. The series R-C element represents a dielectric/dipole response, attributed to a Ca_{Zr}''- $V_O^{\cdot\cdot}$ pair. The activation energy for the dielectric component increased with *x*. This could be caused by an increase in the number of Ca_{Zr}''-$V_O^{\cdot\cdot}$ pairs or to their coalescence into larger aggregates, causing greater difficulty for the dipole reorientation. The permittivity of the dipole increased with temperature, due to thermal motion, and decreased with *x*, by an increment in the dipole cluster strength. The presence of a local conduction process, such as a dipole reorientation in parallel with the long-range conduction, does not affect the value of the sample bulk conductivity. However, it is evident on fitted impedance data on the most appropriate equivalent circuit.

The electrode response was fitted to a parallel R_{ct}-C_{dl} element in series with a parallel R_{diff}-CPE_{zw} element. These parameters represent a charge transfer resistance (R_{ct}), double layer capacitance (C_{dl}), diffusion processes model with a Warburg impedance as a CPE (CPE_{zw}) and, a finite resistance for the diffusion process (R_{diff}). R_{ct} and R_{diff} were deconvoluted from the total electrode response, and it was found that $R_{ct} << R_{diff}$.

Preliminary results of atmosphere-dependence impedance measurements showed that the limits of the electrolytic domain varied with temperature and composition. Around 400°C, samples of all compositions remained independent of pO_2. Near 930°C, sample with composition x=0.12 showed introduction of n-type conduction, whereas x=0.18 presented p-type conduction. The cause of such n-

type conductivity is an indication of oxygen loss and the p-type conduction of oxygen intake. The electron holes may be located on under-bonded oxygen ions near the surface and/or near acceptor dopants.

Voltage-dependence impedance measurements showed that R_b, R_{gb} and R_{el} decreased with increasing voltages. This effect was enhanced at higher temperatures. R_{el} was the most sensitive to voltage, and R_b, only showed *dc* bias dependence under higher voltages and temperatures. High yttria content zirconia and 8mol%YSZ have shown pO_2- and *dc*- bias dependence [6][7]. The resistance decreases under high pO_2 and with increasing voltages, around 750°C and 800°C. This behaviour was attributed to an introduction of p-type conductivity. Impedance studies of $Y_{0.50}Zr_{0.49}Mg_{0.01}O_{1.74}$ have shown a transition from p-type to n-type conduction above 2V under reducing atmospheres [8]. By comparison with these systems, the voltage-dependence of CSZ was attributed to the introduction of p-type conduction, with the electron holes localised on under-bonded oxygen ions. The application of extreme conditions (250V/cm for 2h at 750°C) resulted in a resistance increment of ~ 4 order of magnitude larger than the original state. The nature of this highly resistive component remained unknown.

10.2 Flash-sans sintering

CSZ samples of composition x=0.15 subjected to flash sintering showed an abrupt increase in conductivity and emission of light. However, no densification was observed during the *flash event*. The implication of these results was that the sintering process could be separated from the emission of light and the increase in conductivity, suggesting that they may be different in nature. The results can be compared to those performed on fully dense samples [9] and single crystals [10], where the increment in conductivity and luminescence was observed and densification was not required. In those studies, it was proposed that the rise in conductivity was due to the creation of e-h pairs while the emission of light resulted from the recombination of these two electronic species.

10.3 Mg-doped Alumina

By impedance spectroscopy it was possible to identify the bulk, grain boundary and electrode response of Mg-doped alumina, with composition 0.05*wt%MgO-*Al_2O_3 (Mg0.05) and 0.5*wt%MgO/*SiO_2-Al_2O_3 (Mg0.5). The literature proposes several defects responsible for the conductivity and/or diffusion in aluminas, such as aluminium vacancies ($V_{Al}^{'''}$), aluminium interstitials ($Al_i^{\bullet\bullet\bullet}$), oxygen vacancies ($V_O^{\bullet\bullet}$) and oxygen interstitials ($O_i^{''}$) [5]–[17]. A similar case is found for the compensation of dopants, suggesting that divalent ions are compensated by $V_O^{\bullet\bullet}$ [10] or $Al_i^{\bullet\bullet\bullet}$ [7]. This study concludes that the main charge compensation mechanism for incorporation of Mg^{2+} ions as a single dopant into the alumina lattice, appears to involve $V_O^{\bullet\bullet}$ creation. This is responsible for the observed oxide ion conduction, for which evidence is provided by the presence of double layer capacitance effects in low frequency impedance data.

Under different atmosphere Mg-doped samples showed pO_2 dependence around 900°C, providing evidence of mixed ionic and p-type electronic conduction. The easy creation of electron holes on oxygen ions, as O^-, is attributed to the under-bonding of certain oxide ions associated with the acceptor dopant Mg^{2+}. Absorption of O_2 molecules and creation of holes may be represented ideally by equation (8.2). These results agree with the literature where conductivity values measured at 1650°C showed pO_2 dependence. The conductivity increased in either reducing or oxidizing atmospheres, separated by an increasingly broadened electrolytic domain in ambient atmospheres as temperature decreased to 1200°C [17].

The sample resistance increased with the application of a *dc* bias. This effect was enhanced at low pO_2, which lead to the conclusion that oxygen loss might occur under high voltages, resulting in an electron-hole recombination and the loss of p-type conductivity.

10.4 Simulation of equivalent circuits and their impedance response

The deconvolution of the impedance spectra has proven to be useful, showing the relative importance of the individual electrical elements to the overall impedance response. It was found that the CPE parameters contribute to the whole impedance response. It was corroborated that a series R-C element in parallel with a typical bulk equivalent circuit, does not contribute to the dc conductivity. Finally, it was observed that in the presence of an inductive effect, in some cases, Rt value does not correspond to the high frequency intercept with Z'.

10.5 References

[1] M. Biesuz and V. M. Sglavo, "Flash sintering of ceramics," *J. Eur. Ceram. Soc.*, vol. 39, no. May 2018, pp. 115–143, 2018.

[2] S. T. Norberg *et al.*, "Structural disorder in doped zirconias, part I: the $Zr_{0.8}Sc_{0.2-x}Y_xO_{1.9}$ ($0.0 \leq x \leq 0.2$) System," *Chem. Mater.*, vol. 23, no. 6, pp. 1356–1364, 2011.

[3] D. Marrocchelli, P. A. Madden, S. T. Norberg, and S. Hull, "Structural disorder in doped zirconias, part II: vacancy ordering effects and the conductivity maximum.," *Chem. Mater.*, vol. 23, no. 6, pp. 1365–1373, 2011.

[4] A. Nakamura and J. B. Wagner, "Defect structure, ionic conductivity, and diffusion in calcia-stabilized zirconia," *J. Electrochem. Soc.*, vol. 127, no. 11, pp. 2325–2333, 1980.

[5] A. Nakamura and J. B. Wagner, "Defect structure, ionic conductivity, and diffusion in yttria stabilized zirconia and related oxide electrolytes with fluorite structure," *J. Electrochem. Soc.*, vol. 133, no. 8, p. 1542, 1986.

[6] M. Jovaní, H. Beltrán-Mir, E. Cordoncillo, and A. R. West, "Atmosphere- and voltage-dependent electronic conductivity of oxide-ion-conducting $Zr_{1-x}Y_xO_{2-x/2}$ ceramics," *Inorg. Chem.*, vol. 56, no. 12, pp. 7081–7088, 2017.

[7] X. Vendrell and A. R. West, "Induced p-type semiconductivity in yttria-stabilized zirconia," *J. Am. Ceram. Soc.*, vol. 102, no. 10, pp. 6100–6106, 2019.

[8] M. Jovaní, H. Beltrán-Mir, E. Cordoncillo, and A. R. West, "Field-induced p-n transition in yttria-stabilized zirconia," *Sci. Rep.*, vol. 9, 2019.

[9] J. M. Lebrun and R. Raj, "A first report of photoemission in experiments related to flash sintering," *J. Am. Ceram. Soc.*, vol. 97, no. 8, pp. 2427–2430, 2014.

[10] D. Yadav and R. Raj, "The onset of the flash transition in single crystals of cubic zirconia as a function of electric field and temperature," *Scr. Mater.*, vol. 134, pp. 123–127, 2017.

[11] J. Pappis and W. D. Kingery, "Electrical Properties of Single-Crystal and Polycrystalline Alumina at High Temperatures," *J. Am. Ceram. Soc.*, vol. 44, no. 9, pp. 459–464, Sep. 1961.

[12] N. M. Tallan and H. C. Graham, "Interfacial Polarization and Electrical Conductivity in Sapphire," *J. Am. Ceram. Soc.*, vol. 48, no. 10, pp. 512–516, 1965.

[13] K. J. W. Atkinson, R. W. Grimes, M. R. Levy, Z. L. Coull, and T. English, "Accommodation of impurities in α-Al_2O_3, α-Cr_2O_3 and α-Fe_2O_3," *J. Eur. Ceram. Soc.*, vol. 23, no. 16, pp. 3059–3070, 2003.

[14] J. Pan, J. Öijerholm, A. B. Belonoshko, A. Rosengren, and C. Leygraf, "Self-diffusion activation energies in α-Al_2O_3 below 1000°C - Measurements and molecular dynamics calculation," *Philos. Mag. Lett.*, vol. 84, no. 12, pp. 781–789, 2004.

[15] J. Öijerholm, "Ionic transport of α -alumina below 1000 °C An in-situ impedance spectroscopy study," RoyalInstitute of Technology, Stockholm, Sweden, 2004.

[16] R. J. Brook, J. Yee, and F. A. Kröger, "Electrochemical Cells and Electrical Conduction of Pure and Doped Al_2O_3," *J. Am. Ceram. Soc.*, vol. 54, no. 9, pp. 444–451, 1971.

[17] K. Kitazawa and R. L. Coble, "Electrical Conduction in Single-Crystal and Polycrystalline

Al_2O_3 at High Temperatures," *J. Am. Ceram. Soc.*, vol. 57, no. 6, pp. 245–250, 1974.
[18] H. P. R. Frederikse and W. R. Holser, *High Temperature Electrical Conductivity of Aluminum Oxide*, vol. 9. Boston, 1975.
[19] S. K. Mohapatra and F. A. Kröger, "Defect Structure of α-Al_2O_3 Doped with Magnesium," *J. Am. Ceram. Soc.*, vol. 60, no. 3–4, pp. 141–148, 1977.
[20] H. A. Wang and F. A. Kröger, "Chemical Diffusion in Polycrystalline Al_2O_3," *J. Am. Ceram. Soc.*, vol. 63, no. 11–12, pp. 613–619, Nov. 1980.
[21] D. S. Phillips, T. E. Mitchell, and A. H. Heuer, "Precipitation in star sapphire III. Chemical effects accompanying precipitation," *Philos. Mag. A Phys. Condens. Matter, Struct. Defects Mech. Prop.*, vol. 42, no. 3, pp. 417–432, 1980.
[22] P. W. M. Jacobs and E. A. Kotomin, "Defect energies for pure corundum and for corundum doped with transition metal ions," *Philos. Mag. A Phys. Condens. Matter, Struct. Defects Mech. Prop.*, vol. 68, no. 4, pp. 695–709, 1993.
[23] K. P. D. Lagerlöf and R. W. Grimes, "The defect chemistry of sapphire (α-Al_2O_3)," *Acta Mater.*, vol. 46, no. 16, pp. 5689–5700, Oct. 1998.

Chapter 11
Future work

11.1 Calcia-stabilised zirconia

The equivalent circuit with the best fit to the bulk response included a dielectric/dipolar component. Two techniques that might reveal more information or further evidence of this dielectric component are: dielectric loss transient spectroscopy (DLTS), and thermally stimulated depolarization current (TSDC). Therefore, CSZ samples of different compositions could be tested using these techniques and their results compared to the ones in chapter 4.

Chapter 5 showed that the limits of the electrolytic domain of CSZ vary with temperature and composition. To corroborate this conclusion, the impedance of samples with composition x=0.1 and 0.2 could be measured as a function of temperature and pO_2. Composition x=0.1 is expected to show n-type conduction and x=0.2 p-type conduction. In addition, the combined effect of pO_2 and applied voltage could be tested.

The nature of the highly resistive component that appeared after the application of 250V/cm for 2h at 750°C requires further study. Information about the elemental composition, concentrations and chemical environments (oxidation states) of the cross-section surface might be useful. This information could be gathered by X-ray photoelectron spectroscopy (XPS).

11.2 Flash-sintering

Flashed sintered samples of 8mol% YSZ have shown enhanced ionic conductivity compared to the ones that were conventionally sintered [1]. To find out if CSZ shows a similar behaviour, the impedance response of compositions that have been conventionally sintered to the one that have been flashed sintered could be compared, as shown in Figure 12.1.

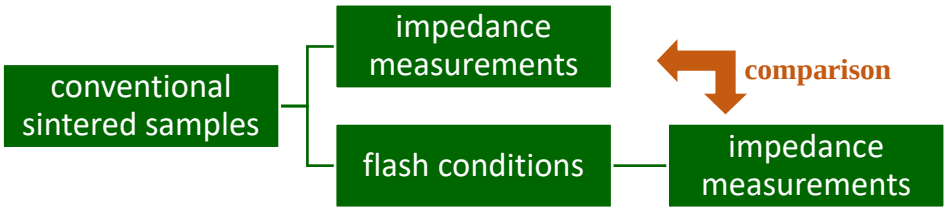

Figure 12.1. *Experiment profile to find out if the flash event changes the ionic conductivity of CSZ samples*

The possibility of starting a mixture of reagents and obtaining a dense single-phase sample a brief flash sintering experiment has been explored and referred to as *reactive flash sintering* [2]–[4]. A comprehensive study could be developed to find out whether CSZ sample could be obtained by this method.

11.3 Mg-doped Alumina

The combined effect of applied voltage and pO_2 dependence in the impedance response of Mg0.05 indicates that under high voltages, oxygen loss occurs. To support this conclusion, samples could be quenched from high temperatures under reducing atmospheres, and their impedance response compared with that of an untreated sample, Figure 12.2

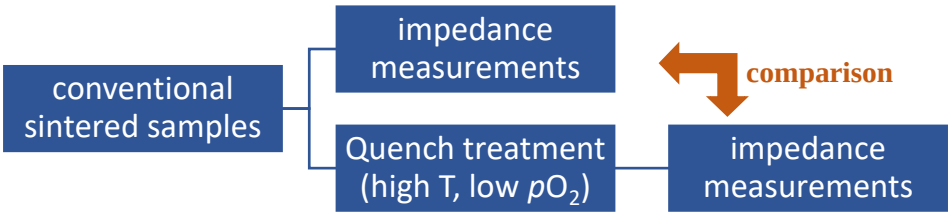

***Figure 12.2**. Experiment profile to find out if Mg-doped Alumina loses oxygen under reducing atmospheres at high temperature.*

Different diffusion and charge transfer processes might occur at each electrode during the application of a *dc* bias. One possible approach to identify them and separate them could be the implementation of a 3-point impedance measurement; by doing this the impedance of the positive and negative electrode could be contrasted.

11.4 References

[1] X. Vendrell, D. Yadav, R. Raj, and A. R. West, "Influence of flash sintering on the ionic conductivity of 8 mol% yttria stabilized zirconia," *J. Eur. Ceram. Soc.*, vol. 39, no. 4, pp. 1352–1358, Apr. 2019.

[2] E. Gil-González, A. Perejón, P. E. Sánchez-Jiménez, M. J. Sayagués, R. Raj, and L. A. Pérez-Maqueda, "Phase-pure $BiFeO_3$ produced by reaction flash-sintering of Bi_2O_3 and Fe_2O_3," *J. Mater. Chem. A*, vol. 6, no. 13, pp. 5356–5366, 2018.

[3] B. Yoon, D. Yadav, S. Ghose, and R. Raj, "Reactive flash sintering: MgO and α-Al_2O_3 transform and sinter into single-phase polycrystals of $MgAl_2O_4$," *J. Am. Ceram. Soc.*, vol. 102, no. 5, pp. 2294–2303, 2019.

[4] V. Avila and R. Raj, "Reactive Flash Sintering of Powders of Four Constituents into a Single phase of a Complex Oxide in a Few Seconds below 700°C," *J. Am. Ceram. Soc.*, vol. 00, p. jace.16625, 2019.